

Submitted by
Philipp Stadler

Submitted at
**Institute of Physical
Chemistry**

Metallic properties of conducting polymers

June 2019



Habilitation Thesis

for the attainment of the permission to lecture

Physical Chemistry

at the Faculty of Engineering and Natural Science of the Johannes
Kepler University Linz

Contents

1	Motivation	4
2	Introduction	6
2.1	State-of-the-art	6
2.2	Metallic conduction and disorder	7
2.3	Phonons and polarons in conducting polymers	12
2.4	Transport in and close to the metallic regime	13
2.5	Magnetoconductivity	16
2.6	Electron coherence and scattering	17
2.7	Weak localization and band mobilities	19
2.8	Functional conducting polymers	24
2.9	Acknowledgements	27
2.10	References	28
3	Publications surveyed in this thesis	38
3.1	Metallic conducting polymers	38
3.2	Functional conducting polymers	43
3.3	Optoelectronic characterization and applications	45
3.4	Book chapter	47
3.5	Review	47
4	Manuscripts	48
4.1	Manuscript 1	48
4.2	Manuscript 2	55
4.3	Manuscript 3	63
4.4	Manuscript 4	72
4.5	Manuscript 5	81
4.6	Manuscript 6	89
4.7	Manuscript 7	99

4.8	Manuscript 8	106
4.9	Manuscript 9	115
4.10	Manuscript 10	124
4.11	Manuscript 11	158
5	Teaching activities	169
5.1	Lectures and courses	169
5.2	Supervision of PhD, Master and Bachelor Students	169
6	List of Publications	171
6.1	Scientific papers (peer reviewed / SCI indexed)	171
6.2	Patent	177
6.3	Book chapters and reviews	177
6.4	Scientific conference proceedings & papers	178
6.5	Thesis	178
7	Curriculum Vitae	179

1 Motivation

The discovery of electrical conductivity and, further, metallic conductivity in polymers has attracted scientists now more than 4 decades^[1,2]. The exploration of metal-like transport in polyacetylene and conductivities up to 10^5 S cm^{-1} led to expectation of transport beyond metals and the possibility of superconducting states^[3-9]. However, the transport in polyacetylene is highly anisotropic, the polymer is unstable and the overall performance still far away from the previous expectations.

Today, the research focus shifted towards stable polymer structures and towards achieving an isotropic metallic transport combined with facile processing and synthesis.

In the past four years I developed such isotropic and metallic conducting polymers. These base on a simple synthesis and processing methods. My results led to a substantial impact in the field of organic electronics. My central motivation was that conducting polymers, other than classic inorganic semiconductors, offer an unique structural tunability. I used this versatility to develop new conducting polymers and I demonstrated discrete applications in the field of optoelectronics and catalysis. These insights and findings were published in high-impact journals and I created a new field in organic electronics and catalysis. The results and performances I achieved show the competitiveness of conducting polymers to become a sustainable technology. The here presented habilitation thesis provides an overview of the relevant publications in the context of the concurrent state-of-the-art. These works demonstrated following central scientific efforts:

- The development of high-quality conducting polymers with explicit isotropic metallic state and superior conductivities as compared to the state-of-the-art^[10,11].
- The study of the electrical transport mechanisms responsible for the metal-insulator transition in metallic and semimetallic conducting polymers based on magnetoconductivity, pressure-dependent magnetoconductivity and the Hall-effect^[12-14].
- The spectroscopic investigation and modeling of the optical and optoelectronic parameters induced by doping in different conjugated or conducting polymer^[15,16].

- The synthesis of a new generation of functional hydrogen-bonded conducting polymers and the exploration of their electrocatalytic properties^[17-19]

I published the summary and conclusions of the habilitation thesis in a young career review in *Synthetic Metals* “*Isotropic metallic transport in conducting polymers*”, 2019^[20].

2 Introduction

2.1 State-of-the-art

Conducting polymers combine excellent processability with facile synthesis and represent a prosperous emerging material class^[21–29]. This merits further investigations to become useful for thermoelectrics, molecular magnetics, bio-electronics and molecular photo- and electrocatalysts (Figure 1)^[18,30–33]. Presently, the central focus in conducting polymer research is the improvement of the electrical conductivity. This parameter is decisive for most applications. Substantial improvements have been achieved in the past decades, however, commonplace conducting polymers are still limited by disorder and a qualitative progress is required. Concepts to improve the order, purity, structure and homogeneity have readily led to metallic conduction, but presently these properties only occurred at low temperatures^[2,10,11,34–39]. There exists a tremendous interest to improve these effects and generate new classes of conducting polymers that can overcome disorder and establish metallic properties also at ambient temperatures and pressures. Such metallic conducting polymers represent a powerful and inexpensive alternative in material research, particularly to replace state-of-the-art inorganic scarce and noble metals. First early achievements from such metallic polymer structures show their potential as future sustainable technology.

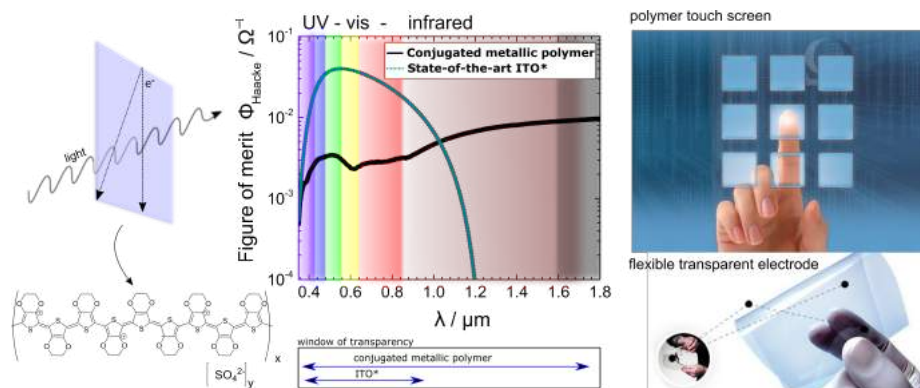


Figure 1: Optical figure of merit of the conducting polymer poly(3,4-ethylenedioxy- thiophene) (PEDOT) from Farka et al.^[10] demonstrating the broad window of transparency with recently demonstrated conductivities beyond 4000 S cm⁻¹ and its possible applications as inexpensive transparent electrode in optoelectronic devices.

2.2 Metallic conduction and disorder

The electrical transport in conducting polymers depends on multiple factors: starting from the quality of the molecules, their arrangement by the processing and post-treatments, the size and nature of the corresponding anion as well as crystallinity, homogeneity and purity^[38,39]. From the composition character, multiple interactions are present that involve covalent, ionic and van-der-Waals (intermolecular) bonds. This creates a complex situation and make polymers prone to disorder, localization and limited conductivity. In summary, the preponderance of conducting polymers used today are affected by local and structural amorphism, inhomogeneity, impurities, structural and molecular defects and, ultimately, thermal disorder^[40].

It was shown that reducing the extrinsic disorder factors (namely all except the thermal), conducting polymers can establish a low-temperature isotropic metallic phase. Such polymers are classified as metallic, however, only nominally, as the metallic phase occurs only at low temperatures (Figure 2)^[10,11,36,41–45]. At ambient temperatures, such polymers still possess a distinct non-metallic transport. This characteristic ambiguity relates to the molecular structure of the system, partly also to the quasi 1D-nature of polymers, as opposed to crystalline systems, induces strong phononic distortions.

Phononic (or thermal) disorder has strong influence on the weak non-covalent intermolecular van-der-Waals bonds and limits the electrical transport. Such distortion can be only reduced at sufficient low temperature below the intermolecular binding energies; therefore, the transport in conducting polymers is persistently situated between insulator and metal, or between thermal activated hopping and classic band transport, and the phononic effects are molecular-inherent. Only substantial strengthening of the intermolecular binding can result in a stronger metallic transport.^[46] In view of the multiple sources of disorder and the ambiguity, transport studies play a central role in conducting polymer research. Temperature-dependent characterization of the conductivity, magnetoconductivity and the Hall-effect are necessary to resolve the underlying transport mechanism and to quantify the magnitude of phononic or extrinsic disorder. Paired with other structural or spectroscopic measurements, a considerably clear picture of the transport can be obtained. These insights are necessary to evaluate the real potential of a system.

In state-of-the-art systems, such as the predominantly used poly(3,4-ethylenedioxythiophene) (PEDOT), intermolecular phonons are well characterized. Best-in-class PEDOTs can achieve isotropic metallicity, preconditioned that synthesis and processing were optimized so that all relevant factors of extrinsic disorder were diminished. Such almost ideal conducting polymers possess a superior electrical conductivity, a weak temperature dependence, and, at lower temperatures, a metal-to-insulator transition (MIT) (Figure 2). The conductivity-temperature profile splits into three regimes: the insulating regime at ambient temperatures, the critical (or transition) regime close to the metal transition, and, ultimately, the metallic regime, beyond the MIT. In the insulating regime, the conductivity decreases by reducing temperature resulting in a negative temperature coefficient of resistivity (TCR). The decrease is exponential (power law with the exponent β , equation 1). In ideal case, the exponent β is close to 1/4 (Figure 1b)^[47].

$$\sigma \propto T^{-\beta} \tag{1}$$

The critical regime represents the gradual transition to the metallic phase, when

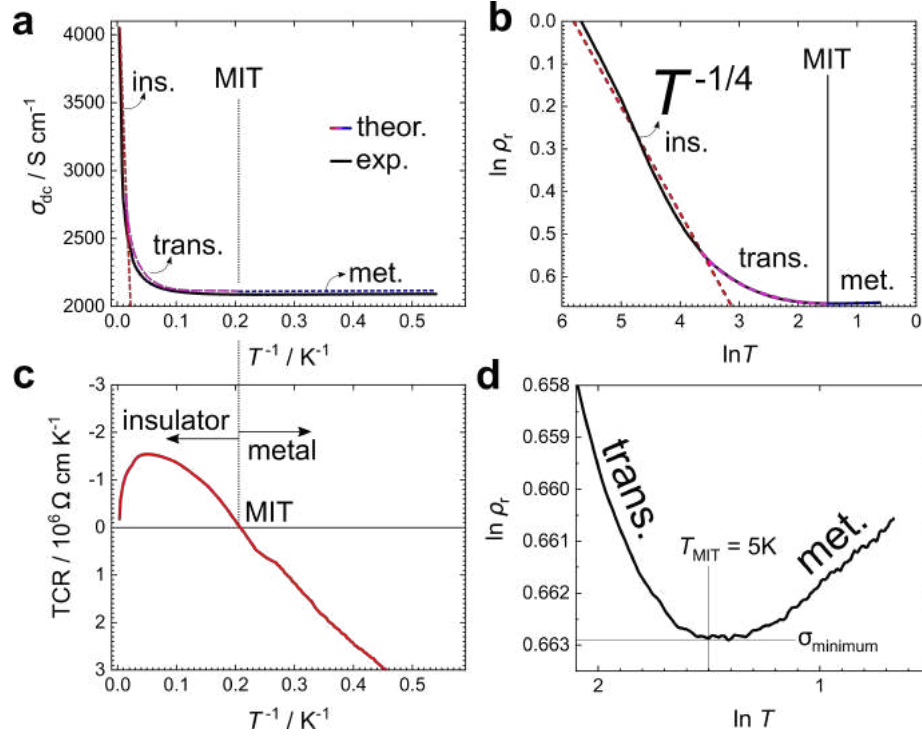


Figure 2: Temperature profile of conductivity (σ_r) of ideal conducting polymers (without extrinsic disorder): (a) Inverse temperature plot shows the different regimes (ins. = insulator; trans. = transition; met. = metal regime). Particularly the low temperature part is at first glance independent. (b) The logarithmic plot of the relative resistivity ($\rho_r = \rho_{300 \text{ K}} / \rho_T$) indicates the exponent β (idealized case is $-1/4$, indicated as red dashed line) between room temperature and low temperature, the transition regime deviating from the power law and the metallic regime with the rise of conductivity. (c) The temperature coefficient of resistivity (TCR) changes at the metal-insulator transition (MIT) observed in the inverse temperature plot and (d) in the logarithmic plot with the local conductivity minimum at the MIT (5 K) and subsequent rise of σ as T is further decreased. Reproduced with permission from^[11].

the exponential dependence is no longer valid. The conductivity is still decreasing with temperature. The local minimum of the conductivity represents the point of the actual metal-insulator transition temperature (T_{MIT}): below, the transport is metallic *i.e.* the conductivity increases with decreasing temperature with a positive TCR as for crystalline metals. The insulating and transition regime can be characterized using the exponent β . The transition to the metallic state occurs at the local minimum of conductivity, where the TRC flips from negative to positive (Figure 2). Conducting polymers without or with minimum extrinsic disorder show such characteristic ambivalent transport: The observation of insulating, critical and metallic regime reflects the strong influence of phonons on the weak molecular interactions. The majority of conducting polymer used today in devices, however, exhibit only two regimes: insulating and critical, but no metal-insulator transition (*i.e.* the conductivity minimum). Such polymers are still governed by extrinsic disorder and classified therefore as quasi- or semi-metallic.

In order to elucidate the quality of a conducting polymer system, it is necessary to understand the origins of disorder. It is important to separate extrinsic from phononic effects. The low-temperature regime and the relative conductivity $\sigma_r(T)$ are useful parameters, and, combined with spectroscopic measurements, magnetometry or magnetic field and structural characterization, yield complementary information about the transport. From that, the exact origin of *e.g.* residual extrinsic disorder and the extent of phononic distortion can be derived. In the transition and metallic regime, scattering parameters and mobility provide further information about the intermolecular binding and the coherence among molecules^[48]. In summary, when all relevant factors, intrinsic and extrinsic, are characterized precisely, it is possible to estimate the exact potential of a conducting polymer system, *e.g.* its maximum intrinsic conductivity and, related to that, its ultimate applicability^[46].

Presently, transport studies are often used to qualitatively characterize the extrinsic disorder effect, *i.e.* which factors limit the conductivity. These can be either local amorphism, substrate and surface effects in thin films, inhomogeneity, but also impurities. In case the extrinsic effects have been diminished, transport studies can be used to evaluate the intrinsic phononic disorder^[11,12,36,41,42,48-50].

The latter case relates to the few metallic conducting polymers, which show a metal-insulator transition as described in Figure 2. Such polymers have been judiciously processed, so that there is only a minor or negligible contribution of extrinsic disorder. There exists at least 3 different systems, namely polypyrrole (PPy), polyacetylene (PA), and recently, PEDOT (Figure 4) with a classic MIT. These results are still rare, but particularly recent results on PEDOT inspired scientific groups to design pathways to create such isotropic metallic conducting polymers^[10,11,36,41,42].^[48,51–53] Based on these results, it is attractive to further advance the metallic character, particularly to reduce the effect of phononic distortion. Theory and first experimental results show that upon reducing the impact of phonons, the metallic character in polymer is strengthened *e.g.* by shifting the metal-insulator transition towards higher temperatures. The ultimate goal is to generate metallic systems already at room temperatures. Theoretical descriptions have predicted intrinsic conductivities beyond classic metals, in case the phononic distortion can be surpassed. However, the desirable scenario of ambient metallic transport requires a much stronger intermolecular binding. Strategies using small anions (doping) paired with hydrostatic pressure have been proposed^[38,41,42,46,54,55]. Alternative strategies suggested to implement hydrogen bonds among molecules in order to reinforce stronger intermolecular overlaps^[17]. First steps in this direction are presented in section 2.8. Apart from such prosperous outlooks and visions, the major focus today lies still on the reduction of the extrinsic disorder effects, and the demonstration of conducting polymers with metallic phases with overall high electrical performance. These properties are required for applications. It is furthermore important to combine high conductivity with facile (solvent) processing in order to generate scalable and industry-relevant technology (Figure 1).

2.3 Phonons and polarons in conducting polymers

Phonons have been discussed in view of the negative impact on the electric transport. However, phonons in conducting polymers entail characteristic fingerprints such as a uniquely broad window of optical transparency and, indirectly, a strong thermo-electric activity^[10,15,16,50,56,57]. The doping of conjugated polymers increases not only the conductivity, but also induces strong electron-phonon coupling. Particularly along the polymer chain, delocalization is high. The quasi one-dimensionality causes strong infrared-activated vibrations (IRAVs) apparent in the mid-infrared spectral regime (Figure 3)^[15,16,51,58]. Interestingly, IRAVs are observed in all types of conducting polymers and they emerge at similar energies characteristically below 150 meV (200 cm^{-1})^[15,49]. The IRAV regime provides an insight of the earlier discussed phonon energies that ultimately have strong influence on the electrical transport. The exact spectroscopic elucidation of the IRAV regime and, related to that, the infrared polaronic features are helpful in order to determine the limits of electrical conductivity, but also to elucidate the exact optical properties^[16]. Studies of different polymers in the fingerprint IRAV and polaron regime revealed consistent oscillator constants suggesting that the underlying intermolecular interactions are very similar for a variety of polymer structures. This finding is in agreement with earlier discussed transport studies that reported *e.g.* similar metal-insulator transition temperatures for different polymers and similar intermolecular binding energies^[15].

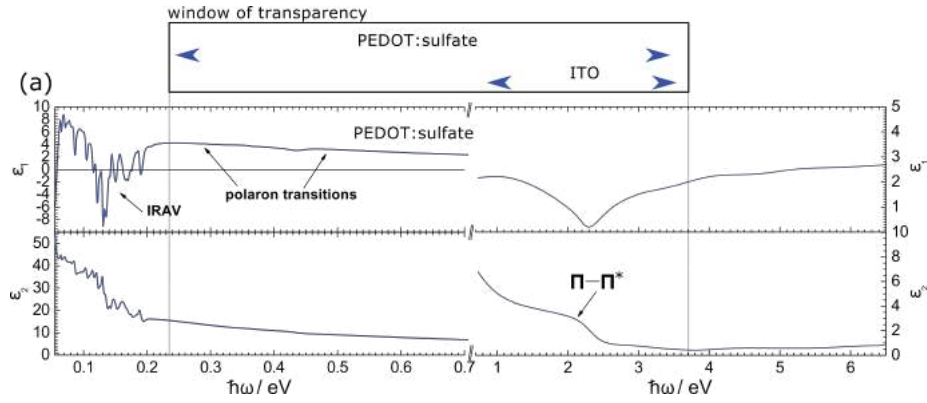


Figure 3: Phononic distortions in conducting polymers: Below 150 meV strong infrared-activated vibrations emerge in the mid-infrared spectrum (dielectric function) in metallic conducting polymer. The phononic distortion reduce the energy of the classic Drude tail in the dielectric function resulting in the broad window of transparency from UV-visible to the infrared. Reproduced with permission from^[10].

2.4 Transport in and close to the metallic regime

Relevant for transport studies is the inverse (or logarithmic) temperature profile of the relative conductivity (σ_r) (Figure 2). In the insulating regime, the conductivity decreases by $T^{-\beta}$. The magnitudes of the exponent β represents a measure of the proximity to an ideal case, without extrinsic disorder. Typically, the exponent increases, when extrinsic disorder is present (equation 1). In ideal polymers, the critical or transition regime is narrow. At sufficient low temperatures, the metal-insulator transition occurs.

In summary, metallic conducting polymers should have an exponent β close to 1/4, and a narrow transition regime with an overall low change in the relative resistivity (ρ_r). The local conductivity minimum marks the actual metal-insulator transition (MIT). As discussed, classic MITs have been reported in the following polymer systems: Polypyrrole, polyaniline, polyacetylene and, recently, PEDOTs (Figure 4)^[10,11,36,41,42]. Interestingly, the local conductivity minima occur consistently at temperatures between 4 to 7 K and point at the discussed relation between the intermolecular binding energy and the phonon energy (that limits the metal-insulator transition temperature $k_b T_{MIT}$ at low temperatures). Intermolecular binding in conducting polymers is characteristically

van-der-Waals type and ultimately dependent on the intermolecular radii. Experiments under hydrostatic pressure demonstrated that the metallic character of polymers, particularly the transition temperatures, increase under pressure^[11,41,54,55]. This observation is in agreement with theoretical description of the intrinsic conductivity in conducting polymers^[11,59-62].

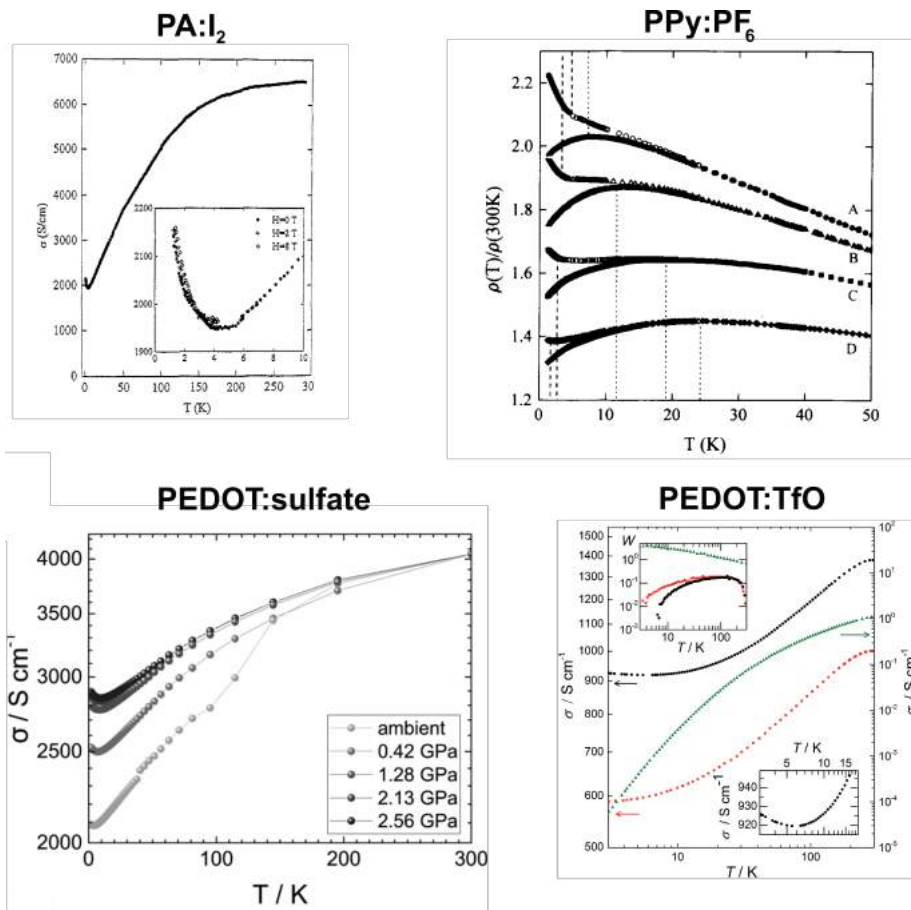


Figure 4: Examples of metallic conducting polymers: Polyacetylene doped with iodine (PA:I₂, metal-insulator transition, MIT or conductivity minimum at 4 K), polypyrrole:PF₆ (PPy:PF₆, MIT at 7 K, other samples B, C, D are under pressure), poly-(3,4-ethylenedioxythiophene):sulfate (PEDOT:sulfate) and PEDOT:triflate, respectively, (MIT at 5 K and 6 K). Reproduced with permission from [11,36,41,42].

2.5 Magnetoconductivity

Magnetoconductivity (including Hall-effect) is applied to expand transport studies from conductivity towards the charge carrier mobility and scattering parameters. For the latter, magnetoconductivity can provide a detailed insight to the intermolecular coherence, the effective mean-free-path of the charge carriers λ_{mfp} and the scattering mechanism^[11–13,13,54,63–66]. Such structural-electronic parameters are necessary in order to quantify the intensity of the intermolecular overlap and the overall order of a conducting polymer. In disordered conductors, the magnetic field can induce both a rise and decrease of the conductivity: Negative impact is caused by electron-electron interactions that are particularly strong in highly-doped semiconductors such as conducting polymers. This effect is also known as magnetolocalization (Figure 5)^[67]. On top, spin-orbit coupling can decrease the conductivity, but is negligible in carbon matter. Opposite to the electron-electron interactions, weak localization can induce a quantum magnetoresonance that increases the conductivity at certain magnetic fields^[62,65]. Such positive magnetoconductivity relates to a destructive resonance among free electron wave functions and it indicates a sufficient level of delocalization^[68]. Both types of magnetic interactions, electron-electron and weak localization are additive (equation 2). Non-metallic conducting polymers show only magnetolocalization (negative magnetoconductivity), whereas metal-like and metallic conducting polymers must have an ambiguous magnetoconductivity, particularly at low fields and temperatures (equation 2). Magnetoconductivity is consequently used to determine the proximity of a system to the metallic state.

$$\Delta\sigma = -0.041\alpha \cdot \left(\frac{g\mu_B}{k_B}\right)^2 \cdot \gamma F_\sigma \cdot T^{-\frac{3}{2}} \cdot B^2 + \left(\frac{1}{12\pi^2}\right) \cdot \left(\frac{e}{\hbar}\right)^2 \cdot G_0 \cdot B^2 \cdot (\lambda_{\text{mfp}})^3 \quad (2)$$

The negative magnetoconductivity relates to the empiric prefactor γ and the parameter F_σ (from the Hartee-Fock approximation of the electron-electron interactions), the diffusion parameter α , the gyromagnetic ratio or g-factor g , Bohr magneton μ_B , the Boltzmann constant k_B , inverse temperature (with exponent $\frac{3}{2}$) and magnetic field (with exponent 2). The positive term is strong at lower fields (Figure 6) and depends on the

conductance quantum G_0 , the magnetic field B and the volume of the mean-free-path of the free charge carriers λ_{mfp}^3 , however in relation to the negative magnetoconductivity, the positive effect can be small (as independent of the base conductivity) and hard to see (Figure 5 and Figure 6).

2.6 Electron coherence and scattering

The positive magnetoconductivity has been discussed as signature of metallic transport. It relates to the effective electron coherence volume λ_{mfp}^3 [54,65]. As described in equation 2 and experimentally shown in Figure 6, there exists a low-field regime where weak localization is dominant and the conductivity rises. At higher fields, the electron-electron localization becomes dominant again and it reduces the conductivity. Both effects cause the characteristic ambiguity reported for conducting polymers with metallic transport. The positive magnetoconductivity can be utilized to quantify mean-free-path of the free charge carriers λ_{mfp} . For this, only the positive term from equation 2 is applied.

$$\Delta\sigma_{\text{positive}} = + \left(\frac{1}{12\pi^2} \right) \cdot \left(\frac{e}{\hbar} \right)^2 \cdot G_0 \cdot B^2 \cdot (\lambda_{\text{mfp}})^3 \quad (3)$$

Disorder reduces λ_{mfp} and, thus, the positive magnetoconductivity effect is insensitive for localized carriers and disappears in non-metallic conducting polymers. The magnitude of the mean-free path λ_{mfp} has to be substantially larger than the molecular dimensions of the polymer. Best-in-class coherence lengths have been reported for isotropic metallic PEDOT at up to 50 nm [10,11]. The exact values for the mean-free-path are derived using equation 3 (slope of the isotherm conductivity versus the magnetic field at low fields) or, alternatively, using the local maximum magnetoconductance (*i.e.* the peak value of the conductivity versus the magnetic field) as reference of the mean-free-path [10,12,13,54]. For the latter evaluation, it is more convenient to plot the magnetic penetration depth (or the Landau orbit size, L_D) (Figure 6 according to equation 4).

$$\lambda_{\text{mfp}} = L_D \quad \text{with} \quad L_D = \sqrt{\frac{\hbar}{e \cdot B}} \quad (4)$$

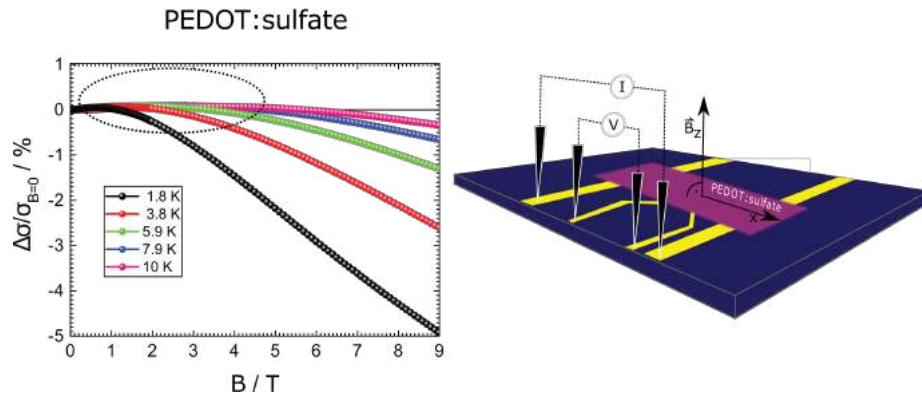


Figure 5: Negative magnetoconductivity in metallic conducting polymer. (a) The relative magnetoconductivity (change in per cent) as function of temperature at different temperatures. At low fields almost without change, the magnetolocalization (decrease of the conductivity) becomes stronger at higher magnetic fields and lower temperatures. (b) Schematic of the sample specimen: 4-wire probe in parallel direction to probe ρ_{xx} . Reproduced with permission from^[10].

The magnitude of λ_{mfp} is the average electron coherence or scattering length *i.e.* the order and strength of the intermolecular overlap (the electronic bands) of a system. The power of the magnetoconductivity is that this technique can be applied to a large number of polymers used today including all quasi-metallic or semimetallic systems.

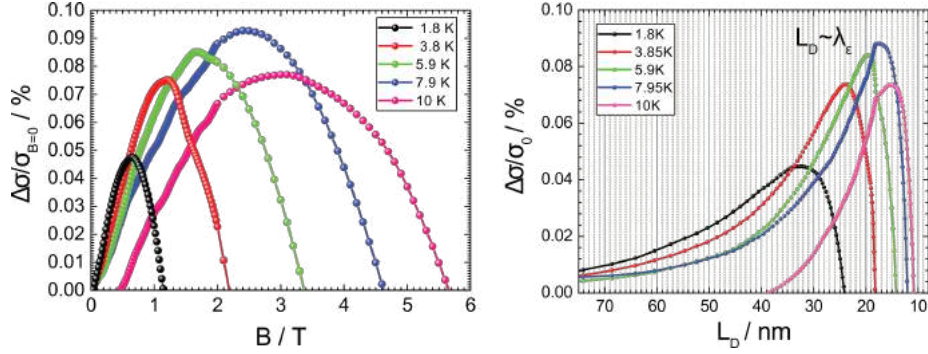


Figure 6: Positive magnetoconductivity in metallic conducting polymer. (Left) Zoom in the low-field regime of the magnetoconductivity reveals the increase of conductivity with the magnetic field showing a peak maximum. The maximum shifts to higher magnetic fields as the temperature increases. (Right) Plot of the positive magnetoconductivity using the magnetic penetration depth (the Landau orbit size, L_D). The peak (maximum quantum resonance condition) corresponds to the mean free scattering path λ_{mfp} . Reproduced with permission from [10].

2.7 Weak localization and band mobilities

According to equation 2, the positive magnetoconductivity has no temperature term. However, in weak localization, it is the mean-free-path λ_{mfp} that scales with temperature, exactly with the exponential relation $T^{-3/4}$ [63,63,65,67,68]. Such unusual exponent is characteristic for an inelastic scattering mechanism and has been also found in other disordered conductors in the critical regime (Figure 7).

At the metal-insulator transition, the inelastic scattering mechanism changes to elastic scattering. Therefore, the exponent can change indicating elastic scattering, but this transition is gradual in conducting polymers. Therefore, the temperature dependence of the positive magnetoconductivity is complex because there exists an coexistence of inelastic and elastic scattering [11,20].

The analysis of scattering by magnetoconductivity confirms that the metal-insulator transition is likely a molecular phase transition, where the intermolecular overlap becomes larger than the phonon energy. This is the main interpretation from the scattering results, that the metallic state establishes only beyond the phononic limit [69]. Applying hydrostatic pressure can increase the transition temperature by enhancing

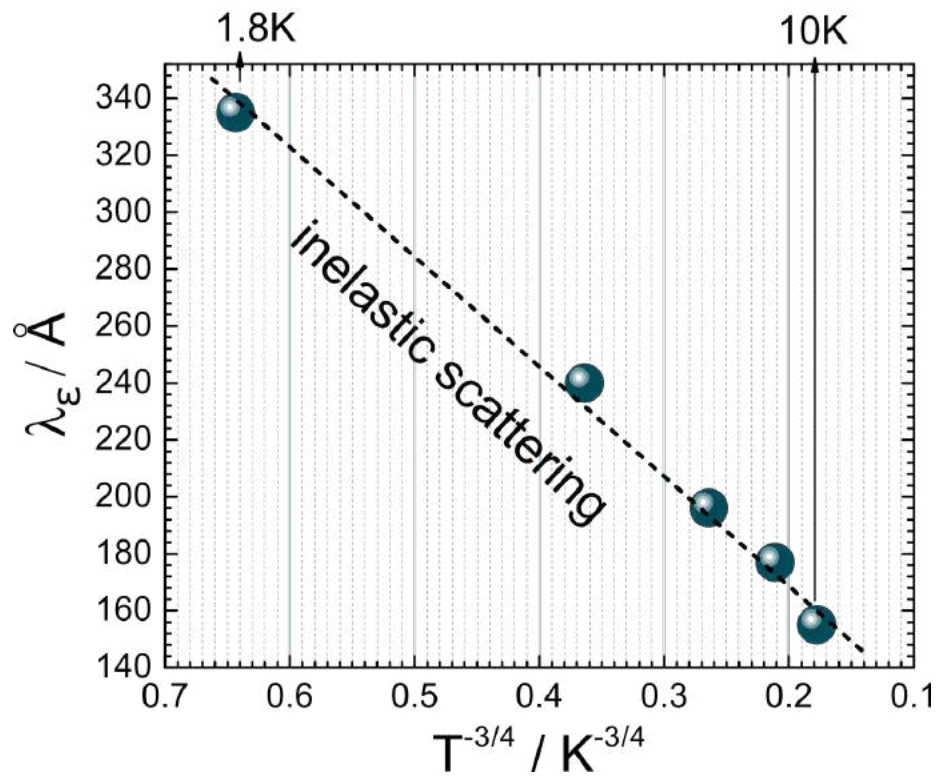


Figure 7: Temperature dependence of the positive magnetoconductivity in metallic conducting polymer. Linear fit of λ_{mfp} vs. $T^{-3/4}$ indicates an inelastic scattering process at the transition regime of the metallic polymer in the weak localization regime^[63]. Reproduced with permission from^[10].

the intermolecular overlap. Such observations were demonstrated in isotropic metallic PEDOTs^[11].

Complementary to magnetoconductivity, the Hall-effect in conducting polymers can help to resolve the transport mechanisms, particular the band mobility. Like the positive magnetoconductivity, the Hall-effect requires sufficient order *i.e.* electron coherence and band-character; metallic polymers possess a Hall-constant that can be measured classically as for highly-doped crystalline semiconductors and metals at low temperatures. Best-in-class polymers achieve mobilities up to $50 \text{ cm}^2 \text{ V}^{-1} \text{ s}^{-1}$ (beyond or close to the MIT)^[10,70]. The situation is more complex above the metal-insulator transition temperature, since the Hall-effect becomes screened by phononic disorder. One conclusion is that upon rising disorder, localization becomes dominant and only a few charge carriers remain band-type. The Hall voltage subsequently decreases strongly with rising temperature. The decrease is the product of reduced mobility and, on top, Hall-effect screening by phononic disorder. The exact evaluation of the Hall-voltage in the transition and insulating regime is subsequently complex. One has to compensate the Hall screening in order to derive the band mobility. Molecular phase model were proposed that reconcile the phonon effects in relation to the weak intermolecular overlap resulting in the weak band character of the transport^[48,71,72]. One additional problem is that the Hall screening can reduce the Hall voltage below the noise level of usual Hall setups, *e.g.* below 10^{-6} V . Recently it was shown that the experimental limits can be resolved applying an amplified high-sensitivity Hall probing based on an *ac*-lockin techniques. Such technique allows to probe the Hall-voltage in semimetallic and metallic PEDOTs at temperatures between 300 K and 30 K. These experimental parameters use molecular phase models in order to derive band mobilities (Figure 8)^[14]. Such results represent a milestone in magnetotransport, since they proof the weak contribution of band-transport in conducting polymers is present also at room temperature. They also show that the Hall-effect can be used to derive the corresponding band mobility. These *ac*-Hall mobilities were crosschecked using complementary non-destructive mobility measurements (*e.g.* terahertz domain spectroscopy). Furthermore, the results are in agreement with earlier results and interpretations on the relative conductivity and magnetoconductivity. In summary, all these parameters provide a consistent pic-

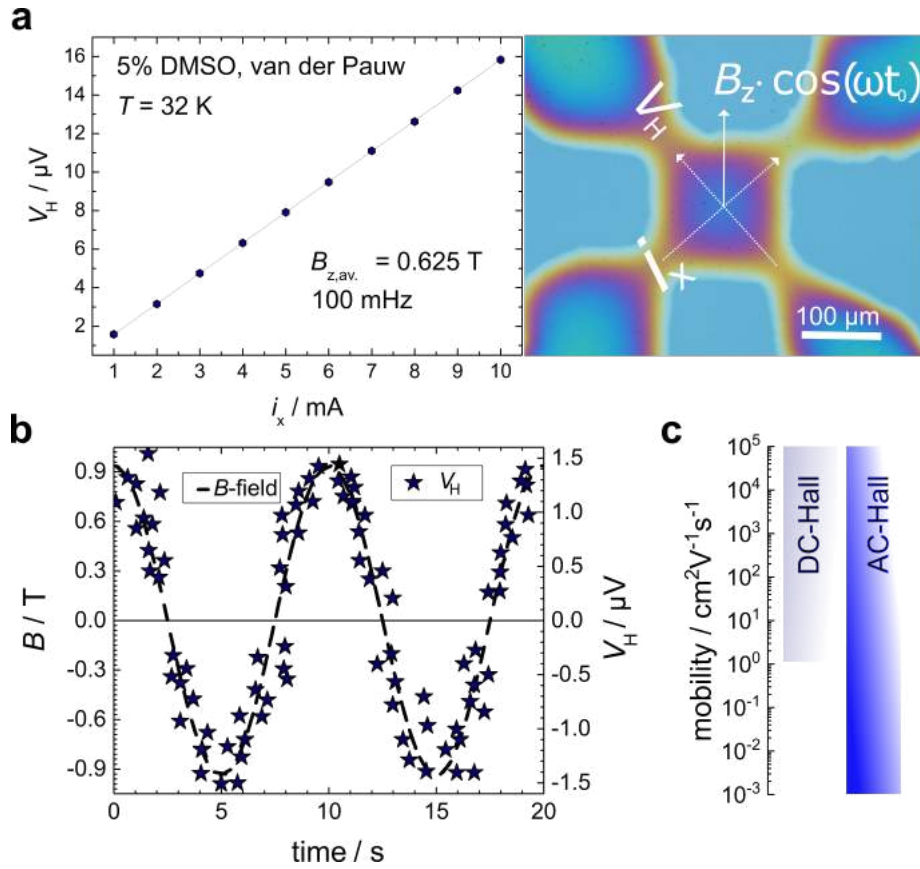


Figure 8: *ac*-Hall detection. (a) Average Hall-potential (i_x between 1 to 10 mA) of various PEDOTs (conductivity at 32 K is 500 S cm^{-1}) as derived from a simple van der Pauw geometry (picture). (b) 2 loops at 100 mHz of repeating magnetic ac-modulated Hall signal output from sinusoidal applied magnetic field B . (c) Mobility expansion from *ac*-Hall diminishes misalignment potentials expanding the Hall mobility range to $10^{-3} \text{ cm}^2 \text{ V}^{-1} \text{ s}^{-1}$. Reproduced with permission from^[14].

ture on the transport in conducting polymers that is situated between localization and band-type character. The band-character in conducting polymers is weak, unless at low temperatures, the phononic limit can be surpassed and an isotropic metallic phase is formed.

2.8 Functional conducting polymers

The limits of electrical transport, particularly, the effect of disorder have been discussed in this thesis in detail. Theoretical and experimental results led to the conclusion that, ultimately, intermolecular binding among the polymer chains has to be increased, in order to surpass the phononic limits at higher temperatures than reported earlier. This strategy could create a superior generation of fully metallic polymers without such dominant non-metallic transport in a wide range of temperature^[46,69].

Pathways to strengthen the intermolecular binding energies have been suggested, *e.g.* applying hydrostatic pressure or using small dopants. The strategy applied in this thesis sought to improve the molecular overlap by incorporation of hydrogen bonds among the polymer chains. Since the hydrogen binding energy is larger than van-der-Waals bonds, a rigid intermolecular association and, thus, a much stronger intermolecular overlap can be achieved. Consequently, hydrogen-bonded conducting polymers could have a superior conductivity and a pronounced metallic transport possible even at ambient temperatures. Intermolecular hydrogen bonds play a central role in biologic matter, however, there are only few conjugated and hydrogen-bonded polymers. In the field of conducting polymers, hydrogen bonded monomers represent an entirely new field, since, presently, the materials pool concentrated on the classic placeholders such as PEDOT. One attractive material that incorporates the required hydrogen bond functionality (*i.e.* an alternating sequence of amines and hydroxyl- or keto-groups) is polydopamine (Figure 9a). The base monomer dopamine can be readily polymerized similar to the classic structures and leads to the formation of a functional and conducting polydopamine. However, polydopamine adopts a complex molecular structure: in contrast to non-functionalized monomers, dopamine offers three functional and reactive groups that, in parallel to the polymerization and doping, react and form a cascade of intermediates such as dopaminequinone (DAQ), leucodopaminechrome (LDC) and 5,6-dihydroxyindole (DHI) (Figure 9a). Therefore, polydopamine consists of a complex sequence of dopamine and its derivatives (a statistical monomer, Figure 9). The merit of the system is that it forms a rigid inter- and intramolecular network of hydrogen bonds and therefore is chemically very stable and robust against oxidation. It

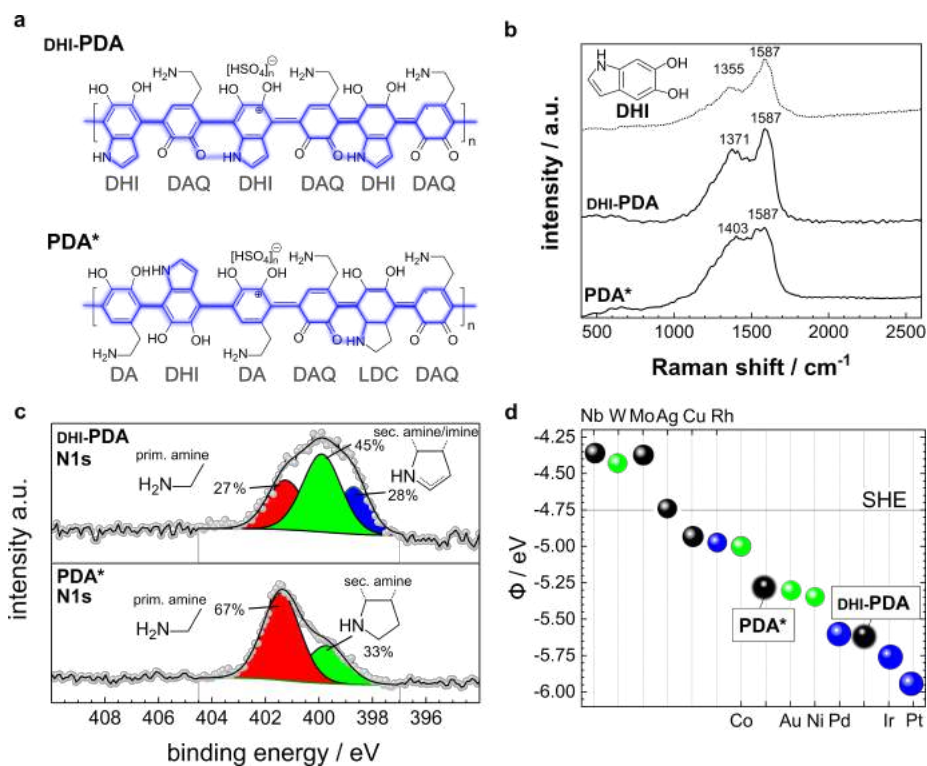


Figure 9: Electronic and structural properties of polydopamines mimicking noble metal surfaces. (a) Statistical monomer of two types of functional polydopamine using X-ray photoelectron and Raman spectroscopy including the fragmental sequence (DA, dopamine; DAQ, dopaminequinone; LDC, leucodopaminechrome; DHI, dihydroxyindole) of the structure. (b) The Raman shifts show the differences due to changed functionalization. (c) The N1s photoelectron peaks reveal the change in the functional sites and the induced shift in (d) the work functions. The values are similar to various catalytic metals. The standard hydrogen electrode (SHE) is shown for comparison. The lower work function polydopamine offers similar catalytic properties as iridium and platinum. Reproduced with permission from [19].

shows no degradation in acidic and basic environment and other aggressive media. At the same time, it possesses an electrical conductivity in the order of 1 S cm^{-1} , which is still low compared to other conducting polymers, but there is a lot of room for improvements. The intimate incorporation of functional groups has another positive side-effect that can be harnessed for electrocatalysis: The hydrogen-bonds are electrically linked to the conjugated-conducting backbone. As such, the polydopamine surface shares some properties with frequently used catalytic metals. It is chemically stable, insoluble in water, possesses a high work function and has a high surface density of electrically active functional sites (three functional groups per monomer). These features make polydopamine a serious contender in various electrocatalytic reactions such as the hydrogen evolution and CO_2 reduction^[17-19]. Polydopamines were demonstrated as excellent non-metallic electrocatalyst materials (Figure 9d). Further developments are attractive, not only for applications in catalysis, but also with directions on strengthening the metallic character to increase the conductivity. This could be a future field to generate a class of highly-stable and bio-inspired metallic conductors^[17-19].

2.9 Acknowledgements

I acknowledge all collaborators, co-authors and supportors from the past four years. Furthermore, I acknowledge following funding agencies for financial support: The Austrian Exchange service (OEAD) for the Indian-Austrian Grant “*Nanomorphology, localization and charge transport in conducting polymers*” (IN10/2015), the US-Army Research Office (ARO) for the support to organize an international symposium at the Material Reserach Society Meeting in Phoenix 2017 (W911NF-17-1-0169), the Austrian Science Foundation (FWF) to grant the international joint project “*Sustainable Catalysis*” (I3822-N37), the Linz Institute of Technology (LIT) to fund the young career grant at the Johannes Kepler University Linz (LIT-2017-4-YOU-005) and the research program “*Innovative Upper Austria 2020*” (EFRE) to grant the project *Artificial Food* (IWB 2014-2020, 2018-98299).

2.10 References

- [1] C. K. Chiang, C. R. Fincher, Y. W. Park, A. J. Heeger, H. Shirakawa, E. J. Louis, S. C. Gau, A. G. MacDiarmid, Electrical Conductivity in Doped Polyacetylene, *Physical Review Letters* 39 (17) (1977) 1098–1101. doi:10.1103/PhysRevLett.39.1098.
- [2] A. J. Heeger, Semiconducting and Metallic Polymers: The Fourth Generation of Polymeric Materials †, *The Journal of Physical Chemistry B* 105 (36) (2001) 8475–8491. doi:10.1021/jp011611w.
- [3] H. Naarmann, N. Theophilou, New process for the production of metal-like, stable polyacetylene, *Synthetic Metals* 22 (1) (1987) 1–8. doi:10.1016/0379-6779(87)90564-9.
URL <https://linkinghub.elsevier.com/retrieve/pii/0379677987905649>
- [4] T. Schimmel, W. Rieß, J. Gmeiner, G. Denninger, M. Schwoerer, H. Naarmann, N. Theophilou, DC-conductivity on a new type of highly conducting polyacetylene, N-(CH)_x, *Solid State Communications* 65 (11) (1988) 1311–1315. doi:10.1016/0038-1098(88)90083-X.
URL <https://linkinghub.elsevier.com/retrieve/pii/003810988890083X>
- [5] N. Theophilou, D. Swanson, A. Macdiarmid, A. Chakraborty, H. Javadi, R. McCall, S. Treat, F. Zuo, A. Epstein, Highly conducting polyacetylene, *Synthetic Metals* 28 (3) (1989) D35–D42. doi:10.1016/0379-6779(89)90671-1.
URL <https://linkinghub.elsevier.com/retrieve/pii/0379677989906711>
- [6] A. Epstein, A. Macdiarmid, Structure, order and the metallic state in polyaniline and its derivatives, *Synthetic Metals* 41 (1-2) (1991) 601–606. doi:10.1016/0379-6779(91)91142-W.

URL [https://linkinghub.elsevier.com/retrieve/pii/037967799191142W](https://linkinghub.elsevier.com/retrieve/pii/S037967799191142W)

- [7] N. Basescu, Z.-X. Liu, D. Moses, A. J. Heeger, H. Naarmann, N. Theophilou, High electrical conductivity in doped polyacetylene, *Nature* 327 (6121) (1987) 403–405. doi:10.1038/327403a0.
URL <https://doi.org/10.1038/327403a0><http://www.nature.com/articles/327403a0>
- [8] J. Tsukamoto, A. Takahashi, K. Kawasaki, Structure and Electrical Properties of Polyacetylene Yielding a Conductivity of 10⁵ S/cm, *Japanese Journal of Applied Physics* 29 (Part 1, No. 1) (1990) 125–130. doi:10.1143/JJAP.29.125.
- [9] H. H. S. Javadi, A. Chakraborty, C. Li, N. Theophilou, D. B. Swanson, A. G. MacDiarmid, A. J. Epstein, Highly conducting polyacetylene: Three-dimensional delocalization, *Physical Review B* 43 (3) (1991) 2183–2186. doi:10.1103/PhysRevB.43.2183.
- [10] D. Farka, H. Coskun, J. Gasiorowski, C. Cobet, K. Hingerl, L. M. Uiberlacker, S. Hild, T. Greunz, D. Stifter, N. S. Sariciftci, R. Menon, W. Schoefberger, C. C. Mardare, A. W. Hassel, C. Schwarzinger, M. C. Scharber, P. Stadler, Anderson-Localization and the Mott-Ioffe-Regel Limit in Glassy-Metallic PEDOT, *Advanced Electronic Materials* (2017) 1700050 doi:10.1002/aelm.201700050.
- [11] D. Farka, A. O. Jones, R. Menon, N. S. Sariciftci, P. Stadler, Metallic conductivity beyond the Mott minimum in PEDOT: Sulphate at low temperatures, *Synthetic Metals* 240 (2018) 59–66. doi:10.1016/j.synthmet.2018.03.015.
- [12] P. Stadler, D. Farka, H. Coskun, E. D. Głowacki, C. Yumusak, L. M. Uiberlacker, S. Hild, L. N. Leonat, M. C. Scharber, P. Klapetek, R. Menon, N. S. Sariciftci, Local order drives the metallic state in PEDOT:PSS, *J. Mater. Chem. C* 4 (29) (2016) 6982–6987. doi:10.1039/C6TC02129H.
- [13] D. Farka, H. Coskun, P. Bauer, D. Roth, B. Bruckner, P. Klapetek, N. S. Sariciftci, P. Stadler, Increase in electron scattering length in PEDOT:PSS by a triflic acid

- post-processing, *Monatshefte für Chemie - Chemical Monthly* 148 (5) (2017) 871–877. doi:10.1007/s00706-017-1973-1.
- [14] P. Stadler, L. N. Leonat, R. Menon, H. Coskun, S. van Frank, C. Rankl, M. C. Scharber, Stable Hall voltages in presence of dynamic quasi-continuum bands in poly(3,4-ethylene-dioxythiophene), *Organic Electronics* 65 (2019) 412–418. doi:10.1016/j.orgel.2018.12.001.
- [15] C. Cobet, J. Gasiorowski, R. Menon, K. Hingerl, S. Schlager, M. S. White, H. Neugebauer, N. S. Sariciftci, P. Stadler, Influence of molecular designs on polaronic and vibrational transitions in a conjugated push-pull copolymer, *Scientific Reports* 6 (2016) 35096. doi:10.1038/srep35096.
- [16] C. Cobet, J. Gasiorowski, D. Farka, P. Stadler, Polarons in Conjugated Polymers, in: K.-J. Hinrichs, Karsten, Eichhorn (Ed.), *Ellipsometry of Functional Organic Surfaces and Films*, 2018, pp. 355–387. doi:10.1007/978-3-319-75895-4_16.
- [17] H. Coskun, A. Aljabour, L. Uiberlacker, M. Strobel, S. Hild, C. Cobet, D. Farka, P. Stadler, N. S. Sariciftci, Chemical vapor deposition - based synthesis of conductive polydopamine thin-films, *Thin Solid Films* 645 (August 2017) (2018) 320–325. doi:10.1016/j.tsf.2017.10.063.
- [18] H. Coskun, A. Aljabour, P. De Luna, D. Farka, T. Greunz, D. Stifter, M. Kus, X. Zheng, M. Liu, A. W. Hassel, W. Schöfberger, E. H. Sargent, N. S. Sariciftci, P. Stadler, Biofunctionalized conductive polymers enable efficient CO₂ electroreduction, *Science Advances* 3 (8) (2017) e1700686. doi:10.1126/sciadv.1700686.
- [19] H. Coskun, A. Aljabour, P. D. Luna, H. Sun, N. Nishiumi, T. Yoshida, G. Koller, M. G. Ramsey, T. Greunz, D. Stifter, A. W. Hassel, N. S. Sariciftci, E. H. Sargent, P. Stadler, Bio-inspired hydrogen-bonded polymers mimic noble metal electrocatalysts, submitted.

- [20] P. Stadler, Isotropic metallic transport in conducting polymers, *Synthetic Metals* early view. doi:10.1016/j.synthmet.2019.06.004.
- [21] O. Bubnova, Z. U. Khan, A. Malti, S. Braun, M. Fahlman, M. Berggren, X. Crispin, Optimization of the thermoelectric figure of merit in the conducting polymer poly(3,4-ethylenedioxythiophene), *Nature Materials* 10 (6) (2011) 429–433. doi:10.1038/nmat3012.
- [22] Y. H. Kim, C. Sachse, M. L. Machala, C. May, L. Müller-Meskamp, K. Leo, Highly Conductive PEDOT:PSS Electrode with Optimized Solvent and Thermal Post-Treatment for ITO-Free Organic Solar Cells, *Advanced Functional Materials* 21 (6) (2011) 1076–1081. doi:10.1002/adfm.201002290.
- [23] N. Kim, B. H. Lee, D. Choi, G. Kim, H. Kim, J.-R. Kim, J. Lee, Y. H. Kahng, K. Lee, Role of Interchain Coupling in the Metallic State of Conducting Polymers, *Physical Review Letters* 109 (10) (2012) 106405. doi:10.1103/PhysRevLett.109.106405.
- [24] Y. Xia, K. Sun, J. Ouyang, Solution-Processed Metallic Conducting Polymer Films as Transparent Electrode of Optoelectronic Devices, *Advanced Materials* 24 (18) (2012) 2436–2440. doi:10.1002/adma.201104795.
- [25] A. Ugur, F. Katmis, M. Li, L. Wu, Y. Zhu, K. K. Varanasi, K. K. Gleason, Low-Dimensional Conduction Mechanisms in Highly Conductive and Transparent Conjugated Polymers, *Advanced Materials* 27 (31) (2015) 4604–4610. doi:10.1002/adma.201502340.
- [26] B. J. Worfolk, S. C. Andrews, S. Park, J. Reinspach, N. Liu, M. F. Toney, S. C. B. Mannsfeld, Z. Bao, Ultrahigh electrical conductivity in solution-sheared polymeric transparent films, *Proceedings of the National Academy of Sciences* 112 (46) (2015) 14138–14143. doi:10.1073/pnas.1509958112.
- [27] X. Crispin, F. L. E. Jakobsson, a. Crispin, P. C. M. Grim, P. Andersson, a. Volodin, C. van Haesendonck, M. Van der Auweraer, W. R. Salaneck, M. Berggren,

- 2006_200_The Origin of the High Conductivity of (PEDOTPSS) Plastic Electrodes.pdf, *Chemistry of Materials* 18 (4) (2006) 4354–4360. [arXiv:1211.2668](#), [doi:10.1021/cm061032+](#).
- [28] O. Bubnova, Z. U. Khan, H. Wang, S. Braun, D. R. Evans, M. Fabretto, P. Hojati-Talemi, D. Dagnelund, J.-B. Arlin, Y. H. Geerts, S. Desbief, D. W. Breiby, J. W. Andreasen, R. Lazzaroni, W. M. Chen, I. Zozoulenko, M. Fahlman, P. J. Murphy, M. Berggren, X. Crispin, Semi-metallic polymers, *Nature Materials* 13 (2) (2014) 190–194. [doi:10.1038/nmat3824](#).
- [29] A. a. Farah, S. a. Rutledge, A. Schaarschmidt, R. Lai, J. P. Freedman, A. S. Helmy, Conductivity enhancement of poly(3,4-ethylenedioxythiophene)-poly(styrenesulfonate) films post-spincoating, *Journal of Applied Physics* 112 (11) (2012) 113709. [doi:10.1063/1.4768265](#).
- [30] E. Jin Bae, Y. Hun Kang, K.-S. Jang, S. Yun Cho, Enhancement of Thermoelectric Properties of PEDOT:PSS and Tellurium-PEDOT:PSS Hybrid Composites by Simple Chemical Treatment, *Scientific Reports* 6 (November 2015) (2016) 18805. [doi:10.1038/srep18805](#).
- [31] T. Park, C. Park, B. Kim, H. Shin, E. Kim, Flexible PEDOT electrodes with large thermoelectric power factors to generate electricity by the touch of fingertips, *Energy & Environmental Science* 6 (3) (2013) 788. [doi:10.1039/c3ee23729j](#).
- [32] H. Park, S. H. Lee, F. S. Kim, H. H. Choi, I. W. Cheong, J. H. Kim, Enhanced thermoelectric properties of PEDOT:PSS nanofilms by a chemical dedoping process, *J. Mater. Chem. A* 2 (18) (2014) 6532–6539. [doi:10.1039/C3TA14960A](#).
- [33] M. Scholdt, H. Do, J. Lang, A. Gall, A. Colsmann, U. Lemmer, J. D. Koenig, M. Winkler, H. Boettner, Organic Semiconductors for Thermoelectric Applications, *Journal of Electronic Materials* 39 (9) (2010) 1589–1592. [doi:10.1007/s11664-010-1271-8](#).
- [34] M. N. Gueye, A. Carella, N. Massonnet, E. Yvenou, S. Brenet, J. Faure-Vincent, S. Pouget, F. Rieutord, H. Okuno, A. Benayad, R. Demadrille, J.-P. Simonato,

- Structure and Dopant Engineering in PEDOT Thin Films: Practical Tools for a Dramatic Conductivity Enhancement, *Chemistry of Materials* 28 (10) (2016) 3462–3468. doi:10.1021/acs.chemmater.6b01035.
- [35] T.-R. Chou, S.-H. Chen, Y.-T. Chiang, Y.-T. Lin, C.-Y. Chao, Highly conductive PEDOT:PSS films by post-treatment with dimethyl sulfoxide for ITO-free liquid crystal display, *J. Mater. Chem. C* 3 (15) (2015) 3760–3766. doi:10.1039/C5TC00276A.
- [36] N. Massonnet, A. Carella, A. de Geyer, J. Faure-Vincent, J.-P. Simonato, Metallic behaviour of acid doped highly conductive polymers, *Chem. Sci.* 6 (1) (2015) 412–417. doi:10.1039/C4SC02463J.
- [37] A. G. MacDiarmid, A. J. Heeger, Organic metals and semiconductors: The chemistry of polyacetylene, (CH)_x, and its derivatives, *Synthetic Metals* 1 (2) (1980) 101–118. doi:10.1016/0379-6779(80)90002-8.
- [38] S. Kivelson, W.-P. Su, J. R. Schrieffer, A. J. Heeger, Missing bond-charge repulsion in the extended Hubbard model: Effects in polyacetylene, *Physical Review Letters* 58 (18) (1987) 1899–1902. doi:10.1103/PhysRevLett.58.1899.
- [39] M. J. Winokur, J. Maron, Y. Cao, A. J. Heeger, Disorder and staging in iodine-doped polyacetylene, *Physical Review B* 45 (17) (1992) 9656–9662. doi:10.1103/PhysRevB.45.9656.
- [40] T. Harada, H. Ito, Y. Ando, S. Watanabe, H. Tanaka, S.-i. Kuroda, Signature of the insulator–metal transition of a semicrystalline conjugated polymer in ionic-liquid-gated transistors, *Applied Physics Express* 8 (2) (2015) 021601. doi:10.7567/APEX.8.021601.
- [41] R. Menon, C. Yoon, D. Moses, A. Heeger, Pressure and magnetic field dependence of the low temperature resistivity of PF6-doped polypyrrole, *Synthetic Metals* 64 (1) (1994) 53–57. doi:10.1016/0379-6779(94)90274-7.

- [42] R. Menon, Conductivity and magnetoconductance in iodine-doped polyacetylene, *Synthetic Metals* 80 (2) (1996) 223–229. doi:10.1016/S0379-6779(96)03706-X.
- [43] C. Yoon, M. Reghu, A. Heeger, E. Park, Y. Park, K. Akagi, H. Shirakawa, Effect of anisotropy on conductivity and magnetoconductance in heavily doped polyacetylene, *Synthetic Metals* 69 (1-3) (1995) 79–80. doi:10.1016/0379-6779(94)02372-6.
- [44] K. Väkiparta, R. M., M. R. Andersson, Y. Cao, D. Moses, A. J. Heeger, Temperature dependence of the electrical conductivity of potassium-doped polyacetylene as a function of pressure and magnetic field, *Physical Review B* 47 (15) (1993) 9977–9980. doi:10.1103/PhysRevB.47.9977.
- [45] Y. Park, A. J. Heeger, M. A. Druy, A. G. MacDiarmid, Electrical transport in doped polyacetylene, *The Journal of Chemical Physics* 73 (2) (1980) 946–957. doi:10.1063/1.440214.
- [46] S. Kivelson, A. Heeger, Intrinsic conductivity of conducting polymers, *Synthetic Metals* 22 (4) (1988) 371–384. doi:10.1016/0379-6779(88)90108-7.
- [47] A. I. Larkin, D. E. Khmel'nitskii, Activation conductivity in disordered systems with large localization length, *Soviet Physics, JETP* 56 (3) (1982) 647–652.
- [48] H. T. Yi, Y. N. Gartstein, V. Podzorov, Charge carrier coherence and Hall effect in organic semiconductors, *Scientific Reports* 6 (1) (2016) 23650. doi:10.1038/srep23650.
- [49] K. Kang, S. Watanabe, K. Broch, A. Sepe, A. Brown, I. Nasrallah, M. Nikolka, Z. Fei, M. Heeney, D. Matsumoto, K. Marumoto, H. Tanaka, S.-i. Kuroda, H. Siringhaus, 2D coherent charge transport in highly ordered conducting polymers doped by solid state diffusion, *Nature Materials* 15 (8) (2016) 896–902. doi:10.1038/nmat4634.
- [50] S. D. Kang, G. J. Snyder, Charge-transport model for conducting polymers, *Nature Materials* 16 (2) (2017) 252–257. doi:10.1038/nmat4784.

- [51] R. S. Kohlman, A. Zibold, D. B. Tanner, G. G. Ihas, T. Ishiguro, Y. G. Min, A. G. MacDiarmid, A. J. Epstein, Limits for Metallic Conductivity in Conducting Polymers, *Physical Review Letters* 78 (20) (1997) 3915–3918. doi:10.1103/PhysRevLett.78.3915.
- [52] A. B. Kaiser, Systematic Conductivity Behavior in Conducting Polymers: Effects of Heterogeneous Disorder, *Advanced Materials* 13 (12-13) (2001) 927–941. doi:10.1002/1521-4095(200107)13:12/13<927::AID-ADMA927>3.0.CO;2-B.
- [53] A. Aleshin, R. Kiebooms, R. Menon, A. Heeger, Electronic transport in doped poly (3,4-ethylenedioxythiophene) near the metal-insulator transition, *Synthetic Metals* 90 (1) (1997) 61–68. doi:10.1016/S0379-6779(97)81227-1.
- [54] R. Menon, K. Väkiparta, Y. Cao, D. Moses, Pressure dependence of the conductivity and magnetoconductance in oriented iodine-doped polyacetylene, *Physical Review B* 49 (23) (1994) 16162–16170. doi:10.1103/PhysRevB.49.16162.
- [55] R. Menon, C. Yoon, D. Moses, Y. Cao, A. Heeger, Tuning through the critical regime of the metal-insulator transition in conducting polymers by pressure and magnetic field, *Synthetic Metals* 69 (1-3) (1995) 329–332. doi:10.1016/0379-6779(94)02471-A.
- [56] A. Girlando, A. Painelli, Z. G. Soos, Electron-phonon coupling in conjugated polymers: Reference force field and transferable coupling constants for polyacetylene, *The Journal of Chemical Physics* 98 (9) (1993) 7459–7465. doi:10.1063/1.464684.
- [57] H. Wang, U. Ail, R. Gabrielsson, M. Berggren, X. Crispin, Ionic Seebeck Effect in Conducting Polymers, *Advanced Energy Materials* 5 (11) (2015) 1500044. doi:10.1002/aenm.201500044.
- [58] K. Lee, A. Heeger, Optical investigation of intra and interchain charge dynamics in conducting polymers, *Synthetic Metals* 128 (3) (2002) 279–282. doi:10.1016/S0379-6779(02)00006-1.

- [59] Y. Cao, P. Smith, A. J. Heeger, Mechanical and electrical properties of highly oriented polyacetylene films, *Synthetic Metals* 41 (1-2) (1991) 181–184. doi:10.1016/0379-6779(91)91033-7.
- [60] W. P. Su, J. R. Schrieffer, A. J. Heeger, Soliton excitations in polyacetylene, *Physical Review B* 22 (4) (1980) 2099–2111. doi:10.1103/PhysRevB.22.2099.
- [61] N. Mott, *Metal-Insulator Transitions*, Taylor & Francis LTD, 1974.
- [62] G. Bergmann, Physical interpretation of weak localization: A time-of-flight experiment with conduction electrons, *Physical Review B* 28 (6) (1983) 2914–2920. doi:10.1103/PhysRevB.28.2914.
- [63] G. Bergmann, Weak localization in thin films, *Physics Reports* 107 (1) (1984) 1–58. doi:10.1016/0370-1573(84)90103-0.
- [64] Y. Nogami, H. Kaneko, H. Ito, T. Ishiguro, T. Sasaki, N. Toyota, A. Takahashi, J. Tsukamoto, Low-temperature electrical conductivity of highly conducting polyacetylene in a magnetic field, *Physical Review B* 43 (14) (1991) 11829–11839. doi:10.1103/PhysRevB.43.11829.
- [65] T. F. Rosenbaum, R. F. Milligan, G. A. Thomas, P. A. Lee, T. V. Ramakrishnan, R. N. Bhatt, K. DeConde, H. Hess, T. Perry, Low-Temperature Magnetoresistance of a Disordered Metal, *Physical Review Letters* 47 (24) (1981) 1758–1761. doi:10.1103/PhysRevLett.47.1758.
- [66] I. Shlimak, M. Kaveh, State of Mott minimal metallic conductivity in a scaling approach to the metal-insulator transition in doped semiconductors, *Physical Review B* 58 (23) (1998) 15333–15335. doi:10.1103/PhysRevB.58.15333.
- [67] A. L. Efros, B. I. Shklovskii, Coulomb gap and low temperature conductivity of disordered systems, *Journal of Physics C: Solid State Physics* 8 (4) (1975) L49–L51. doi:10.1088/0022-3719/8/4/003.
- [68] P. A. Lee, T. V. Ramakrishnan, Disordered electronic systems, *Reviews of Modern Physics* 57 (2) (1985) 287–337. doi:10.1103/RevModPhys.57.287.

- [69] J. Ma, J. Fischer, Y. Cao, A. Heeger, X-ray structural study of trans-polyacetylene at high pressure, *Solid State Communications* 83 (6) (1992) 395–399. doi:10.1016/0038-1098(92)90075-K.
- [70] K. Seeger, W. Gill, T. Clarke, G. Street, Conductivity and Hall effect measurements in doped polyacetylene, *Solid State Communications* 28 (10) (1978) 873–878. doi:10.1016/0038-1098(78)90177-1.
- [71] T. Uemura, M. Yamagishi, J. Soeda, Y. Takatsuki, Y. Okada, Y. Nakazawa, J. Takeya, Temperature dependence of the Hall effect in pentacene field-effect transistors: Possibility of charge decoherence induced by molecular fluctuations, *Physical Review B* 85 (3) (2012) 035313. doi:10.1103/PhysRevB.85.035313.
- [72] J.-F. Chang, T. Sakanoue, Y. Olivier, T. Uemura, M.-B. Dufourg-Madec, S. G. Yeates, J. Cornil, J. Takeya, A. Troisi, H. Sirringhaus, Hall-Effect Measurements Probing the Degree of Charge-Carrier Delocalization in Solution-Processed Crystalline Molecular Semiconductors, *Physical Review Letters* 107 (6) (2011) 066601. doi:10.1103/PhysRevLett.107.066601.

3 Publications surveyed in this thesis

3.1 Metallic conducting polymers

The publications reflect the systematic and chronologic development and improvement of metallic conducting polymers.

Manuscript 1

P. Stadler*, D. Farka, H. Coskun, E. D. Głowacki, C. Yumusak, L. M. Uiberlacker, S. Hild, L. N. Leonat, M. C. Scharber, P. Klapetek, R. Menon, N. S. Sariciftci, Local order drives the metallic state in PEDOT:PSS, *J. Mater. Chem. C* 4 (29) (2016) 6982–6987. doi:10.1039/C6TC02129H.

Contribution

*Corresponding author; Direction of the study, concept and idea and contribution to synthesis (film grow), electrical transport and magnetotransport experiments, spectroscopic analysis, scattering parameter extraction and writing.

Summary

Manuscript 1 demonstrated a shallow semi-metallic state first time demonstrated by magnetoconductivity in poly(3,4-ethylene dioxythiophene):polystyrene sulfonate (PEDOT:PSS). These systems has been transferred to a the semimetallic state using solution-casting (self-organization). The superior ordering of the polymers is shown by a complementary X-ray diffraction study, atomic-force microscopy and a elaborate conductivity and magnetoconductivity study.

Manuscript 2

D. Farka, H. Coskun, P. Bauer, D. Roth, B. Bruckner, P. Klapetek, N. S. Sarıçiftci, **P. Stadler***, Increase in electron scattering length in PEDOT:PSS by a triflic acid post-processing, *Monatshefte für Chemie - Chemical Monthly* 148 (5) (2017) 871–877. doi:10.1007/s00706-017-1973-1.

Contribution

*Corresponding author; Direction of the study, concept and idea, contribution to all (magneto)transport experiments, synthesis and processing, analysis and writing.

Summary

Manuscript 2 focused a novel strategy to generate superior conductivity in PEDOT:PSS using an post-casting acid treatment. This post-processing led to conductivities of up to 2000 S cm^{-1} , one of the highest conductivities reported for this system at that time. The transport of this novel conducting polymer system has been systematically analyzed by magnetoconductivity (scattering parameters).

Manuscript 3

D. Farka, H. Coskun, J. Gasiorowski, C. Cobet, K. Hingerl, L. M. Uiberlacker, S. Hild, T. Greunz, D. Stifter, N. S. Sariciftci, R. Menon, W. Schoefberger, C. C. Mardare, A. W. Hassel, C. Schwarzinger, M. C. Scharber, **P. Stadler***, Anderson-Localization and the Mott-Ioffe-Regel Limit in Glassy-Metallic PEDOT, *Advanced Electronic Materials* (2017) 1700050

doi:10.1002/aelm.201700050.

Contribution

*Corresponding author; Direction of the study, concept and idea, contribution to all (magneto)transport experiments, Hall measurements, synthesis and processing, analysis and writing.

Summary

Manuscript 3 was the first generation of metallic conducting polymers. A new synthesis for PEDOT was first time proposed using a chemical vapor deposition process. This led to a superior degree of purity, order and crystallinity and one of the highest electrical conductivities reported for the same system at 4000 S cm^{-1} . The system showed an explicit metal-like behavior at low temperatures with clear signs of a metal-insulator transition. The exact transport parameters, including scattering length, Hall-voltage and band mobility as well as the relative conductivity were thoroughly analyzed. To date, this system is one of the most powerful PEDOT-based conducting polymers compared to the international state-of-the-art. A superior order was confirmed using aiding structural and spectroscopic techniques such as a precise analysis of the optical constants from 6.5 eV to 0.2 eV. The optical figure of merit shows a broad window of transparency and the potential application as transparent conductor is discussed.

Manuscript 4

D. Farka, A. O. Jones, R. Menon, N. S. Sariciftci, **P. Stadler***, Metallic conductivity beyond the Mott minimum in PEDOT: Sulphate at low temperatures, *Synthetic Metals* 240 (2018) 59–66. doi:10.1016/j.synthmet.2018.03.015.

Contribution

*Corresponding author; Direction of the study, concept and idea, contribution to all (magneto)transport and pressure-transport measurements, synthesis and processing, film structural characterization using X-ray diffraction and grazing-incident (small angle) X-ray scattering, analysis of data and manuscript writing.

Summary

Manuscript 4 is a fundamental study on the low-temperature transport of optimized PEDOT from manuscript 3. This polymer is synthesized as bulk films and studied under magnetic field and pressure. The complementary structural and conductivity study reveals an almost ideally-ordered polymer without extrinsic disorder (amorphism, inhomogeneity, purity). The system shows a clear metal-insulator transition at 5 K and possesses an isotropic metallic phase below this temperature. The isotropic phase can be increased up to 10 K under pressure. This study also presents detailed scattering parameters based on magnetotransport, particularly at the transition point between metallic and critical phase. The polymer represents one out of 2-3 conducting polymer systems with an isotropic metallic phase and the first pressure-dependent study on metallic PEDOTs.

Manuscript 5

P. Stadler*, L. N. Leonat, R. Menon, H. Coskun, S. van Frank, C. Rankl, M. C. Scharber, Stable Hall voltages in presence of dynamic quasi-continuum bands in poly(3,4-ethylene-dioxythiophene), *Organic Electronics* 65 (2019) 412–418. doi:10.1016/j.orgel.2018.12.001.

Contribution

*Corresponding author; direction of the study, concept and idea; contribution to all *ac*-Hall-measurements and conductivity measurements, synthesis and processing of thin-films, analysis of terahertz data and writing.

Summary

Manuscript 5 represents a survey study of various highly-conducting semimetallic PEDOT systems. These were evaluated by Hall- and conductivity measurements, particularly at room temperatures. The study conveys an novel advanced *ac*-lockin Hall measurement technique. The demonstrated accuracy in probing the Hall voltage and the implementation of a random phase model allowed first time the analysis of the Hall voltage for mobility characterization in semimetallic PEDOT systems at room temperatures. The mobilities from the Hall-measurement were compared to Terahertz measurements.

3.2 Functional conducting polymers

These publications focused the synthesis and characterization (and application) of conducting polydopamines. These results showed for the first time the synthesis of bio-inspired functional monomers to conducting and functional polymers.

Manuscript 6

H. Coskun, A. Aljabour, P. De Luna, D. Farka, T. Greunz, D. Stifter, M. Kus, X. Zheng, M. Liu, A. W. Hassel, W. Schöfberger, E. H. Sargent, N. S. Sariciftci, **P. Stadler***, Biofunctionalized conductive polymers enable efficient CO₂ electroreduction, *Science Advances* 3 (8) (2017) e1700686. doi:10.1126/sciadv.1700686.

Contribution

*Corresponding author; Direction of the study, concept and idea, contribution to all transport studies, spectroscopic characterization, synthesis and processing, electrochemical analysis and electrocatalysis, spectroelectrochemical analysis and discussion of DFT-results, analysis of spectroscopic data and writing.

Summary

Manuscript 6 is a publication in a highly-renowned international journal (*Science Advances*) that reported the use of conducting functional polymers as electrocatalysts. The astonishing-high surface activity in catalysis, merit of the functional sites inside the conjugated polymer backbone, offer completely new opportunities in the field of electro- and photoelectrocatalysis. The polydopamine achieved a moderate electrical performance and was able to compete with state-of-the-art catalytic metals in the field of CO₂ electrocatalysis.

Manuscript 7

H. Coskun, A. Aljabour, L. Uiberlacker, M. Strobel, S. Hild, C. Cobet, D. Farka, **P. Stadler**, N. S. Sariciftci, Chemical vapor deposition - based synthesis of conductive polydopamine thin-films, *Thin Solid Films* 645 (August 2017) (2018) 320–325. doi:10.1016/j.tsf.2017.10.063.

Contribution

Co-author. Direction of the study, concept and idea, contribution to transport study, spectroscopic characterization, synthesis and processing, discussion of ellipsometry results, analysis of spectroscopic data and contribution to writing.

Summary

Manuscript 7 is a detailed presentation of the synthesis of conducting polydopamines and the detailed discussion of the relevant electronic, optical and structural properties. In particular the structural conformation, the hydrogen-bonded networks inside the structure are elucidated using Raman spectroscopy.

3.3 Optoelectronic characterization and applications

The optical characterization, particularly the infrared spectroscopic regime, of polymers between the pristine and doped-conducting state are matter of interest. Here, the fundamental understanding of the phononic interactions is elucidated, but also the optical constants to harness conducting polymers as potential (solution-cast) transparent electrode in optoelectronic devices.

Manuscript 8

C. Cobet, J. Gasiorowski, R. Menon, K. Hingerl, S. Schlager, M. S. White, H. Neugebauer, N. S. Sariciftci, **P. Stadler***, Influence of molecular designs on polaronic and vibrational transitions in a conjugated push-pull copolymer, *Scientific Reports* 6 (2016) 35096. doi : 10.1038/srep35096.

Contribution

*Corresponding author; Direction of the study, concept and idea, contribution to in-situ doping experiments, spectroscopic characterization, analysis of spectroscopic data and writing.

Summary

Manuscript 8 is an in-situ spectroscopic doping study of commonplace conjugated polymers, with a particular focus on state-of-the-art conjugated backbones such as the widespread polythiophenes and push-pull co-polymers. The fundamentals of polaronic features and the complex and mutual interaction among and inside the molecules is discussed. Therefore, new in-situ techniques based on spectroscopic ellipsometry and FTIR are conducted. This work provided the insight to understand the later discussed phononic distortion on the electrical transport.

Manuscript 9

G. Adam, M. Kaltenbrunner, E. D. Głowacki, D. H. Apaydin, M. S. White, H. Heilbrunner, S. Tombe, **P. Stadler**, B. Ernecker, C. W. Klampfl, N. S. Sarıçiftci, M. C. Scharber, Solution processed perovskite solar cells using highly conductive PEDOT:PSS interfacial layer, *Solar Energy Materials and Solar Cells* 157 (2016) 318–325. doi:10.1016/j.solmat.2016.05.011

Contribution

Co-author. Spectroscopic analysis and transport measurements of the conducting polymer used here for perovskite photovoltaic cells. Contribution to the writing.

Summary

In **Manuscript 9** the conducting polymer plays a central role to harness its properties as transparent electrode for perovskite solar cells. The optimized conducting polymer is shown to equal the performance obtained by inorganic contenders.

3.4 Book chapter

Manuscript 10

C. Cobet, J. Gasiorowski, D. Farka, **P. Stadler**, Polarons in Conjugated Polymers, in: K.-J. Hinrichs, Karsten, Eichhorn (Ed.), Ellipsometry of Functional Organic Surfaces and Films, 2018, pp. 355–387. doi : 10.1007/978-3-319-75895.

Contribution

Co-author; discussion and analysis of spectroscopic and transport data, literature survey and writing.

Summary

Manuscript 10 is a book chapter on polaronic features and the general optical and electronic properties in the transition regime between conjugated and conducting polymers. The book chapter provides an general overview on the emergence of polarons in doped conjugated polymers.

3.5 Review

Manuscript 11

P. Stadler, Isotropic metallic transport in conducting polymers, Synthetic Metals (2019) *early view*. doi:10.1016/j.synthmet.2019.06.004.

Contribution

Single author paper (early review).

Summary

Manuscript 11 is a review article about the metallic properties in conducting polymers. The work discusses the state-of-the-art polymers that achieve a metallic state and the limits and opportunities based on these results.

4 Manuscripts

4.1 Manuscript 1



Cite this: *J. Mater. Chem. C*, 2016, 4, 6982

Local order drives the metallic state in PEDOT:PSS†

Philipp Stadler,^{*a} Dominik Farka,^a Halime Coskun,^a Eric D. Głowacki,^a Cigdem Yumusak,^a Lisa M. Uiberlacker,^b Sabine Hild,^b Lucia N. Leonat,^c Markus C. Scharber,^a Petr Klapetek,^d Reghu Menon^e and N. Serdar Sariciftci^a

Weak localization describes a metallic system, where due to the presence of disorder the electrical transport is governed by inelastic electron relaxation. Therefore the theory defines a threshold of spatial and of energetic disorder, at which a metal–insulator transition takes place. To achieve a metallic state in an inherently disordered system such as a conductive polymer, one has to overcome the threshold of localization. In this work we show that the effective suppression of disorder is possible in solution-processible poly(3,4-ethylenedioxythiophene)–poly(styrene sulfonate). We grow polymer films under optimized conditions allowing self-organization in solution. Interestingly, we find the requisite threshold, at which the system becomes finally metallic. We characterize the transition using a complementary morphology and magneto-electrical transport study and find coherent electron interactions, which emerge as soon as local order exceeds the macromolecular dimensions. These insights can be used for discrete improvement in the electrical performance, in particular for tailoring conductive polymers to alternative metal-like conductors.

Received 23rd May 2016,
Accepted 22nd June 2016

DOI: 10.1039/c6tc02129h

www.rsc.org/MaterialsC

1 Introduction

The generation of an intrinsically metallic conductive polymer (CP) is one of the primary goals in developing powerful organic and bio-organic electronics.^{1–7} However, the question, when a CP is regarded as metallic, has caused ambiguous discussions.^{1,2,5,8–10} This relates to the fact that CPs are highly anisotropic – their solid state structure reflects a mutual interplay of different interactions: a polymer strain is covalently connected along the chain direction, while between the adjacent macromolecules stacking forces are dominant. Finally, conductive polymers also have a strong ionic character, as in the doped form, (delocalized) carriers on the polymer chain are counterbalanced by immobile ions. Furthermore, the polymers themselves are prone to condense dispersively with alternating amorphous and crystalline regions. Taking these views into consideration the formation of a

metallic state appears to be strongly dependent on the local order – accepting the fact that some disorder is inherently present. This is an important information, as even classic metals change their electrical transport drastically in the presence of disorder. The physics are therefore described by weak localization (WL).¹¹ WL specifies a system in the presence of disorder, when the electrical transport is governed by inelastic scattering processes. This translates to a change in the sign of the temperature coefficient of the conductivity $\frac{d\sigma}{dT}$ to a positive value. At low temperatures, a minimum is reached – Mott's minimum conductivity, σ_{\min} . At this point inelastic and elastic processes are equally present. In practice, the σ_{\min} for CPs is close to $T = 0$ and therefore experimentally difficult to observe. We therefore shift our attention to the mean inelastic electron scattering lengths, which can be measured above σ_{\min} to obtain a direct insight of the local order.^{12–15} With this information it is possible to resolve the ambiguity of the electrical transport in conductive polymers. Shedding light on the inelastic scattering processes allows us to resolve the metal–insulator-transitions as described by Mott and Anderson.^{16,17} In this work we harness the great potential of self-organization in solution and set up an experimental study to demonstrate finally the metallic state established by the subsequent local order. This represents the crucial ingredient needed to drive the metallic state – even in systems having at first sight a moderate conductivity at room temperature. The experimental path

^a Institute of Physical Chemistry, Johannes Kepler University Linz, Altenbergerstr. 69, 4040 Linz, Austria. E-mail: philipp.stadler@jku.at; Fax: +43 732 2468 1213; Tel: +43 732 2468 8770

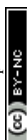
^b Institute of Polymer Science, Johannes Kepler University Linz, Altenbergerstr. 69, 4040 Linz, Austria

^c The National Institute for Electrical Engineering, ICPPE-CA, Splaiul Unirii 313, 030138 Bucharest, Romania

^d Central European Institute of Technology, Koliste 13a, 602 00 Brno, Czech Republic

^e Department of Physics, Indian Institute of Science, Bangalore 560012, India

† Electronic supplementary information (ESI) available. See DOI: 10.1039/c6tc02129h



towards the metal-insulator-transition and the fundamental insight into the electron scattering is presented in detail.

2 Sample growth, measurement techniques and characteristics

We apply a facile route *via* supramolecular self-organization in solution to intrinsically achieve the metallic state in poly(3,4-ethylenedioxythiophene):polystyrenesulfonate (PEDOT:PSS) with alternating concentrations of dimethylsulphoxide (DMSO) and alternating thickness. The films are prepared from the original commercial dispersion (PH1000, Heraeus) using 4 main recipes with various intermediate blends: no DMSO (ref), 2% (*i.e.* 20 μ l per ml volume), 5% and 10% DMSO, both spin-coating and drop-casting. The dispersion is vigorously stirred at 60 °C overnight. For the thicker films we used drop-casting with variable volumes of the dispersion (1 ml to 0.1 ml) dropped on a glass wafer (2.54 \times 2.54 cm²), which is dried at 60 °C for 2 h. The as-gained films (1 to 10 mm) are elevated from the glass and dried once more in an inert atmosphere over CaH₂ at 100 °C. For the thin-films the dispersion is spin-cast using various recipes to obtain thin-film systems ranging from 10 nm up to 100 nm. All films are subsequently dried for 3 days in an inert atmosphere to remove residual DMSO and water. The free-standing bulk films are cut to rectangular 1.5 \times 10 mm² slices and contacted with gold-patterns *in vacuo* as shown in the photograph (Fig. 5D) and mounted on the cryomagnet system, so that the *B*-field is perpendicular to the film plane (*B*_z). In a similar manner, as cast thin-films on sapphire are contacted directly by as-deposited gold. We denote that due to the change in the processing steps between thicker and thinner films, we find minor thickness-effect on the electrical performance (see Fig. 1A and B). Finally, the voltage drop across the inner leads is measured (at *I*_x = 50 μ A) as a function of *T* and *B*-fields. The metallic film picks are characterized further by repeating scans for conductivity and magneto-conductivity, respectively. Similarly, for the XRD spectra the films are cut into 1 \times 1 cm² squares and analyzed using a Bruker AXS diffractometer equipped with a CuK_α source. For the atomic force microscopy (AFM), the bulk-films are cut with a Leica Ultracut microtome and the polished cross-sections are analyzed using a Asylum Research MFP-3D Stand Alone AFM. The thin-films are analyzed directly on the surface as grown on the sapphire substrate.

3 Results and discussion

The casting process for PEDOT:PSS has been investigated in detail earlier – in particular the co-solvent treatment has lead to substantial improvements in the conductivities.^{4,10,18–21} An established pair represents PEDOT:PSS and DMSO as co-solvent.^{20,22–24} This is the system of choice in this work.

We start with a number of thin-film PEDOT:PSS recipes yielding 10 nm thickness and successively increase the width to access a more and more bulk phase up to 10 mm. In addition

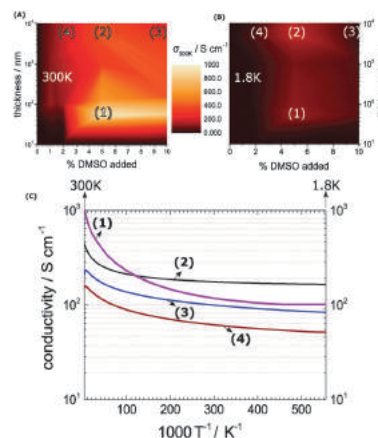
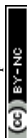


Fig. 1 (A) Room-temperature mapping of PEDOT:PSS conductivities at different DMSO-concentrations and thicknesses. (B) Repeats the map at 1.8 K. (C) The temperature profiles of the conductivities are significantly different between bulk and thin-films. The in detail study systems are highlighted in the map at 55 nm and 5% DMSO (1), 8.4 μ m and 5% DMSO (2), 8.4 μ m and 10% DMSO (3) and finally 8.4 μ m and 2% DMSO (4).

we modify the co-solvent present between 0 and 10% of the original volume dispersion. Our goal is to attain a detailed insight of the co-solvent concentration and of the final film thickness into the resulting conductivities (Fig. 1A). We consistently find excellent electrical performances at DMSO concentrations around 5%. Here we achieve peak conductivities of 1000 S cm⁻¹ at a thickness of 55 nm as seen in the map in Fig. 1A denoted further as (1). The effect is less pronounced at lower and higher DMSO concentrations, which is in agreement with previous studies.^{22,23}

When the film thickness expands to a bulk system greater than 1 μ m we see a similar increase of the electrical performance on the DMSO concentration. Nonetheless, the bulk-films achieve a maximum of 490 S cm⁻¹ at 5% DMSO and 8.4 μ m respectively (2). So the map in Fig. 1A exhibits a consistent out-performance of thin-films over bulk films. Other detailed studied systems are 10% DMSO and 8.4 μ m (3) and 2% DMSO and 8.4 μ m (4).

When we repeat the mapping at 1.8 K we obtain a first insight, where in the map the local order allows the formation of a metallic state (Fig. 1B). According to Mott's minimum conductivity, regions off the metallic regime exhibit an infinite low conductivity, which is valid for the preponderant dark regions seen in the 1.8 K map. Regimes in proximity to a metal-insulator transition (MIT) appear still conductive – they are found in the same hotspots as at room temperature with an important changeover: at 1.8 K, the bulk systems outperform the thin-films. The reason for this lies in the pronounced temperature-dependence of the thin film conductivities. Meanwhile, the bulk film conductivities exhibit a moderate temperature-profile in agreement with weak localization with a flattening as the temperature approaches 0 (Fig. 1C).



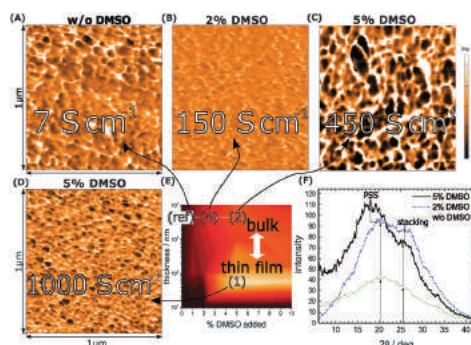


Fig. 2 In panels (A–C) the cross-sectional morphologies by AFM of no DMSO (ref), (4) and (2) are shown. In (D) the morphology of (1) by AFM is depicted (surface scan). (E) Conductivity map at 1.8 K. The XRD-spectra in (F) highlight the improved crystallinity in (4) and (2) as compared to (ref) by increasing the DMSO concentration during film-growth.

In combination, the maps show us the optimum region, which lies between 2 and 5% DMSO and 8.4 μm layer thickness (2) and (4). At 5% DMSO and 1.8 K, for example, the bulk-conductivity (2) exceeds the 55 nm thin-film (1) conductivity by a factor of nearly 2. This minor temperature-sensitivity points out that the thickness plays a role in terms of local order – it relates to the different parameters in the processing and to a suppressed substrate-effect in the bulk-systems. To support our findings from the conductivity maps we view the morphologies by AFM and XRD, in particular in the optimum region (Fig. 2).

For the bulk films we plot the XRD spectra at no (ref), 2% (4) and 5% DMSO (2). A sharpened profile in terms of crystallinity correlates with the presence of DMSO during growth.^{25,26} (Fig. 2E). In general the increase of the electrical conductivity from Fig. 1A is reflected in a pronounced signal, which underlines the higher degree of crystallinity. The discrete peak originating from the π -stacking of PEDOT emerges at 25 deg. It is overlapped by the broad response of the PSS halo with a maximum at 20 deg. The spectral shaping through DMSO consequently supports our argument of improved crystallization in the presence of DMSO valid for both components, PEDOT and PSS, respectively. To clarify, we present a comparison of PEDOT and regio-regular poly(-3-hexylthiophene) (π -P3HT) grown under similar conditions in the ESL.[†] A supplementary view of the morphological changes induced by DMSO is outlined by atomic force microscopy (AFM). As shown in the phase images in Fig. 2A–D we find different grain sizes at each representative (conductivity) area (marked as a white rectangular frame) from the conductivity map (Fig. 2E). Fig. 2D depicts the thin-film phase image revealing a randomized distribution of structured domains with different grain sizes. This is reminiscent to the bulk-film without DMSO, where polydispersity is detected again. Obviously, the presence of small amounts of DMSO (2%) and thicker films (4) improves the homogeneity a lot as shown in Fig. 2B, where the grains of the structure become smaller. To achieve a growing grain size and a homogeneous dispersion

the concentration has to be further increased to 5% (2), where we find the point of merit in terms of conductivity, crystallinity and morphology in the bulk-films. We denote that we derive the bulk-film morphology from cross-sectional scans in order to allow a meaningful comparison between bulk and thin-film morphologies.

The morphology response of the different conductivity-stages reveals the importance of long-range order plus the role of dispersivity seen in growing ordered domains of similar size, which explains the improved electrical performance at low- T .

Back in Fig. 1 we outline the positive temperature coefficient $\frac{d\sigma}{dT}$ with finite conductivity as T approaches 0 best seen in (4), (1) and (2). This behaviour corresponds to weak localization. To resolve the low- T regime, we use the derivative of the conductivity in the logarithmic scale $\frac{d(\ln \sigma)}{d(\ln T)}$ further denoted as W .²⁷

The metallic character is expressed by the slope and magnitude of $W(T)$. As seen in Fig. 3 the system without DMSO (ref) shows a constant W with quantities greater than 1 (insulating regime). In contrast, (4), (1) and (2) deviate – $W(T)$ is not constant. In particular, at low temperature it illustrates that on which side of the MIT the system is situated. In the case of bulk 5% DMSO (2), the slope of $W(T)$ becomes positive indicating a metallic state (Fig. 3B). We denote that in particular the thin-film response from (1) shows a clear non-metallic fingerprint at low- T , which we assign to the role of dispersivity.

The proximity of the metallic state can be tested by applying a high magnetic field perpendicular to the substrate plane ($B_z = 9$ T). The field induces localization and quenches the metallic state as shown in Fig. 3. A substantial change in $W(T)$ by B is therefore seen below 10 K. There W splits up into a critical-metallic

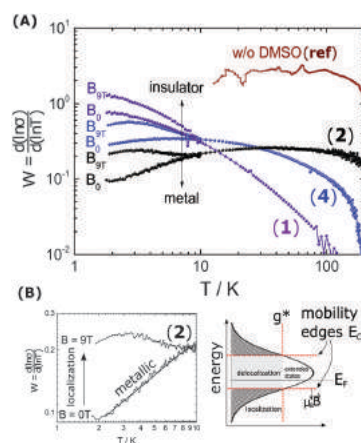
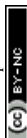


Fig. 3 (A) Highlights the exponent of the power-law dependence $\frac{d \ln \sigma}{d \ln T}$ (W), in particular at low temperatures ($T \leq 10$ K) and high magnetic field ($B = 9$ T). While the first sample (no DMSO) (ref) operates beyond the transition line at $W = 1$, we see a shift towards a metal in (1), (2) and (4) and high B -field localization resulting in a negative magnetoconductivity.



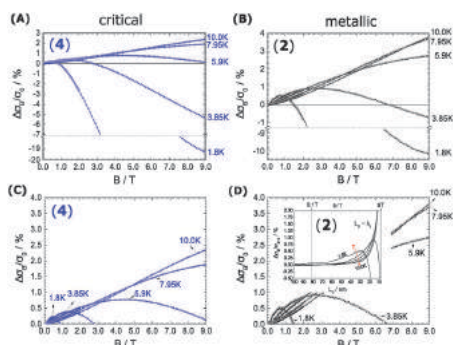


Fig. 4 (A) 2% (4) and (B) 5% DMSO-cast (2) PEDOT:PSS systems reflect the interplay between positive and negative magnetoconductivity (MC) at low T . For each T the positive effects dominate first at low B followed by a flip to the negative by increasing B (at 1.8 K, 3.85 K and 5.9 K). At higher T (7.95 and 10.0 K) the MC is only positive. We denote that the negative effect is more pronounced in the critical sample. In (C) and (D) we expand the positive side and show the semicircular development of each MC with B . In the metallic sample (1) we depict its MC as a function of the Landau orbit size L_D in addition to show the interference under resonance conditions, when the mean inelastic scattering length λ_c and L_D are of similar dimension (inset).

($B = 0$ T) and non-metallic regime ($B = 9$ T). This is true for both (4) and (2) (only for the bulk systems), where a shallow metallic behaviour is observed at T below 10 K.

So far, we have created a system with sufficient local order. We prove the metallic behaviour in the bulk samples between 1.8 K and 10 K seen by $W(T)$ in Fig. 3B. In addition we demonstrate that a high magnetic fields can disrupt the local order of a metallic state, in particular at low temperatures.

When we take the view to the lower B -field, interestingly we find a concomitantly stimulating effect on the metallic character in our samples of merit (2 and 4). In contrast to Fig. 3 low B -fields enhance the conductivity. A detailed view of the magnetoconductivity $\frac{\Delta\sigma_B}{\sigma_0}$ as a function of B shows this positive contribution (Fig. 4).

We observe the conductivity increasing up to 4% of the original value. It is followed by a significant decrease to the negative as the field is increased. The negative effect is damped at high temperatures, where the turn to the negative is indicated at high B and not seen at all at temperatures above 6 K. One explanation for magnetic stimulation relates to a electromagnetic resonance, earlier found in systems defined by weak localization: In fact, the stimulation reflects an interaction among the electron wave functions, as soon as the inelastic mean free path of electrons λ_c and the Landau orbit size L_D ,^{28–30} become comparable.

$$L_D \approx \lambda_c \text{ with } L_D = \sqrt{\frac{\hbar}{e \cdot B}} \quad (1)$$

Eqn (1) depicts the relation of L_D (or B) and of λ_c (Fig. 4). At 1.8 K, for example, the $\Delta\sigma_B$ -value increases up to 1 T (2),

before it collapses to the negative by increasing B (Fig. 4C and D). The peak maximum of $\Delta\sigma_B$ corresponds to the amplitude of the local order or λ_c , respectively. It can be consequently read out by plotting L_D instead of B . A similar but right-shifted profile is observed at 3.85 K. At higher temperatures the stimulations do not collapse meaning that λ_c exceeds the maximum field at $B_{\max} = 9$ T or $L_D = 8.1$ nm according to eqn (1), as λ_c decreases below the maximum magnetic field as we increase the temperature. Positive magnetoconductivity has been reported solely in combination with metallic samples – it reveals a coherence among electron wave functions and B .^{28,30–37} In our case this is supported by the morphology study (homogeneous domains of similar size, Fig. 3). Other theories assign the stimulating magneto-effect to the spin-orbit coupling. However, in organic matter these effects can be neglected.¹¹ We use the coherent electron interactions as a direct consequence of long-range order inside the polymer. To quantitatively evaluate the magnetoconductivity, we derive concrete values for λ_c statistical parameters to visualize the local order. Kawabata has posted a relation between magnetoconductivity and the relaxation time (hence the mean free path λ_c).²⁸ We can derive the magnitude by plotting $+\sigma_B$ versus B^2 according to

$$\Delta\sigma_{MC} = +(4\pi) \cdot \frac{e^2}{\hbar^2} \cdot G_0 \cdot \lambda_c^3 \cdot (B)^2 \quad (2)$$

using the elemental charge e and the Plank constant \hbar and the conductance quantum $G_0 = \frac{2e^2}{h}$. The corresponding Fig. 5 shows the temperature-variant slopes and the accompanying linear fits for each temperature. In the best case in (2) the electron coherence quantitatively translates to a scattering

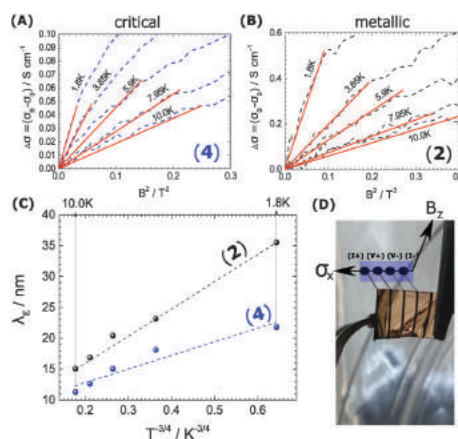


Fig. 5 (A and B) Depict the linear dependence of the magnetoconductivity $\Delta\sigma_B$ and B^2 at low fields in the samples of merit (2) and (4). The slope (linear fit) is proportional to the mean inelastic scattering length λ_c . (C) Shows the T -dependence of λ_c . For inelastic scattering an exponent of $-\frac{3}{2}$ is typical. This is only the case in the metallic 5% DMSO sample (2). (D) Depicts the sample (free-standing PEDOT:PSS film with 4 Au leads) ready for loading into the cryomagnet.

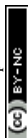


Table 1 Electrical parameters of the metallic and critically-metallic phase in PEDOT:PSS

Label	Thickness/ nm	% DMSO	$\sigma_{300K}/$ S cm ⁻¹	$\sigma_{1.8K}/$ S cm ⁻¹	Ratio $\sigma_{300K}/\sigma_{1.8K}$	λ_c /nm (at 1.8 K)
(ref)	8400	0	7.1	N/A	N/A	N/A
(1)	55	5	1000	101.5	9.83	N/A
(2)	8300	5	490	170	2.54	35.5
(3)	9200	10	275	80	3.42	N/A
(4)	8300	2	155	50	2.96	21.8

length of 35.5 nm at 1.8 K. This value exceeds the macromolecular dimensions and explains the metallic fingerprint of the system. We summarized all relevant parameters in Table 1. With the $T^{(-\frac{1}{3})}$ vs. λ_c plot in Fig. 5C we include the temperature-dependence with the exponent 0.75 typical for inelastic scattering.²⁹ The dimensions of λ_c are exponentially decreasing by increasing the temperature – as we go off the metallic regime, we observe a deviation as visible in the critically transition regime in (4).

4 Conclusions

We underline here the value of magnetoconductivity to display local order, which is crucial to establish a metallic state in a conductive polymer. The order can be surfaced by the coherent transport and represents a strong argument for achieving a metallic state. We show that it is possible to improve on the electrical performance, when the morphology becomes homogeneous and locally ordered. This is demonstrated by expanding the sample's dimension towards a bulk-phase and by allowing self-organization. Thus our strategy can be a model system for various CP-systems to strengthen their electrical transport properties towards an intrinsically-metallic, alternative conductor.

Acknowledgements

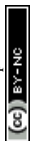
This work has been supported by the OEAD (WTZ, IN10/2015) and the Austrian Fund for Advancement of Science (FWF) within the Wittgenstein Prize scheme (Z222-N19 Solare Energiewandlung).

References

- K. Lee, S. Cho, S. Heum Park, A. J. Heeger, C.-W. Lee and S.-H. Lee, *Nature*, 2006, **441**, 65–68.
- Y. H. Kim, C. Sachse, M. L. Machala, C. May, L. Müller-Meskamp and K. Leo, *Adv. Funct. Mater.*, 2011, **21**, 1076–1081.
- D. Alemu Mengistie, P.-C. Wang and C.-W. Chu, *J. Mater. Chem. A*, 2013, **1**, 9907.
- O. Bubnova, Z. U. Khan, H. Wang, S. Braun, D. R. Evans, M. Fabretto, P. Hojati-Talemi, D. Dagnelund, J.-B. Arlin, Y. H. Geerts, S. Desbief, D. W. Breiby, J. W. Andreasen, R. Lazzaroni, W. M. Chen, I. Zozoulenko, M. Fahlman, P. J. Murphy, M. Berggren and X. Crispin, *Nat. Mater.*, 2013, **13**, 190–194.
- D. A. Mengistie, P.-C. Wang and C.-W. Chu, *ECS Trans.*, 2013, **58**, 49–56.
- N. Massonnet, A. Carella, A. de Geyer, J. Faure-Vincent and J.-P. Simonato, *Chem. Sci.*, 2015, **6**, 412–417.
- E. Stavrinidou, R. Gabriellson, E. Gomez, X. Crispin, O. Nilsson, D. T. Simon and M. Berggren, *Sci. Adv.*, 2015, **1**, e1501136.
- J. Huang, P. Miller, J. de Mello, A. de Mello and D. Bradley, *Synth. Met.*, 2003, **139**, 569–572.
- Y. Xia, K. Sun and J. Ouyang, *Adv. Mater.*, 2012, **24**, 2436–2440.
- B. J. Worfolk, S. C. Andrews, S. Park, J. Reinspach, N. Liu, M. F. Toney, S. C. B. Mannsfeld and Z. Bao, *Proc. Natl. Acad. Sci. U. S. A.*, 2015, **112**, 14138–14143.
- G. Bergmann, *Phys. Rep.*, 1984, **107**, 1–58.
- S. D. Baranovskii, *Phys. Status Solidi B*, 2014, **251**, 487–525.
- H. C. F. Martens, J. A. Reedijk, H. B. Brom, D. M. de Leeuw and R. Menon, *Phys. Rev. B: Condens. Matter Mater. Phys.*, 2001, **63**, 073203.
- A. Aleshin, R. Kiebooms, R. Menon and A. Heeger, *Synth. Met.*, 1997, **90**, 61–68.
- R. Menon, C. O. Yoon, D. Moses, A. J. Heeger and Y. Cao, *Phys. Rev. B: Condens. Matter Mater. Phys.*, 1993, **48**, 17685–17694.
- P. W. Anderson, *Phys. Rev.*, 1958, **109**, 1492–1505.
- N. F. Mott, *Philos. Mag.*, 1972, **26**, 1015–1026.
- S. Jönsson, J. Birgeron, X. Crispin, G. Greczynski, W. Osikowicz, A. Denier van der Gon, W. Salaneck and M. Fahlman, *Synth. Met.*, 2003, **139**, 1–10.
- O. Bubnova, Z. U. Khan, A. Malti, S. Braun, M. Fahlman, M. Berggren and X. Crispin, *Nat. Mater.*, 2011, **10**, 429–433.
- J. Gasiorowski, R. Menon, K. Hingerl, M. Dachev and N. S. Sariciftci, *Thin Solid Films*, 2013, **536**, 211–215.
- X. Crispin, F. L. E. Jakobsson, A. Crispin, P. C. M. Grim, P. Andersson, A. Volodin, C. V. Haesendonck, M. V. D. Auweraer, W. R. Salaneck and M. Berggren, *Chem. Mater.*, 2006, **18**, 4354–4360.
- I. Cruz-Cruz, M. Reyes-Reyes, M. Aguilar-Frutis, A. Rodriguez and R. López-Sandoval, *Synth. Met.*, 2010, **160**, 1501–1506.
- C. Pathak, J. Singh and R. Singh, *Curr. Appl. Phys.*, 2015, **15**, 528–534.
- T.-R. Chou, S.-H. Chen, Y.-T. Chiang, Y.-T. Lin and C.-Y. Chao, *J. Mater. Chem. C*, 2015, **3**, 3760–3766.
- Q. Wei, M. Mukaida, Y. Naitoh and T. Ishida, *Adv. Mater.*, 2013, **25**, 2831–2836.
- C. M. Palumbiny, F. Liu, T. P. Russell, A. Hexemer, C. Wang and P. Müller-Buschbaum, *Adv. Mater.*, 2015, **27**, 3391–3397.
- E. B. Aleksandrov, I. V. Sokolov, A. Gatti, M. Kolobov, L. Lugiatto and T. Vartanyan, *Usp. Fiz. Nauk*, 2001, **171**, 1263.
- A. Kawabata, *Solid State Commun.*, 1980, **34**, 431–432.
- P. A. Lee and T. V. Ramakrishnan, *Rev. Mod. Phys.*, 1985, **57**, 287–337.
- A. B. Kaiser, *Rep. Prog. Phys.*, 2001, **64**, 1.
- B. Chapman, R. G. Buckley, N. T. Kemp, A. B. Kaiser, D. Beaglehole and H. J. Trodahl, *Phys. Rev. B: Condens. Matter Mater. Phys.*, 1999, **60**, 13479–13483.




- 32 F. Pikus and G. Pikus, *Solid State Commun.*, 1996, **100**, 95–99.
- 33 T. F. Rosenbaum, R. F. Milligan, G. A. Thomas, P. A. Lee, T. V. Ramakrishnan, R. N. Bhatt, K. DeConde, H. Hess and T. Perry, *Phys. Rev. Lett.*, 1981, **47**, 1758–1761.
- 34 R. Menon, K. Väkiparta, Y. Cao and D. Moses, *Phys. Rev. B: Condens. Matter Mater. Phys.*, 1994, **49**, 16162–16170.
- 35 Y. Nogami, H. Kaneko, H. Ito, T. Ishiguro, T. Sasaki, N. Toyota, A. Takahashi and J. Tsukamoto, *Phys. Rev. B: Condens. Matter Mater. Phys.*, 1991, **43**, 11829–11839.
- 36 H. H. S. Javadi, A. Chakraborty, C. Li, N. Theophilou, D. B. Swanson, A. G. MacDiarmid and A. J. Epstein, *Phys. Rev. B: Condens. Matter Mater. Phys.*, 1991, **43**, 2183–2186.
- 37 G. Bergmann, *Phys. Rev. B: Condens. Matter Mater. Phys.*, 1983, **28**, 2914–2920.



4.2 Manuscript 2

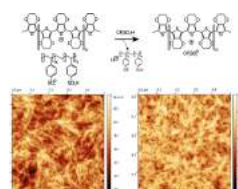
Increase in electron scattering length in PEDOT:PSS by a triflic acid post-processing

Dominik Farka¹  · H. Coskun¹ · P. Bauer² · D. Roth² ·
B. Bruckner² · Petr Klapetek³ · N. Serdar Sariciftci¹ ·
P. Stadler¹

Received: 12 December 2016 / Accepted: 23 March 2017 / Published online: 31 March 2017
© The Author(s) 2017. This article is an open access publication

Abstract A stringent limitation in many optoelectronic devices, such as solar cells and light emitting diodes, is the intrinsic need for a transparent electrode. Uniting relevant aspects, indium tin oxide (ITO) is often the material of choice, however, alternatives are sought and being in particular found in conductive polymers. In this work, we present a novel doping strategy to arrive at highly conducting polymeric material based on poly-3,4-ethylenedioxythiophene (PEDOT). Based on commercial high conductivity PEDOT:PSS (Clevios PH 1000), and a post processing with aqueous triflic acid delivers a material that is both transparent and of low resistivity ($5.23 \times 10^{-4} \Omega \text{ cm}$). Furthermore, this material retains its conductive character over a large temperature range, indicating metallic behaviour. This is further supported by positive magnetoconductance effects at low temperatures (1.8–10 K) and extended mean free paths of the conduction electrons are observed—evidencing for a metallic state in this polymer.

Graphical abstract



Keywords Transparent conductive electrodes · Conductive metallic polymers · Anderson localization · Mott–Ioffe–Regel limit · Infrared transparency

Introduction

In recent years, the rise of consumer electronics with liquid crystal displays, organic light emitting diode (OLED)-based displays [1], OLED-based home lighting [2], and the introduction of concepts such as photovoltaic windows [3] led to a dramatic increase in demand for transparent electrode materials. This demand led to a substantial price-increase of the current state-of-the-art material, indium-doped tin oxide (ITO) [4].

An alternative to inorganic oxides for transparent electrodes can be found in organic, conductive polymers. The primary advantage of organic polymers lies in their reliance on organic synthesis, opening a limitless multitude of possible structures, virtually only limited by the researchers' fantasy. Chemically or electrochemically doping of an organic, conjugated polymer then delivers a conducting material from a semiconducting (or even insulating)

Electronic supplementary material The online version of this article (doi:10.1007/s00706-017-1973-1) contains supplementary material, which is available to authorized users.

✉ Dominik Farka
dominik.farka@jku.at

¹ Linz Institute for Organic Solarcells (LIOS), Institute of Physical Chemistry, Johannes Kepler University Linz, Altenberger Strasse 69, 4040 Linz, Austria

² Department of Physics, Atom and Surface Physics, Johannes Kepler University Linz, Altenbergerstr. 69, 4040 Linz, Austria

³ Department of Nanometrology, Czech Metrology Institute, Okružní 31, 63800 Brno, Czech Republic

starting system. This doping process, however, introduces disorder into the system—as opposed to inorganic semiconductors, where doping process replaces atoms. Organic molecules and counterions need to move inside the film, introducing disorder and thereby quenching the materials metallic properties [5–7].

In recent years, doped poly-3,4-ethylenedioxythiophene (PEDOT) has become the material of choice in the industry among the transparent, organic conductors, and many researchers have combined their efforts in its development [8–13]. To date, the commercially available doped PEDOT polymer combines both, good conductivity and transparency, it has found use in various types of devices and applications [14–19].

In this publication, we present a method to increase the conductivity of commercially available PEDOT:PSS by counter-ion exchange. Based on commercial Clevios PH1000 (high conductivity PEDOT:polystyrene sulfonate), a comparison between the conductivity of the material arrived at by spin-coating the dispersion as is (referred to as PEDOT:PSS), with addition of DMSO (5% by volume; PEDOT:PSS*), and with additional processing by triflic acid (PEDOT:TA) exposure will be comparatively presented. Furthermore, we investigated the correlation between PEDOT-content and resistivity in aforementioned systems. The enhanced metallic character of PEDOT:TA made magnetotransport measurements possible at low temperatures.

Results and discussion

Relying solely on solution processing, the herein presented films were spin-coated on top of glass or sapphire (1110) substrates. The schematics of film preparation can be found in Fig. 1. In this study, we compared three materials based on commercial PEDOT:PSS (Clevios PH1000): plain PEDOT:PSS (obtained from untreated dispersion), PEDOT:PSS* (obtained from a dispersion with 5% DMSO content), and PEDOT:TA (the latter substance treated with excess of equimolar, aqueous triflic acid, neutralized by rinsing with excess 18 M Ω cm water). As the exposure to

triflic acid leads to dramatic decrease in film thickness, multiple-layers of PEDOT were spin-coated to achieve films of thicknesses similar to other materials.

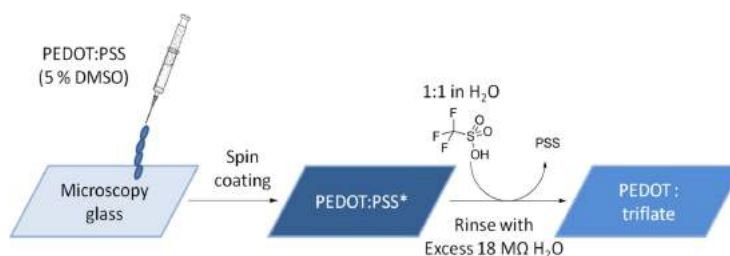
To compare resistivity, a number of versions of PEDOT were processed on top of sapphire samples containing previously deposited electrodes (Cr/Au, 8 nm/80 nm, respectively) in van-der-Pauw and four-in-line geometries. In this way, artefacts originating from geometric effects were minimized. A thorough resistivity-scan over a wide range of temperatures was performed. The results can be found in Fig. 2a.

As expected, samples obtained from spin-coating the as-is dispersion showed a strongly expressed dependence on temperature (PEDOT:PSS), the films becoming virtually insulating upon cooling. This points towards a purely, temperature-activated process requiring a high activation energy of 8.6 meV. The DMSO-treated samples (PEDOT:PSS*) showed substantially better resistivity dependence on temperature, albeit overshadowed by the performance of PEDOT:TA.

The dynamics during spin-coating deposition are quite complex, since varying turning speeds and tuning the DMSO concentration effect substantially different film properties. One role we attribute to DMSO is the improvement of the morphology of the resulting PEDOT:PSS films by acting as a co-solvent. The second contribution is the improvement of film purity as shown by RBS results. This is true regarding the stoichiometry between conducting polymer and doping agent as well as for the removal of other impurities (see Supplementary Material Figs. 1 and 2, respectively).

Since DMSO is a good solvent (polar and aprotic) it dissolved impurities and excess PSS, leaving behind a 1:1 ratio of PEDOT:PSS with diminished impurities (see Supplementary Material Figs. 1 and 2, respectively). With decreasing temperature, PEDOT:PSS* electron-transport properties worsened by a full order of magnitude. This hints to a metallic behaviour within this material, and can be seen as low resistivity at low temperatures rather unusual for a conductive polymer—probably due to the advantageous effects of DMSO mentioned above [20, 21].

Fig. 1 Preparation of PEDOT:triflate films via solution processing



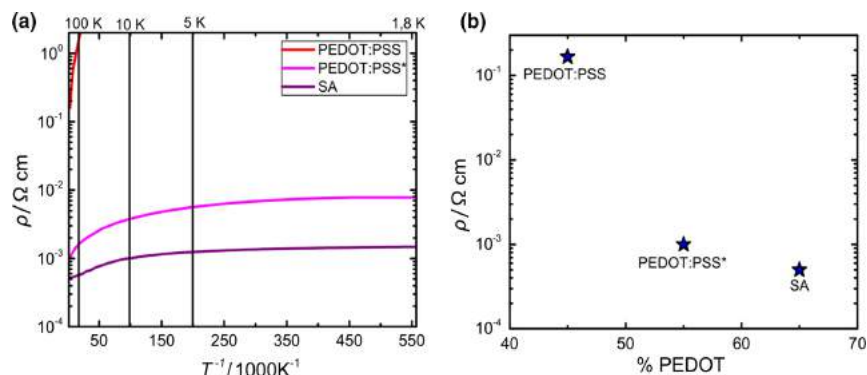


Fig. 2 a Comparison of resistivity profiles of PEDOT derivatives over a temperature range between 300 and 1.8 K. Note the dramatic decrease in PEDOT:PSS. A heavy reliance on thermally activated transport is required. **b** Correlation of PEDOT-content and

conductivity aforementioned PEDOT derivatives. An exponential drop in resistivity (on a log-scale) with the content of conducting material within the film can be observed

Strikingly, the material receiving triflic acid-treatment still showed even lower resistivities at temperatures below 2 K, namely $1.4 \times 10^{-3} \Omega \text{ cm}$ —a more than fivefold improvement over PEDOT:PSS*. This overall low resistivity of PEDOT:TA and good retention of performance over a large temperature range indicate enhanced order within the film meaning that the disorder introduced during the anion-exchange is comparably small, its adverse effects by far outweighed by the positive ones. This picture, however, does not include the possibility of a correlation between enhanced electro-transport and the amount of conductive material within the film.

To be able to exclude the possibility of a sole “concentration effect” of conductor versus counterion [21], the content of PEDOT (by molecular %) within the sample was investigated using Rutherford Backscattering (RBS, see SI for original data). From that, the PEDOT-content within the film was derived. The results of the comparison are shown in Fig. 2b.

The results clearly indicate a partial dependence of PEDOT content. As expected, a large excess of PSS in PEDOT:PSS correlated well with its electrical performance at room temperature. Truly, an increased amount of PEDOT within the triflate-treated films was found, over PEDOT:PSS*. A 20% increase in content of conducting material over PEDOT:PSS* within the thin-films resulted in a de facto halving of the resistivity at room temperature.

To further strengthen the argument of order over “concentration”, Atomic Force Microscopy (AFM) was performed on PEDOT:PSS* (Fig. 3b) and PEDOT:TA (Fig. 3c). It appeared that the global order within the film remained similar, yet smoother films with fewer depressions were obtained. In Fig. 3d and e, we compare the same

films via Transmission Electron Microscopy (TEM). Also there, an increase of order in the form of a more uniform distribution of moieties within the film can be observed after acid-treatment.

However, no global connectivity was observed in either case—even worse, a picture of many separate grains was observed. Hence, it seemed feasible, that the increased conductivity is indeed mainly caused by the elevated PEDOT-content.

As PEDOT:TA already showed metallic fingerprints in the form of a rather low and flat resistivity-temperature profile we looked for magnetoresistance behaviour at low temperatures, typical for metals. As such effects are expected to be most pronounced at low temperatures, scans at 1.8, 3.8, 5.9, 7.9, and 10 K were performed at fields ranging between 0 and 9 T (see Fig. 4a). At the lowest two temperatures, 1.8 and 3.8 K, the described effect is best visible. At first, a negative magnetoresistance can be observed at lower fields (up to 0.74 and 3.4 T, respectively).

On the contrary, upon trespassing this threshold, positive magnetoresistance was observed as the metallic behaviour was disordered by the field. Having both contributions is a hallmark of metallic polymers. From that, it is possible to calculate the Landau orbit size, L_D , which corresponds to the magnetic penetration depth. In that way, the electron scattering length, λ_e , can be derived (Eq. 1).

$$L_D = \lambda_e \quad L_D = \sqrt{\frac{\hbar}{e \cdot B}} \quad (1)$$

For the obtained fields, the corresponding electron scattering length at 1.8 K corresponds to 58.4 nm and to 27.2 nm for 3.9 K. These are truly astonishing findings for a conducting polymer, especially in comparison with

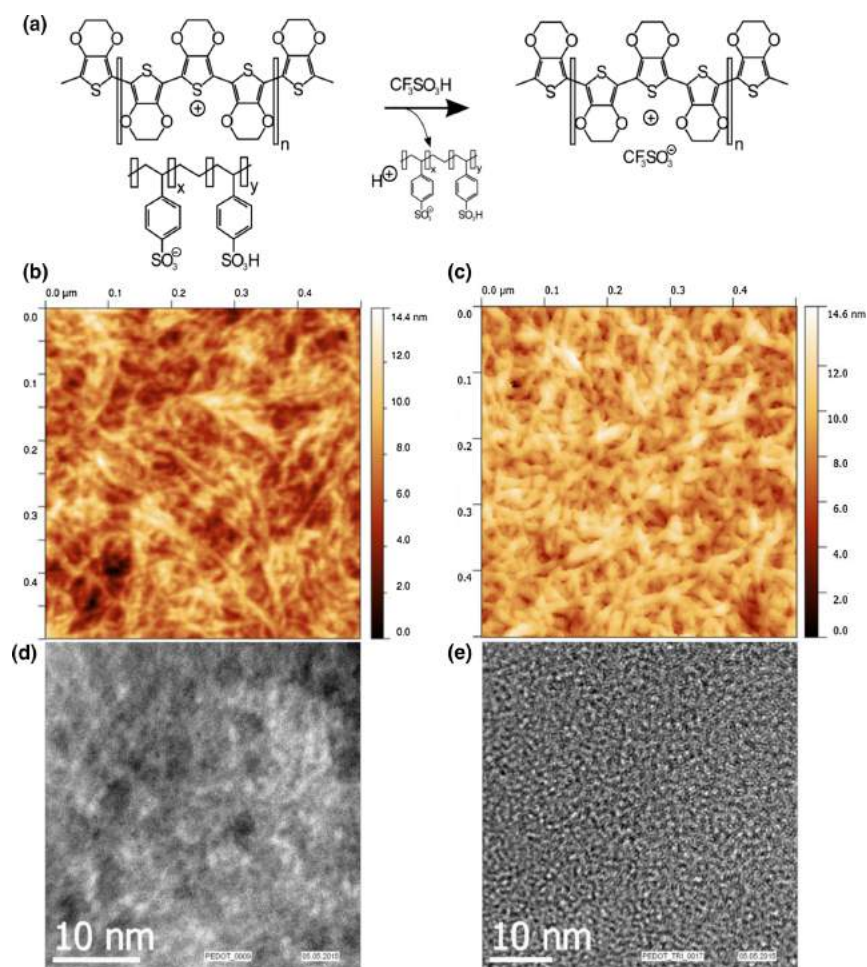


Fig. 3 **a** Counterion exchange mechanism. **b** AFM image of PEDOT:PSS* on a 500×500 nm area compared to PEDOT:TA on the same scale. **c** Note the decrease in roughness as fewer voids are left within the film, corresponding to enhanced electro-transport

properties. **d, e** Comparison of TEM images of these films. A more uniform distribution of moieties within the film can be observed, correlating well with the AFM results

values reported earlier for PEDOT:PSS* [7]. As high PEDOT-content alone does not explain this effect local order of the polymer appears to be improved to explain such behaviour.

As the measurement of magnetoconductivity was possible, we were further interested, to see the difference between the resistivity profile when exposed to a strong magnetic field (9 T) and none (0 T). The results of such a measurement can be plotted in the so-called W -plot, reported by Zabdrowskii and Zinojeva [22]. Here, $\log T$ is

plotted versus the negative value of the first derivative of resistivity after temperature, helping to visualize the type of transport of the material of question.

$$W = - \left(\frac{\delta \ln \rho}{\delta \ln T} \right) \quad (2)$$

W is used to expand the low- T transition regime between critically metallic behaviour ($\frac{\Delta W}{\Delta T} \sim \text{const.}$) and actually metallic ($W < 0$). The log-log plot in Fig. 4b exactly shows such a trend in PEDOT:TA, i.e. W exponentially

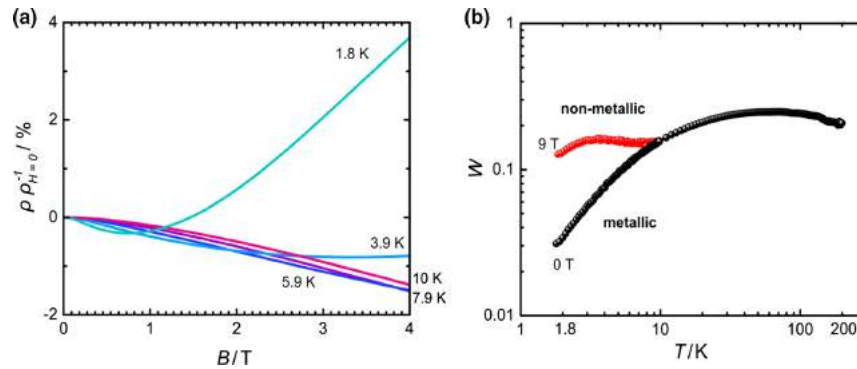


Fig. 4 **a** Magnetoconductivity of PEDOT:TA. The minima 0.74 and 3.4 T correspond to mean free electron paths of 58.4 and 27.2 nm. **b** Zabrodskii diagrams of PEDOT:TA. The so-called W -plot describes a change from an Anderson insulator to a glassy metal [22]. The

application of a magnetic field of 9 T at 1.8 K effects a disturbance within the materials way of conduction, thus leading destroying the metallic properties within the material

approaches 0 with decreasing temperature characteristic for Anderson transitions in (metallic) conductive polymers.

As one can clearly see, at the absence of a magnetic field, the material clearly behaves as a glassy metal, getting closer to a metallic behaviour with decreasing temperature. This would indicate that order is induced with cooling the sample, supporting metallic transport modes. Repeating the same experiment at a high field (9 T), a different behaviour is observed. When cooling the sample, a flat profile for W versus T is observed, this means that the metallic features are disrupted by the strong external magnetic field. All those effects are strong indications for a metallic state in this polymer, which was achieved by anion exchange and solution processing.

Conclusion

Three different solution-processed, PEDOT-based conducting materials were compared for their resistivity. In the case of PEDOT:TA (triflate), a flat temperature profile of resistivity down to 1.8 K is observed, indicating metallic behaviour. A correlation between the materials content of conducting polymer and the resistivity was observed. Structural film-analysis via AFM and SEM indicated no global order within the film. Rough and globally disordered films were obtained upon treatment with triflic acid. Those films, however, showed a positive magnetoresistance, typical for metals. Also, at low temperatures (1.8 and 3.9 K), tremendous values for mean free path of electrons conducted by PEDOT:TA were found, ranging in the hundreds of Angstroms implying local order within the material. This was further supported by the results of the

W -plots, where the metallic properties were quenched by applying a strong magnetic field, implying a metallic state.

Experimental

Substrate preparation

Sapphire (polished, 1110) and glass (for AFM measurements) substrates were used as substrates for all experiments. For cleaning, a four-step washing procedure (15 min steps) by consecutive sonication in different solvents was conducted: acetone (technical grade, room temperature), 2-propanol (50 °C), Hellmanex detergent (70 °C), and deionized water (room temperature). The electrical contacts were deposited using PVD through the van-der-Pauw and four-in-line mask (8 nm Cr/80 nm Au), respectively.

Conductive polymer deposition

All samples were prepared using spin-coating. PEDOT:PSS thin-films were achieved by spin-coating of commercial Clevios PH1000 (a dispersion) as obtained from the manufacturer (Heraeus) on top of the respective substrate. PEDOT:PSS* and PEDOT:TA thin-films were both prepared in the following way: 5% DMSO (v/v) was added to dispersions of Clevios PH1000 (by the Heraeus company), freshly before spin-coating. For all spin-coating steps the same recipe was used (recipe: 10 rps, 2 s ramp, 30 s spinning; 100 rps, 2 s ramp, 30 s spinning).

To achieve PEDOT:TA, the prepared sample was exposed to an excess of an equimolar solution of triflic acid

in water for 1 min followed by three consecutive steps of exposure to an excess 18 M Ω cm water. After exposure, the samples were dried by spin-coating using the same recipe as mentioned above. For conductivity measurements, the active area of the samples measured was protected by drop-casting PMMA (in anhydrous toluene) on top of the measured area. Coating was performed on top of sapphire substrates and microscopy glass slides. For TEM measurements, the same procedure was applied on top of a copper-grid.

Film characterization

AFM data were obtained using Dimension Icon SPM from Bruker in ScanAsyst regime which is an intermittent contact measurement procedure suitable for soft samples. Scanasyst-Air probes were used, with nominal probe radius in range of 2–12 nm. Scanning speed was approximately 0.2 Hz (for individual fast scan axis profiles). All TEM measurements were done using a JEOL JEM-2011. The samples (PEDOT:PSS* and PEDOT:TA) were deposited on top of a copper grid as described above. All pictures shown in this publication were obtained using the same focus and a voltage of 100 kV.

Rutherford backscattering spectrometry (RBS) measurements were performed at the Department of Atomic Physics and Surface Science (JKU) using the AN-700 van de Graaff accelerator in a HV chamber (base pressure in the 10⁻⁷ mbar range), which is equipped with two semiconductor surface barrier (SSB) detectors: a LN₂-cooled high resolution detector [23] situated at 150.1° in Cornell geometry (FWHM \sim 3 keV), and a standard SSB detector of larger solid angle in 154.6° in IBM geometry. Energy spectra of the PEDOT:PSS samples on Si were recorded using 200 keV D⁺ ions and normal incidence of the ion beam, for the PEDOT:PSS samples on sapphire 220 keV D⁺ ions and an angle of incidence of 60° were used to optimize depth resolution. To avoid charging effects due to sapphire substrate, prior to the RBS measurements the samples were coated with a thin gold layer. The experimental spectra were evaluated employing the SIMNRA simulation software [24]; the uncertainty of the final compositions is \sim 10–20% with higher values for the samples on sapphire substrates.

The PMMA-covered PEDOTs were contacted using indium solder and loaded to the magnetotransport system (DynaCool PPMS, QuantumDesign and Lakeshore 8040 series, respectively). The electrical resistivity ρ_{xx} was characterized as function of temperature between 300 and 1.8 K. A reproduction in the Lakeshore system between 300 and 10 K was done using the van-der-Pauw electrode-geometry. In the Dynacool system, magnetoresistance

measurements were conducted at fields between 0 and 9 T for following temperatures: 1.8, 3.8, 5.9, 7.9, and 10 K.

Acknowledgements Open access funding provided by Austrian Science Fund (FWF). P.S., N.S.S. and D.F. are grateful to OEAD (WTZ, IN10/2015) and the Austrian Fund for Advancement of Science (FWF) within the Wittgenstein Prize scheme (Z222-N19 Solare Energieumwandlung) for financial support. N.S.S. and D.F. would like to thank the Austrian Research Promotion Agency FFG for financial support (FFGP13540004 3D-OFET). The authors thank Eitan Ehrenfreund and Eric D. Głowacki for fruitful discussions. We acknowledge the Centre Surface and Nanoanalytics (ZONA, G. Hesser, Prof. K. Hingerl) for TEM measurements.

Open Access This article is distributed under the terms of the Creative Commons Attribution 4.0 International License (<http://creativecommons.org/licenses/by/4.0/>), which permits unrestricted use, distribution, and reproduction in any medium, provided you give appropriate credit to the original author(s) and the source, provide a link to the Creative Commons license, and indicate if changes were made.

References

1. Tsujimura T (2012) OLED displays: fundamentals and applications. Wiley, New Jersey
2. Eritt M, May C, Leo K, Toerker M, Radehaus C (2010) Thin Solid Films 518:3042
3. Zhang W, Lu L, Peng J, Song A (2016) Energy Build 128:511
4. Meiss J, Uhrich CL, Fehse K, Pfuetzner S, Riede MK, Leo K (2008) Transparent electrode materials for solar cells. SPIE Proc 7002:1
5. Coclite AM, Howden RM, Borrelli DC, Petruczuk CD, Yang R, Yagüe JL, Ugur A, Chen N, Lee S, Jo WJ, Liu A, Wang X, Gleason KK (2013) Adv Mater 25:5392
6. Kang K, Watanabe S, Broch K, Sepe A, Brown A, Nasrallah I, Nikolka M, Fei Z, Heeney M, Matsumoto D, Marumoto K, Tanaka H, Kuroda S, Siringhaus H (2016) Nat Mater 15:896
7. Stadler P, Farka D, Coskun H, Głowacki ED, Yumusak C, Uiberlacker LM, Hild S, Leonat LN, Scharber MC, Klapeček P, Menon R, Sariciftci NS (2016) J Mater Chem C 4:6982
8. Du X, Wang Z (2003) Electrochim Acta 48:1713
9. Perepichka IF, Levillain E, Roncali J (2004) J Mater Chem 14:1679
10. Greczynski G, Kugler T, Keil M, Osikowicz W, Fahlman M, Salaneck WR (2001) J Electron Spectrosc Relat Phenom 121:1
11. Farah A, Rutledge S, Schaarschmidt A, Lai R, Freedman JP, Helmy AS (2012) J Appl Phys 112:113709
12. Casado N, Hernández G, Veloso A, Devaraj S, Mecerreyes D, Armand M (2016) ACS Macro Lett 5:59
13. Jönsson SKM, Birgerson J, Crispin X, Greczynski G, Osikowicz W, Denier van der Gon AW, Salaneck WR, Fahlman M (2003) Synth Met 139:1
14. Bhandodkar AJ, Nuñez-Flores R, Jia W, Wang J (2015) Adv Mater 27:3060
15. Okuzaki H, Suzuki H, Ito T (2009) Synth Met 159:2233
16. Lang U, Rust P, Dual J (2008) Microelectron Eng 85:1050
17. Kaltenbrunner M, Adam G, Głowacki ED, Drack M, Schwödi-auser R, Leonat L, Apaydin DH, Groiss H, Scharber MC, White MS, Sariciftci NS, Bauer S (2015) Nat Mater 14:1032
18. Stavridou E, Gabriellsson R, Gomez E, Crispin X, Nilsson O, Simon DT, Berggren M (2015) Sci Adv 1:e1501136

19. Admassie S, Zhang F, Manoj AG, Svensson M, Andersson MR, Inganäs O (2006) *Sol Energy Mater Sol Cells* 90:133
20. Chen S, Lu BY, Xu JK, Qin LQ, Wang ZP, Duan XM (2013) *J Appl Polym Sci* 129:1717
21. Stöcker T, Köhler A, Moos R (2012) *J Polym Sci Part B Polym Phys* 50:976
22. Zabrodskii AG, Zinov'eva KN (1984) *Zh Eksp Teor Fiz* 86:727
23. Geretschläger M (1983) *Nucl Instrum Methods Phys Res* 204:479
24. Mayer M (1999) *AIP Conf Proc* 475:541

4.3 Manuscript 3

Anderson-Localization and the Mott–Ioffe–Regel Limit in Glassy-Metallic PEDOT

Dominik Farka, Halime Coskun, Jacek Gasiorowski, Christoph Cobet, Kurt Hingerl, Lisa Maria Uiberlacker, Sabine Hild, Theresia Greunz, David Stifter, Niyazi Serdar Sariciftci, Reghu Menon, Wolfgang Schoefberger, Cezarina Cela Mardare, Achim Walter Hassel, Clemens Schwarzinger, Markus Clark Scharber, and Philipp Stadler*

Conductive polymers represent a rare case in which free-carrier absorption is shifted to the far-infrared—an attractive advantage in light of the requirement of highly transparent conductors across the visible and near-infrared. Unfortunately, prior approaches to doping these polymers—imperative for high conductance—have consistently led to strong localization arising from fluctuating band alignment among polymer chains. Here, this study overcomes this problem of doping-induced Anderson localization for the first time in polymers by developing a new conductive polymer synthesis strategy. This study achieves polymerization and doping simultaneously, thereby using an alternative nonmetal oxidant and thereby avoiding the introduction of excess energy that normally arises from exergonic polymerization. The resulting conductive polymer is the first to provide electron coherence in a metallic polymer thin film. The conductivity reaches a remarkable 3300 S cm^{-1} at 1.8 K and the mean electron scattering length a record 330 Å. This enhancement drives the glassy metal transition in the vicinity of the Mott–Ioffe–Regel (MIR) limit. The new metallic polymer achieves $10^{-2} \Omega^{-1}$ figure of merit, making it a contender for transparent conductive contacts previously only accessible using inorganics. The new material offers a uniquely broad transparency window spanning the UV to the mid-infrared.

There exists a tremendous interest in metallic polymers as they combine facile processing, high conductivity and transparency. However, to date no straightforward method has been found to engineer a system that unites high doping and high order.^[1–6] The apparent conflict lies in the nature of doping of a conducting polymer, which occurs through a distinct mechanism compared to inorganic semiconductors. Severe lattice distortions arise in the doping of conducting polymers as a result of the penetration of ions into the system. Consequently, the solid-state order becomes disrupted—it transforms from a former homogeneous organic van der-Waals crystal into a disordered salt. To form a substantial degree of order, growth methods have to consider the effect of ion penetration.^[7–16]

Small molecular systems have the advantage that they can be dissolved in polar solvents. Thus they can be grown in the doped form as a salt dissolved from

D. Farka, H. Coskun, Prof. N. S. Sariciftci, Dr. M. C. Scharber, Dr. P. Stadler
 Linz Institute of Organic Solarcells (LIOS), Institute of Physical
 Chemistry

Johannes Kepler University Linz
 Altenberger Strasse 69, 4040 Linz, Austria
 E-mail: philipp.stadler@jku.at

Dr. J. Gasiorowski, Dr. C. Cobet, Prof. K. Hingerl, T. Greunz, Dr. D. Stifter
 Center for Surface and Nanoanalytics

Johannes Kepler University Linz
 Altenberger Strasse 69, 4040 Linz, Austria

Dr. J. Gasiorowski
 Department of Physics
 Technical University of Chemnitz
 Reichenheiner Strasse 70, 09126 Chemnitz, Germany


L. M. Uiberlacker, Prof. S. Hild
 Institute of Polymer Science
 Johannes Kepler University Linz
 Altenberger Strasse 69, 4040 Linz, Austria

Prof. R. Menon
 Department of Physics
 Indian Institute of Science
 Bangalore 560012, India

Dr. W. Schoefberger
 Institute of Organic Chemistry
 Johannes Kepler University Linz
 Altenberger Strasse 69, 4040 Linz, Austria

Dr. C. C. Mardare, Prof. A. W. Hassel
 Christian Doppler Laboratory for Combinatorial Oxide Chemistry
 (COMBOX) at Institute for Chemical Technology of Inorganic Materials
 Johannes Kepler University Linz
 Altenberger Strasse 69, 4040 Linz, Austria

Dr. C. Schwarzinger
 Institute for Chemical Technology of Organic Materials
 Johannes Kepler University Linz
 Altenberger Strasse 69, 4040 Linz, Austria

 The ORCID identification number(s) for the author(s) of this article can be found under <http://dx.doi.org/10.1002/aelm.201700050>.

DOI: 10.1002/aelm.201700050

solution. Such Fabre–Bechgaard salts have created an entire field of synthetic metals and superconductors.^[17–20] In polymers, however, the macromolecular nature hampers the formation of a thermodynamic solution.^[19] Consequently, conductive thin films are generated by two-step processes (first casting, then doping).^[17–37] Such methods effectively disturb the order and thus result in an Anderson insulator rather than a metallic conductor.

Oxidative chemical vapor deposition (o-CVD) is a quasi-1-step technique, where doping and polymerization are combined.^[38] State-of-the-art processes rely on vigorous reactants such as metal chlorides (FeCl₃, SbCl₅). Although the production of high-performance polymers has been demonstrated, overoxidation leads to severe structural distortions.^[39,40] Here we develop a new process that achieves superior metallic properties but overcomes the prior reliance on lattice-disrupting metal dopants. The o-CVD is performed at ambient pressure and uses nitrogen as carrier gas, which is saturated with the monomer ethylene-(3,4-dioxythiophene) (EDOT). In the reactor zone the vapor is contacted with gaseous sulfuric acid to condense as oxidatively polymerized and p-doped polyethylene-(3,4-dioxythiophene):sulfate (PEDOT:sulfate) on the substrate. The bluish, air-stable, and semitransparent thin film precipitates as homogeneous layer on the substrate. We are in particular interested in the magnetoelectric and the optoelectronic properties and the structural composition, which we present in detail in this work. We find striking results such as a temperature-coefficient typical for glassy metals close to the Mott–Ioffe–Regel (MIR) limit.^[41–43] We observe the Hall effect and calculate the mean inelastic scattering path of charge carriers. Furthermore, we present the optical dielectric function and resolve the chemical composition. The hallmark of the PEDOT:sulfate prepared by o-CVD with sulfuric acid is the excellent electrical performance manifested by metallic fingerprints such as the positive magnetoconductivity. All these findings indicate that the new and facile synthesis route for PEDOT leads to an outstanding degree of order and purity inside the polymer with the consequence of a metallic nature beyond Anderson localization.

We choose two common chemicals EDOT and sulfuric acid in order to synthesize PEDOT:sulfate by o-CVD. The advantage of using EDOT is in particular its low oxidation potential, which can be easily overcome by sulfuric acid as oxidizing agent. By balancing the concentration and reaction, and deposition temperature we pursue an immediate, selective polymerization and avoid harsh conditions, which lead to overoxidation. With this we generate high-quality, semitransparent thin films of PEDOT:sulfate using a simple o-CVD-setup, where the quasi-1-step polymerization and doping reaction (Figure 1) takes place. The optimum temperature found to react EDOT readily with the vaporized sulfuric acid is 200 °C. We achieve the reaction conditions by preheating the saturated nitrogen carrier gas. The subsequent evaporation of sulfuric acid and immediate polymerization- and oxidation-reaction takes place at ambient pressure.

For comparison, we generate several reference PEDOT-systems, which originate from the classic solution-based processing routes based on the commercially available PEDOT:polystyrene sulfonate (PEDOT:PSS) dispersions. One straightforward route processes PEDOT:PSS with additives (i.e., DMSO, further denoted as PEDOT:PSS*) to reach a conductivity

value of 1000 S cm⁻¹. To obtain a similar reference system such as PEDOT:sulfate, we substitute the PSS polyanion. Therefore we treat as-deposited PEDOT:PSS with aqueous triflic acid (equimolar aqueous solution) further denoted as PEDOT:triflate.^[6] This system serves as a solution-derived reference PEDOT-system having a similar composition but different processing origin as o-CVD grown PEDOT:sulfate.^[3,44]

Similar to solution-based PEDOT:PSS, o-CVD yields homogeneous coverage on top of various substrates. Measurements of the surface morphology of films grown on glass (Figure 1b) show a uniform film with an average RMS-smoothness of 4.5 nm. PEDOT-fingerprint structural information is furthermore identified by ATR-FTIR, solid-state NMR and MALDI-MS, and high-resolution X-ray photoelectron spectroscopy (XPS). These studies (in detail discussed in the Supporting Information) include the reconstruction of the ratio between a monomer unit and sulfate at approximately (2.8):1, signature interaction in shifts in the ¹³C NMR, and the molar mass distribution at 10–12 EDOT units (median value) as well as characteristic interband absorptions (polarons) and infrared-activated vibrations (IRAVs).

X-ray diffraction pattern on 150 nm thin films confirm the crystallinity of PEDOT:sulfate by the (020) reflection (fingerprint for PEDOT-stacks) appearing pronounced at 25.5 2 θ (3.5 Å stacking distance) (Figure 2). Similar features in PEDOT:triflate and PEDOT:PSS* (without and with annealing) have not been observed.

The intense peak (020) in the diffractogram relates to the excellent electrical performance of PEDOT:sulfate (outperforming all solution-derived systems across the entire temperature range between 300 and 1.8 K) (Figure 1c). It exhibits a room temperature conductivity as great as 4050 S cm⁻¹ (PEDOT:triflate: 2100 S cm⁻¹, PEDOT:PSS* 1000 S cm⁻¹, and PEDOT:PSS 7 S cm⁻¹), which changes slightly across the studied temperature range. At 1.8 K in the proximity of $T \rightarrow 0$ the magnitude of the conductivity displays the crucial role of disorder: As-cast PEDOT:PSS follows an Arrhenius-type temperature-activated transport and has practically 0 conductivity (Figure 1d). Additive-assisted PEDOT:PSS* has a finite conductivity—but a factor 10 lower as compared to room temperature. PEDOT:triflate performs similarly having an overall better performance but similar drop by a factor of 3. We used similar thicknesses to remain in a 3D bulk regime for meaningful comparison of these different kinds of PEDOT thin films.

In addition we include the resistivity versus absolute temperature ρ_T (Figure 1e). Thereby, PEDOT:triflate and PEDOT:sulfate display significantly the transition from an Anderson insulator to a glassy metal. ρ_T in PEDOT:sulfate remains T-independent at low-T, which is characteristic for a glassy metal and similarly observed in alloys such as Al₃₃Ti₆₇. In contrast, ρ_T in PEDOT:triflate increases severely below 10 K. Furthermore, the magnitude of ρ_T in PEDOT:sulfate (247 $\mu\Omega$ cm⁻¹) is close to the Mooij correlation or the MIR limit, which define the border between glassy and crystalline metals. Besides overcoming Anderson localization in PEDOT:sulfate, we create a conductive polymer critically close to a crystalline metal. The origin of Mooij correlation is still a mystery today, and so is the fact that the temperature coefficient of the resistivity can be negative in the apparently metallic regime approaching the Anderson transition (denoted here as glassy metal).^[41] The material synthesized here is of a very

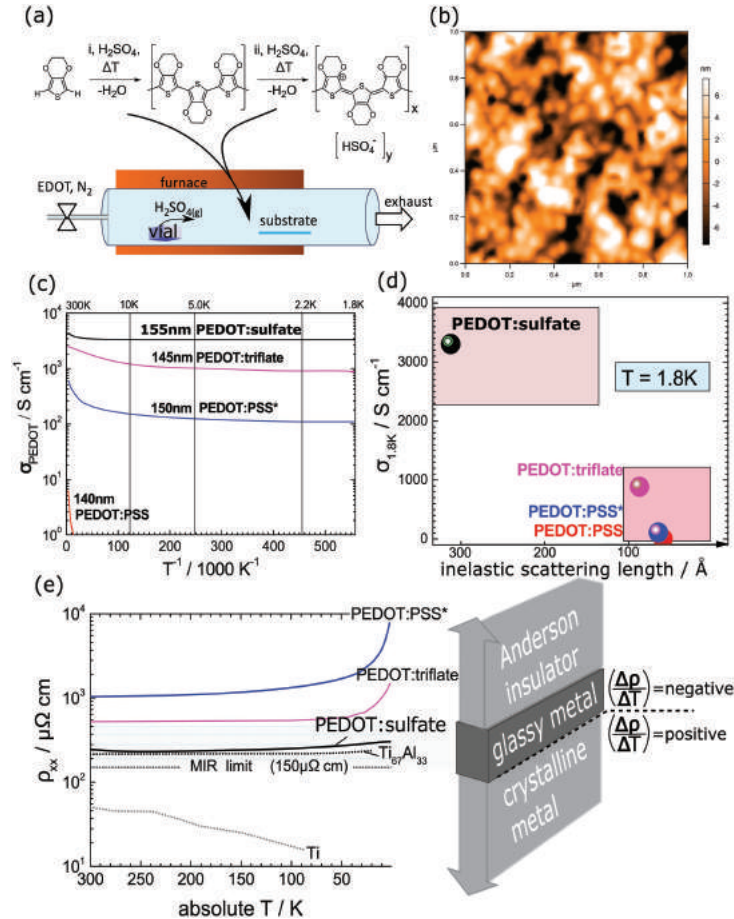


Figure 1. a) The o-CVD technique is depicted including the proposed reaction scheme of the synthesis. b) A typical surface topography of o-CVD grown PEDOT:sulfate thin film showing an RMS roughness of 4.5 nm. c) ρ_T -plot highlighting the flat T -profile of PEDOT:sulfate in particular at low temperatures. Quantitatively, the solution-based reference systems (PEDOT:PSS, PEDOT:PSS*, and PEDOT:triflate) exhibit lower performances. d) Schematic displaying the role of disorder on $\sigma_{T=1.8K}$. e) MIR describes a critical resistivity ($150 \mu\Omega \text{ cm}$), at which the sign of the T -coefficient of resistivity $\frac{d\rho}{dT}$ in a metal changes (glassy to crystalline). PEDOT:sulfate is situated close to the Mott–Ioffe–Regel (MIR) limit behaving similar to glassy metal alloys such as $\text{Al}_{33}\text{Ti}_{67}$.

different nature from those studied by Mooij and Tsuei, yet it seems to present the same universal physics driven by the Anderson phenomenon.^[43] As such the enhancements clearly point to local order established by sulfuric-acid based o-CVD. We reach a magnitude as great as 3304 S cm^{-1} at 1.8 K, which is a retention of 81% as compared to 300 K and a 30-fold increase in conductivity over widely used PEDOT:PSS*. In Anderson localization the conductivity changes are evaluated using the logarithmic temperature coefficient $W = -\frac{d \ln \rho}{d \ln T}$ (Figure 3). The analysis provides the discrimination of the transport mechanisms, in particular distinguishing between the critical regime of the

metal-insulator transition (W_T is constant) and the glassy metallic regime beyond Anderson localization and before MIR-limit ($W_T \ll 1$ and positive sign; W_T decreases with decreasing T). Beyond the MIR-limit W_T has a negative sign as for a crystalline metal.^[45–48] The glassy metallic regime indicated by the slope of W_T (Figure 3a) is found for PEDOT:sulfate and, less-pronounced, for solution-derived PEDOT:triflate. Comparable electrical performances in conductive polymers have previously been observed in stretch-oriented, doped polyacetylene and poly-p-phenylenevinylene.^[5,8,10–12,15,16,45–49] In addition we check the impact of a strong magnetic field ($B = 9 \text{ T}$). This allows us to switch between metallic and critical regime (magnetolocalization). In both cases,

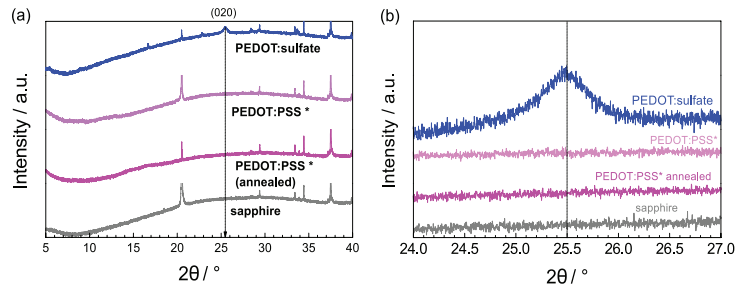


Figure 2. a) XRD on single crystalline sapphire shows the diffractograms of PEDOT:sulfate and of reference PEDOT:PSS (as-cast and annealed to 100 °C). We confirm the fingerprint peak at 25.6 2 θ as observed from thin films (150 nm) on glass. The reference solution-cast PEDOT thin films are amorphous. b) (020) feature zoom of diffractogram showing details in relation to substrate (sapphire) and PEDOT:PSS* and annealed PEDOT:PSS* shows the feature at 25.5 2 θ (corresponds to a stacking distance of 3.5 Å).

the magneto-effect is consistently pronounced, as the emergence of B disrupts the metallic state seen in the constant and increased W_T -profile at 9 T. Magnetoconductivity (MC) sensitizes in particular the electron scattering mechanisms. Their mean free path reflects directly the degree of local order established in PEDOT. We apply a classic four-probe specimen (Figure 3c) to characterize the ambiguous impact of the magnetic field.^[1,5,8,10–12,15,16,49] While high fields consistently reduce the conductivity by magnetolocalization, lower magnetic fields improve the

conductivity. Such interplay is a hallmark of metallic polymers exhibiting a constructive and a destructive MC-part (Figure 3d).

The destructive-negative MC is described according to

$$\Delta\sigma_T \propto \sqrt{B} \quad (B \geq 4 \text{ T}) \quad (1)$$

Its power/magnitude is reflected in the slope of $\Delta\sigma_T$ versus $B^{0.5}$ (Figure S9, Supporting Information) and correlates with temperature T and the proximity to the metallic state (brief

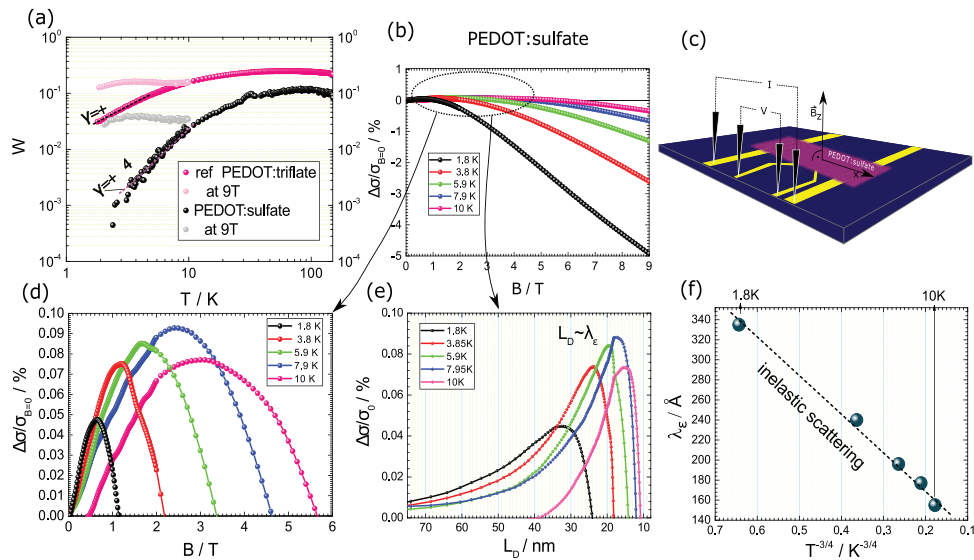


Figure 3. a) W_T -values $-\frac{d \ln \sigma}{d \ln T}$ reflect the T -dependency according to Anderson-localization (weak localization). Beyond the metal-insulator transition, W_T has a positive slope (≈ 2.4) and quantitatively approximates 0. At $B = 9$ T and low- T the W_T -values split due to magnetolocalization. PEDOT:sulfate has superior metallic fingerprints (quantity of W_T) as compared to the reference system (solution-based PEDOT:triflate). In (b), the magnetoconductivity (MC) of PEDOT:sulfate at five temperatures is depicted. The interference between positive (low-field) and negative (high-field) MC is shown. c) Schematic of the four-probe specimen used to characterize MCs. In (d), a zoom into the constructive MC owing to the resonance between electrons and B . e) The corresponding plot of the Landau orbit size L_D (magnetic penetration depth) and MC is used for determining the mean free path of electrons ($L_D \sim \lambda_e$) at maximum resonance. f) The linear dependence of λ_e versus $T^{-3/4}$ is characteristic for weak-localization (inelastic scattering dominates the electrical transport).

description in Supporting Information). At 10 K in the more critical regime the destructive effect is subsequently weaker (<0.5% at 9 T), while at 1.8 K (metallic regime) the conductivity decreases by 5% at 9 T.

The constructive-positive MC appears at lower magnetic fields ($B < 4$ T) and allows us to evaluate the mean free path (Figure 3e). It displays directly the electron-relaxation becoming resonant with the magnetic field B .^[48,50–53] The magnetic stimulus thereby drives a rise of the conductivity (Figure 3d). The magnetic field can be reformulated as magnetic penetration depth (the Landau orbit size L_D , Equation (2)) to read out the mean free path of scattered electrons λ_e at the peak maximum at resonance condition (Figure 3e). This is possible due to the extended scattering length found in anisotropic matter with inelastic processes dominating the transport. We denote that spin-orbit coupling effects play an insignificant role in the present system

$$L_D = \lambda_e \quad L_D = \sqrt{\frac{\hbar}{e \cdot B}} \quad (2)$$

In PEDOT:sulfate such resonance is seen between 1 and 6 T translating to 80 and 400 Å, respectively. Within the temperature window of 10 to 1.8 K the electrical transport is consequently coherent (Figure 3f) indicated by the fit of λ_e versus $T^{-3/4}$ characteristic for electrical transport dominated by inelastic relaxation.^[1,50]

In addition, we characterize the Hall effect using the van-der-Pauw geometry (Figure 4b). We observe the Hall potential U_{Hall} linearly arising within the coherent regime below 10 K as function of B (except for the part with B exceeding 8 T in the low temperature regime at 1.8 and 2.85 K, where destructive-negative MC disrupts the metallic phase) (Figure 4a). For evaluating the mobility from U_{Hall} (and from conductivity) we include a statistical-mechanical approach of degenerate metals. This is necessary in PEDOT:sulfate (and generally noncrystalline solids), since disorder effects can disrupt the wave functions of holes so that regular drift equations are not valid. Proper Hall models have to include the random energy distribution emerging from topological disorder.^[47,54,55] Based on drift evaluations

$$\sigma = en\mu_{Drift} \quad R_H = (en)^{-1} \quad U_{Hall} = R_H \frac{I_{xx} B}{d} \quad (3)$$

with e the electrical charge, n the carrier concentration, μ_{Drift} the drift mobility, R_H the Hall constant, I_{xx} (current), and d (layer thickness), we refer to Friedman, who proposes a random phase model (RPM), in particular for calculating the Hall conductivity in highly doped semiconductors such as PEDOT:sulfate.^[56] RPM is applicable, when λ_e exceeds molecular dimensions as demonstrated for the low- T regime. There we observe U_{Hall} arising at significant magnitude (i.e., 0.1–1 mV at $B = 5$ T) scaling (linearly) with the mean inelastic scattering lengths λ_e (or temperature) (Figure 4d). Further rising of T (e.g., above 10 K)

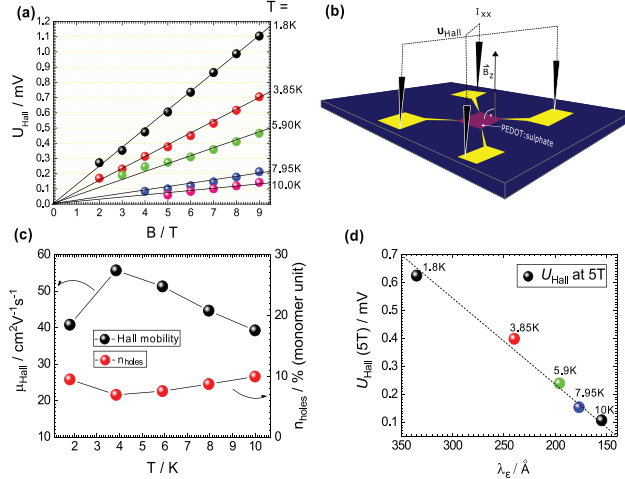


Figure 4. a) The Hall effect here shown as Hall voltage U_{Hall} arising linearly with B in PEDOT:sulfate at low- T in the metallic regime. b) Schematic of a van-der-Pauw specimen used to extract the Hall potential in eight possible geometries. c) In combination with the conductivity (i.e., 3305 S cm^{-1} at 1.8 K) the charge carrier mobility (and doping degree per monomer unit) of holes are calculated for the metallic regime below 10 K using Friedman's random phase model.^[56] d) The magnitude of the Hall potential U_{Hall} (here for B at 5 T) scales linearly with the magnitude of hole coherence (here quantified as λ_e). Lower mean free path leads to less pronounced metallic behavior (and lower Hall potential).

reduces U_{Hall} below $10 \mu\text{V}$ (the noise limit of the cryo-magneto-electric setup). We explain such behavior by localization effects becoming dominant at higher T when conductivity is governed by hopping meaning that $k_B T$ becomes greater than the band width W_B (i.e., for thermal activation). With decreasing T below 10 K hopping is effectively suppressed and conduction occurs in the band at E_F . To visualize these different transport regimes we use a semilogarithmic $\ln \sigma$ versus T^{-1} plot that reveals a T -independent (metallic) part below 10 K and the T -linear (hopping) part above 10 K (Figure S8, Supporting Information). The latter allows us to estimate the band width W_B (i.e., the activation energy) of charge carriers in PEDOT:sulfate

$$\ln \frac{\sigma_T}{\sigma_{300K}} = -\frac{W_B}{k_B T} \quad W_B = (E_C - E_F) = 1 \text{ meV} \quad (4)$$

These insights are particularly useful in RPM in order to evaluate Hall potentials correctly. Accordingly, drift and Hall mobilities relate by the fraction of $k_B T$ over W_B as followed

$$\mu_{Hall} = \frac{4k_B T}{W_B} \mu_{Drift} = \frac{4T}{11.3} \mu_{Drift} \quad (5)$$

We apply Equation (5) in combination with Equation (3) and now obtain constant carrier concentrations n , Hall mobilities μ_{Hall} (and conductivities) in the coherent (metallic) regime ($40 \text{ cm}^2 \text{ V}^{-1} \text{ s}^{-1}$ for μ_{Hall} and 10% free carriers per monomer PEDOT:sulfate) (Figure 4c). Note, we use the stoichiometric factor of 2.8 from XPS analysis (Figure S3, Supporting

Table 1. Electrical parameters of PEDOT:sulfate at low-T.

σ [S cm ⁻¹]	σ_r ref. σ_{300K} ^{a)}	$(eR_H)^{-1}$ [cm ⁻²]	$n_{free}^{b)}$ [%PEDOT:sulfate]	μ_{Hall} [cm ² V ⁻¹ s ⁻¹]	$D\mu V^{c)}$ [cm ² s ⁻¹]	λ_D [Å]
1.8 K						
3305	0.81	$5.1 \cdot 10^{20}$	9.5	40.8	0.0063	335
10 K						
3336	0.82	$5.3 \cdot 10^{20}$	10	39.2	0.0338	155

^{a)} σ_{300K} is 4050 S cm⁻¹; ^{b)} n_{free} is (hole) carrier per PEDOT:sulfate monomer unit in %; ^{c)} $D\mu_{Hv}$ is the diffusion constant (Einstein diffusion).

Information). A detailed discussion of RPM and its application to PEDOT:sulfate is presented in the Supporting Information. In summary, we find that Hall effect in combination with MC yields congruent results pointing at the metallic transport mechanisms in the low-T regime in PEDOT:sulfate. For overview we sum up all the relevant parameters in **Table 1**.

Finally, we explore the optical properties of PEDOT:sulfate thin films to examine the transparency of PEDOT:sulfate (**Figure 5**). Our main interest is focused on the optical constants of PEDOT:sulfate between mid-IR (0.055 eV) and UV-part (6.5 eV). Therefore we use angle-resolved spectroscopic ellipsometry to generate the dielectric function $\epsilon_1(\omega)$ and $\epsilon_2(\omega)$ (**Figure 5a**). Typically for conductive polymers is the deviation

from the Drude model seen in the finger-print mid-IR region dominated by IRAVs and electronic ingap polaron transitions. The main band-gap transition of PEDOT appears at 2.4 eV. We denote that the model used is Kramers–Kronig relation consistent. Differently to oxide-based transparent conductors the absence of a discrete plasma frequency in the investigated spectral region—we report on a consistently positive $\epsilon_1(\omega)$ upon the IRAVs—results in transparency throughout the entire spectrum. Consequently, the transmission of

30 nm PEDOT:sulfate thin film is reasonably transparent from UV to mid-infrared. Though PEDOT:sulfate has residual absorption especially in its intrinsic band gap region (**Figure 5b**), this effect is compensated with its transparency in the low-energy IR. We visualize the electro-optical performance in the complementary figure of merit according to Haacke (**Figure 5c**).^[57]

The quantity $\Phi = \sigma d^2 TR^{10}$ from PEDOT:sulfate (TR is transmission) compared to convenient PEDOT:PSS* and to indium tin oxide (ITO), **Table 2** highlights the unique properties of transparency and conductivity over a large spectral regime. In summary, our complementary magnetoelectric and optoelectronic study on PEDOT:sulfate provides strong arguments to consider this material as serious alternative for a transparent

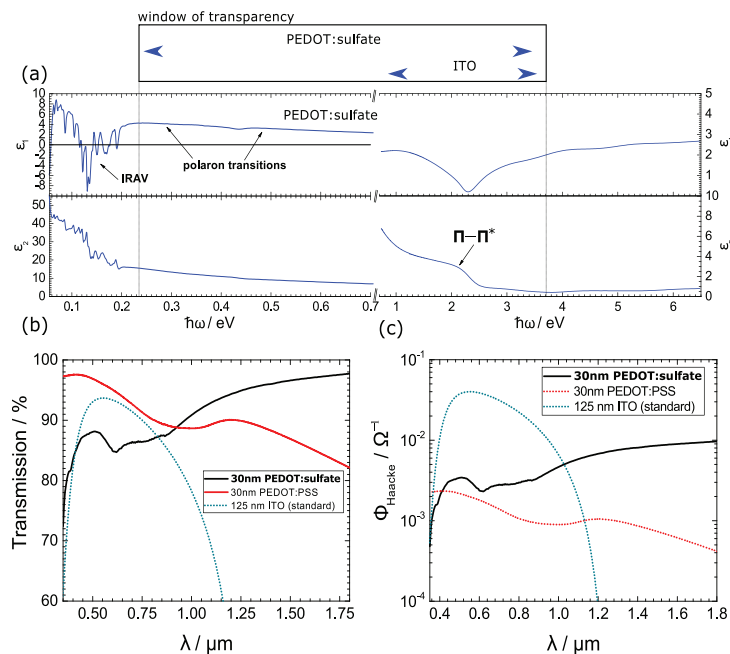


Figure 5. a) The dielectric function (experiment and model) of PEDOT:sulfate between UV- and mid-IR regime reveals the fingerprint electronic (polarons) and vibronic (IRAV) transitions. b) The latter non-Drude behavior is particularly displayed in the transmission (30 nm thin film on glass) including reference values for PEDOT:PSS. Different to ITO (plasma frequency at 0.8 eV), the window of transparency in PEDOT:sulfate is extended to the mid-infrared. c) This advantage is highlighted in the figure of merit (according to Haacke, 90% transparency) pointing at the improvements of PEDOT:sulfate as compared to PEDOT:PSS* and as compared to ITO when considering the expanded infrared-window.

Table 2. Optoelectrical parameters of PEDOT:sulfate, PEDOT:PSS*, PEDOT (FeCl₃), and indium tin oxide (ITO).

Electrode	Processing/ treatment	σ_{DC} [S cm ⁻¹]	$\Phi_{FOM,550nm}$ [Ω^{-1}]	$\Phi_{FOM,1800nm}$ [Ω^{-1}]
ITO	Sputtering	5600	0.03	N/A
PEDOT:sulfate	o-CVD (H ₂ SO ₄)	4050	0.003	0.01
PEDOT:PSS*	Spin coat, DMSO	1000	0.0025	0.0004
PEDOT (FeCl ₃) ^[97]	o-CVD (FeCl ₃)	3700	N/A	N/A

metallic conductor, which offers in addition the advantage of a straightforward, facile processing all potentially interesting for industrial large-area applications.

Prior reports of conductive polymers have referred to the potential for metallic transport; however, practical objections such as disadvantageous processing and doping-related localization have led to disorder-governed systems finally limiting conductivity. We sought to overcome this limits by a quasi-1-step deposition technique, which we adapted from inorganic semiconductors. Our o-CVD grown PEDOT:sulfate opens various new prospects. Based on enhancement of the local order it assesses the metallic regime offering high conductivity as shown by low temperatures studies on the Hall effect and magneto-electronic interactions. PEDOT-based conducting polymers are commonly used materials in transistors, electrodes, and related optoelectronic devices. In view of the growing interest, our work has substantial impact, as we push the system closer to the MIR limit with keeping its optical transparency. These insights open prospects toward highly conducting polymers based on facile, quasi-1-step processing technique. The new materials offer the possibility of low-cost transparent conductive materials of particular interest to the display- and solar industries.

Experimental Section

For the low-*T* measurements, sapphire with Cr/Au contacts was used. For optical and spectroscopic measurements, glass served as substrate. They were cleaned using ultrasonic bath 15 min each in acetone, isopropyl alcohol, Hellmanex-detergent (Hellma, 70 °C), and deionized water. The metal-contacts were deposited using physical vapor deposition (PVD) through a van-der-Pauw and a four-in-line contact-mask, respectively (Figure 3c, Figure 4b). In order to apply o-CVD for PEDOT:sulfate, following protocol was used. In a tube furnace (Carbolite company, glass tube length: 45 cm, tube thickness inside: 2.4 cm), the substrates were loaded onto a glass holder (Figure 1c), and inserted at the end of the tube (at 40–43 cm). 1 mL of sulfuric acid (97%) is mixed with 1 g of sodium sulfate and loaded into the middle of the tube (20–25 cm). The exhaust gas was flushed through a potassium hydroxide solution to capture residual acid-fumes. Before starting the reaction, the tube was flushed with pure N₂ gas at 200 °C at 0.083 m³ h⁻¹. Then the carrier gas (N₂) was bubbled through a reservoir of EDOT to start the reaction. This time was designated as reaction start. Depending on flow rate and reaction time, films of different thickness were achieved. An example for possible reaction times and corresponding thickness can be found in Table 2 (see the Supporting Information). To stop the reaction, the tube was retrieved from the furnace but kept under N₂-flow in order to cool the samples before exposure to air. After cooling to room temperature, the samples were removed from the tube and washed with isopropyl alcohol.

The samples were stored under inert conditions to avoid humidity. Before electrical characterization, the samples were sealed by drop casting a poly(methyl methacrylate) (PMMA) film on top of the active area. For testing magnetoconductivity, van-der-Pauw geometry and four-probe structured patterned substrates were used with consistently 140–155 nm thin films. For comparison, films of PEDOT:triflate, PEDOT:PSS (and PEDOT:PSS*, respectively) were processed using following recipe: PH1000 (Clevios) dispersion (as-is, PEDOT:PSS and mixed with 5% DMSO, PEDOT:PSS*) were spin-coated to thin films using the following recipe: 10 rps, 2 s ramp, 30 s spinning; 100 rps, 2 s ramp, 30 s spinning. For the PEDOT:triflate, PEDOT:PSS was cast to a thin film and in a second step exposed to excess triflic acid (1:1 molar in water) for 1 min and washed 3 times with 18 M Ω cm water. The resulting solution-based thin films had a comparative thickness of 140 nm (similar to the oCVD-processed thin films). These films were characterized by variable-angle spectroscopic ellipsometry (VASE, Wollam M-2000 with rotating compensator ellipsometer) and modeled using *w*VASE program. For fitting Gaussian oscillators have been used, the IR part was fitted by a Tauc-Lorentz dielectric function. All of these model functions were Kramer–Kronig consistent. Atomic force microscopy (AFM) was performed using an Asylum Research MFP-3D Stand Alone AFM. For XPS (Theta Probe from Thermo Fisher Scientific with monochromatic AlK α X-ray source), glass substrates were covered with Cr/Au (Cr 8 nm, Au 100 nm) prior PEDOT-deposition (spin coating at 100 rps, 100 s). XPS surveys as well as high-resolution spectra of the C1s, O1s, S2p peaks were acquired from films with a nominal thickness of 20 nm. The S2p peaks were used to calculate the stoichiometry between PEDOT and PSS or sulfate, respectively. The S2p response from the thiophene ring and the PSS or sulfate was distinctively different ($\Delta = 4$ eV), while the S2p signals from sulfonate and sulfate were practically identical. Solid-state nuclear magnetic resonance (NMR) measurements were taken on a Bruker AvanceIII 500 MHz spectrometer equipped with a cross-polarization magic-angle spinning (MAS) probe. ¹³C MAS spectra were recorded at 125 MHz at a spinning rate of 17 kHz at a temperature of 298 K. For matrix-assisted laser desorption/ionization–mass spectrometry (MALDI-MS) samples were prepared by intensive mixing with an 100-fold excess of dithranol (1,8,9-Anthracenetriol) in an agate mortar and transferring an aliquot with a spatula onto a ground steel target. The mass spectra were recorded on a Bruker Autoflex III Smartbeam in linear mode with a scan range from 1000 to 4000 *m/z*. For each measurement, 2500–3500 individual spectra were averaged and baseline corrected. All X-ray diffraction (XRD) measurements were performed using Philips Pro X'Pert system working in Bragg-Bretano geometry with CuK α radiation. ATR-FTIR (attenuated total reflection - Fourier transform infrared) spectral measurements were performed using a Bruker IFS66/S spectrophotometer. The exact spectral measurements were conducted on ATR-ZnSe crystals (parallelepiped 1 × 1 cm²) in the near- and mid-IR spectral regime. For the electrical measurements, the van-der-Pauw method was used to detect the Hall potential. For the magnetoconductivity, classic four-in-line probe contacts were used. The PMMA-covered PEDOTs were contacted using indium solder and loaded to the magnetotransport system (DynaCool PPMS, QuantumDesign). The electrical resistivity (thus conductivity) ρ_{xx} and ρ_{xy} were characterized as function of temperature and magnetic field between 300 and 1.8 K and 0 to 9 T, respectively.

Supporting Information

Supporting Information is available from the Wiley Online Library or from the author.

Acknowledgements

P.S., N.S.S., and D.F. are grateful to OEAD (WTZ, IN10/2015) and the Austrian Fund for Advancement of Science (FWF) within the Wittgenstein Prize scheme (Z222-N19 Solare Energiewandlung) for financial support. The authors thank Eitan Ehrenfreund and Eric D. Glowacki for fruitful discussions. C.C.M., A.W.H., T.G., and D.S. gratefully

acknowledge the financial support by the Austrian Federal Ministry of Science, Research and Economy and the National Foundation for Research, Technology and Development in the frame of the Christian Doppler Laboratories COMBOX and MS-MACH, respectively.

Conflict of Interest

The authors declare no conflict of interest.

Keywords

Anderson localization, conductive metallic polymers, infrared transparency, Mott–Ioffe–Regel limit, transparent conductive electrodes

Received: February 6, 2017

Revised: March 8, 2017

Published online: April 25, 2017

- [1] P. Stadler, D. Farka, H. Coskun, E. D. Głowacki, C. Yumusak, L. M. Uiberlacker, S. Hild, L. N. Leonat, M. C. Scharber, P. Klapetek, R. Menon, N. S. Sariciftci, *J. Mater. Chem. C* **2016**, *4*, 6982.
- [2] C. Cobet, J. Gasiorowski, R. Menon, K. Hingerl, S. Schlager, M. S. White, H. Neugebauer, N. S. Sariciftci, P. Stadler, *Sci. Rep.* **2016**, *6*, 35096.
- [3] N. Massonnet, A. Carella, A. de Geyer, J. Faure-Vincent, J.-P. Simonato, *Chem. Sci.* **2015**, *6*, 412.
- [4] K. Lee, S. Cho, S. H. Park, A. J. Heeger, C.-W. Lee, S.-H. Lee, *Nature* **2006**, *441*, 65.
- [5] M. Ahlskog, R. Menon, A. J. Heeger, T. Noguchi, T. Ohnishi, *Phys. Rev. B* **1997**, *55*, 6777.
- [6] M. N. Gueye, A. Carella, N. Massonnet, E. Yvenou, S. Brenet, J. Faure-Vincent, S. Pouget, F. Rieutord, H. Okuno, A. Benayad, R. Demadrille, J.-P. Simonato, *Chem. Mater.* **2016**, *28*, 3462.
- [7] H. C. F. Martens, J. A. Reedijk, H. B. Brom, D. M. de Leeuw, R. Menon, *Phys. Rev. B* **2001**, *63*, 73203.
- [8] R. Menon, K. Väkiparta, Y. Cao, D. Moses, *Phys. Rev. B* **1994**, *49*, 16162.
- [9] O. Bubnova, Z. U. Khan, H. Wang, S. Braun, D. R. Evans, M. Fabretto, P. Hojati-Talemi, D. Dagnelund, J.-B. Arlin, Y. H. Geerts, S. Desbief, D. W. Breiby, J. W. Andreasen, R. Lazzaroni, W. M. Chen, I. Zozoulenko, M. Fahlman, P. J. Murphy, M. Berggren, X. Crispin, *Nat. Mater.* **2013**, *13*, 190.
- [10] A. Aleshin, R. Kiebooms, R. Menon, A. J. Heeger, *Synth. Met.* **1997**, *90*, 61.
- [11] R. Menon, C. O. Yoon, D. Moses, Y. Cao, A. J. Heeger, *Synth. Met.* **1995**, *69*, 329.
- [12] R. Menon, C. O. Yoon, D. Moses, A. J. Heeger, Y. Cao, *Phys. Rev. B* **1993**, *48*, 17685.
- [13] A. J. Heeger, *J. Phys. Chem. B* **2001**, *105*, 8475.
- [14] A. J. Heeger, N. S. Sariciftci, E. B. Namdas, *Semiconducting and Metallic Polymers*, Oxford University Press, Oxford, UK **2011**, Vol. 21, pp. 391.
- [15] Y. Nogami, H. Kaneko, H. Ito, T. Ishiguro, T. Sasaki, N. Toyota, A. Takahashi, J. Tsukamoto, *Phys. Rev. B* **1991**, *43*, 11829.
- [16] H. H. S. Javadi, A. Chakraborty, C. Li, N. Theophilou, D. B. Swanson, A. G. MacDiarmid, A. J. Epstein, *Phys. Rev. B* **1991**, *43*, 2183.
- [17] D. Jérôme, *Chem. Rev.* **2004**, *104*, 5565.
- [18] B. J. Powell, R. H. McKenzie, *J. Phys.: Condens. Matter* **2006**, *18*, R827.
- [19] R. S. Manna, M. de Souza, A. Brühl, J. A. Schlueter, M. Lang, *Phys. Rev. Lett.* **2010**, *104*, 16403.
- [20] P. Lunkenheimer, J. Müller, S. Krohns, F. Schrettle, A. Loidl, B. Hartmann, R. Rommel, M. de Souza, C. Hotta, J. A. Schlueter, M. Lang, *Nat. Mater.* **2012**, *11*, 755.
- [21] J. E. Frommer, *Acc. Chem. Res.* **1986**, *19*, 2.
- [22] B. J. Worfolk, S. C. Andrews, S. Park, J. Reinspach, N. Liu, M. F. Toney, S. C. B. Mannsfeld, Z. Bao, *Proc. Natl. Acad. Sci. USA* **2015**, *112*, 14138.
- [23] B. Chapman, R. G. Buckley, N. T. Kemp, A. B. Kaiser, D. Beaglehole, H. J. Trodahl, *Phys. Rev. B* **1999**, *60*, 13479.
- [24] T.-R. Chou, S.-H. Chen, Y.-T. Chiang, Y.-T. Lin, C.-Y. Chao, *J. Mater. Chem. C* **2015**, *3*, 3760.
- [25] Y. Xia, K. Sun, J. Ouyang, *Adv. Mater.* **2012**, *24*, 2436.
- [26] C. M. Palumbiny, F. Liu, T. P. Russell, A. Hexemer, C. Wang, P. Müller-Buschbaum, *Adv. Mater.* **2015**, *27*, 3391.
- [27] Q. Wei, M. Mukaida, Y. Naitoh, T. Ishida, *Adv. Mater.* **2013**, *25*, 2831.
- [28] J. Y. Kim, J. H. Jung, D. E. Lee, J. Joo, *Synth. Met.* **2002**, *126*, 311.
- [29] J.-Y. Kim, M.-H. Kwon, Y.-K. Min, S. Kwon, D.-W. Ihm, *Adv. Mater.* **2007**, *19*, 3501.
- [30] J. Huang, P. F. Miller, J. C. de Mello, A. J. de Mello, D. D. C. Bradley, *Synth. Met.* **2003**, *139*, 569.
- [31] C. S. S. Sangeeth, M. Jaiswal, R. Menon, *J. Appl. Phys.* **2009**, *105*, 63713.
- [32] S. K. Jönsson, J. Birgerson, X. Crispin, G. Greczynski, W. Osikowicz, A. D. van der Gon, W. Salaneck, M. Fahlman, *Synth. Met.* **2003**, *139*, 1.
- [33] X. Crispin, F. L. E. Jakobsson, A. Crispin, P. C. M. Grim, P. Andersson, A. Volodin, C. Van Haesendonck, M. Van Der Auweraer, W. R. Salaneck, M. Berggren, *Chem. Mater.* **2006**, *18*, 4354.
- [34] B. Winther-Jensen, J. Chen, K. West, G. Wallace, *Macromolecules* **2004**, *37*, 5930.
- [35] A. M. Coclite, R. M. Howden, D. C. Borrelli, C. D. Petruczuk, R. Yang, J. L. Yagüe, A. Ugur, N. Chen, S. Lee, W. J. Jo, A. Liu, X. Wang, K. K. Gleason, *Adv. Mater.* **2013**, *25*, 5392.
- [36] P. Kovacic, G. del Hierro, W. Livernois, K. K. Gleason, *Mater. Horiz.* **2015**, *2*, 221.
- [37] A. Ugur, F. Katmis, M. Li, L. Wu, Y. Zhu, K. K. Varanasi, K. K. Gleason, *Adv. Mater.* **2015**, *27*, 4604.
- [38] H. Meng, D. F. Perepichka, F. Wudl, *Angew. Chem.* **2003**, *115*, 682.
- [39] S. Lee, K. K. Gleason, *Adv. Funct. Mater.* **2015**, *25*, 85.
- [40] K. Kang, S. Watanabe, K. Broch, A. Sepe, A. Brown, I. Nasrallah, M. Nikolka, Z. Fei, M. Heeney, D. Matsumoto, K. Marumoto, H. Tanaka, S. Kuroda, H. Sirringhaus, *Nat. Mater.* **2016**, *15*, 896.
- [41] J. H. Mooij, *Phys. Status Solidi* **1973**, *17*, 521.
- [42] P. A. Lee, T. V. Ramakrishnan, *Rev. Mod. Phys.* **1985**, *57*, 287.
- [43] C. C. Tsuei, *Phys. Rev. Lett.* **1986**, *57*, 1943.
- [44] T. J. Wood, P. S. Brown, J. P. S. Badyal, *Chem. Commun.* **2013**, *49*, 7741.
- [45] E. B. Aleksandrov, I. V. Sokolov, A. Gatti, M. I. Kolobov, L. A. Lugiatto, T. A. Vartanyan, *Usp. Fiz. Nauk* **2001**, *171*, 1263.
- [46] P. W. Anderson, *Phys. Rev.* **1958**, *109*, 1492.
- [47] N. F. Mott, *Philos. Mag.* **1972**, *26*, 1015.
- [48] A. B. Kaiser, *Rep. Prog. Phys.* **2001**, *64*, 1.
- [49] R. Menon, *Synth. Met.* **1996**, *80*, 223.
- [50] G. Bergmann, *Phys. Rep.* **1984**, *107*, 1.
- [51] G. Bergmann, *Phys. Rev. B* **1983**, *28*, 2914.
- [52] T. F. Rosenbaum, R. F. Milligan, G. A. Thomas, P. A. Lee, T. V. Ramakrishnan, R. N. Bhatt, K. DeConde, H. Hess, T. Perry, *Phys. Rev. Lett.* **1981**, *47*, 1758.
- [53] A. Kawabata, *Solid State Commun.* **1980**, *34*, 431.
- [54] R. Kubo, *J. Phys. Soc. Jpn.* **1957**, *12*, 570.
- [55] L. Friedman, N. F. Mott, *J. Non-Cryst. Solids* **1972**, *7*, 103.
- [56] L. Friedman, *J. Non-Cryst. Solids* **1971**, *6*, 329.
- [57] G. Haacke, *J. Appl. Phys.* **1976**, *47*, 4086.

4.4 Manuscript 4



Contents lists available at ScienceDirect

Synthetic Metals

journal homepage: www.elsevier.com/locate/synmet



Metallic conductivity beyond the Mott minimum in PEDOT: Sulphate at low temperatures



Dominik Farka^{a,*}, Andrew O.F. Jones^b, Reghu Menon^c, Niyazi Serdar Sariciftci^a, Philipp Stadler^a

^a Linz Institute for Organic Solar Cells (LIOS) Physical Chemistry, Johannes Kepler University Linz, Altenbergerstraße 69, 4040, Linz, Austria

^b Institute of Solid State Physics, Graz University of Technology, Petersgasse 16, 8010 Graz, Austria

^c Department of Physics, Indian Institute of Science, Bangalore 560012, India

ARTICLE INFO

Keywords:

PEDOT:sulphate
Magnetoelectricity
Metallic conductive polymer
Conductivity minimum
Pressure dependence
Mott minimum

ABSTRACT

Elastic scattering mechanisms dominate the charge transport in crystalline metals, resulting in a characteristic increase in conductivity at low temperatures. However, disorder – arising, for example, from alloying – can hamper transport and lead to decreased coherence among scattered electrons (*i.e.* inelastic scattering). This is typically the situation in non-crystalline metals. Likewise, conductive polymers are particularly prone to defect states with decreased carrier mobility (*i.e.* electrical conductivity).

We present the first report of conduction in the elastic scattering regime in conductive polymers without the detrimental effect on conductivity. As in a crystalline metal, conductivity increases upon cooling. More specifically, we observed a minimum conductivity in free-standing metallic PEDOT:sulphate at around 4 K. The polymer chains, which form crystallites of around 800 Å in size, exhibit an extraordinary degree of spatial and energetic order. We show that increasing pressure enabled us to shift the minimum upwards, thus achieving metallic conductivity at up to 10 K with a calculated mean-free path of around 250 Å. These results underline the existence of true metallic states in conductive polymers at low temperatures.

1. Introduction

Recent years have seen great advances in organic polymeric conductors. Novel materials of high purity and with low levels of disorder exhibit very high conductivities ($> 5000 \text{ S cm}^{-1}$) [1–3]. Nevertheless, the question remains of how to bridge the gap to true metallic conductivity, that is, how to achieve a positive temperature coefficient of resistance (TCR) as is typical of classical metals [4–9]. Conductive polymers (CPs) are different from metals, particularly in their inherent quasi-one-dimensional nature, which makes them especially prone to disorder. However, there are also similarities, for example, to alloys and amorphous metals [10–12], in which – unlike crystalline metals – conductivity does not increase with decreasing temperature [13,14].

Building on the theory of Anderson and Mott, we hypothesized that weak localization is directly linked to disorder in the system. The next step in the development of conductive polymers therefore consists of overcoming the critical density of states g^* to make the transition to a metallic and – potentially – in the longer term to a superconductive system [15–21].

Fornari et al. [22], arrived at a similar conclusion, claiming that only two distinct parameters influence conductivity: the activation energy of

electrical transport (which is given by the chemical structure of the molecule) and disorder. Hence, to achieve high conductivity, not only the choice of molecule is crucial, but, even more so, its processing into thin films.

Based on these conclusions, we decided to investigate the conductive material poly(3,4-ethylenedioxythiophene) (PEDOT), which is known for its structural advantages and mass production worldwide, and processed it in a novel way to minimize disorder during thin-film deposition and doping.

In this work, we investigate films of PEDOT:sulphate deposited via oxidative Chemical Vapour Deposition (oCVD). A previous publication reported that, due to an extraordinary degree of structural order, this material exhibits the hallmarks of a glassy metal [23]. Here, we present a study of bulk properties with the aim to eliminate effects related to the substrate.

We applied high pressures to compress the molecules in the van-der-Waals crystal, further suppress disorder, and thus to facilitate carrier transport [24–26] between polymer chains. Our assumption was that we could bridge the phenomenological gap between metals and conductive polymers by promoting diffusive electron motion and thus increasing the overlap between wavefunctions.

* Corresponding author.

E-mail addresses: dominik.farka@jku.at, dominik.farka@gmx.at (D. Farka).

<https://doi.org/10.1016/j.synmet.2018.03.015>

Received 29 November 2017; Received in revised form 6 March 2018; Accepted 16 March 2018

Available online 30 March 2018

0379-6779/ © 2018 The Authors. Published by Elsevier B.V. This is an open access article under the CC BY-NC-ND license (<http://creativecommons.org/licenses/by-nc-nd/4.0/>).

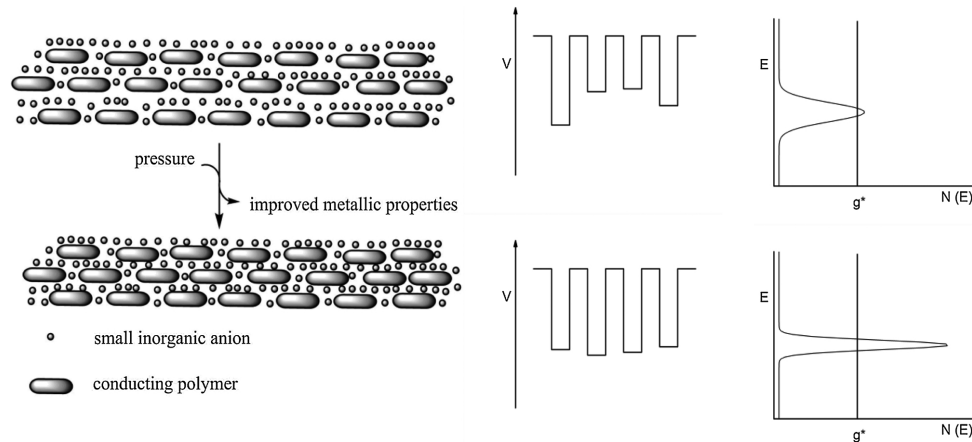


Fig. 1. Illustration of the effects of pressurizing PEDOT:sulphate. Without pressure (upper), structural order is already present, but the distances between the polymer chains are large, which results in a broader density of states. A metallic state (the g^* -limit) is reached, but applying hydrostatic pressure may improve the material's performance (lower). Rising hydrostatic pressure induces denser packing, thus increasing the overlap between the wave functions of the polymer chains. This leads in turn to equalization of the hypothetical Bloch equations, and to electrons becoming able to move freely within the material as the mobility edge is transcended. It is highly likely that crystallites interact with their surroundings in a similar way.

Pressurizing the bulk specimen (~ 1000 nm) removes minor imperfections in the polycrystalline material, as it causes structural rearrangements that minimize disorder and thus narrow the distribution of states in the material [24,27].

A second effect of pressurization (which also applies to highly ordered systems, such as ours) is that increased packaging density promotes electron transport both between polymer chains and between crystal grains (see Fig. 1). This boosts the material's electrical performance, as diffusive electron transport is further enhanced. Hence, improved coherence among scattered charge carriers – as in a classical metallic conductor – is expected.

Due to the correlation between disorder and electrical performance mentioned above, structural characterization was paramount in this study. If conductivity depends mainly on local order, achieving crystallinity is critical to reach the metallic state. Hence, we conducted X-ray studies including specular X-Ray Diffraction (XRD) and X-Ray Reflectivity (XRR) to determine structural order in tandem with (magneto-)conductivity. We identified a strong relationship between the observed conductivity and structural order, and found single crystallites of sizes hitherto unreported in conductive polymers. Our findings are supported by results from Transmission Electron Microscopy (TEM).

1.1. Background and theory

Although inorganic (semi-)conductors differ intrinsically from their organic counterparts, many concepts, such as Anderson localization, have been accepted to be valid for both [28–33].

We characterized the structural properties of PEDOT:sulphate by XRR and XRD. In XRR, through observation of the position of the critical angle of total external reflection α_c , the electron density can be calculated from the formula

$$\alpha_c = \sqrt{2\delta} \quad (1)$$

where δ is the refractive index decrement used to calculate the refractive index n in the equation

$$n = 1 - \delta + ic \quad (2)$$

and

$$\delta = \left(\frac{\lambda^2}{2\pi} \right)^2 r_e \cdot \rho_e \quad (3)$$

where δ is the absorption index, λ the wavelength of the incident radiation, r_e the classical electron radius, and ρ_e the electron density.

Crystallite sizes in the films can be estimated from the full width at half maximum (FWHM, β) of the peaks observed in the XRD spectra. To this end, the Scherrer formula is applied:

$$\tau = \frac{0.9 \cdot \lambda}{\beta \cdot \cos\theta} \quad (4)$$

where τ is the average crystallite size, λ is the wavelength of the incident radiation, β is the FWHM of a selected Bragg peak, and θ is half of the scattering angle 2θ . Unless further corrections are applied, the result obtained from this calculation presents the minimum crystal size to be expected.

Once the degree of disorder in the material under study is known, the electrical properties must be characterized. In conductive polymers, crucial questions to be answered typically concern the metal-insulator transition (MIT; specifically, on which side of it the material is located), the dimensionality of the conductor with respect to carrier transport, and the electron scattering processes involved [34–38].

A particularly useful tool for visualizing the MIT of an electrical conductor is the W- or Zhabrodskiy-plot [30], in which the dimensionless parameter W is plotted against temperature, corresponding to Eq. (5).

$$W = - \frac{d \ln \rho}{d \ln T} \quad (5)$$

In such a plot, W (or, more precisely, its slope) allows distinguishing between a temperature-activated process in the critical regime of the MIT (W_T constant), a glassy metal just shy of the Mott-Ioffe-Regel (MIR) limit [39–42] ($W_T \ll 1$ and $W_T \propto T$), and a crystalline metal when the MIR limit is reached ($W_T < 0$ and $W \propto T$).

Beyond the temperature of the MIT, the correlation lengths of carriers become particularly interesting. A charge carrier's correlation length depends on various factors such as phonon-electron interactions, impurity scattering, and electron-electron interactions. These scattering processes are expected to change in character when lower temperatures are reached [43,44].

In conductive polymers (i.e. in disordered systems), these effects have been well described by Kaiser et al [13,45,46]. When carriers move through a disordered conductor, two scenarios will occur: at low temperatures elastic scattering processes will dominate, while at high temperatures inelastic scattering processes will. As in the case of the former (almost) no energy exchange between phonons and electrons occurs, the mobility of the carriers is dependent only on their intrinsic energy: localization occurs even on shallow traps and conductivity is thus low. In the case of the latter, exchange of energy between the “lattice” and the electrons occurs (emission or absorption of a phonon), helping the delocalization of carriers: conductivity is thus expected to rise, i.e. a negative temperature coefficient of resistivity (TCR) will be observed. This process is often referred to as weak localization.

The effects on conductivity are thus on the contrary of what is expected from a metal, where a positive TCR, i.e. an increase in conductivity upon cooling is expected. Concerning phonon scattering, an exponential dependence on temperature T is expected when $\ll \theta_D$, the Debye temperature, while a linear dependence is expected at $T \sim \theta_D$ [44].

Electron-scattering mechanisms can best be monitored by performing magnetoconductivity (MC) measurements. Varying the magnetic field at a fixed temperature affects a material’s conductivity. In highly disordered conductive polymers, typically only magnetolocalization (i.e., a decrease in σ vs. B) can be observed [47,48]. As the magnetic field is ramped, carriers become increasingly localized due to electron-electron interactions. In the rare case of metallic conductive polymers, however, an interplay between magnetolocalization and magnetoconductivity can be observed. Weak magnetic fields result in a resonance effect with the free carriers (due to weak localization), thus increasing the conductivity observed. At higher temperatures, this effect is thought to originate from weak localization. At high fields, weak localization is suppressed by electron-electron interactions increasingly resulting in magnetolocalization [23,34,37]. (Supporting Information, Fig. S1)

These positive and negative MCs are proportional to H^2 and $H^{1/2}$, respectively (Supporting Information, Fig. S2 and S3) [34].

If both localization and delocalization are present, the magnetic field can be reformulated to the magnetic penetration depth or the Landau orbit size L_D :

$$L_D = \sqrt{\frac{h}{e \cdot B}} \quad (6)$$

The resulting maximum then corresponds to the mean free path of charge carriers, $L_D \approx \lambda_{ei}$, as the resonance condition is fulfilled.

A charge carrier’s correlation length corresponds to various factors, such as phonon-electron interactions and electron-electron interactions. These processes, also referred to as scattering, is expected to change in character when lower temperatures are reached [7,13,43]. In a conductive polymer in the critical regime, a charge carrier is subject to inelastic scattering processes, and thus an inverse relationship between temperature and mean free path is expected. In the metallic regime, however, carriers are subject to elastic scattering processes, which allows scattering against the direction of carrier movement. At the transition from critical to metallic regime, a drop in the mean free path of carriers is therefore expected.

2. Experimental

Prepared by oCVD, all PEDOT:sulphate films were grown on glass and sapphire substrates. The synthesis is described in full detail elsewhere [23]. The growth time for micrometer-thick films was determined to be 1 hour for a 3 L/min carrier gas flow. Using a clean wooden toothpick to remove the film from the glass surface, we obtained mechanically stable, free-standing films.

For the samples used in XRD and XRR measurements, proportionally

shorter growth times and flow rates of 1 L/min were used in order to obtain thin films with thicknesses of approximately 10 and 43 nm. Sapphire (0000) substrates served as carrier substrates.

Specular XRD and XRR data were collected on a PANalytical EMPYREAN diffractometer using Cu K_α radiation ($\lambda = 1.54 \text{ \AA}$). On the primary side, a parallel beam was generated using a multilayer X-ray mirror. On the secondary side, an anti-scatter slit and a Soller slit with a spacing of 0.02 rad were used with a PANalytical PIXcel^{3D} detector.

All conductivity measurements were performed using a Quantum Design-Dynacool PPMS system and the necessary (CuBe) pressure cell. This special alloys interaction with magnetic fields is minimal, allowing magneto-transport measurements. The sample is introduced to the cell in a pressurization-medium-filled teflon-cap and screwed shut. In order to apply a pressure load, a hydraulic press acting on a pressurization pin exerts pressure on the cells inside. Hence, the screwing cap can be further tightened, allowing measurements at elevated load pressures. (Fig. S4, SI)

For conductivity measurements, free-standing films of PEDOT:sulphate were mounted on a 4-probe sample board (4 in-line gold contacts, 1 mm separation) and inserted into the pressure cell. Daphne 7373 oil was used as pressurization medium. Silver paste was used to contact sample and sample board. This was sufficient to maintain stable contact over the whole temperature range (1.85–300 K). Magnetic fields of 0 to 9 T were applied at pressure loads of 0, 0.42, 1.28, 2.13, and 2.56 GPa.

All TEM measurements were performed using a JEOL JEM-2011. The bulk film was transferred to a copper grid as described above. All images presented in this publication were obtained using the same focus and a voltage of 100 kV.

3. Results and discussion

Since we hypothesized that excellent structural properties are a prerequisite for metallic transport properties, we decided to determine the structural aspects first. Both reflectivity and diffraction X-ray studies of films with a nominal thickness of $\sim 43 \text{ nm}$ (see Fig. 2) were conducted to investigate material parameters electron density, crystallite size, and preferred orientation with respect to the substrate. For this purpose, thin films of PEDOT:sulphate were grown on sapphire substrates. By means of XRR measurements, we first investigated the electron density in PEDOT:sulphate films (see Fig. 2a). In the measurement of PEDOT:sulphate, two critical angles of total external reflection (α_c) were observed. The critical angle of the substrate, the larger of the two in Fig. 2a, was determined by measuring the sapphire substrate alone and indicates – as expected – a higher electron density of the substrate compared to the film. The first critical angle then corresponds to the film and was observed at 0.195° in 2θ . From this value the electron density of the PEDOT:sulphate film can be calculated as 543 nm^{-3} [23].

Additionally, the XRR measurements give information about film roughness. The steep decrease in intensity at angles above the critical angle and the absence of Kiessig fringes suggest a relatively rough film.

In specular XRD measurements probing the out-of-plane film structure (see Fig. 2b), we observed three sharp Bragg peaks corresponding to the PEDOT:sulphate film at 2θ angles of 6.59, 19.80, and 23.74° , which correspond to d -spacings of 1.341, 0.448, and 0.375 nm, respectively. No further peaks from the film were observed at higher 2θ angles. The other peaks visible in the XRD measurement of the film can be assigned to the sapphire substrate. The small number of peaks from the film suggests a preferred orientation of the crystallites with respect to the substrate; the positions of the peaks imply that the first and third peaks belong to the same peak series (e.g. the 001 and 003 reflections), where the peaks at 6.59° and 19.80° are respectively the first -order and the third-order reflection of the same series. This is a further indication that there is a strongly preferred orientation of the crystallites within the thin film. Since only few peaks are observed that correspond to the

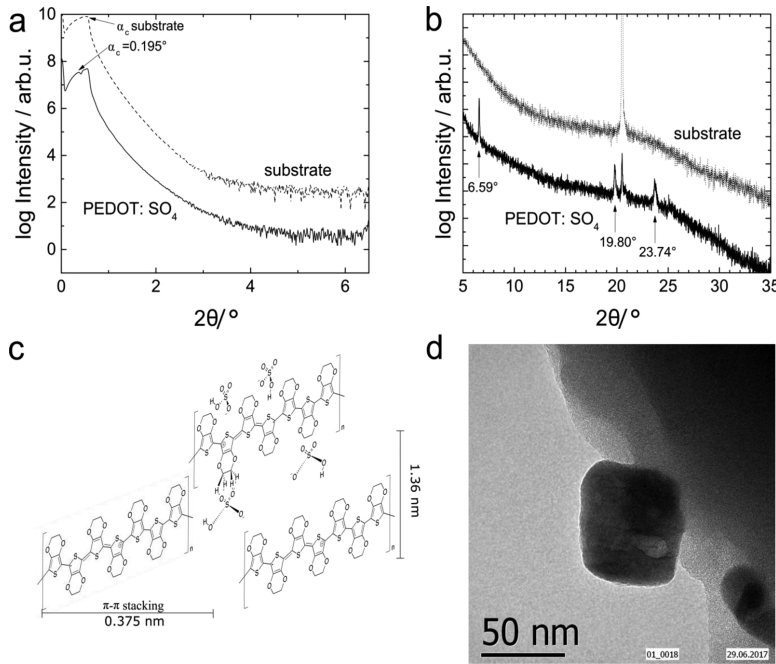


Fig. 2. Specular X-ray reflectivity and diffraction measurements. (a) Specular X-ray reflectivity curves of PEDOT:sulphate on sapphire (0000) and of pristine substrate. The critical angles α_c of both film and substrate are indicated. (b) Specular X-ray diffraction measurements of PEDOT:sulphate on sapphire compared with a measurement of the substrate alone. Peaks arising from the PEDOT:sulphate film are marked. (c) Schematic of the proposed packing in PEDOT:sulphate films. (d) TEM of a PEDOT:sulphate crystallite grain. The corresponding crystal diffraction pattern can be found in the SI (Fig. S2).

PEDOT:sulphate film no conclusions can be drawn about the crystal structure within the thin film, which - to the best of our knowledge- has not yet been published.

Based on the d -spacings observed, some information regarding the packing of the polymer chains can be made; a possible packing motif is shown in Fig. 2c. A layer spacing of 1.341 nm suggests that the majority of the polymer chains are standing upright on the substrate surface, as this d -spacing is of the same order of magnitude as the polymer chain length, accounting for the first two Bragg peaks. As specular XRD probes only the crystal structure perpendicular to the substrate, it yields no information about the in-plane crystal structure (parallel to the substrate surface). The Bragg peak at 23.74° ($d = 0.375$ nm) could correspond to a π - π interaction between neighbouring polymer chains. That this peak was observed in the out-of-plane direction means that polymer chains may also lie flat on the substrate surface. Therefore, the polymer chains probably lie in two different orientations with respect to the substrate: one in which they stand upright (represented by the spacing of 1.341 nm and the higher order reflection) and a second in which they lie flat on the substrate surface such that the direction of the π - π interaction is in the out-of-plane direction (based on the d -spacing of 0.375 nm).

The specular XRD measurement can also provide information about approximate crystallite size in the out-of-plane direction. The FWHM of the first peak ($2\theta = 6.59^\circ$) suggests a crystallite size of ~ 80 nm perpendicular to the substrate surface, which dwarfs PEDOT crystallite sizes hitherto reported. Such a result highlights the high degree of order present in the films and explains the origin of the roughness encountered in XRR. In thin-films, a structure of islands (~ 80 nm) significantly larger than the nominal film thickness connected by thinner film areas (~ 43 nm) is present. Note that for the electrical measurements in this study the situation differed, as thick films (~ 1000 nm) exceeding the crystallite size were investigated. This structure of connected crystallites accords well with results obtained for other conductive polymers, but with an extraordinary degree of structural order

[49–51]. In our case, these islands are essentially single crystalline grains; the XRD data available do not allow any conclusions to be drawn about the lateral crystallite size.

To gain a better understanding of the overall crystallite size, we performed TEM experiments and found crystallite sizes of up to 50 nm in thick films (see Fig. 2d, SI Fig. S5 which accords well with the results from XRD

At ambient pressure, the films exhibited a flat conductivity profile, retaining 52% of their room-temperature value even at low temperatures, specifically 2100 S cm^{-1} at 1.85 K (see Fig. 3a). In general, the conductivity plots in Fig. 3a indicate that two types of transport occur: temperature-independent band transport resembling that in a crystalline metal at low temperatures and temperature-activated transport resembling that in a disordered metal at elevated temperatures.

Further, compared to thin films, a new and important feature appeared in these measurements: a minimum in the conductivity value at 3.9 K (Fig. 3b), which corresponds to the minimum conductivity expected when the Fermi level approaches the mobility edge. This increase in conductivity is clearly attributed to the enhanced coherence in transport as electron-phonon scattering becomes weaker, and is a hallmark of the MIT (see Fig. 3c). Pressurizing the sample to 0.42 GPa shifted the minimum to 7.2 K. Upon gradual increase in pressure to 2.56 GPa, a further shift to 9.6 K was observed. At the same time, the material retained more of its room-temperature electron-transport properties at when pressurized, gradually approaching the flatter contour behaviour encountered in thin films, while the metallic minimum in conductivity became more pronounced (see Fig. 3d). This behaviour indicates an increasingly metallic character: increasing pressure improves the overlap between the wavefunctions of individual polymer chains and crystallite grains. We conclude that this effect is not caused by the samples Joule heating overcoming the systems cooling power. (see SI)

We were interested in observing the effects of a magnetic field on the transport properties. As both the minimum in conductivity and the

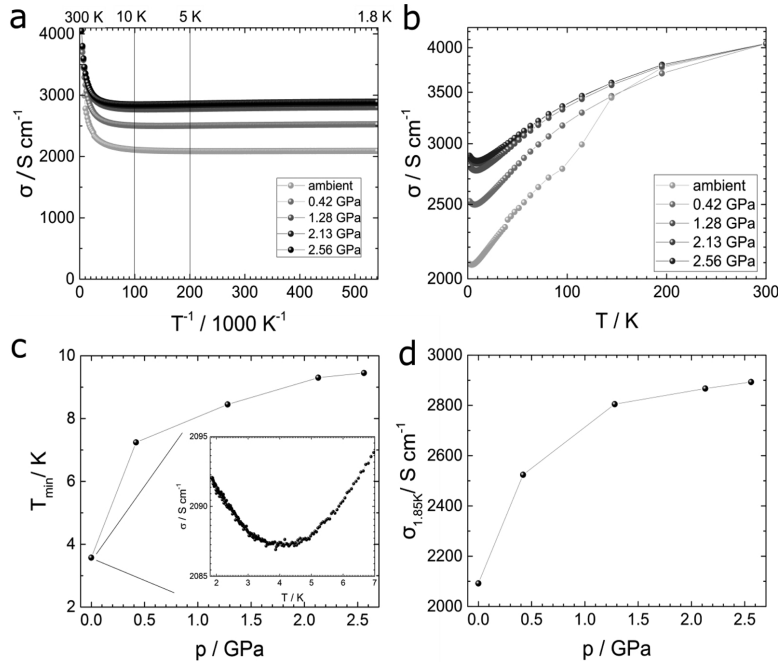


Fig. 3. Conductivity of PEDOT:sulphate free-standing films at various pressures at between 1.85 and 300 K. (a) Conductivity plotted against inverse temperature. The conductivity is comprised of two contributions: a temperature-activated transport term, which gradually diminishes with cooling, and a flat part corresponding to a metallic type of carrier transport. (b) Conductivity plotted against temperature. Note that the minimum in conductivity is found at temperatures below 10 K and shifts towards higher temperatures with increasing pressure, which points to a positive correlation between pressure and metallic character in PEDOT:sulphate. (c) Temperature at minimum conductivity under various pressures. The positive influence of higher pressure seems to approach a maximum to which T_{min} can be shifted. (d) Conductivity at 1.85 K for various pressures. As in the case of minimum conductivity, the positive effect of the applied pressure saturates.

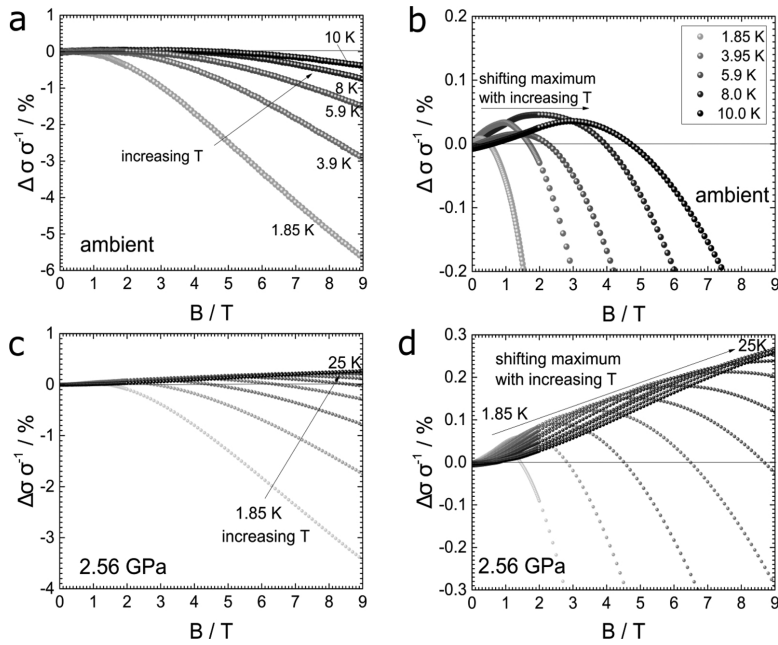


Fig. 4. Magnetoconductivity of PEDOT:sulphate at various temperatures and magnetic fields. (a) Magnetoconductivity (MC) change in percent at ambient pressures at temperatures between 1.85 and 10 K. (b) Enlarged version of Fig. 3a. The turning points at which destructive MC begins to dominate as a consequence of the strong magnetic field are clearly visible and manifest as a maximum. At higher temperatures, this maximum shifts to higher magnetic fields, as more energy is required to induce magnetolocalization. The positive effect was strongest at 8 K. (c) MC at 2.56 GPa pressure applied between 1.85 and 25 K (step size 2.31 K). (d) Enlarged version of Fig. 3c. The positive effect of the magnetic field on conductivity scales directly with temperature. As expected, a shift of the maximum to higher fields at higher temperatures was observed. Note that at temperatures above 20 K only positive MC was observed.

improved transport properties at higher pressures pointed to a material on the metallic side of the MIT, the question arose of how a magnetic field influences conductivity. In the case of a material on the metallic side of the MIT, interplay between positive and negative MC is to be expected. (see Fig. 4)

Subjecting the free-standing film to magnetic fields of 0–9 T at low temperatures resulted in the expected interplay (see Fig. 4a). The effect of magnetolocalization (*i.e.* negative MC) was most pronounced at 9 T and 1.8 K with a conductivity decrease of 5.8%. Higher temperatures, however, shifted the onset of magneto-localization to higher fields, with the positive MC becoming the dominant contribution (see Fig. 4b). This was most pronounced at a magnetic field of 2 T at 8 K, which resulted in a conductivity increase of 0.05%. Note that positive MC depends on B^2 , whereas magnetolocalization shows a dependence on $B^{1/2}$ (for details see Figs. S2a and S3a, SI).

Upon pressurization, inter-grain and inter-chain transport improved, and the positive MC was further enhanced (see Fig. 4c). This is reflected by the maximum in MC shifting to higher magnetic fields with increasing temperature; at temperatures above 10 K, it was no longer possible to induce magnetolocalization (with the equipment available). Note that, upon exceeding 20 K, the positive MC effect was found to exceed 0.25% - an impressive value for a CP (see Fig. 4d) [52,53]. An evaluation of the magnitude of magnetolocalization can be found in the Supporting Information (see S2b and S3b, SI). Positive and destructive MCs showed the same relations to B as in the equivalent unpressurized setting.

We relied on MC to investigate the scattering mechanisms in the material, correlating them to metallic transport properties.

To this end, we reformulated the magnetic field strength B into the Landau orbit size L_D (Eq. (6); Fig. 5). At the maximum, the highest resonance between the magnetic field and the wave functions of the delocalized carriers is observed. This, we conclude, corresponds to the mean free path of electrons.

The results at ambient pressure (see Fig. 5a) indicate a hybrid scattering mechanism in PEDOT:sulphate films at minimum conductivity. While at temperatures of up to 3.9 K, a single resonance peak with a maximum scattering length of up to 49 nm (at 1.85 K) was found, the scattering length gradually decreased with temperature. At temperatures above 6 K, the maximum split, and a shoulder that indicates the coexistence of two scattering mechanisms appeared. We assume that this is caused by the difference in scattering within the crystallites and at the grain boundary. Higher temperatures diminish the two-phase resonance, thus enhancing that of shorter scattering length. We conclude that a phase transition from crystalline metallic to glassy metallic occurs in the two-phase regime, which is in agreement with the conclusions drawn from conductivity scans.

The coexistence of multiple resonances can be better understood when observing the MCs at elevated pressures (see Fig. 5b). Clearly resolved single peaks were observed when the elevated pressure fully masked the temperature effect (as previously observed), which supports our previous claim that increasing pressure increases the overlap between crystallite grains, thus favouring diffusive transport. Under pressure, the metallic phase established at higher temperatures, resulting in a scattering length of close to 40 nm, while the resonance value decreased gradually and arrived at 23 nm at 10 K. This is reminiscent of scattering theory stating that a transition from inelastic to elastic scattering leads to lower mean free paths as scattering becomes more coherent.

For better visualization, the collective results at different pressures applied are summarized in Fig. 5c and d. In general, higher temperatures resulted in shorter scattering lengths. When the sample was pressurized, a distinct change in behaviour was also clearly visible. The effect of increasing the pressure load saturated when approaching higher temperatures. Note that, irrespective of the level of pressure applied, scattering length approached a similar value with rising temperatures (see Fig. 5c).

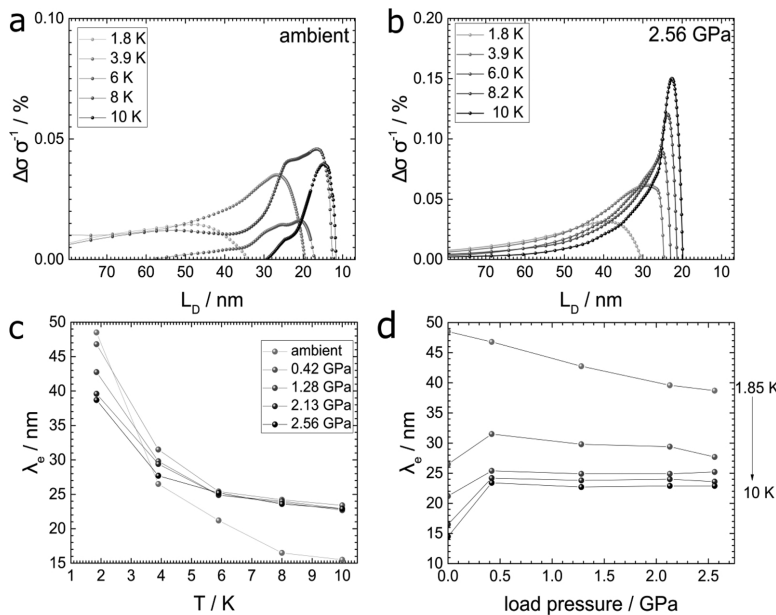


Fig. 5. Scattering lengths of free charge carriers at various pressures. (a) Landau orbit size or mean free path of carriers at various temperatures and ambient pressure. The maximum corresponds to a resonance of the magnetic field with conductivity. Note the shoulder above 6 K indicating a twin-resonance energy. This suggests the coexistence of elastic and inelastic scattering processes in the material. (b) Landau orbit size at various temperatures. The mean free path of carriers decreases with temperature. In contrast to the ambient pressure measurements, a single peak was observed, indicating the absence of a transition between scattering mechanisms. This trend was observed for any pressures applied (Supporting information, Fig. S7). (c) Correlation between mean free path of carriers and temperature. A common trend can be observed: higher temperatures correlate with a decrease in mean free path. This trend, however, is more pronounced in non-pressurized samples, as is to be expected. If pressurized, the mean free path decreases, approaching a value independent of pressure. (d) Correlation of mean free path of carriers with load pressure. For

all pressures, at 1.85 K, elastic scattering and a linear decrease in mean free path can be observed. At higher temperatures, however, an interplay of two effects is visible: longer scattering lengths are increased by improved overlap between polymer chains and decreased by the transition from inelastic to elastic scattering. As the former effect saturates with pressure, an overall decrease in scattering length results.

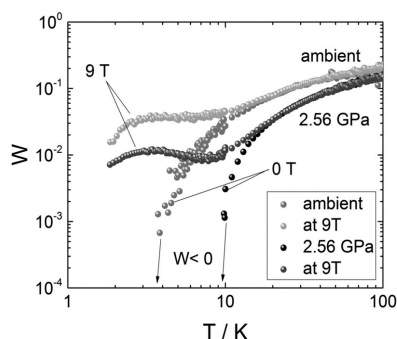


Fig. 6. W-plot and correlation between pressure and structural order. (a) W-plot at ambient pressure and at 2.56 GPa. In both cases, cooling the sample below 3.8 and 10 K, respectively, induced crystalline metal behaviour (*i.e.* a negative value of W), which correlates well with the expected behaviour. Elevated magnetic fields (9 T) quenched the metallic state to a certain degree and induced the critical regime of the MIT.

After an initial increase in mean free path upon pressurization (0.42 GPa), the effect of higher pressures on scattering length became limited (see Fig. 5d). This is a consequence of two competing phenomena occurring at the same time. On one hand, pressure improves the overlap between the polymer chains' wave functions, which increases conductivity and thus coherence among scattered electrons (see Figs. 2c and Figure 5d or SI Fig. S6). This "masks" the transition from inelastic to elastic scattering, where the improvement of the overlap is strongest. On the other hand, as scattering becomes increasingly elastic and the overlap approaches its optimum, the mean free path decreases in the expected way.

At 1.85 K, however, a decrease was observed regardless of the pressure applied, as the material was already on the metallic side of the MIT; elevated pressures immediately resulted in a drop in coherence length.

Finally, the data obtained from MC measurements allowed us to study the MIT in greater detail. We visualized the transitions between the various transport states in PEDOT:sulphate in the form of Zbrodskii- or W-plots (see Fig. 6). The effect of a strong magnetic field on the MIT was also investigated.

In the W-plots, measurements at ambient and elevated load pressures are quite distinct. In the absence of a magnetic field, the W-value of both decreases gradually upon cooling of the sample, as is to be expected of a glassy metal [23,34,52]. At some point, however, a transition towards the crystalline metal occurs as the W-value becomes negative. This happens when the sample's intrinsic conductivity starts to increase upon cooling, just as expected of a structurally ordered metal.

Upon applying a magnetic field of 9 T, the metallic properties become quenched in both cases, and the material enters a quasi-critical regime. Further cooling, however, gradually restores the behaviour of a glassy metal, as the destructive effects of the magnetic field are overcome.

The results constitute direct proof of our hypothesis that by significantly suppressing disorder, metallic properties can be induced in a polymeric conductor (see Fig. 1). The phenomenological gap (*i.e.* reaching a positive TCR) between inorganic and organic electrical conductors has been bridged, which shows that it is indeed possible to reach metallic properties in the absence of an elementary metal.

4. Conclusions

In bulk films of PEDOT:sulphate, charge carrier transport akin to

that of a crystalline metal occurs due to a high degree of order. Hydrostatic pressure-induced shifts of the minimum conductivity σ_{\min} show that anisotropic systems show transition from (weak) localization to metallic transport.

A look at magnetoconductivity reveals that the metallic regime exists readily at low temperatures. In particular, we observed a minimum at 3.9 K in highly crystalline CP samples. Furthermore, we have demonstrated that the crystalline-metallic regime can be expanded by elevated pressures, the effect saturating for higher pressures. Even relatively small pressures show significant effect. By raising the pressure to an extreme of 2.56 GPa, the MIT occurs already at 10 K, which represents a paradigm shift in conductive polymers.

Thus, we have confirmed that the metallic state depends on structural order and is well achievable in CPs. Expanding the metallic phase towards room temperature becomes thus the primary goal. We expect that achieving this in p-doped conductors will require chemically novel, yet simple, organic conductive materials.

Acknowledgements

P.S., N.S.S., and R.M. are grateful to OEAD (WTZ, IN10/2015). N.S.S. and D.F. acknowledge support from the Austrian Fund for Advancement of Science (FWF) within the Wittgenstein Prize scheme (Z222-N19 Solare Energieumwandlung) and the Austrian Research Promotion Agency (FFG; 842496, 3D OFET). The authors thank Markus Clark Scharber for fruitful discussions and Günter Hesser (Center for Surface and Nanoanalytics, Johannes Kepler University Linz) for TEM measurements.

Appendix A. Supplementary data

Supplementary material related to this article can be found, in the online version, at doi:<https://doi.org/10.1016/j.synthmet.2018.03.015>.

References

- [1] M.N. Gueye, A. Carella, N. Massonnet, E. Yvenou, S. Brenet, J. Faure-Vincent, S. Pouget, F. Rieutord, H. Okuno, A. Benayad, R. Demadrille, J.P. Simonato, Structure and dopant engineering in PEDOT thin films: Practical tools for a dramatic conductivity enhancement, *Chem. Mater.* 28 (2016) 3462–3468, <http://dx.doi.org/10.1021/acs.chemmater.6b01035>.
- [2] N. Massonnet, A. Carella, D.G. Arnaud, J. Faure-Vincent, J.-P.-P. Simonato, A. De Geyer, J. Faure-Vincent, A. de Geyer, J. Faure-Vincent, J.-P.-P. Simonato, Metallic behaviour in acid doped highly conductive polymers, *Chem. Sci.* 6 (2014) 412–417, <http://dx.doi.org/10.1039/C4SC02463J>.
- [3] A. Ugur, F. Katmis, M. Li, L. Wu, Y. Zhu, K.K. Varanasi, K.K. Gleason, Low-dimensional conduction mechanisms in highly conductive and transparent conjugated polymers, *Adv. Mater.* 27 (2015) 4604–4610, <http://dx.doi.org/10.1002/adma.201502340>.
- [4] N. Kim, B.H. Lee, D. Choi, G. Kim, H. Kim, J.R. Kim, J. Lee, Y.H. Kahng, K. Lee, Role of interchain coupling in the metallic state of conducting polymers, *Phys. Rev. Lett.* 109 (2012) 1–5, <http://dx.doi.org/10.1103/PhysRevLett.109.106405>.
- [5] K. Lee, E.K. Miller, A.N. Aleshin, R. Menon, A.J. Heeger, J.H. Kim, C.O. Yoon, H. Lee, Nature of the metallic state in conducting polypyrrole, *Adv. Mater. (Weinheim, Ger)* 10 (1998) 456.
- [6] O. Bubnova, Z.U. Khan, H. Wang, S. Braun, D.R. Evans, M. Fabretto, P. Hojati-Talemi, D. Dagnelund, J.-B. Arlin, Y.H. Geerts, S. Desbief, D.W. Breiby, J.W. Andreasen, R. Lazzaroni, W.M. Chen, I. Zozoulenko, M. Fahlman, P.J. Murphy, M. Berggren, X. Crispin, Semi-metallic polymers, *Nat. Mater.* 13 (2013) 190–194, <http://dx.doi.org/10.1038/nmat3824>.
- [7] K. Kang, S. Watanabe, K. Brochi, A. Sepe, A. Brown, I. Nasrallah, M. Nikolka, Z. Fei, M. Heeney, D. Matsumoto, K. Marumoto, H. Tanaka, S.I. Kuroda, H. Sirringhaus, 2D coherent charge transport in highly ordered conducting polymers doped by solid state diffusion, *Nat. Mater.* 15 (2016) 896–902, <http://dx.doi.org/10.1038/nmat4634>.
- [8] J. Hynynen, D. Kiefer, L. Yu, R. Kroon, R. Munir, A. Amassian, M. Kemerink, C. Müller, Enhanced electrical conductivity of molecularly p-doped poly(3-hexylthiophene) through understanding the correlation with solid-state order, *Macromolecules* 50 (2017) 8140–8148, <http://dx.doi.org/10.1021/acs.macromol.7b00968>.
- [9] A. Hamidi-Sakr, L. Biniak, J.L. Bantignies, D. Maurin, L. Herrmann, N. Leclerc, P. Lévêque, V. Vijayakumar, N. Zimmermann, M. Brinkmann, A versatile method to fabricate highly in-plane aligned conducting polymer films with anisotropic charge

- transport and thermoelectric properties: the key role of Alkyl side chain layers on the doping mechanism, *Adv. Funct. Mater.* 27 (2017) 1–13, <http://dx.doi.org/10.1002/adfm.201700173>.
- [10] A.B. Kaiser, Low-conductivity metals and comparison with highly conducting, *Electron. Prop. Conj. Polym.* (1987), pp. 2–11.
- [11] J.H. Mooij, Electrical conduction in concentrated disordered transition metal alloys, *Phys. Status Solid* 17 (1973) 521–530, <http://dx.doi.org/10.1002/pssa.2210170217>.
- [12] A.B. Kaiser, V. Skákalová, Electronic conduction in polymers, carbon nanotubes and graphene, *Chem. Soc. Rev.* 40 (2011) 3786, <http://dx.doi.org/10.1039/c0cs00103a>.
- [13] A.B. Kaiser, C.K. Subramaniam, B. Wessling, Electronic transport properties of conducting polymers, *Int. Conf. Sci. Technol. Synth. Met.* 64 (1994) 1–49 <http://stacks.iop.org/0034-4885/64/i=1/a=201?key=crossref.95177e1e4908618ad4c8ee079a7a8b85>.
- [14] G. Bergmann, Weak localization in thin films: a time of flight experiment with conduction electrons, *Phys. Rep.* 107 (1984) 1.
- [15] N.F. Mott, *Metal-Insulator Transitions*, 1st ed., Taylor & Francis LTD, London, 1974.
- [16] N.F. Mott, Metal-insulator transition, *Rev. Mod. Phys.* 40 (1968) 677–683, <http://dx.doi.org/10.1103/RevModPhys.40.677>.
- [17] N.F. Mott, Introductory talk; conduction in non-crystalline materials, *J. Non. Cryst. Solids* 8–10 (1972) 1–18, [http://dx.doi.org/10.1016/0022-3093\(72\)90112-3](http://dx.doi.org/10.1016/0022-3093(72)90112-3).
- [18] D. Belitz, T.R. Kirkpatrick, The Anderson-Mott transition, *Rev. Mod. Phys.* 66 (1994) 261–380, <http://dx.doi.org/10.1103/RevModPhys.66.261>.
- [19] F. Evers, A.D. Mirlin, Anderson transitions, *Rev. Mod. Phys.* 80 (2008) 1355–1417, <http://dx.doi.org/10.1103/RevModPhys.80.1355>.
- [20] A. Lagendijk, B. Van Tiggelen, D.S. Wiersma, Fifty years of Anderson localization, *Phys. Today* 62 (2009) 24–29, <http://dx.doi.org/10.1063/1.3206091>.
- [21] M. Imada, A. Fujimori, Y. Tokura, Metal-insulator transitions, *Rev. Mod. Phys.* 70 (1998) 1039–1263, <http://dx.doi.org/10.1103/RevModPhys.70.1039>.
- [22] R.P. Fornari, P.W.M. Blom, A. Troisi, How Many Parameters Actually Affect the Mobility of Conjugated Polymers? *Phys. Rev. Lett.* 118 (2017) 86601, <http://dx.doi.org/10.1103/PhysRevLett.118.086601>.
- [23] D. Farka, H. Coskun, J. Gasiorowski, C. Cobet, K. Hingerl, L.M. Uiberlacker, S. Hild, T. Greunz, D. Stifter, N.S. Sariciftci, R. Menon, W. Schoefberger, C.C. Mardare, A.W. Hassel, C. Schwarzwinger, M.C. Scharber, P. Stadler, Anderson-Localization and the Mott-Ioffe-Regel Limit in Glassy-Metallic PEDOT, *Adv. Drug Deliv. Rev.* (2017), <http://dx.doi.org/10.1002/adrm.201700050>.
- [24] K. Murata, K. Yokogawa, S. Arumugam, H. Yoshino, Pressure effect on organic conductors, *Crystals* 2 (2012) 1460–1482, <http://dx.doi.org/10.3390/cryst2041460>.
- [25] S.G. Duyker, V.K. Peterson, G.J. Kearley, A.J. Studer, C.J. Kepert, Extreme compressibility in $\text{LnFe}(\text{CN})_6$ coordination framework materials via molecular gears and torsion springs, *Nat. Chem.* 8 (2016) 270–275, <http://dx.doi.org/10.1038/nchem.2431>.
- [26] E. Magos-Palasyuk, K.J. Fijalkowski, T. Palasyuk, Chemically driven negative linear compressibility in sodium amidoborane, $\text{Na}(\text{NH}_2\text{BH}_3)$, *Sci. Rep.* 6 (2016) 28745, <http://dx.doi.org/10.1038/srep28745>.
- [27] S.O. Dwyer, H. Xie, M. Knaapila, S. Guha, Conducting polymers under pressure: synchrotron x-ray determined structure and structure related properties of two forms of poly(octyl-thiophene), *J. Phys. Condens. Matter.* 10 (1998) 7145–7154 <http://iopscience.iop.org/article/10.1088/0953-8984/10/32/006>.
- [28] N. Mott, *Electrons in glass*, Nobel Lect. *Nature* (1977).
- [29] I. Solomon, Disordered semiconductors: The Mott-Anderson localization, *J. Optoelectron. Adv. Mater.* 4 (2002) 419–423 http://www.inoe.ro/JOAM/pdf4_3/Solomon.pdf.
- [30] A.G. Zbrodskii, K.N. Zinov'eva, Low-temperature conductivity and metal-insulator transition in compensate n-Ge, *Zh. Eksp. Teor. Fiz.* 86 (1984) 727–742.
- [31] A.J. Heeger, N.S. Sariciftci, E.B. Namdas, *Semiconducting and Metallic Polymers* 21 Oxford Univ. Press, 2011, pp. 391–393, <http://dx.doi.org/10.1007/s10904-011-9458-x>.
- [32] L. Torsi, M. Magliulo, K. Manoli, G. Palazzo, Organic field-effect transistor sensors: a tutorial review, *Chem. Soc. Rev.* 42 (2013) 8612, <http://dx.doi.org/10.1039/c3cs60127g>.
- [33] H. Wang, U. Ail, R. Gabrielsson, M. Berggren, X. Crispin, Ionic seebeck effect in conducting polymers, *Adv. Energy Mater.* 5 (2015), <http://dx.doi.org/10.1002/aenm.201500044>.
- [34] R. Menon, C.O. Yoon, D. Moses, A.J. Heeger, Y. Cao, Transport in polyaniline near the critical regime of the metal-insulator transition, *Phys. Rev. B.* 48 (1993) 17685–17694, <http://dx.doi.org/10.1103/PhysRevB.48.17685>.
- [35] A. Aleshin, R. Kiebooms, R. Menon, A.J. Heeger, Electronic transport in doped poly(3,4-ethylenedioxythiophene) near the metal-insulator transition, *Synth. Met.* 90 (1997) 61–68, [http://dx.doi.org/10.1016/S0379-6779\(97\)81227-1](http://dx.doi.org/10.1016/S0379-6779(97)81227-1).
- [36] K. Lee, S. Cho, S.H. Park, A.J. Heeger, C.-W. Lee, S. Lee, Metallic transport in polyaniline, *Nature* 441 (2006) 65–68, <http://dx.doi.org/10.1038/nature04705>.
- [37] P. Stadler, D. Farka, H. Coskun, E.D. Glowacki, C. Yumusak, L.M. Uiberlacker, S. Hild, L.N. Leonat, M.C. Scharber, P. Klapetek, R. Menon, N.S. Sariciftci, Local order drives the metallic state in PEDOT:PSS, *J. Mater. Chem. C.* 4 (2016) 6982–6987, <http://dx.doi.org/10.1039/C6TC02129H>.
- [38] E. Helgren, K. Penney, M. Diefenbach, M. Longnickel, M. Wainwright, E. Walker, S. Al-Azzawi, H. Erhahon, J. Singley, Electrodynamic of the conducting polymer polyaniline on the insulating side of the metal-insulator transition, *Phys. Rev. B - Condens. Matter Mater. Phys.* 95 (2017) 1–8, <http://dx.doi.org/10.1103/PhysRevB.95.125202>.
- [39] P.A. Lee, T.V. Ramakrishnan, Disordered electronic systems, *Rev. Mod. Phys.* 57 (1985) 287–337, <http://dx.doi.org/10.1103/RevModPhys.57.287>.
- [40] C.C. Tsuei, Nonuniversality of the mooj correlation the temperature coefficient of electrical resistivity of disordered metals, *Phys. Rev. Lett.* 57 (1986) 1943–1946, <http://dx.doi.org/10.1103/PhysRevLett.57.1943>.
- [41] N.E. Hussey, K. Takenaka, H. Takagi, Universality of the Mott-Ioffe-Regel limit in metals, *Philos. Mag.* 84 (2004) 2847–2864, <http://dx.doi.org/10.1080/14786430410001716944>.
- [42] M.I. Daunov, I.K. Kamilov, S.F. Gabibov, Concept of mobility threshold: The Ioffe-Regel rule, *Phys. Solid State.* 52 (2010) 2019–2025, <http://dx.doi.org/10.1134/S1063783410100033>.
- [43] G. Bergmann, Physical interpretation of weak localization: A time-of-flight experiment with conduction electrons, *Phys. Rev. B.* 28 (1983) 2914–2920, <http://dx.doi.org/10.1103/PhysRevB.28.2914>.
- [44] Ashcroft Mermin, *Solid State Phys.* (1976).
- [45] A.B. Kaiser, Metallic behaviour in highly conducting polymers, *Synth. Met.* 45 (1991) 183–196, [http://dx.doi.org/10.1016/0379-6779\(91\)91802-H](http://dx.doi.org/10.1016/0379-6779(91)91802-H).
- [46] A.B. Kaiser, Systematic conductivity behavior in conducting polymers: Effects of heterogeneous disorder, *Adv. Mater.* 13 (2001) 927–941, [http://dx.doi.org/10.1002/1521-4095\(200107\)13:12<927::AID-ADMA927>3.0.CO;2-B](http://dx.doi.org/10.1002/1521-4095(200107)13:12<927::AID-ADMA927>3.0.CO;2-B).
- [47] M. Reghu, C.O. Yoon, D. Moses, P. Smith, A.J. Heeger, Y. Cao, Magnetoresistance in polyaniline networks near the percolation threshold, *Synth. Met.* 69 (1995) 271–272, [http://dx.doi.org/10.1016/0379-6779\(94\)02446-6](http://dx.doi.org/10.1016/0379-6779(94)02446-6).
- [48] A. Aleshin, R. Kiebooms, H. Yu, M. Levin, I. Shlimak, Conductivity and magnetoconductivity below 1 K in films of poly(3,4-ethylenedioxythiophene) doped with CF_3SO_3 , *Synth. Met.* 94 (1998) 157–159.
- [49] R. Noriega, J. Rivnay, K. Vandewal, F.P.V. Koch, N. Stingelin, P. Smith, M.F. Toney, A. Salleo, A general relationship between disorder, aggregation and charge transport in conjugated polymers, *Nat. Mater.* 12 (2013) 1038–1044, <http://dx.doi.org/10.1038/nmat3722>.
- [50] C.G. Wu, S.S. Chang, Nanoscale measurements of conducting domains and current-voltage characteristics of chemically deposited polyaniline films, *J. Phys. Chem. B.* 109 (2005) 825–832, <http://dx.doi.org/10.1021/jp046259b>.
- [51] S. Dongmin Kang, G. Jeffrey Snyder, Charge-transport model for conducting polymers, *Nat. Mater.* 1 (2016) 1–7, <http://dx.doi.org/10.1038/nmat4784>.
- [52] R. Menon, Conductivity and magnetoconductance in iodine-doped polyacetylene, *Synth. Met.* 80 (1996) 223–229, [http://dx.doi.org/10.1016/S0379-6779\(96\)03706-X](http://dx.doi.org/10.1016/S0379-6779(96)03706-X).
- [53] M. Ahlskog, M. Reghu, Magnetoconductivity in doped poly(p-phenylenevinylene), *J. Phys. Condens. Matter.* 101 (1998) 6779 <http://iopscience.iop.org/0953-8984/10/4/012>.

4.5 Manuscript 5



Contents lists available at ScienceDirect

Organic Electronics

journal homepage: www.elsevier.com/locate/orgel

Stable Hall voltages in presence of dynamic quasi-continuum bands in poly(3,4-ethylene-dioxythiophene)



Philipp Stadler^{a,*}, Lucia N. Leonat^{a,b}, Reghu Menon^c, Halime Coskun^a, Sandrine van Frank^d, Christian Rankl^d, Markus C. Scharber^a

^a Institute of Physical Chemistry, Johannes Kepler University Linz, Altenberger Straße 69, 4040, Linz, Austria

^b National Institute for Materials Physics, Atomistilor Str., No. 405A PO Box MG 7, 077125, Magurele, Romania

^c Indian Institute of Science, Department of Physics, Bangalore, India

^d Research Center for Non Destructive Testing GmbH, 4040, Linz, Austria

ARTICLE INFO

Keywords:
Hall-effect
Conducting polymers
Weak localization
Organic phase model
Electron coherence
PEDOT

ABSTRACT

Topological and thermal disorder complicate the mobility characterization in poly(3,4-ethylenedioxythiophene) systems and presently leaves the exact transport mechanisms not fully understood. Here we show that *ac*-Hall measured by lock-in amplifier is able to resolve the Hall voltage in semimetallic polymers between room temperature and 32 K. These results are evaluated using an organic random phase model. This accounts for the role of tail states and, particularly, for thermal disorder of molecular semiconductors. We report band mobilities up to $3.7 \text{ cm}^2 \text{ V}^{-1} \text{ s}^{-1}$ in semimetallic polymers occurring in delocalized bands that originate from significant electron coherence across the polymer chains.

1. Introduction

In crystalline semiconductors the Hall-effect represents the method to derive the charge carrier mobility. However, in disordered, emerging semiconductors it is rarely applied, because the band continuum becomes disrupted with the consequence of significantly decreased charge carrier mobilities and, hence, reduced Hall voltages [1–6]. These effects are amplified in molecular semiconductors, because on top of topological disorder, thermal disorder plays major role [7–15]. The related phonon-dynamics cause a significant stronger disorder screening of the Hall voltages as compared to inorganic systems and, subsequently, makes Hall characterization elaborate. For inorganic systems such as highly-doped silicon, there exist theoretical transport models that relate mainly the topological effects on the transverse Lorenz forces: we refer here to Friedman, who proposed such compensation in his random phase model (RPM) [1–4,16]. However, for disordered molecular semiconductors the phase model requires adaptations, in particular the relation of localization and doping. An organic phase model reconciling molecular dynamics had been suggested by Yi et al. [8]. It bases on the assumption that the transverse Lorenz forces are practically compensated by hopping carriers and that only the band carriers contribute to the Hall-effect. This leads to a significant reduced Hall voltage *i.e.* Hall voltage screening, which has to be considered in mobility calculation.

The classic hypothesis of quasi-band continuum (coherent band-like transport) was here adapted for molecular systems to allow the extraction of mobilities in the presence of dynamic disorder. We concluded that at moderate disorder the residual band widths would be larger than the random disorder potentials fluctuations emerging from thermal and topological disorder. This would yield ultimately transport with persistent band contribution and stable Hall voltages (Fig. 1).

Our main assumption was that such situation is established in semimetallic conducting polymers - a class of molecular semiconductor, where the electrical conductivities are in the range of 1000 S cm^{-1} . These systems possess a metal-insulator transition at lower temperatures [17–26], so there exists evidence of a band contribution to the transport.

We demonstrate the characterization and evaluation of the screened Hall effect in commonplace, semimetallic poly(3,4-ethylene-dioxythiophenes) (PEDOTs) with the help of the organic phase model and as such we derive band mobilities from the Hall voltages. The study includes a complementary terahertz (THz) spectroscopy mobility characterization [27,28] for the system with the highest conductivity showing a similar mobility. We discuss the effect of long-range electron coherence among the polymer chains and the subsequent semimetallic transport properties (Anderson localization) with stable Hall voltages as result order from optimized solvent processing and post-processing treatments

* Corresponding author. Present: Linz Institute of Technology (LIT) and Institute of Physical Chemistry, Johannes Kepler University Linz, Altenberger Straße 69, 4040, Linz, Austria.

E-mail address: Philipp.Stadler@jku.at (P. Stadler).

<https://doi.org/10.1016/j.orgel.2018.12.001>

Received 1 June 2018; Received in revised form 26 November 2018; Accepted 2 December 2018

Available online 03 December 2018

1566-1199/ © 2018 The Authors. Published by Elsevier B.V. This is an open access article under the CC BY-NC-ND license (<http://creativecommons.org/licenses/by-nc-nd/4.0/>).

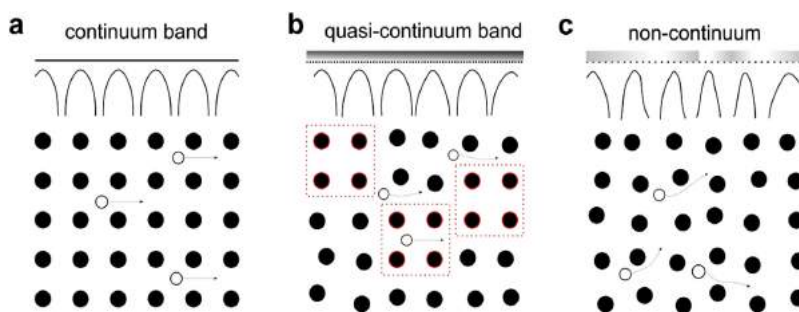


Fig. 1. (a) The change of the band structure upon increase of disorder leads to full disruption of the continuum as schematically proposed by (c). (b) Intermediate state of a quasi-band continuum is the existence of adjacently ordered domains inside a moderately disordered system.

[21–26,29–31].

Our Hall study includes three representative semimetallic PEDOT systems. In all these PEDOTs we are able to measure finite Hall-voltages. To probe these, we advanced the experimental setting using magnetic lock-in amplification (i.e. an *ac*-magnetic field B_{ac} combined with an electrical *dc* measurement, further denoted as *ac*-Hall). This technique expands the noise limit to 10^{-7} V in a van der Pauw Hall-specimen. Our experimental precision allowed us to measure consistent stable Hall voltages in the range of 10^{-6} V, which were then evaluated by the organic phase model between 32 and 300 K. In the best PEDOT, we calculate band mobilities of up to $3.7 \text{ cm}^2 \text{ V}^{-1} \text{ s}^{-1}$ [32–36] and these values are in agreement results from the contactless THz spectroscopy. We demonstrated that the hypothesis of quasi-band continuum can be utilized for the Hall effect in semimetallic polymers, where despite of the dynamic disorder, significant electron coherence resulted in stable Hall voltages and comparatively significant mobilities [37–40].

2. Results and discussion

As the diffusive band transport is significantly affected by dynamic disorder effects, the measurement of reduced Hall voltages (V_H) and its interpretation is often regarded as a challenging task. In this work we resolved the experimental and theoretical difficulties for the class of conducting polymers. We demonstrated that in semimetallic systems a consistent Hall voltage exists, which were evaluated by an organic phase model. We elucidated additive and acid-treated PEDOT-systems, which were applied as transparent electrodes and thermoelectric layers earlier. In general, latest advancements boosted the electrical conductivities of PEDOT-composites to metal-like regimes. These results relied on precise solvent processing and post-treatment steps and conductivities as high as 5000 S cm^{-1} and beyond have been achieved. Although these conductivity values are of impressive magnitude, the Hall-effect was not extensively studied [41–43].

We refer to processing strategies which utilized high boiling point polar co-solvents to obtain long-range order. Such additives were combined with spin-coating, blade-coating and printing and led typically to semimetallic transport. One common additive is dimethylsulfoxide (DMSO). DMSO-based formulations of PEDOT:PSS were matter of extensive studies, one of which is presented in the [supplementary information \(SI\)](#). In addition, we elucidated an alternative post-processing treatment with trifluoromethylsulfonic acid (TfOH). Exposure to the strong acid removes the polystyrenesulfonate anion (PSS^-) leading to the class of PSS-free PEDOT-systems (here subsequently called PEDOT:TfO with a conductivity of approx. 2000 S cm^{-1} and semimetallic transport behaviour). Both the DMSO and TfOH-treatments led to high electrical performance – ideal to conduct the combined transport and Hall-survey [44,45] (Table 1).

Table 1

PEDOT-systems for the Hall study covering state-of-the-art treatment strategies and conductivities.

System	treatment	impact	Anion	$\sigma_{300K}/ \text{S cm}^{-1}$	
1	PEDOT:PSS	10% DMSO	co-solvent additive	PSS^-	640
2	PEDOT:PSS*	5% DMSO	co-solvent additive	PSS^-	997
3	PEDOT:TfO	TfOH	solid-state, post-casting	TfO	1987

For the complementary temperature-dependent electrical conductivity $\sigma(T)$ and Hall voltage $V_H(T)$ we used 4-point probe and/or van der Pauw configurations between 300 K and 2 K (Fig. 2). As earlier reported we observed a transition regime between localization and delocalization (weak localization). The overlap was apparent at approximately $10 \text{ K} \pm 3 \text{ K}$, where the system is dominated either by temperature-activated Arrhenius-type transport (equation (1)) or by metal-like and rather *T*-independent transport (following Mott's theorem) [46]. We focussed the overlap regime at higher *T* and determine the activation energies E_A for each system from a $\log \sigma$ vs. T^{-1} plot (Table 2). The values reported here were in agreement with earlier findings. They correspond to the effective band width ($E_A \approx W_B$) of the quasi-band structure [16,46].

W_B can be used as estimate for the degree of disorder and the distribution between band and hopping carriers. The value also corresponds to the extent of a quasi-continuum i.e. the energy offset within the band between Fermi energy E_F and mobility edge E_C . (Fig. 2c and d).

$$\ln \frac{\sigma_T}{\sigma_{min}} = -\frac{E_C - E_F}{k_B} \frac{1}{T} \quad \text{when } W_B \cong E_C - E_F \quad (1)$$

Among the investigated systems, W_B was lowest in PEDOT:TfO at 0.76 meV (in agreement with the higher conductivities), while in PEDOT:PSS(*) it increases to 0.86 meV and 1.11 meV, respectively (Table 2). In a next step, we probed the probe the Hall voltage in parallel for all systems as function of temperature (Fig. 3). Therefore we patterned a PEDOT cloverleaf from a mastered substrate and process the polymer directly to a van der Pauw (vdP) specimen resulting in a symmetry factor close to unity. Across the edges we applied a 1 mA *dc*-current i_x constantly (note that all PEDOT-systems are electrically stable up to 10 mA under day-long high-current stress tests) (Fig. 3a). On top, a magnetic *ac*-field 0.625 T root mean square (RMS) amplitude (B_{ac}) was sinusoidally modulated at a frequency of 100 mHz to generate the *ac*-Hall voltage that was read out through a lock-in amplifier (Fig. 3b). The technique improves the signal-to-noise ratio and the noise limit of the setup through effective Faraday and misalignment compensation so that the Hall mobilities μ_{H1} of down to $10^{-3} \text{ cm}^2 \text{ V}^{-1} \text{ s}^{-1}$ can be measured (Fig. 3c).

For example, we present the PEDOT:PSS* system (1) at 32 K: A Hall

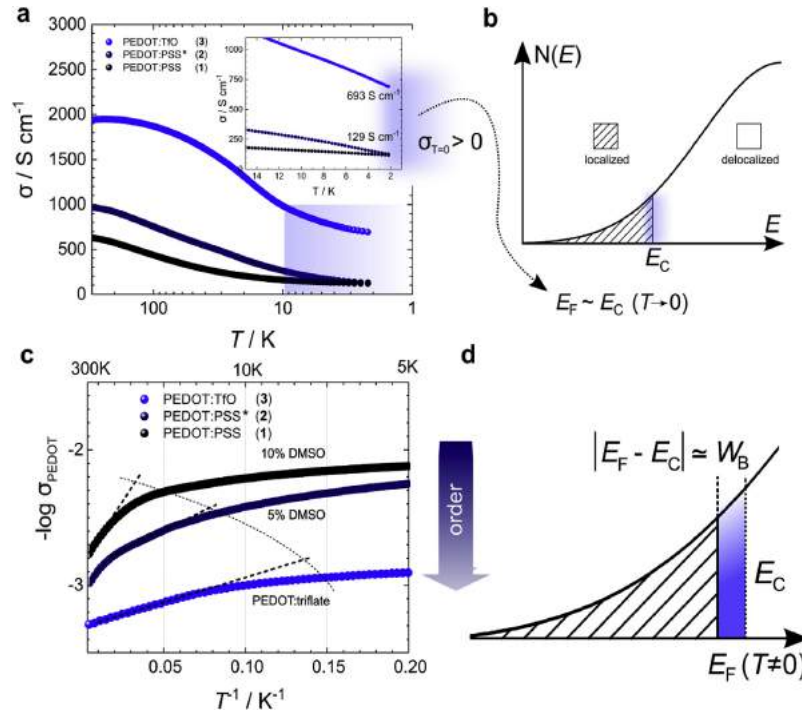


Fig. 2. Determination of band width W_B from $\sigma-T$ plots (a) Semilog $\sigma-T$ of various PEDOT-systems showing finite conductivity as T approaches 0 (inset: linear plot of $\sigma-T$ below 10K). (b) Schematic of the shallow transport regime at E_F close to E_C in PEDOT-systems. (c) Expanded plot for comparison: Note the slope (indicated as linear fits) at high- T are proportional to the band width W_B . (d) Schematic of band width $W_B \sim E_C - E_F$ in the vicinity of the metal-insulator transition regime (Anderson localization).

Table 2
Energies (band widths) as derived from $\log \sigma$ vs. T^{-1} plots (Fig. 2b).

System	slope/ K	W_B / meV	σ_{300K} / S cm $^{-1}$	σ_{2K} / S cm $^{-1}$
1 PEDOT:PSS	12.9	1.11	640	120
2 PEDOT:PSS*	10.0	0.86	997	130
3 PEDOT:TfO	8.9	0.76	1987	690

voltage as large as $1.3 \cdot 10^{-6}$ V was generated at 1 mA *dc*-current and at modulated magnetic field with maximum amplitude at 0.91 T at 100 mHz. The Hall voltages increases linearly with increasing i_x between 1 and 10 mA (Fig. 3a).

The *ac*-Hall measurement was performed across all temperatures between 300 K and 32 K. Below 32 K, the *ac*-modulation has not been accessible because of Eddy current heating of the substrate holder (Fig. 4). All samples showed a Hall voltage range between $0.3 \cdot 10^{-6}$ V up to $6.0 \cdot 10^{-6}$ V at 1 mA. The absolute resistance of the specimen was in the range between 200 and 20 Ω . The sample thickness corresponded to typical dimensions used in applications ranging between 30 nm and 60 nm. The *ac*-modulation included a statistical evaluation – we reported a standard deviation for V_H at 1% for 100 repetitions. The measurement time expands to about 1 h per point with 100 repetitions at 100 mHz frequency.

From the data we derived the Hall constants R_H and the product of the Hall constant and conductivity *i.e.* the measured mobility μ (Table 3). The Hall parameters are comparable only the thickness is different. The $R_H(T)$ shows an inverse profile as compared to that of $\sigma(T)$ (Fig. 4). This result reflects the ambiguity of the transport in

polymers depicting the overlap of metallic and non-metallic transport mechanisms and the contribution of thermal-activation at higher T s. Consequently the product $\sigma R_H(T)$ is constant and its magnitude correlates to the electrical performances of the PEDOT-systems with PEDOT:TfO showing the highest (see Table 4).

The observations on $R_H(T)$ were in agreement with the organic phase model through (topological and thermal) disorder in molecular systems. Direct consequence is the comparatively low V_H and, subsequently, low R_H values (situated here at 10^{-4} cm 3 C $^{-1}$, as compared to approximately 10^{+2} in p-Si, from *ac*-Hall demonstrated in the SI). The product $\sigma R_H(T)$ *i.e.* the measured mobilities *i.e.* σR_H are far below the intrinsic band mobility, as suggested by the electrical conductivity values and their corresponding metal-like low-temperature behaviour.

Obviously, there exists a strong discrepancy between the *band* mobility μ_{band} and *hopping* mobility $\mu_{hopping}$ in the polymers as result of probing conditions and disorder *i.e.* thermal effects, anisotropy and hole-hole interaction. We utilized now the organic phase model to estimate the band mobility μ . Therefore we used the ratio β between $\mu_{hopping}$ and μ_{bands} , as well as the factor γ as the distribution of delocalized carriers upon temperature with g as the degeneration factor and the activation energy E_A or band width W_B . In case of 3 dimensions g is equal to 6 (equation (2)). Such evaluations are also suggested in inorganic, disordered systems, where the μB product is significantly below unity (*e.g.* $1 \cdot 10^{-5}$ for the here studied PEDOTs at 0.625 T B_{ac} and measured μ around 0.1 and below) [47–49].

$$\mu \cdot B \ll 1 \quad \frac{\mu_{hopping}}{\mu_{band}} = \beta \ll 1 \quad \frac{n_{band}}{n_{total}} = 1 - g^{-1} \cdot e^{-\left(\frac{E_A}{kT}\right)} = \gamma \ll 1 \quad (2)$$

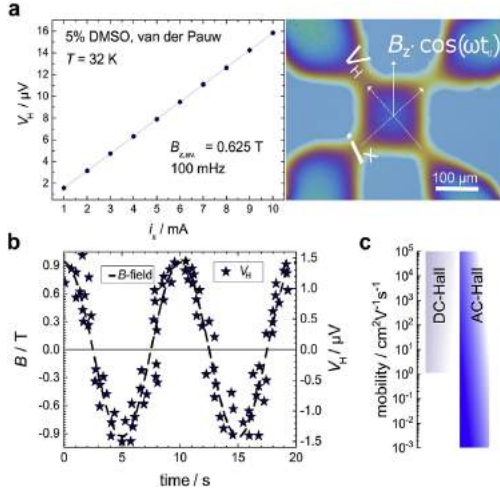


Fig. 3. ac-Hall detection (a) Average Hall-potential (i_x between 1 and 10 mA) of typical PEDOT:PSS (conductivity at 32 K is 500 S cm^{-1}) as derived from a simple van der Pauw geometry (picture). (b) 2 loops at 100 MHz of repeating magnetic ac-modulated Hall signal output (in μV) from sinusoidal applied magnetic field B . (c) Mobility expansion from ac-Hall diminishes misalignment potentials expanding the Hall mobility range to $10^{-3} \text{ cm}^2 \text{ V}^{-1} \text{ s}^{-1}$.

To compensate now the effect of Hall voltage screening, it was suggested by Li et al. [8] in their organic phase model that the band mobility μ_{band} can be estimated by inserting the correction factors β and γ : accordingly, only band carriers contribute to the Hall voltage, but they represent a minority in the Arrhenius regime above 10 K. We reconciled the disorder screening and the subsequent underestimation of the band mobility by assuming lower hopping than band mobility ($\beta < 1$) and, similarly, a low band contribution of the carriers (γ in the range of 10^{-4} , as calculated from equation (2)). This intermediate band contribution scenario led to a situation, where the band mobility was much higher than the measured Hall mobility μ in the weak B -field regime at moderate disorder, where the transverse electric fields E_y are low as compared to the longitudinal E_x (equation (3)).

$$\mu = \mu_{\text{band}} \cdot \frac{\gamma}{\gamma - \beta\gamma + \beta} \left(= \frac{E_y}{E_x B} \right) n_{\text{total}} = n_{\text{measured}} \cdot \frac{(\gamma - \gamma\beta + \beta)^2}{\gamma} \quad (3)$$

For our case of semimetallic polymers we employed the intermediate hopping contribution regime assuming a weak band-like

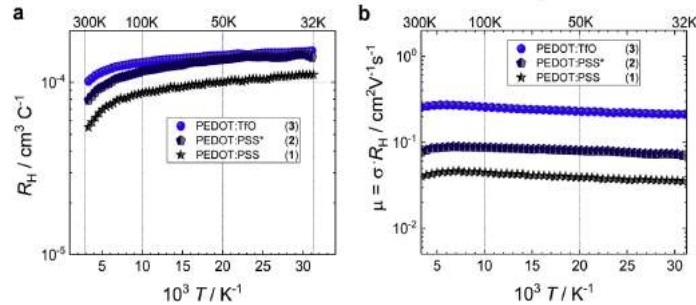


Fig. 4. (a) Experimental Hall-constant R_H vs. temperature reveals the quenched Hall voltage at the order of R_H at $10^{-4} \text{ cm}^3 \text{ C}^{-1}$ (i.e. the corresponding Hall voltage is 10^{-6} V). The R_H depends on the temperature reciprocal to the conductivity σ . (b) The measured mobility $\mu = \sigma R_H$ is thus constant.

Table 3

Hall parameters at room temperature (300 K).

System	$d_{\text{film}} / \text{nm}$	(ac-)B-field/T	i_x / A	$R_H / \text{cm}^3 \text{ C}^{-1}$
1 PEDOT:PSS	61	0.625	10^{-3}	$5.5 \cdot 10^{-5}$
2 PEDOT:PSS*	54	0.625	10^{-3}	$7.9 \cdot 10^{-5}$
3 PEDOT:TfO	30	0.625	10^{-3}	$1.0 \cdot 10^{-4}$

character and calculate $\gamma(T)$ using the band widths from the conductivity temperature profile ($W_B = E_A$) (equation (2)).

$$\gamma = (\gamma - \gamma\beta + \beta)^2 \quad \mu(T) = \mu_{\text{band}} \cdot \sqrt{\gamma(T)} \quad (4)$$

We use the re-formulated equation to derive β (equation (5)),

$$\beta^{-1} = 1 + \frac{1}{\sqrt{\gamma}} \quad (5)$$

and subsequently the corrected n_{total} and μ_{band} across the measured temperature regime (300–32 K). (Fig. 5). We show the organic phase model yields the volumetric carrier concentration n_{total} (Fig. 5a). The calculated μ_{band} shows the weak band-like temperature profile i.e. it decreases with temperature (Fig. 5b) and the band-character correlates with the magnitude of the conductivity i.e. most pronounced for PEDOT:TfO. We found that the organic phase model delivers reasonable values for the PEDOT-systems: The Hall voltage corresponds to a calculated n_{total} below the maximum doping ratio limited by the polymer's mass density, molar mass and maximum 1 dopant per monomers, $3.1 \cdot 10^{+21} \text{ cm}^{-3}$ maximum). The profile of $n_i(T)$ indicates that at low temperatures the doping ratios saturate at the maximum limit. Hence, the transport is ultimately approaching the band regime. This is in agreement with earlier results at low temperatures in semimetallic PEDOT:TfO [20]. In order to confirm the band mobility, we included an alternative measurement of the transport parameters by Terahertz (THz) spectroscopy for PEDOT:TfO. The results yield slightly higher mobilities ($3.1 \text{ cm}^2 \text{ V}^{-1} \text{ s}^{-1}$). The corresponding analysis and frequency-dependent conductivity is presented in the SI.

For PEDOT:TfO the maximum μ_c found is $3.7 \text{ cm}^2 \text{ V}^{-1} \text{ s}^{-1}$, whereas in PEDOT:PSS* μ_{band} are lower between 1.0 and $0.5 \text{ cm}^2 \text{ V}^{-1} \text{ s}^{-1}$, respectively. The temperature profiles for conductivity, mobility and carrier concentration suggest weak band contribution at higher temperatures, while at lower temperatures the band regime dominates. This follows the theory of weak localization i.e. there exists an overlap regimes between localized and delocalized transport and a transition regime around 10 K.

The magnitudes of μ_{band} are comparatively high in view of results on similar molecular semiconductors. Our results show that polymers possess a systematic degree of structural order. This had been reflected by their superior electrical performances and by our findings on the Hall-effect, which are in agreement with the literature discussing the

Table 4
Hall parameters at room temperature (300 K).

System		μ_{band} at 300 K/ $\text{cm}^2 \text{V}^{-1} \text{s}^{-1}$	n_{total} at 300 K/ cm^{-3}	μ_{band} at 32 K/ $\text{cm}^2 \text{V}^{-1} \text{s}^{-1}$	n_{total} at 32 K/ cm^{-3}
1	PEDOT:PSS	0.5	$8.0 \cdot 10^{+20}$	0.15	$3.1 \cdot 10^{+21}$
2	PEDOT:PSS*	1.0	$4.3 \cdot 10^{+20}$	0.33	$2.0 \cdot 10^{+21}$
3	PEDOT:TfO	3.7	$2.3 \cdot 10^{+20}$	1.03	$1.3 \cdot 10^{+21}$

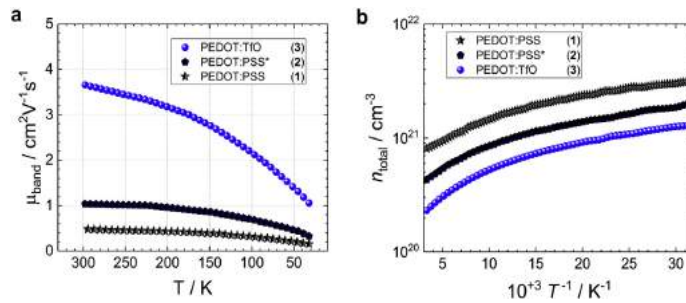


Fig. 5. Organic phase model applied to PEDOTs to evaluate the Hall-effect in the presence of dynamic disorder. (a) The band mobilities (μ_{band}) decrease with temperature, while in (b) the free carrier concentration increases at lower temperatures (less contribution from trapping, phonons).

extent of order in PEDOT-systems by electron coherence among the polymer chains [29].

3. Conclusion

The impact of disorder on the Hall-effect has frequently been discussed for organic semiconductors. Here, we explored the transport in semimetallic conducting polymers and apply an organic phase model described earlier. This regards the role of dynamic disorder on the experimentally observed Hall-voltage screening through strong hopping contribution. We observed a stable Hall voltage from semimetallic conducting polymers and we could utilize these experimental results to derive temperature-dependent band mobilities and carrier concentrations. The organic phase model yields comparatively high mobilities, in particular for the PEDOT:TfO system. This was in agreement with in parallel performed THz mobility characterization. We explained the magnitude of the charge carrier mobility by the electron coherence. Analogous conclusions have been reported in semimetallic polymers from magnetometric experiments. Our results can be adopted for related emerging and disordered semiconductors such as perovskites polymorphs or nanocrystalline solids and it shows a path to interpret the Hall-effect of conducting polymers.

4. Methods

4.1. *ac*-Hall specimen fabrication

To obtain the van der Pauw cloverleaf (Figs. 3a), 1×1 cm sapphire substrates were previously cleaned in water (and detergent), then rinsed thoroughly with distilled water and with isopropyl alcohol. After drying with nitrogen, the substrates were treated for 5 min in oxygen plasma. Using a shadow mask, we evaporated 50 nm of tetra-tetracontane (TTC, Sigma Aldrich) to define the four contact arms at the edge of the cloverleaf. Then the samples were exposed to an trichloro (1H,1H,2H,2H-perfluorooctyl)silane (FOS) rich atmosphere inside a Petri dish to cover the surface around the TTC layer (negative of the final structure). After few minutes, the samples were taken outside and TTC and excess fluoroalkylsilane was removed by washing with toluene and acetone to expose a FOS-free cloverleaf structure in the centre of the substrate. On these patterned substrates, different formulations of

PEDOT:PSS (PH1000, Heraeus Inc., stock solution specific addition of DMSO, 5–10 %_{volume}), were spun in two consecutive stages of 25 rounds per second (rps) (2s second ramp, 10s duration) and 100 rps (2s ramp, 10s duration) followed by thermal treatment in inert atmosphere at 120 °C for 10 min, resulting in layers with 50–70 nm thickness. The post-processing using TfOH is directly performed after spin-coating (exposure of with trifluoromethanesulfonic acid, Sigma Aldrich 97%, 1:1 molar in water, 10 min plus washing with water, repeating 3 times). To assure proper contacts, 4 supporting gold electrode arms (140 nm) were evaporated to touch the cloverleaf-edges at $3.6 \cdot 10^{-6}$ mbar at a rate of 0.1–0.3 nm s⁻¹.

4.2. *ac*-Hall measurements

For *ac*-Hall the as-patterned thin films are bonded to the electrical setup and transferred to the cryogenic magneto-system. The samples are then left overnight in He-atmosphere at 300 K for drying. After that, the specimens were characterized using resistivity and *ac*-Hall characterization (in a LakeShore Hall Measurement System 8400 and Quantum Design DynaCool PPMS). We applied temperature loops starting from 2 K and scanned up to 300 K for the resistivity. The *ac*-Hall technique could be applied from 32 K up to 300 K. The magnetic field is swept between 0 and 0.91 T (with a room mean square field B_{ac} of 0.625 T) at 100 mHz. This leads to a dc-voltage for the resistivity and an *ac*-voltage for the Hall signal. We apply consistently 1 mA dc-current across the sample specimen using the van der Pauw geometry. These measurements are repeated at higher current up to 10 mA (current stressing). We exclude degradation effect from local heating. The film thickness is determined by DekTak (Bruker) in the probing space area after the cryogenic measurement cycles.

TEM measurements are performed using a grid substrate mounted on the sapphire substrate to imitate identical surrounding as for the transport measurements. PEDOT-systems are then cast as described above. We denote in the present resolution, we did not find changes in the structure between PEDOT:PSS (10% DMSO treated) and PEDOT:PSS* (5% DMSO treated). Indeed we find changes in the structure between TfOH-treated and PEDOT:PSS*. All room temperature conductivity measurements and thickness measurements for the DMSO-treatment map have been recorded using a 4-probe setup for the conductivities and DekTak (Bruker) to measure the thickness values.

For the entire map, approximately 40 samples have been investigated.

4.3. Terahertz spectroscopy

Terahertz (THz) spectroscopy is a non-contact and non-destructive method that can locally follow carrier dynamics on timescales of pico- to nanoseconds. In THz spectroscopy the electric field is directly recorded and as such both the amplitude and phase are extracted. We measured a PEDOT:TfO film (thickness 262 nm) an insulating glass substrate and determined the complex-valued conductivity according to:

$$\sigma(\omega) = \left(\frac{1 + N_{\text{sub}}}{Z_0 d_{\text{film}}} \right) \left(\frac{E_{\text{sub}}(\omega)}{E_{\text{samp}}(\omega)} - 1 \right)$$

where N_{sub} is the complex refractive index of the substrate, Z_0 the free space impedance, d_{film} the thickness of the PEDOT:TfO, ω the radial frequency of the THz field and E_{sub} and E_{samp} the Fourier transforms of the THz electric field transmitted through the substrate and the sample, respectively [27].

The THz setup allowed us to estimate the average conductivity σ_{DC} ($\sigma_{\text{THz}} = 1582 \text{ S cm}^{-1}$ between 0.1 and 1.1 THz, value which given the high plasma frequency and scattering rate (estimated at $\omega_p = 3.99 \cdot 10^{15} \text{ Hz}$ and $\Gamma = 9.1 \cdot 10^{14} \text{ Hz}$, respectively) corresponds to the DC conductivity [28]). This leads to a mobility of $\mu_{\text{THz}} = 3.1 \text{ cm}^2 \text{ V}^{-1} \text{ s}^{-1}$.

Competing interest

The authors declare no competing interests.

Author contributions

P. S. designed and directed the study. P.S. contributed to all experiments. P.S. H.C. and L.N.L. designed the film growth process and carried out the experimental work and corresponding analytical measurements. Hall- and conductivity measurements were carried out by L.N.L. and P.S. S.V.F, H.C. and C.R. conducted the THz spectroscopy. P.S. and M.C.S. carried out the modelling and the relevant calculations. M.C.S., R.M. and P.S. analysed the data. P.S. wrote the manuscript. All authors commented on the paper.

Acknowledgements

P.S. and R.M. are grateful to OeAD Austria (WTZ, IN10/2015) for financial support. P.S. acknowledges the financial support of the Austrian Science Foundation (FWF I3822-N37, "Nachhaltige Katalyse"). The authors thank Dominik Farka and N. Serdar Sariciftci for fruitful discussions. This project was supported by the strategic economic- and research program "Innovative Upper Austria 2020" of the province of Upper Austria.

Appendix A. Supplementary data

Supplementary data to this article can be found online at <https://doi.org/10.1016/j.orgel.2018.12.001>.

References

- [1] D. Emin, The sign of the Hall effect in hopping conduction, *Philos. Mag. A* 35 (1977) 1189–1198, <https://doi.org/10.1080/14786437708232944>.
- [2] J.W. Orton, M.J. Powell, The Hall effect in polycrystalline and powdered semiconductors, *Rep. Prog. Phys.* 43 (1980) 1263 <http://stacks.iop.org/0034-4885/43/i=11/a=001>.
- [3] L. Friedman, N.F. Mott, The Hall effect near the metal-insulator transition, *J. Non-Cryst. Solids* 7 (1972) 103–108, [https://doi.org/10.1016/0022-3093\(72\)90021-X](https://doi.org/10.1016/0022-3093(72)90021-X).
- [4] L. Friedman, Hall conductivity of amorphous semiconductors in the random phase model, *J. Non-Cryst. Solids* 6 (1971) 329–341, [https://doi.org/10.1016/0022-3093\(71\)90024-X](https://doi.org/10.1016/0022-3093(71)90024-X).
- [5] R. Kubo, Statistical-mechanical theory of irreversible processes. I. General theory and simple applications to magnetic and conduction problems, *J. Phys. Soc. Japan* 12 (1957) 570–586, <https://doi.org/10.1143/JPSJ.12.570>.
- [6] B. Lee, Y. Chen, D. Fu, H.T. Yi, K. Czelen, H. Najafov, V. Podzorov, Trap healing and ultralow-noise Hall effect at the surface of organic semiconductors, *Nat. Mater.* 12 (2013) 1125–1129, <https://doi.org/10.1038/nmat3781>.
- [7] Y. Chen, H.T. Yi, V. Podzorov, High-resolution ac measurements of the Hall effect in organic field-effect transistors, *Phys. Rev. Appl.* 5 (2016) 034008, <https://doi.org/10.1103/PhysRevApplied.5.034008>.
- [8] H.T. Yi, Y.N. Gartstein, V. Podzorov, Charge Carrier coherence and Hall effect in organic semiconductors, *Sci. Rep.* 6 (2016) 23650, <https://doi.org/10.1038/srep23650>.
- [9] R. Fujimoto, S. Watanabe, Y. Yamashita, J. Tsurumi, H. Matsui, T. Kushida, C. Mitsui, H.T. Yi, V. Podzorov, J. Takeya, Control of molecular doping in conjugated polymers by thermal annealing, *Org. Electron.* 47 (2017) 139–146, <https://doi.org/10.1016/j.orgel.2017.05.019>.
- [10] J. Takeya, K. Tsukagoshi, Y. Aoyagi, T. Takenobu, Y. Iwasa, Hall effect of quasi-hole gas in organic single-crystal transistors, *Jpn. J. Appl. Phys.* 44 (2005) L1393–L1396, <https://doi.org/10.1143/JJAP.44.L1393>.
- [11] N. Karl, Charge Carrier transport in organic semiconductors, *Synth. Met.* 133–134 (2003) 649–657, [https://doi.org/10.1016/S0379-6779\(02\)00398-3](https://doi.org/10.1016/S0379-6779(02)00398-3).
- [12] K. Imaeda, Y. Yamashita, Y. Li, T. Mori, H. Inokuchi, M. Sano, Hall-effect observation in the new organic semiconductor bis(1,2,5-thiadiazolo)-p-quinobis(1,3-dithiolo)(BTQBT), *J. Mater. Chem.* 2 (1992) 115, <https://doi.org/10.1039/jm9920200115>.
- [13] J. Takeya, J. Kato, K. Hara, M. Yamagishi, R. Hirahara, K. Yamada, Y. Nakazawa, S. Ikehata, K. Tsukagoshi, Y. Aoyagi, T. Takenobu, Y. Iwasa, In-Crystal and surface charge transport of electric-field-induced carriers in organic single-crystal semiconductors, *Phys. Rev. Lett.* 98 (2007) 196804, <https://doi.org/10.1103/PhysRevLett.98.196804>.
- [14] J.-F. Chang, T. Sakanoue, Y. Olivier, T. Uemura, M.-B. Dufourg-Madec, S.G. Yeates, J. Cornil, J. Takeya, A. Troisi, H. Sirringhaus, Hall-effect measurements probing the degree of charge-Carrier delocalization in solution-processed crystalline molecular semiconductors, *Phys. Rev. Lett.* 107 (2011) 066601, <https://doi.org/10.1103/PhysRevLett.107.066601>.
- [15] V. Podzorov, E. Menard, J.A. Rogers, M.E. Gershenson, Hall effect in the accumulation layers on the surface of organic semiconductors, *Phys. Rev. Lett.* 95 (2005) 226601, <https://doi.org/10.1103/PhysRevLett.95.226601>.
- [16] N.F. Mott, *Metal-Insulator Transitions*, Taylor & Francis Ltd, 1974.
- [17] C. Cobet, J. Gasiorowski, D. Farka, P. Stadler, Polarons in conjugated polymers, in: K.-J. Hinrichs, Eichhorn Karsten (Eds.), *Ellipsom. Funct. Org. Surfaces Film*, 2018, pp. 355–387, https://doi.org/10.1007/978-3-319-75895-4_16.
- [18] F. Dominik, A.O.F. Jones, R. Menon, N.S. Sariciftci, P. Stadler, Metallic conductivity beyond the Mott minimum in PEDOT: sulphate at low temperatures, *Synth. Met.* 240 (2018) 59–66, <https://doi.org/10.1016/j.synthmet.2018.03.015>.
- [19] D. Farka, H. Coskun, P. Bauer, D. Roth, B. Bruckner, P. Klapetek, N.S. Sariciftci, P. Stadler, Increase in electron scattering length in PEDOT:PSS by a triflic acid post-processing, *Monatshfte Für Chemie - Chem. Mon.* 148 (2017) 871–877, <https://doi.org/10.1007/s00706-017-1973-1>.
- [20] D. Farka, H. Coskun, J. Gasiorowski, C. Cobet, K. Hingerl, L.M. Uiberlacker, S. Hild, T. Greunz, D. Stifter, N.S. Sariciftci, R. Menon, W. Schoefberger, C.C. Mardare, A.W. Hassel, C. Schwarzingler, M.C. Scharber, P. Stadler, Anderson-localization and the mott-loffte-regel limit in glassy-metallic PEDOT, *Adv. Electron. Mater.* (2017) 1700050, <https://doi.org/10.1002/aeml.201700050>.
- [21] P. Stadler, D. Farka, H. Coskun, E.D. Glowacki, C. Yumusak, L.M. Uiberlacker, S. Hild, L.N. Leonat, M.C. Scharber, P. Klapetek, R. Menon, N.S. Sariciftci, Local order drives the metallic state in PEDOT:PSS, *J. Mater. Chem. C* 4 (2016) 6982–6987, <https://doi.org/10.1039/C6TC02129H>.
- [22] S.D. Kang, G.J. Snyder, Charge-transport model for conducting polymers, *Nat. Mater.* 16 (2017) 252–257, <https://doi.org/10.1038/nmat4784>.
- [23] A. Hamidi-Sakr, L. Biniak, J.-L. Bantignies, D. Maurin, L. Herrmann, N. Leclere, P. Lévêque, V. Vijayakumar, N. Zimmermann, M. Brinkmann, A versatile method to fabricate highly in-plane aligned conducting polymer films with anisotropic charge transport and thermoelectric properties: the key role of alkyl side chain layers on the doping mechanism, *Adv. Funct. Mater.* 27 (2017) 1700173, <https://doi.org/10.1002/adfm.201700173>.
- [24] M.N. Gueye, A. Carella, N. Massonnet, E. Yvenou, S. Brenet, J. Faure-Vincent, S. Pouget, F. Rieutord, H. Okuno, A. Benayad, R. Demadrille, J.-P. Simonato, Structure and dopant engineering in PEDOT thin films: practical tools for a dramatic conductivity enhancement, *Chem. Mater.* 28 (2016) 3462–3468, <https://doi.org/10.1021/acs.chemmater.6b01035>.
- [25] J. Rivnay, S. Inal, B.A. Collins, M. Sessolo, E. Stavrinidou, X. Strakosac, C. Tassone, D.M. Delongchamp, G.G. Malliaras, Structural control of mixed ionic and electronic transport in conducting polymers, *Nat. Commun.* 7 (2016) 11287, <https://doi.org/10.1038/ncomms11287>.
- [26] B.J. Worfolk, S.C. Andrews, S. Park, J. Reinspach, N. Liu, M.F. Toney, S.C.B. Mannsfeld, Z. Bao, Ultrahigh electrical conductivity in solution-sheared polymeric transparent films, *Proc. Natl. Acad. Sci. Unit. States Am.* 112 (2015) 14138–14143, <https://doi.org/10.1073/pnas.1509581112>.
- [27] B.G. Alberding, P.A. DeSario, C.R. So, A.D. Dunkelberger, D.R. Rolison, J.C. Owrutsky, E.J. Heilwell, Static and time-resolved terahertz measurements of photoconductivity in solution-deposited ruthenium dioxide nanofilms, *J. Phys. Chem. C* 121 (2017) 4037–4044, <https://doi.org/10.1021/acs.jpcc.6b12382>.
- [28] R. Ulbricht, E. Hendry, J. Shan, T.F. Heinz, M. Bonn, Carrier dynamics in semiconductors studied with time-resolved terahertz spectroscopy, *Rev. Mod. Phys.* 83

- (2011) 543–586, <https://doi.org/10.1103/RevModPhys.83.543>.
- [29] K. Kang, S. Watanabe, K. Broch, A. Sepe, A. Brown, I. Nasrallah, M. Nikolka, Z. Fei, M. Heeney, D. Matsumoto, K. Marumoto, H. Tanaka, S. Kuroda, H. Sirringhaus, 2D coherent charge transport in highly ordered conducting polymers doped by solid state diffusion, *Nat. Mater.* 15 (2016) 896–902, <https://doi.org/10.1038/nmat4634>.
- [30] T.-R. Chou, S.-H. Chen, Y.-T. Chiang, Y.-T. Lin, C.-Y. Chao, Highly conductive PEDOT:PSS films by post-treatment with dimethyl sulfoxide for ITO-free liquid crystal display, *J. Mater. Chem. C* 3 (2015) 3760–3766, <https://doi.org/10.1039/C5TC00276A>.
- [31] A. Ugur, F. Katmis, M. Li, L. Wu, Y. Zhu, K.K. Varanasi, K.K. Gleason, Low-Dimensional conduction mechanisms in highly conductive and transparent conjugated polymers, *Adv. Mater.* 27 (2015) 4604–4610, <https://doi.org/10.1002/adma.201502340>.
- [32] O.J. Sandberg, M. Nyman, S. Dahlström, S. Sandén, B. Törngren, J.-H. Smått, R. Österbacka, On the validity of MIS-CELV for mobility determination in organic thin-film devices, *Appl. Phys. Lett.* 110 (2017) 153504, <https://doi.org/10.1063/1.4980101>.
- [33] O.J. Sandberg, Effect of the depletion layer capacitance on the mobility determination using transient current extraction of doping-induced charge carriers, *J. Photon. Energy* 8 (2018) 1, <https://doi.org/10.1117/1.JPE.8.032208>.
- [34] M. Nyman, O.J. Sandberg, S. Dahlström, D. Spoltore, C. Körner, Y. Zhang, S. Barlow, S.R. Marder, K. Leo, K. Vandewal, R. Österbacka, Doping-induced carrier profiles in organic semiconductors determined from capacitive extraction-current transients, *Sci. Rep.* 7 (2017) 5397, <https://doi.org/10.1038/s41598-017-05499-3>.
- [35] Y. Du, X. Cui, L. Li, H. Tian, W.-X. Yu, Z.-X. Zhou, Dielectric properties of DMSO-doped-PEDOT:PSS at THz frequencies, *Phys. Status Solidi* 255 (2018) 1700547, <https://doi.org/10.1002/psb.201700547>.
- [36] M. Yamashita, C. Otani, H. Okuzaki, M. Shimizu, Nondestructive measurement of Carrier mobility in conductive polymer PEDOT:PSS using Terahertz and infrared spectroscopy, XXXth URSI Gen. Assem. Sci. Symp. IEEE, 2011, pp. 1–4, <https://doi.org/10.1109/URSIGASS.2011.6050616> 2011.
- [37] G. Bergmann, Weak localization in thin films, *Phys. Rep.* 107 (1984) 1–58, [https://doi.org/10.1016/0370-1573\(84\)90103-0](https://doi.org/10.1016/0370-1573(84)90103-0).
- [38] P.A. Lee, T.V. Ramakrishnan, Disordered electronic systems, *Rev. Mod. Phys.* 57 (1985) 287–337, <https://doi.org/10.1103/RevModPhys.57.287>.
- [39] V. D'Innocenzo, A. Luzzio, H. Abdalla, S. Fabiano, M.A. Loi, D. Natali, A. Petrozza, M. Kemerink, M. Caironi, Two-dimensional charge transport in molecularly ordered polymer field-effect transistors, *J. Mater. Chem. C* 4 (2016) 11135–11142, <https://doi.org/10.1039/C6TC03897B>.
- [40] Y. Chen, H.T. Yi, X. Wu, R. Haroldson, Y.N. Gartstein, Y.I. Rodionov, K.S. Tikhonov, A. Zakhidov, X.-Y. Zhu, V. Podzorov, Extended Carrier lifetimes and diffusion in hybrid perovskites revealed by Hall effect and photoconductivity measurements, *Nat. Commun.* 7 (2016) 12253, <https://doi.org/10.1038/ncomms12253>.
- [41] E. Helgren, K. Penney, M. Diefenbach, M. Longnickel, M. Wainwright, E. Walker, S. Al-Azzawi, H. Erhahon, J. Singley, Electrostatics of the conducting polymer polyaniline on the insulating side of the metal-insulator transition, *Phys. Rev. B* 95 (2017) 125202, <https://doi.org/10.1103/PhysRevB.95.125202>.
- [42] E. Jin Bae, Y. Hun Kang, K.-S. Jang, S. Yun Cho, Enhancement of thermoelectric properties of PEDOT:PSS and tellurium-PEDOT:PSS hybrid composites by simple chemical treatment, *Sci. Rep.* 6 (2016) 18805, <https://doi.org/10.1038/srep18805>.
- [43] A. Malti, J. Edberg, H. Granberg, Z.U. Khan, J.W. Andreasen, X. Liu, D. Zhao, H. Zhang, Y. Yao, J.W. Brill, I. Engquist, M. Fahlman, L. Wågberg, X. Crispin, M. Berggren, An organic mixed ion-electron conductor for power electronics, *Adv. Sci.* 3 (2016), <https://doi.org/10.1002/advs.201500305> n/a-n/a.
- [44] N. Massommet, A. Carella, A. de Geyer, J. Faure-Vincent, J.-P. Simonato, Metallic behaviour of acid doped highly conductive polymers, *Chem. Sci.* 6 (2015) 412–417, <https://doi.org/10.1039/C4SC02463J>.
- [45] N. Kim, S. Kee, S.H. Lee, B.H. Lee, Y.H. Kahng, Y.-R. Jo, B.-J. Kim, K. Lee, Highly conductive PEDOT:PSS nanofibrils induced by solution-processed crystallization, *Adv. Mater.* 26 (2014) 2268–2272, <https://doi.org/10.1002/adma.201304611>.
- [46] N.F. Mott, Conduction in non-crystalline systems IX. the minimum metallic conductivity, *Philos. Mag. A* 26 (1972) 1015–1026, <https://doi.org/10.1080/14786437208226973>.
- [47] W.C. Mitchell, P.M. Hemenger, Temperature dependence of the Hall factor and the conductivity mobility in p-type silicon, *J. Appl. Phys.* 53 (1982) 6880–6884, <https://doi.org/10.1063/1.330028>.
- [48] F. Szmulowicz, Calculation of the mobility and the Hall factor for doped p-type silicon, *Phys. Rev. B* 34 (1986) 4031–4047, <https://doi.org/10.1103/PhysRevB.34.4031>.
- [49] J.F. Lin, S.S. Li, L.C. Linares, K.W. Teng, Theoretical analysis of hall factor and hall mobility in p-type silicon, *Solid State Electron.* 24 (1981) 827–833, [https://doi.org/10.1016/0038-1101\(81\)90098-8](https://doi.org/10.1016/0038-1101(81)90098-8).

4.6 Manuscript 6

ENGINEERING

Biofunctionalized conductive polymers enable efficient CO₂ electroreduction

Halime Coskun,¹ Abdalaziz Aljabour,^{1,2} Phil De Luna,³ Dominik Farka,¹ Theresia Greunz,⁴ David Stifter,⁴ Mahmut Kus,² Xueli Zheng,⁵ Min Liu,⁵ Achim W. Hassel,⁶ Wolfgang Schöfberger,⁷ Edward H. Sargent,⁵ Niyazi Serdar Sariciftci,¹ Philipp Stadler^{1*}

Selective electrocatalysts are urgently needed for carbon dioxide (CO₂) reduction to replace fossil fuels with renewable fuels, thereby closing the carbon cycle. To date, noble metals have achieved the best performance in energy yield and faradaic efficiency and have recently reached impressive electrical-to-chemical power conversion efficiencies. However, the scarcity of precious metals makes the search for scalable, metal-free, CO₂ reduction reaction (CO₂RR) catalysts all the more important. We report an all-organic, that is, metal-free, electrocatalyst that achieves impressive performance comparable to that of best-in-class Ag electrocatalysts. We hypothesized that polydopamine—a conjugated polymer whose structure incorporates hydrogen-bonded motifs found in enzymes—could offer the combination of efficient electrical conduction, together with rendered active catalytic sites, and potentially thereby enable CO₂RR. Only by developing a vapor-phase polymerization of polydopamine were we able to combine the needed excellent conductivity with thin film–based processing. We achieve catalytic performance with geometric current densities of 18 mA cm⁻² at 0.21 V overpotential (–0.86 V versus normal hydrogen electrode) for the electrosynthesis of C₁ species (carbon monoxide and formate) with continuous 16-hour operation at >80% faradaic efficiency. Our catalyst exhibits lower overpotentials than state-of-the-art formate-selective metal electrocatalysts (for example, 0.5 V for Ag at 18 mA cm⁻¹). The results confirm the value of exploiting hydrogen-bonded sequences as effective catalytic centers for renewable and cost-efficient industrial CO₂RR applications.

INTRODUCTION

Electrocatalysis of CO₂ has become crucial in generating renewable carbon feedstock and synthetic fuels (1–15). Reductive recycling is essential not only to mitigate anthropogenic climate change but also to use CO₂ as a future nonfossil carbon feedstock. The immense expected throughput of emissions (greater than 30 gigatons of emitted CO₂ per annum) requires superior, inexpensive materials that catalyze the reduction at high energy efficiency. Reducing overpotentials is therefore one important aim to justify the use of renewable energy resources for the energy-intensive production of CO and related hydrocarbons.

Various (noble) metal electrocatalysts are currently available for synthesizing fuels and carbon feedstocks at acceptable energy yields (2, 5–7, 9, 11, 16–19). However, in view of the massive scale-up necessary for industrial use, alternative materials with comparable performance that do not require rare elements with high socioecological impact are urgently needed. One way to eliminate metals that are attracting growing interest is to use renewable and easily recyclable organic electrocatalysts (13, 20–25). This renewable approach is inspired by nature, particularly on the activity of enzymes that catalyze CO₂ reduction at high faradaic and energy efficiency.

Increasingly, principles from enzymology are being incorporated into the design of organic electrocatalysts (21–23). For example, enzyme-related motifs are highly present in polydopamine (PDA), a bio-derived

system based on eumelanin pigments (26). PDA's functional richness (1:1 ratio of hydrogen bond to monomer unit) makes it a catalytic system that offers a significant density of potential hydrogen-bonded active sites (27–40). The catalytic motifs consist of amines and hydroxyl-carbonyl associated via hydrogen bonds (Fig. 1) (41). Within immediate proximity, they are coordinated in inter- or intramolecular conformation and feature a latent nucleophilic sequence that facilitates CO₂ binding.

The role of hydrogen bonding and its nucleophilic character has previously been discussed for electrosynthetic applications, specifically in the context of the nonpolymeric hydrogen-bonded pigments quinacridone and epindolidione (23, 42). They were used in catalytic processes, but at high overpotentials and/or with limited product yields because hydrogen-bonded pigments have an intrinsically low capability for electron transport (23, 42). Consequently, the functional sites dangle and provide poor electrical connection to the carrier electrode showing poor catalytic reactivity.

Here, we first used density functional theory (DFT) to investigate the interactions between CO₂ and the proposed hydrogen-bonded catalytic active sites. We found interactions between hydrogen-bonded sites with latent nucleophilicity and CO₂ were energetically favored.

Inspired by these initial calculations hinting at favorable CO₂ energetics, we sought to overcome the severe limitations of poor electrical transport. We found that conductive PDA is an ideal candidate for developing an effective organic electrocatalytic system when it covers a nonmetallic carrier electrode (carbon fibers): The conductive chain on the inside serves as a wire to supply electrons to the peripheral active sites (Fig. 2). Electrons travel across the entire system as PDA brings together the carrier electrode, conductive body, and catalytic functional groups, which makes it a powerful electrocatalyst.

To achieve conductivity, we established charge doping in the conjugated carrier, which is essential for conductive-conjugated wires that use the effective surface activity. Note that direct doping is hampered

Copyright © 2017
The Authors, some
rights reserved;
exclusive licensee
American Association
for the Advancement
of Science. No claim to
original U.S. Government
Works. Distributed
under a Creative
Commons Attribution
NonCommercial
License 4.0 (CC BY-NC).

Downloaded from <http://advances.sciencemag.org/> on January 22, 2018

¹Linz Institute for Organic Solar Cells, Institute of Physical Chemistry, Johannes Kepler University Linz, Altenberger Strasse 69, 4040 Linz, Austria. ²Department of Chemical Engineering, Selçuk University, 42075 Konya, Turkey. ³Department of Materials Science and Engineering, University of Toronto, 10 King's College Road, Toronto, Ontario M5S 3G4, Canada. ⁴Center for Surface and Nanoanalytics, Johannes Kepler University Linz, 4040 Linz, Austria. ⁵Edward S. Rogers Sr. Department of Electrical and Computer Engineering, University of Toronto, Toronto, Ontario M5S 3G4, Canada. ⁶Christian Doppler Laboratory for Combinatorial Oxide Chemistry (COMBOX) at Institute for Chemical Technology of Inorganic Materials, Johannes Kepler University Linz, 4040 Linz, Austria. ⁷Institute of Organic Chemistry, Johannes Kepler University Linz, 4040 Linz, Austria.

*Corresponding author. Email: philipp.stadler@jku.at

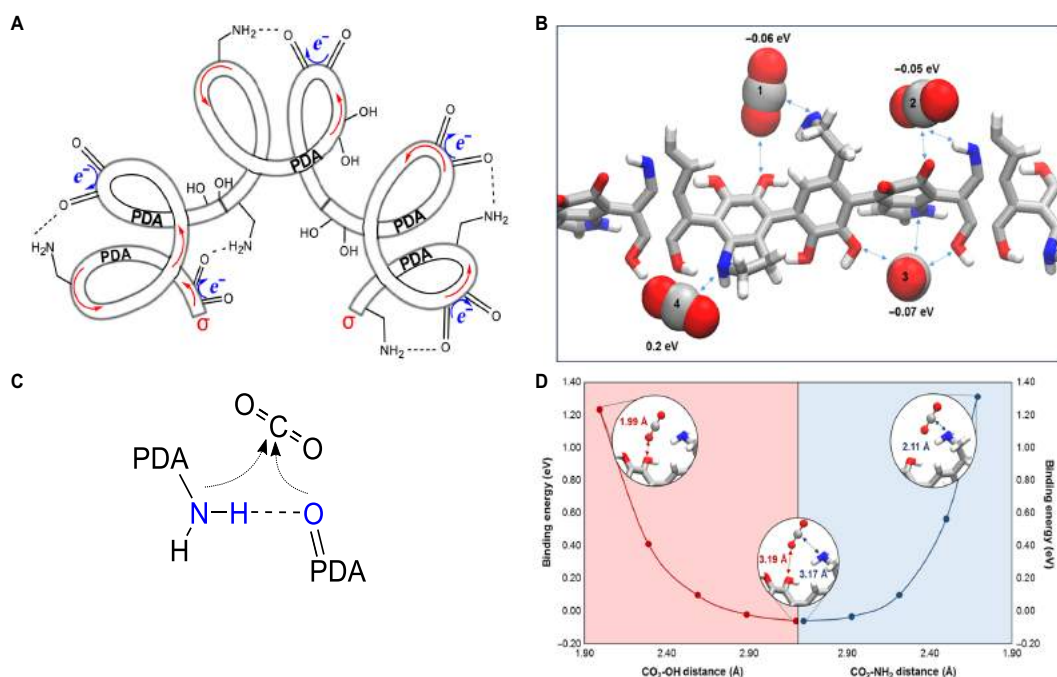


Fig. 1. Hydrogen bonds as catalytic motifs for CO₂ reduction. (A) PDA electrocatalytic wires consisting of a conjugated-conductive body with functional groups on a carbon-based carrier electrode. (B to D) The functional groups drive the selective reduction of CO₂, (B) BEs at this site (DFT calculation) for CO₂, (C) two-spot delocalized amine-carbonyl hydrogen-bonded catalytic center on PDA, and (D) BEs shown as functions of the distances between nitrogen and CO₂ (1.99 Å) and oxygen and CO₂ (2.11 Å), indicating the most favorable energy-steric conformation.

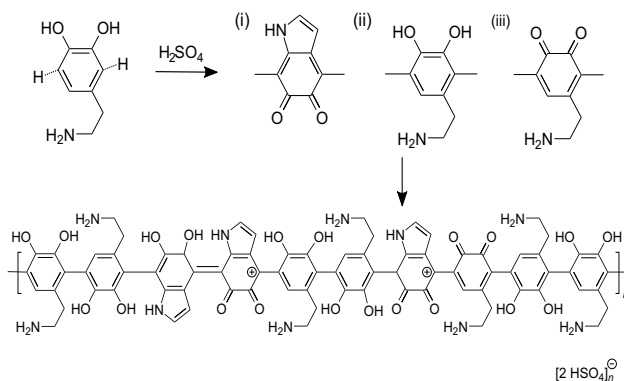


Fig. 2. Synthesis of conductive-catalytic PDA. Reaction of dopamine to conductive PDA by contact with sulfuric acid as oxidant during vapor-phase polymerization involves building blocks such as (i) condensed and oxidized diketoinole, (ii) dopamine, and (iii) oxidized dopamine, yielding the final product with periodically repeating units of conductive PDA.

because hydrogen-bonded frameworks show high inertness (43). To realize this, we introduce a more promising path toward creating conductive bodies: oxidative chemical vapor deposition (oCVD). This method integrates charge doping into the synthesis (polymerization and doping reaction) and creates persistent conductive-conjugated materials; this approach has emerged in the context of established con-

ductive polymers such as PEDOT [poly(3,4-ethylenedioxythiophene)] to provide metal-like conductivities (44, 45). We used the same concept to generate, for the first time, conductive PDA and yielded conductivities of 0.43 S cm⁻¹ without compromising catalysis.

Furthermore, the vapor-phase technique used facilitates ease of deposition and effective infiltration of large-surface, sponge-type carbon felt (CF).

This enabled us to demonstrate metal-free electrocatalysis of CO₂ to CO and formate at low overpotentials (210 mV) on par with best-in-class metal-based or transition metal dichalcogenide-based electrocatalysts (3, 4, 4–7, 11, 46). Remarkably, our cathodes exhibited no notable degradation after 16 hours of use.

In particular, the low overpotential paired with significant current densities (approximately 1.4 mA cm⁻² for CO and 16.9 mA cm⁻² for formate) and significant turnover demonstrates the power of conductive PDA as a renewable electrocatalyst (the formate turnover frequency is 1.23 hour⁻¹). An investigation of the mechanism responsible for this effectiveness by in situ spectroscopy showed that the hydrogen-bonded sites are ideal for catalysis. Their unexpectedly high performance demonstrates an untapped potential for replacing expensive metals in electrocatalytic applications in a fully renewable scenario.

RESULTS AND DISCUSSION

We began by using DFT to calculate the binding energies (BEs) for hydrogen-bonded sites to CO₂ on PDA periodic structures. We found three favored CO₂ positions (negative BEs between -0.05 and -0.07 eV) proximate to the amine hydroxyl-carbonyl proposed catalytic sites (Fig. 1B) (29). The actual CO₂ distance between nitrogen and oxygen sites varies with local optimum BEs found at 1.99 Å for CO₂-hydroxyl-carbonyl and 2.11 Å for CO₂-amine slightly favoring the former (Fig. 1C). We investigated this initial finding—CO₂ nucleation over carbonyl—by in situ spectral investigations as mentioned later.

Motivated by initial calculations on PDA, we developed a novel conductive synthesis. Conventionally, PDA is derived from aqueous dopamine solutions using oxidative polymerization with ambient O₂ as a reagent. The result is a complex organic system—depending on the exact conditions under which PDA is grown, different structural varieties have been reported (27–30). We transferred the entire established standard synthesis to the gas phase and found that sulfuric acid offers sufficient oxidation power to improve polymerization and doping so that an electrically conducting hydrogen-bonded system can be produced by oCVD (Fig. 2). The resulting polymer forms a polyparaphenylene (PPP) core with periodically repeating patterns of functional groups. As shown earlier, the functionalization is based on variable moieties. We found evidence of (i) indole (condensed secondary amine in an aromatic system with oxidized keto functions), (ii) dopamine, and, in the greatest quantity, (iii) oxidized dopamine (carbonyl function). These dominated other intermediates, which are compounds thereof. The pre-

cise nature of the repeating unit in the polymer was identified by detailed spectral investigations (figs. S12 to S16).

Structural investigations revealed characteristic spectral fingerprints indicative of free charge carriers in the PPP core (Fig. 3A). These are signature infrared-activated vibrations originating from the strong electron-phonon coupling due to doping-induced distortions (47, 48). We also synthesized nonconductive PDA, the spectrum of which lacked these kinds of features. Conductive PDA thin films (typically with thicknesses between 0.5 and 1 μm) exhibit an average (electrical) dc conductivity of 0.43 ± 0.1 S cm⁻¹ (Fig. 3B). Additionally, we found distinctive carbonyl oscillations. These spectral features confirm that vapor-based synthesis particularly favors type (iii) moieties (that is, carbonyl over hydroxyl), which play a crucial role in electrocatalysis. We note that the DFT-calculated BEs of CO₂ in between the amine and carbonyl groups were favorable at -0.05 eV.

Initial experiments in electrocatalysis of conductive PDA thin films showed significant dependence of the current on the CO₂ concentration within the electrochemical window of reversibility. We examined the electrochemical parameters thoroughly by defining the applicable window of electrochemical potential [0 to -1800 mV versus normal hydrogen electrode (NHE)] using acetonitrile-water solution [1 volume % water, saturated with N₂ and CO₂ (0.27 M)] (fig. S1).

These results motivated us to demonstrate more effective CO₂ reduction reaction (CO₂RR) by improving the geometric configuration (Fig. 4). To this end, we modified the electrochemical setup and used CF networks as supporting carrier electrodes because they offer a large surface area (of up to 22,000 m⁻¹) and have negligible catalytic activity toward CO₂. Vapor deposition enabled us to effectively infiltrate the felt with conductive PDA to generate a homogeneously covered network for maximum catalytic activity. The corresponding cyclic voltammograms and chronoamperometric scans of the working electrode (WE) as generated show the full performance of our electrocatalyst (Fig. 4A). We observed reductive currents of up to 110 mA cm⁻² at -1560 mV versus NHE in the presence of CO₂. Insights into the fibrous structure were gained by high-resolution (HR) scanning electron microscopy (SEM) before and after synthesis for 8 hours (Fig. 4B). SEM images reveal a structural roughening of the PDA surface after electrosynthesis. For chronoamperometry, we used an operating potential of -860 mV versus NHE, where we find the best compromise in terms of faradaic efficiency, current density, and overpotential. We performed experimental runs for 16 hours with frequent product cross-checks in parallel (cathode space only). We found H₂, CO, and formate as reaction products. Over

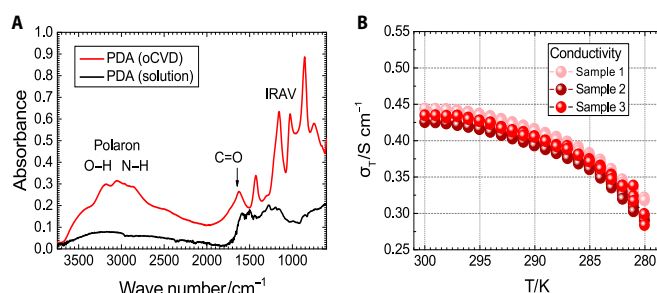


Fig. 3. Fingerprints of free charge carriers in conductive PDA. (A) Mid-infrared spectra of nonconductive PDA and conductive PDA, showing fingerprint spectral features for free-carrier generation in the conjugated system, confirmed in particular by signature infrared-activated vibrations (IRAVs). Note the strong carbonyl oscillation, which indicates dominant oxidation of the original hydroxyl groups. (B) The dc electrical conductivity (versus T) was as high as 0.43 S cm⁻¹ at 300 K in conductive PDA.

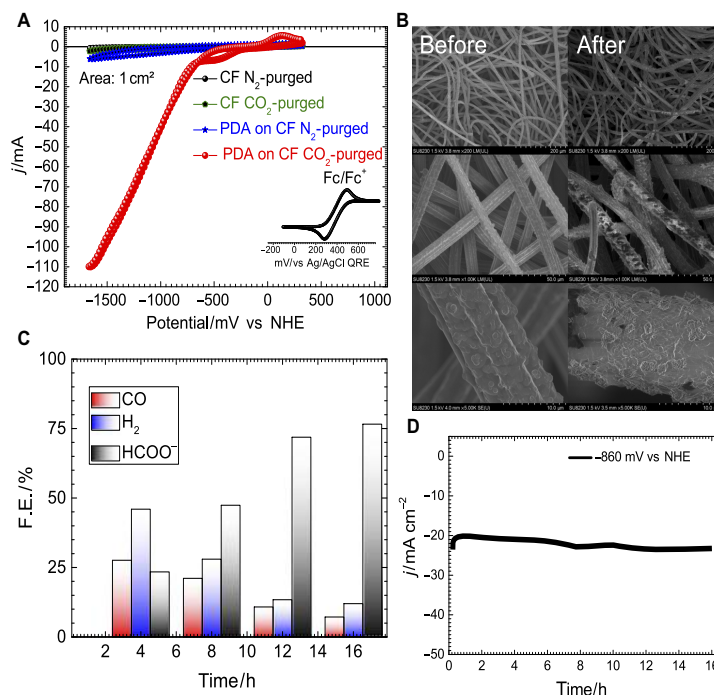


Fig. 4. PDA on CF for the electrocatalysis of CO₂. (A) Cyclic voltammogram of conductive PDA on a CF electrode (area, 1 cm²) including control scans. The catalytic activity shows a reductive current in acetonitrile-water purged with CO₂. Fc/Fc⁺, ferrocene/ferrocenium; QRE, quasi-reference electrode. (B) SEMs of conductive PDA on CF before and after 8-hour electrocatalysis. (C) Faradaic efficiencies (F.E.) of CO, H₂, and formate as functions of time. (D) Sixteen-hour chronoamperometric scans (potential, -860 mV versus NHE) showing current stability.

time, we observed a preference for formate, which we attribute to the accumulation of formate and subsequent changes in the local pH (semidiscontinuous electrochemical setting) (Fig. 4C). After 16 hours of operation, the total faradaic efficiency was almost quantitative (95.8%) with 12% for the hydrogen evolution reaction and 83.8% for CO₂RR (7.2% for CO and 76.6% for formate) (Fig. 4D). Note that we used acetonitrile-water (2.65 mole percent H₂O) to avoid precipitation of carbonate and unwanted side reactions in the anode space. The complete electrochemical system released O₂ at the anode and synthesis gas-formate at the cathode. Hence, the operating potential at -860 mV versus NHE corresponded to an overpotential ($E_{\text{CO,CO}_2,\text{CH}_3\text{CN}}^0$ is -650 mV versus NHE) of as little as 210 mV for CO (and formate) (49). This result is on a par with state-of-the-art catalysis and shows the potential of incorporating enzymatic molecular motifs into electrocatalytic processes. Note that the CO₂ origin of electrocatalytic-derived products is confirmed in a separate experiment [marked ¹³CO₂ in deuterated solvents by nuclear magnetic resonance (NMR); fig. S4].

Insights into the mechanism and the intermediate processes were gained by in situ spectroelectrochemistry (isSEC) in the fingerprint regime (Fig. 5). This technique enabled us to explore an exact sequence of the electrosynthesis (as a function of the applied potential) and acquire a deeper understanding of why our system favors C₁ species (that is, CO and formate) as dominant products.

The isSEC method allowed us to discriminate between emerging and fading features on the basis of the spectral signs. Although, for in-

stance, the signal of carbonyl-PDA (keto-carbonyl at 1730 cm⁻¹) pointed downward (fading) and that of CO₂ and carbonyl-amide (1650 and 1635 cm⁻¹) pointed upward (emerging). The detailed mechanism in combination with the spectra suggests that CO₂ first attaches to carbonyl-PDA, as can be seen from its subsequent depletion with increasing CO₂ concentration. The final intermediate step involves carbonyl-amide, which forms after attachment and subsequent reduction. This agrees with our calculation, which identified the favored position of the oxygen for initial CO₂ attachment. The subsequent reduction via amide explains the preference for CO and formate and is indicative of the coupling between amino and carbonyl functions via hydrogen bonding.

Active-site enhancement in conductive PDA has the potential to enable industrial electrosynthesis of C₁ carbon feedstocks. Renewable materials are abundant and readily available in natural bio-derived materials. They combine two attractive goals: (i) eliminating expensive (noble) metals and (ii) further reducing overpotentials for superior energy yields in CO₂RR. The latter is a major concern to reduce the amount of energy that must be dissipated in the form of heat at high current densities in industrial-scale electrosynthesis. Furthermore, the approach can be extended to include related enzyme-inspired molecular structures and change the product yield toward higher hydrocarbons or use organic electrosynthesis for hydrogen reactions in fuel cells. Hence, conductive functional materials provide a universal principle for developing efficient electrodes for energy-related electrocatalysis.

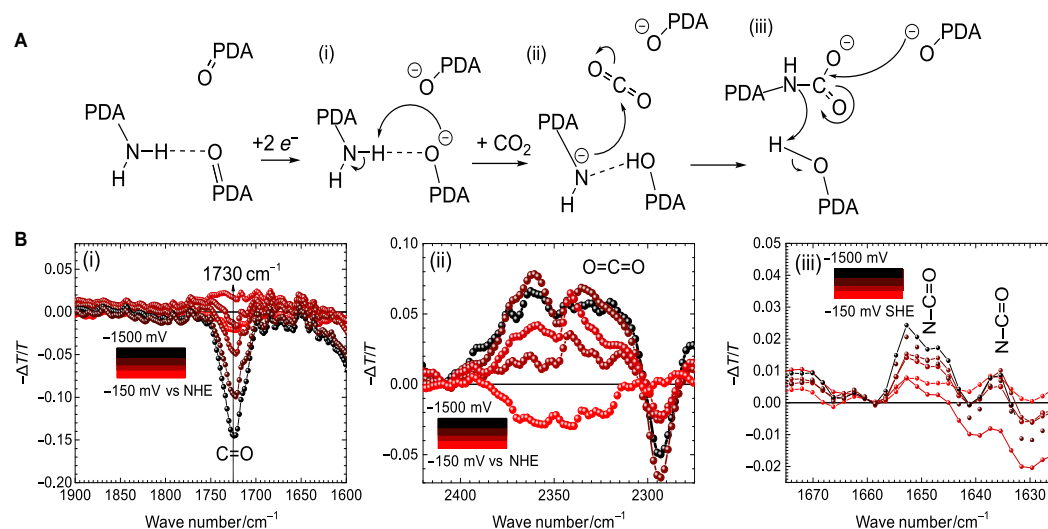


Fig. 5. Electrochemical activation of amine-carbonyl hydrogen bridge to a nucleophilic center. (A) Initial steps driving CO_2RR in conductive PDA: (i) electrochemical activation of the hydrogen-stabilized carbonyl group, (ii) subsequent formation of a nucleophilic center via the adjacent amine, and (iii) attachment to CO_2 creating an amide. (B) The in situ Fourier transform infrared (FTIR) differential spectra plot the individual initial steps shown above. The negative signs reflect the depletion of PDA-carbonyl, whereas positive signs correspond to the emergence of new absorptions, that is, CO_2 -related vibrations (2350 cm^{-1}) and amide-carbonyl vibrations (1650 and 1635 cm^{-1}). SHE, standard hydrogen electrode.

METHODS

oCVD was conducted on fluorine-doped tin oxide (FTO) glass and CF ($10\text{ mm} \times 10\text{ mm}$) purchased from the SGL Group–The Carbon Company for electrochemical studies, whereas for low-temperature measurements, sapphire ($10\text{ mm} \times 10\text{ mm} \times 0.5\text{ mm}$) purchased from CrysTec Kristalltechnologie with Cr/Au ($8\text{ nm}/100\text{ nm}$) electrodes was used. The substrates were cleaned in an ultrasonic bath for 15 min each in acetone, isopropyl alcohol, Hellmanex detergent (Hellma, 70°C), and deionized water. The metal contacts were deposited by physical vapor deposition through a 4-inch-line contact mask. Before synthesis, dopamine hydrochloride (Sigma-Aldrich) was dried overnight in an oven at 150°C in the presence of CaH_2 (95%, Sigma-Aldrich) to remove any residual water. The reaction was carried out in a tube furnace (Carbolite; glass tube length, 45 cm; tube diameter, 2.4 cm; reaction temperature, 300°C) under nitrogen atmosphere with a carrier gas flow of 3 liter min^{-1} . Sulfuric acid (95 to 97%, J.T.Baker) and sodium sulfate ($\geq 99.0\%$, Sigma-Aldrich) were used as oxidation agents in the synthesis. The reaction time was varied to reach the desired film thickness. A deposition time of 30 min yielded 50-nm films. For electrical characterization, the samples were stored under inert conditions to avoid humidity and were sealed by drop-casting a poly(methyl methacrylate) (PMMA) film on the active area.

The PMMA-covered PDA films on sapphire were contacted using indium solder and loaded to the PPMS DynaCool (Quantum Design). The electrical conductivity was characterized as a function of temperature between 300 and 180 K.

We used FTO and CF as WEs. For this purpose, the FTO substrates were cut into $8\text{-mm} \times 60\text{-mm}$ pieces and cleaned as described above. PDA was then deposited in the tube furnace at 300°C for 1 hour, which resulted in a film thickness of 100 nm. The procedure for CF was the same, except that it was kept in a glove box atmosphere before synthesis

to avoid adsorption of oxygen from the air, and the sponges were pretreated in the tube furnace at 150°C for 30 min to prevent any moisture absorption.

To evaluate PDA as an electrocatalyst for CO_2 reduction, we conducted electrochemical studies in a standard three-electrode arrangement in an H-cell configuration. A PDA-coated FTO glass slide and/or CF was used as a WE, Pt as a counter electrode (CE), and Ag/AgCl as a QRE. All were suspended in a 0.1 M tetrabutylammonium hexafluorophosphate (TBA- PF_6) (99.0%, Fluka) in acetonitrile-water (1 volume % H_2O , 0.55 M) as the electrolyte solution. This system offers high CO_2 solubility (approximately 0.27 M) (50). The WE and QRE were placed in one compartment of the H-cell, and the CE in the other (fig. S2). The compartments were connected by a bridge with a membrane (glass frit, porosity no. 2) in between. The Ag/AgCl QRE was calibrated against Fc/Fc^+ as an internal reference. All results are given relative to the NHE. The half-wave potential $E_{1/2}$ for Fc/Fc^+ was found at +400 mV versus QRE (and +240 mV versus NHE) (fig. S1D).

The electrochemical setup was characterized by systematic impedance analysis using an IVIUM CompactStat (Netherlands). First, the impedance of the cell (frit-separated H-cell containing acetonitrile + 1 % water, CO_2 -saturated, 0.1 M TBA- PF_6) was measured using two platinum electrodes. The open circuit potential (OCP) was measured for 30 s and then the electrochemical impedance spectrum was recorded (biased at OCP) in the range from 1 MHz to 1 Hz (perturbation amplitude of 10 mV). The high frequency range was dominated by the resistive behavior of the electrolyte with an absolute impedance of 1.36 kilohm (frequencies, 1 MHz to 1 kHz; equal electrode contribution to impedance due to the full symmetry of the setup). In the next step, the WE was replaced by a CF electrode without catalyst, and the impedance was measured using identical parameters. A value of 857 ohm was obtained (frequencies, 1 MHz to 1 kHz). In the next step, a CF electrode

loaded with PDA catalyst (CF-PDA) was used in a three-electrode arrangement (as for electrosynthesis; reference is Ag/AgCl QRE). The branches were characterized individually resulting in values of 907 ohm (Pt-CE against CF-PDA WE) and 741 ohm (QRE against CF-PDA WE). Note that the amplitude was 1 mV to avoid any deterioration of the QRE. Below 1-kHz phases consistently appeared in the range from -20° to -40° . Finally, the Pt-CE-CF-PDA WE combination was characterized using a three-electrode arrangement, in which the potential at the WE was measured using the reference electrode, and the current was measured between CE and WE. In this way, the actual potential drop in the electrolyte (plus frit including all static and kinetic losses at the CE) is compensated by a correspondingly higher or lower potential at the CE. Eventually, this system only had a low uncompensated electrolyte resistance of maximum 65 ohm (1 MHz to 1 kHz) and 129 ohm down (1 kHz to 1 Hz). This last measurement was performed down to frequencies of 100 mHz, and the phase did not exceed values of -30° . The pH values of the electrolyte solution (0.1 M TBA-PF₆ acetonitrile, CO₂-saturated) were obtained in the presence of various volume % of water, and for chronoamperometry, using a precision pH meter (Hanna Instruments, model pH 211).

We performed electrochemical and electrosynthesis experiments using a JAISLE Potentiostat Galvanostat IMP 88 PC. A TRACE Ultra Gas Chromatograph equipped with a thermal conductivity detector was used for analyzing the amount of CO gas produced after electrolysis. All electrochemical experiments were carried out in a glove box atmosphere to avoid moisture absorption. CO₂ was introduced to the glove box via a plastic tube from a bottle that contained 99.995% pure CO₂, and all chemicals used in the electrochemical experiments were stored only in the glove box. The compartments of the H-cell were purged with N₂ and CO₂ to achieve complete saturation of the system and prevent possible electrolyte exchange between the compartments that would lead to a change in the CO₂ concentration in the environment. The headspace volume was kept constant (20 mL). Before each experiment, the cell was flushed with N₂ and then CO₂ for 30 min. For the analysis of the insoluble CO gas, 2-ml samples were taken from the headspace by means of a gas-tight syringe and injected manually into the TRACE Ultra Gas Chromatograph (Thermo Fisher Scientific). Helium was used as carrier gas at a flow rate of 20 ml min⁻¹. The thermal conductivity detector was kept at 200°C.

FTIR measurements were carried out with a Bruker Vertex 80 with a range of 8000 to 600 cm⁻¹ and a resolution of 4 cm⁻¹. The in situ spectroelectrochemical [attenuated total reflection (ATR)-FTIR] measurements were performed on a Bruker IFS 66/S spectrometer. For the in situ technique, a sealed electrochemical cell (figs. S9 to S11) with Pt as CE, PDA as WE, and Ag/AgCl QRE was mounted in the spectrometer. The system was continuously flushed with 0.1 M TBA-PF₆ in acetonitrile. PDA was deposited onto a germanium crystal as a reflection element. During the spectroscopic recording, a cyclic voltammogram was captured between 0 and -2000 mV versus Ag/AgCl.

The chemical surface composition of PDA on Au and CF was evaluated on the basis of x-ray photoelectron spectroscopy (XPS). We used a Theta probe from Thermo Fisher Scientific with an Al K α (1486.7 eV) source. The charge was compensated by a dual flood gun (1 to 2 eV electrons and Ar⁺ ions), and the lens mode was set to standard. The energy pass amounted to 200 eV for the survey scan and 50 eV for HR scans, with energy steps of 1 and 0.1 eV, respectively. We used the Advantage v5.32 software package for data analysis. The data fittings were in agreement with the results described in the literature. The elemental concentrations were determined by survey and HR scans (figs.

S12 to S16, PDA on Au). The sulfur concentration was determined on the basis of the S2p and S2s levels. The sulfur concentration was higher than expected [theoretical value, ~ 2 atomic % (at %); measured values, ~ 10.7 at % (S2p) and ~ 8 at % (S2s)].

The N1s level suggested that nitrogen was present in two different chemical environments, predominantly as a primary amine: $-R-NH_2$ (401.8 ± 0.3 eV) and $-R-NH-R-$ (399.9 ± 0.1 eV). The fitting for the C1s spectrum was obtained with three components corresponding to the carbon atoms: CH_x (284.4 ± 0.1 eV), C-O/C-N (286.1 ± 0.2 eV), and C=O (287.7 ± 0.4 eV). The O1s spectrum showed three major contributions: O=C (531.0 ± 0.2 eV), HSO₄⁻ (531.7 ± 0.2 eV), and O-C (533.0 ± 0.2 eV). HR scans for the elements C, N, O, and S can be seen in figs. S13 to S16. The potential chemical structure of PDA proposed on this basis is shown in Fig. 2.

In addition to the extensive spectroscopic method (XPS and FTIR), we used computational methods for PDA based on DFT (29). This study used a cluster model of four monomer units and Gaussian basis sets for their ab initio simulations. Inspired by this previous study, we began by building a periodic model of a representative system for PDA whereby each monomer type (according to Fig. 2) was accounted for in the polymer structure. We chose this configuration to elucidate the energetics of CO₂ binding to each possible monomer unit. The four-unit polymer was placed into a periodic box with dimensions of $17 \text{ \AA} \times 15 \text{ \AA} \times 15 \text{ \AA}$ whereby the polymer chain passes through the periodic boundary along the x axis. At least 12 Å of vacuum space along the y and z axes was provided to avoid mirror image effects.

Marked ¹³C₂O was used for a control experiment to verify that the source of the electrosynthetic product formate was CO₂. After chronoamperometric scans, 450 μl of the product solution was used to record ¹³C NMR on a Bruker Ascend 700 spectrometer equipped with a cryogenically cooled probe (TXI). We use deuterated solvents for the NMR experiments (CD₃CN and 1% D₂O) (fig. S4).

DFT calculations were performed with the Vienna ab initio simulation package (51). The Perdew-Burke-Ernzerhof generalized gradient approximation exchange correlation functional was used with the projector augmented wave (PAW) method (52, 53). All-electron frozen-core PAW pseudopotentials with Blöchl plane wave basis sets were used with a cutoff energy of 500 eV and a Fermi smearing width of 0.1 eV (54). Long-range van der Waals interactions and dipole corrections were used. Monkhorst-Pack mesh was used for *k*-point sampling with $6 \times 1 \times 1$ *k*-points sampled for the structure optimization (55). Structural and unit cell optimizations were performed until the maximum cutoff was less than 0.02 eV per atom with the structures being fully optimized. CO₂ was placed in between the amino and carbonyl groups in the hydrogen bond motif of each monomer as a starting point and then fully relaxed (Fig. 1C). The BE for CO₂ was calculated as: $BE = E_{PDA+CO_2} - (E_{PDA} + E_{CO_2})$, where E_{PDA+CO_2} is the electronic energy of the system with PDA and the CO₂ near the hydrogen bond motif, E_{PDA} is the energy of PDA alone, and E_{CO_2} is the energy of gas-phase CO₂. Single point calculations were used (CO₂ BE as a function of distance) (Fig. 1D) in the two functional sites (oxygen and nitrogen). All images were visualized using the Visual Molecular Dynamics software (56).

SUPPLEMENTARY MATERIALS

Supplementary material for this article is available at <http://advances.sciencemag.org/cgi/content/full/3/8/e1700686/DC1>

fig. S1. Window of redox stability of conductive PDA.

fig. S2. Electrochemical setup for electrocatalytic CO₂RR.

fig. S3. Local pH as measured in the electrolyte system (0.1 M TBA-PF₆, 25°C, acetonitrile, CO₂-saturated) at various amounts of water added.
 fig. S4. ¹³C NMR spectra.
 fig. S5. Conductivity versus time.
 fig. S6. Conductivity (dc) of PDA in various liquids.
 fig. S7. pH values during electrosynthesis of formate in acetonitrile-water (0.1 M TBA-PF₆) blends at 25°C, CO₂-purged (30 min).
 fig. S8. Chronoamperometric scan (continuous and semicontinuous).
 fig. S9. Stability aspects and mechanisms shown by in situ FTIR.
 fig. S10. Differential in situ spectra in the spectral fingerprint regime.
 fig. S11. ATR-FTIR (in situ measurement cell) with reference 0.1 M TBA-formate and saturated CO₂.
 fig. S12. XPS survey scan of conductive PDA.
 fig. S13. N1s HR XPS scan.
 fig. S14. C1s HR XPS scan.
 fig. S15. O1s HR XPS scan.
 fig. S16. O1s HR XPS scan.
 table S1. State-of-the-art CO₂RR electrocatalysts, namely, for CO, formate, and related (hydro) carbon products.
 table S2. Electrochemical impedance data.

REFERENCES AND NOTES

- M. S. Xie, B. Y. Xia, Y. Li, Y. Yan, Y. Yang, Q. Sun, S. H. Chan, A. Fisher, X. Wang, Amino acid modified copper electrodes for the enhanced selective electroreduction of carbon dioxide towards hydrocarbons. *Energy Environ. Sci.* **9**, 1687–1695 (2016).
- Z. Wang, G. Yang, Z. Zhang, M. Jin, Y. Yin, Selectivity on etching: Creation of high-energy facets on copper nanocrystals for CO₂ electrochemical reduction. *ACS Nano* **10**, 4559–4564 (2016).
- M. Asadi, K. Kim, C. Liu, A. V. Addepalli, P. Abbasi, P. Yasaei, P. Phillips, A. Behranginia, J. M. Cerrato, R. Haasch, P. Zapol, B. Kumar, R. F. Klie, J. Abiade, L. A. Curtiss, A. Salehi-Khojin, Nanostructured transition metal dichalcogenide electrocatalysts for CO₂ reduction in ionic liquid. *Science* **353**, 467–470 (2016).
- S. Gao, Y. Lin, X. Jiao, Y. Sun, Q. Luo, W. Zhang, D. Li, J. Yang, Y. Xie, Partially oxidized atomic cobalt layers for carbon dioxide electroreduction to liquid fuel. *Nature* **529**, 68–71 (2016).
- T. S. Safaei, A. Mephram, X. Zheng, Y. Pang, C.-T. Dinh, M. Liu, D. Sinton, S. O. Kelley, E. H. Sargent, High-density nanosharp microstructures enable efficient CO₂ electroreduction. *Nano Lett.* **16**, 7224–7228 (2016).
- M. Liu, Y. Pang, B. Zhang, P. De Luna, O. Voznyy, J. Xu, X. Zheng, C. T. Dinh, F. Fan, C. Cao, F. P. G. de Arquer, T. S. Safaei, A. Mephram, A. Klinskova, E. Kumacheva, T. Filleter, D. Sinton, S. O. Kelley, E. H. Sargent, Enhanced electrocatalytic CO₂ reduction via field-induced reagent concentration. *Nature* **537**, 382–386 (2016).
- H. Mistry, A. S. Varela, C. S. Bonifacio, I. Zegkinoglou, I. Sinev, Y.-W. Choi, K. Kisslinger, E. A. Stach, J. C. Yang, P. Strasser, B. R. Cuenya, Highly selective plasma-activated copper catalysts for carbon dioxide reduction to ethylene. *Nat. Commun.* **7**, 12123 (2016).
- M. Asadi, B. Kumar, A. Behranginia, B. A. Rosen, A. Baskin, N. Reppin, D. Pisasale, P. Phillips, W. Zhu, R. Haasch, R. F. Klie, P. Král, J. Abiade, A. Salehi-Khojin, Robust carbon dioxide reduction on molybdenum disulfide edges. *Nat. Commun.* **5**, 4470 (2014).
- Q. Lu, J. Rosen, Y. Zhou, G. S. Hutchings, Y. C. Kimmel, J. G. Chen, F. Jiao, A selective and efficient electrocatalyst for carbon dioxide reduction. *Nat. Commun.* **5**, 3242 (2014).
- Y. Gong, J. Lin, X. Wang, G. Shi, S. Lei, Z. Lin, X. Zou, G. Ye, R. Vajtai, B. I. Yakobson, H. Terrones, M. Terrones, B. K. Tay, J. Lou, S. T. Pantelides, Z. Liu, W. Zhou, P. M. Ajayan, Vertical and in-plane heterostructures from WS₂/MoS₂ monolayers. *Nat. Mater.* **13**, 1135–1142 (2014).
- R. Kas, K. K. Hummadi, R. Kortlever, P. de Wit, A. Milbrat, M. W. J. Luiten-Olieman, N. E. Benes, M. T. M. Koper, G. Mul, Three-dimensional porous hollow fibre copper electrodes for efficient and high-rate electrochemical carbon dioxide reduction. *Nat. Commun.* **7**, 10748 (2016).
- F. Lei, W. Liu, Y. Sun, J. Xu, K. Liu, L. Liang, T. Yao, B. Pan, S. Wei, Y. Xie, Metallic tin quantum sheets confined in graphene toward high-efficiency carbon dioxide electroreduction. *Nat. Commun.* **7**, 12697 (2016).
- S. Lin, C. S. Diercks, Y.-B. Zhang, N. Kornienko, E. M. Nichols, Y. Zhao, A. R. Paris, D. Kim, P. Yang, O. M. Yaghi, C. J. Chang, Covalent organic frameworks comprising cobalt porphyrins for catalytic CO₂ reduction in water. *Science* **349**, 1208–1213 (2015).
- J. A. Buss, T. Agapie, Four-electron deoxygenative reductive coupling of carbon monoxide at a single metal site. *Nature* **529**, 72–75 (2015).
- A. Aljabour, D. H. Apaydin, H. Coskun, F. Ozel, M. Ersoz, P. Stadler, N. S. Sariciftci, M. Kus, Improvement of catalytic activity by nanofibrous CuInS₂ for electrochemical CO₂ reduction. *ACS Appl. Mater. Interfaces* **8**, 31695–31701 (2016).
- C. Janáky, D. Hursán, B. Endrődi, W. Chanmanee, D. Roy, D. Liu, N. R. de Tacconi, B. H. Dennis, K. Rajeshwar, Electro- and photoreduction of carbon dioxide: The twin shall meet at copper oxide/copper interfaces. *ACS Energy Lett.* **1**, 332–338 (2016).
- C. Liu, T. R. Cundari, A. K. Wilson, CO₂ reduction on transition metal (Fe, Co, Ni, and Cu) surfaces: In comparison with homogeneous catalysis. *J. Phys. Chem. C* **116**, 5681–5688 (2012).
- K. P. Kuhl, E. R. Cave, D. N. Abram, T. F. Jaramillo, New insights into the electrochemical reduction of carbon dioxide on metallic copper surfaces. *Energy Environ. Sci.* **5**, 7050 (2012).
- B. A. Rosen, A. Salehi-Khojin, M. R. Thorson, W. Zhu, D. T. Whipple, P. J. A. Kenis, R. I. Masel, Ionic liquid-mediated selective conversion of CO₂ to CO at low overpotentials. *Science* **334**, 643–644 (2011).
- S. Sultana, P. C. Sahoo, S. Martha, K. Parida, A review of harvesting clean fuels from enzymatic CO₂ reduction. *RSC Adv.* **6**, 44170–44194 (2016).
- N. Khadka, D. R. Dean, D. Smith, B. M. Hoffman, S. Raugel, L. C. Seefeldt, CO₂ reduction catalyzed by nitrogenase: Pathways to formate, carbon monoxide, and methane. *Inorg. Chem.* **55**, 8321–8330 (2016).
- Y.-P. Zhu, Y.-P. Liu, Z.-Y. Yuan, Biochemistry-inspired direct synthesis of nitrogen and phosphorus dual-doped microporous carbon spheres for enhanced electrocatalysis. *Chem. Commun.* **52**, 2118–2121 (2016).
- M. Jakešová, D. H. Apaydin, M. Sytnyk, K. Oppelt, W. Heiss, N. S. Sariciftci, E. D. Glowacki, Hydrogen-bonded organic semiconductors as stable photoelectrocatalysts for efficient hydrogen peroxide photosynthesis. *Adv. Funct. Mater.* **26**, 5248–5254 (2016).
- H. A. Hansen, J. B. Varley, A. A. Peterson, J. K. Nørskov, Understanding trends in the electrocatalytic activity of metals and enzymes for CO₂ reduction to CO. *J. Phys. Chem. Lett.* **4**, 388–392 (2013).
- A. M. Appel, J. E. Bercaw, A. B. Bocarsly, H. Dobbek, D. L. DuBois, M. Dupuis, J. G. Ferry, E. Fujita, R. Hille, P. J. A. Kenis, C. A. Kerfeld, R. H. Morris, C. H. F. Peden, A. R. Portis, S. W. Ragsdale, T. B. Rauchfuss, J. N. H. Reek, L. C. Seefeldt, R. K. Thauer, G. L. Waldrop, Frontiers, opportunities, and challenges in biochemical and chemical catalysis of CO₂ fixation. *Chem. Rev.* **113**, 6621–6658 (2013).
- P. Meredith, T. Sarna, The physical and chemical properties of eumelanin. *Pigment Cell Res.* **19**, 572–594 (2006).
- F. Bernsmann, V. Ball, F. Addiego, A. Ponche, M. Michel, J. J. de Almeida Gracio, V. Toniazzo, D. Ruch, Dopamine-melanin film deposition depends on the used oxidant and buffer solution. *Langmuir* **27**, 2819–2825 (2011).
- V. Ball, D. Del Frari, V. Toniazzo, D. Ruch, Kinetics of polydopamine film deposition as a function of pH and dopamine concentration: Insights in the polydopamine deposition mechanism. *J. Colloid Interface Sci.* **386**, 366–372 (2012).
- J. Liescher, R. Mrówczyński, H. A. Scheidt, C. Filip, N. D. Hädade, R. Turcu, A. Bende, S. Beck, Structure of polydopamine: A never-ending story? *Langmuir* **29**, 10539–10548 (2013).
- R. A. Zangmeister, T. A. Morris, M. J. Tarlov, Characterization of polydopamine thin films deposited at short times by autoxidation of dopamine. *Langmuir* **29**, 8619–8628 (2013).
- P. Kanyong, S. Rawlinson, J. Davis, Fabrication and electrochemical characterization of polydopamine redox polymer modified screen-printed carbon electrode for the detection of guanine. *Sens. Actuators B* **233**, 528–534 (2016).
- J. Y. Lee, T. L. Nguyen, J. H. Park, B.-K. Kim, Electrochemical detection of hydrazine using poly(dopamine)-modified electrodes. *Sensors* **16**, 647 (2016).
- L. Fu, G. Lai, D. Zhu, B. Jia, F. Malherbe, A. Yu, Advanced catalytic and electrocatalytic performances of polydopamine-functionalized reduced graphene oxide-palladium nanocomposites. *ChemCatChem* **8**, 2975–2980 (2016).
- C. M. Parnell, B. Chhetri, A. Brandt, F. Watanabe, Z. A. Nima, T. K. Mudalige, A. S. Biris, A. Ghosh, Polydopamine-coated manganese complex/graphene nanocomposite for enhanced electrocatalytic activity towards oxygen reduction. *Sci. Rep.* **6**, 31415 (2016).
- K. Qu, Y. Zheng, S. Dai, S. Z. Qiao, Graphene oxide-polydopamine derived N, S-codoped carbon nanosheets as superior bifunctional electrocatalysts for oxygen reduction and evolution. *Nano Energy* **19**, 373–381 (2016).
- H. Peng, C. Liang, Electrochemical determination of hydrazine based on polydopamine-reduced graphene oxide nanocomposite. *Fullerenes Nanotubes Carbon Nanostruct.* **25**, 29–33 (2016).
- S. Palanisamy, B. Thirumalraj, S.-M. Chen, Y.-T. Wang, V. Velusamy, S. Kannan Ramaraj, A facile electrochemical preparation of reduced graphene oxide@polydopamine composite: A novel electrochemical sensing platform for amperometric detection of chlorpromazine. *Sci. Rep.* **6**, 33599 (2016).
- H. Yang, S. Kang, H. Zou, J. Jin, J. Ma, S. Li, Polydopamine-functionalized multi-walled carbon nanotubes-supported palladium-lead bimetallic alloy nanoparticles as highly efficient and robust catalysts for ethanol oxidation. *RSC Adv.* **6**, 90462–90469 (2016).
- S. Murali, J.-L. Chang, J.-M. Zen, Bismuth oxide nanoparticles as a nanoscale guide to form a silver-polydopamine hybrid electrocatalyst with enhanced activity and stability for the oxygen reduction reaction. *RSC Adv.* **5**, 4286–4291 (2015).

40. L. Fu, G. Lai, B. Jia, A. Yu, Preparation and electrocatalytic properties of polydopamine functionalized reduced graphene oxide-silver nanocomposites. *Electrocatalysis* **6**, 72–76 (2015).
41. R. R. Knowles, E. N. Jacobsen, Attractive noncovalent interactions in asymmetric catalysis: Links between enzymes and small molecule catalysts. *Proc. Natl. Acad. Sci. U.S.A.* **107**, 20678–20685 (2010).
42. D. H. Apaydin, E. D. Glowacki, E. Portenkirchner, N. S. Sariciftci, Direct electrochemical capture and release of carbon dioxide using an industrial organic pigment: Quinacridone. *Angew. Chem. Int. Ed.* **53**, 6819–6822 (2014).
43. C. Enengl, S. Enengl, M. Havlicek, P. Stadler, E. D. Glowacki, M. C. Scharber, M. White, K. Hingerl, E. Ehrenfreund, H. Neugebauer, N. S. Sariciftci, The role of heteroatoms leading to hydrogen bonds in view of extended chemical stability of organic semiconductors. *Adv. Funct. Mater.* **25**, 6679–6688 (2015).
44. A. Ugur, F. Katmis, M. Li, L. Wu, Y. Zhu, K. K. Varanasi, K. K. Gleason, Low-dimensional conduction mechanisms in highly conductive and transparent conjugated polymers. *Adv. Mater.* **27**, 4604–4610 (2015).
45. S. Lee, K. K. Gleason, Enhanced optical property with tunable band gap of cross-linked PEDOT copolymers via oxidative chemical vapor deposition. *Adv. Funct. Mater.* **25**, 85–93 (2015).
46. P. Abbasi, M. Asadi, C. Liu, S. Sharifi-Asl, B. Sayahpour, A. Behranginia, P. Zapol, R. Shahbazian-Yassar, L. A. Curtiss, A. Salehi-Khojin, Tailoring the edge structure of molybdenum disulfide toward electrocatalytic reduction of carbon dioxide. *ACS Nano* **11**, 453–460 (2017).
47. A. J. Fisher, W. Hayes, D. S. Wallace, Polarons and solitons. *J. Phys. Condens. Matter* **1**, 5567–5593 (1989).
48. C. Cobet, J. Gasiorowski, R. Menon, K. Hingerl, S. Schlager, M. S. White, H. Neugebauer, N. S. Sariciftci, P. Stadler, Influence of molecular designs on polaronic and vibrational transitions in a conjugated push-pull copolymer. *Sci. Rep.* **6**, 35096 (2016).
49. C. Costentin, S. Drouet, M. Robert, J.-M. Savéant, A local proton source enhances CO₂ electroreduction to CO by a molecular Fe catalyst. *Science* **338**, 90–94 (2012).
50. Y. Tomita, S. Teruya, O. Koga, Y. Hori, Electrochemical reduction of carbon dioxide at a platinum electrode in acetonitrile-water mixtures. *J. Electrochem. Soc.* **147**, 4164–4167 (2000).
51. J. Hafner, Ab-initio simulations of materials using VASP: Density-functional theory and beyond. *J. Comput. Chem.* **29**, 2044–2078 (2008).
52. P. E. Blöchl, Projector augmented-wave method. *Phys. Rev. B* **50**, 17953–17979 (1994).
53. J. P. Perdew, K. Burke, M. Ernzerhof, Generalized gradient approximation made simple. *Phys. Rev. Lett.* **77**, 3865–3868 (1996).
54. G. Kresse, D. Joubert, From ultrasoft pseudopotentials to the projector augmented-wave method. *Phys. Rev. B* **59**, 1758–1775 (1999).
55. H. J. Monkhorst, J. D. Pack, Special points for Brillouin-zone integrations. *Phys. Rev. B* **13**, 5188–5192 (1976).
56. W. Humphrey, A. Dalke, K. Schulten, VMD: Visual molecular dynamics. *J. Mol. Graph.* **14**, 33–38 (1996).

Acknowledgments: We thank P. Whang, D. H. Apaydin, G. Hinterberger, and L. S. Dumitru for fruitful discussions. **Funding:** P.S. is thankful to OeAD [Scientific & Technological Cooperation (WTZ), IN10/2015] for financial support and acknowledges the government of Upper Austria within the Sabbatical program "Internationalization of the University of Linz." N.S.S. acknowledges financial support from the Austrian Science Foundation (FWF) (Z 222-N19) within the Wittgenstein Prize Scheme. A.A. and M.K. acknowledges Tubitak (The Scientific and Technological Research Council of Turkey) for a scholarship within program 2215. A.W.H. acknowledges the financial support by the Austrian Federal Ministry of Science, Research and Economy and the National Foundation for Research, Technology and Development in the frame of the Christian Doppler Laboratory for Combinatorial Oxide Chemistry (COMBOX). W.S. acknowledges the financial support from the Austrian Science Foundation (FWF) (project FWF-P28167-N34). D.F. acknowledges financial support from the Austrian Research Promotion Agency (FFG) (FFGP13540004). P.D.L. acknowledges the Natural Sciences and Engineering Research Council of Canada for financial support in the form of a Canadian Graduate Scholarship–Doctoral award. **Author contributions:** P.S., A.A., H.C., P.D.L., and E.H.S. designed and directed the study. H.C. and A.A. contributed to all the experiments. H.C. designed the film growth process and carried out the experimental work. A.A. and H.C. performed the electrochemical and corresponding analytical measurements. P.D.L. carried out the DFT simulation and all the corresponding calculations. M.L. performed the HRSEMs. H.C., A.A., and P.S. carried out in situ spectroelectrochemical investigations. A.W.H. conducted impedance measurements. H.C., P.S., and W.S. conducted the NMR experiments. T.G. and D.S. conducted the XPS study. X.Z., E.H.S., H.C., A.A., D.F., M.K., N.S.S., and P.S. analyzed the data. E.H.S., H.C., P.D.L., and P.S. wrote the manuscript. All authors commented on the paper. **Competing interests:** The authors declare that they have no competing interests. **Data and materials availability:** All data needed to evaluate the conclusions in the paper are present in the paper and/or the Supplementary Materials. Additional data related to this paper may be requested from the authors.

Submitted 6 March 2017

Accepted 30 June 2017

Published 4 August 2017

10.1126/sciadv.1700686

Citation: H. Coskun, A. Aljabour, P. De Luna, D. Farka, T. Greunz, D. Stifter, M. Kus, X. Zheng, M. Liu, A. W. Hassel, W. Schöfberger, E. H. Sargent, N. S. Sariciftci, P. Stadler, Biofunctionalized conductive polymers enable efficient CO₂ electroreduction. *Sci. Adv.* **3**, e1700686 (2017).

Biofunctionalized conductive polymers enable efficient CO₂ electroreduction

Halime Coskun, Abdalaziz Aljabour, Phil De Luna, Dominik Farka, Theresia Greunz, David Stifter, Mahmut Kus, Xueli Zheng, Min Liu, Achim W. Hassel, Wolfgang Schöfberger, Edward H. Sargent, Niyazi Serdar Sariciftci and Philipp Stadler

Sci Adv 3 (8), e1700686.
DOI: 10.1126/sciadv.1700686

ARTICLE TOOLS	http://advances.sciencemag.org/content/3/8/e1700686
SUPPLEMENTARY MATERIALS	http://advances.sciencemag.org/content/suppl/2017/07/28/3.8.e1700686.DC1
REFERENCES	This article cites 56 articles, 6 of which you can access for free http://advances.sciencemag.org/content/3/8/e1700686#BIBL
PERMISSIONS	http://www.sciencemag.org/help/reprints-and-permissions

Downloaded from <http://advances.sciencemag.org/> on January 22, 2018

Use of this article is subject to the [Terms of Service](#)

Science Advances (ISSN 2375-2548) is published by the American Association for the Advancement of Science, 1200 New York Avenue NW, Washington, DC 20005. 2017 © The Authors, some rights reserved; exclusive licensee American Association for the Advancement of Science. No claim to original U.S. Government Works. The title *Science Advances* is a registered trademark of AAAS.

4.7 Manuscript 7



Contents lists available at ScienceDirect

Thin Solid Films

journal homepage: www.elsevier.com/locate/tsf

Chemical vapor deposition - based synthesis of conductive polydopamine thin-films



Halime Coskun^{a,*}, Abdalaziz Aljabour^a, Lisa Uiberlacker^b, Moritz Strobel^b, Sabine Hild^b, Christoph Cobet^c, Dominik Farka^a, Philipp Stadler^a, Niyazi Serdar Sariciftci^a

^a Linz Institute for Organic Solar Cells (LIOS) and Institute of Physical Chemistry, Johannes Kepler University Linz, Altenbergerstraße 69, 4040 Linz, Austria

^b Institute of Polymer Science, Johannes Kepler University Linz, Altenbergerstraße 69, 4040 Linz, Austria

^c Center for Surface and Nanoanalytics, Johannes Kepler University Linz, Altenbergerstraße 69, 4040 Linz, Austria

ARTICLE INFO

Keywords:
Polydopamine
Thin film
Chemical vapor deposition
Conjugated bio-inspired material

ABSTRACT

Polydopamine (PDA) represents a family of synthetic bio-inspired pigments offering high functional activity combined with semiconducting properties. To date, it represents one of the main synthetic biopolymers used mainly because of its simple synthesis in aqueous solutions. Thereby dopamine polymerizes in the presence of ambient oxygen to polydopamine. However, its structure renders a sophisticated backbone relating to variations of ambient growth parameters such as temperature, local pH and partial oxygen pressure; preponderant repeating units found in aqueous polydopamine are 5,6-hydroxyl-indole derivatives. However, hydrogen-bonded aggregation competes with the polymerization leading to complex systems. In order to reduce the aggregation we hypothesized that acidic oxidants will direct the polymerization towards C–C coupling and hence create synthetic biopolymers.

In this work we demonstrate oxidative chemical vapor deposition (o-CVD) for PDA, where we obtain the desired consistent biopolymer thin-films as shown by structural analysis. Furthermore, as-gained polydopamine is conductive and renders fingerprint signatures of free charge carriers. Concomitantly it preserves its functionality – imperative for potential applications in catalysis or as bio-linker.

1. Introduction

Natural molecular units, such as hydrogen-bonded pigment molecules, represent an emerging class of conjugated semiconductors proposed for manifold bio-compatible optoelectronic linkers. Bio-compatible semiconductors can be implemented in living tissue and mutually address biologic-electronic signals. In addition, decomposable, non-toxic semiconductors can decrease electronic littering [1–7].

Among other bio-related conjugated systems polydopamines (PDAs) are commonly used conjugated biopolymers. PDAs adopt indole-based conjugated - functional repeating units reminiscent to eumelanins – a group of natural pigments built from 5,6-dihydroxy-indoles and derivatives thereof (Fig. 1). Unlike eumelanins, PDAs assemble to 1 - dimensional structures. Originally, they have been derived from 3,4-dihydroxy-L-phenylalanine – a protein existing in mussels responsible for the high binding strength. Consequently, early research has focused bio-mechanical applications [8–15]. Meanwhile the synthesis procedures have eased and PDAs are used in manifold coatings, template layers and catalyst carriers [15]. The dominant synthesis to date uses

oxidative polymerization of dopamine in aqueous solutions [7,15–18]. Thereby, ambient oxygen serves as C–C coupling agent making the synthesis straightforward (i.e. self-polymerization in a glass beaker). However, the downside of aqueous synthesis is resulting complex structures such as disrupted conjugation. Studies have shown that entire building blocks of hydrogen bond networks (H-aggregates) are formed within PDA and inhibit covalent coupling among the monomers. Hence, aqueous PDAs are often not processable and show limited electronic properties [7,8,15]. In addition, the establishment of consistent growth parameters (i.e. temperature, pressure, local pH) is difficult, as minor changes in ambient conditions significantly alter the final molecular structure [8,9,15,19]. In order to promote covalent polymerization, monomer intermediate formation has to occur under controlled oxidative conditions. Discretely, these are the oxidation of dopamine (DA) to dopamine-quinone (DAQ), the intramolecular cyclization to leucodopaminechrome (LDC) and thereafter the formation and polymerization of indole and its derivatives (Fig.1) [15].

To suppress PDA's affinity to build up H-aggregates, we pursue a synthesis strategy that adopts insights from classic conductive polymers

* Corresponding author.

E-mail address: halime.coskun_aljabour@jku.at (H. Coskun).

<https://doi.org/10.1016/j.tsf.2017.10.063>

Received 2 August 2017; Received in revised form 19 October 2017; Accepted 31 October 2017

0040-6090/ © 2017 The Author(s). Published by Elsevier B.V. This is an open access article under the CC BY-NC-ND license (<http://creativecommons.org/licenses/by-nc-nd/4.0/>).

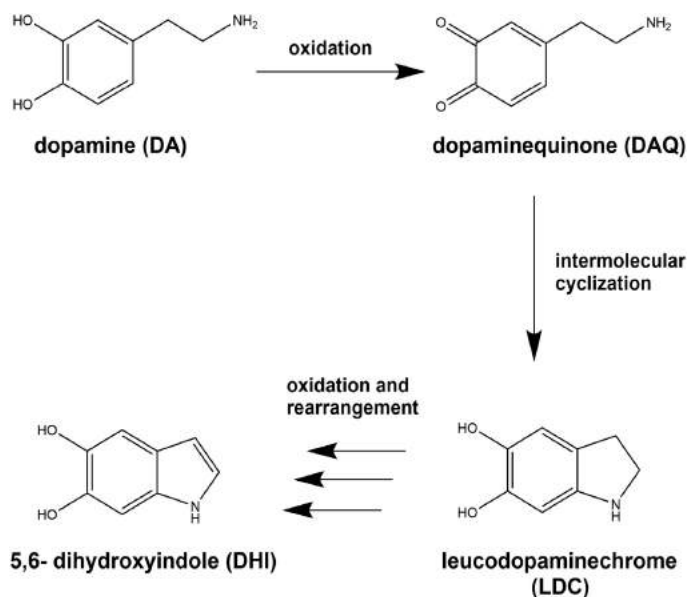


Fig. 1. Chemical structures of the polydopamine (PDA) intermediate steps undergoing numerous oxidation and rearrangement reactions.

[8,15,20]. The aim is to generate conjugated and conductive PDA from dopamine by using oxidative chemical vapor deposition (o-CVD). This technique allows us to use stronger oxidation reagent (as compared to ambient O_2) in combination with acidic surrounding to enforce oxidative C–C coupling. The goal is to arrive at the desired functionalized polyparaphenylene (PPP) type of backbone.

In this work we adapt o-CVD for PDA i.e. we contact gaseous dopamine free base with sulphuric acid. The latter serves as acidic oxidation agent and directs the synthesis to deposit conjugated and conductive PDA thin films; we can define film thickness and deposition on various substrates such as glass, sapphire or carbon-materials for potential (catalytic) applications [21]. We are in particular interested in the consequent structural changes induced by o-CVD (as compared to the aqueous PDA). Therefore, we employ spectroscopic tools such as Fourier Transform Infrared Spectroscopy (FTIR), Raman and variable angle spectroscopic ellipsometry (VASE) on par with structural investigations (atomic force microscopy - AFM). We find evidence of covalent polymerization and high structural consistency in o-CVD PDA on par with a preservation of its functionalization. O-CVD PDA offers higher processability and yields consistent structural conformity leading to electronic activations such as electrical conductivity.

2. Experimental detail

2.1. Materials and methods

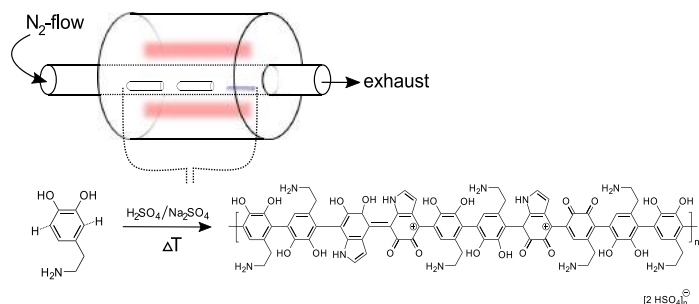
The oxidative chemical vapor deposition (o-CVD) is conducted on glass substrates (20 mm × 20 mm) and sapphire (10 mm × 10 mm × 0.5 mm) purchased from CrysTecKristall technology with Cr/Au electrodes used for the characterization of the polymer films. For the conductivity measurements on sapphire, the metal contacts are deposited by PVD through a 4-in-line contact mask. First, the substrates are cleaned using ultra-sonic bath 15 min each in acetone, isopropyl alcohol, Hellmanex-detergent (Hellma, 70 °C) and deionized water. Before starting the synthesis, dopamine hydrochloride (Sigma Aldrich) is dried in an oven at 150 °C overnight in presence of CaH_2 (95%, Sigma Aldrich) to remove any water residual. The reaction

is carried out in a tube furnace (Carbolite company; glass tube length: 45 cm; tube diameter: 2.4 cm; reaction temperature: 300 °C) under nitrogen atmosphere with a carrier gas-flow of 3 L/min. Sulphuric acid (95–97%, J.T. Baker) and sodium sulphate ($\geq 99.0\%$, Sigma Aldrich) are utilized as oxidation agent and corresponding salt in the synthesis, respectively, in order to shift the balance towards SO_3^- and SO_4^{2-} in the gas phase. The reaction times are varied to reach the desired film thickness. For electrical characterization the samples are stored under inert conditions to avoid humidity and are sealed by drop casting a polymethyl methacrylate (PMMA) film on top of the active area. The simplified structure of vapor phase polydopamine during the one-step polymerization in the tube furnace is presented in Fig. 2.

2.2. Film characterization

The FTIR measurements are done using a Bruker Vertex 80 (8000 cm^{-1} to 600 cm^{-1} ; resolution 4 cm^{-1}). The Raman spectra are recorded at room temperature with a WITec Alpha 300 R-Raman-System (WITec GmbH, Ulm, Germany) instrument. Nd:YAG laser (532 nm) is used for the excitation and thermoelectrically cooled CCD (DU970N-BV) detector is applied for all measurements. A grating of 600 mm^{-1} is used with a resolution of 4 cm^{-1} . For all three molecules $20\times$ Zeiss EC Epiplan (Carl Zeiss Jena GmbH, Germany) objective lens is used, while the laser intensity, integration time and accumulations are varied for the monomer (10 mW, 15 s., 10), aqueous PDA (5 mW, 2 s., 3), and o-CVD PDA (5 mW, 3 s., 20), respectively.

Variable angle spectroscopic ellipsometry (VASE) measurements are conducted using a Wollam M-2000 spectrometer at 6 incident angles. The dielectric model has been derived using VASE program with film thickness used as an input parameter. For electrical characterization PMMA-sealed PDA films are contacted using indium solder and loaded to the cryosystem for electrical probing (Physical Property Measurement System, DynaCool, Quantum Design). The electrical conductivity is characterized as a function of temperature and time (at 300 K). The surface imaging of polydopamine films is taken by MFP 3D-Stand Alone atomic force microscopy (AFM) from Asylum Research with the cantilever OMCL-AC240TS of Olympus. It is operated in the



AC-mode at 60% setpoint and a scan rate of 0.2 Hz. The thickness determination of the polymer films is carried on Bruker DektakXT.

3. Results and discussion

This work utilizes o-CVD to grow conductive PDAs. Prior art on state-of-the-art techniques uses mainly solution-based synthesis (Table 1) [18,22–25].

As discussed, the downside of solution-based synthesis is the difficulty of the control over ambient parameters (temperature, O_2 partial pressure, local pH in growth solution) and the competing H-aggregation disrupting conjugation. We pick one archetype solution route (according to ref. 21) and use it as a control experiment (further denoted as *solution-PDA*) for comparison to our o-CVD processed PDA (*o-CVD PDA*).

o-CVD induces a rapid growth of PDA (Fig. 3) – typical deposition rates are 5–6 nm per minute (within 4 h thin films with high homogeneity and controllable thickness can be deposited). We found that acidic reaction conditions protonate the dopamine free base and as such deactivate the competing H-bond aggregation and hence preserve the functionality (most dominantly on the amine). Furthermore, as typically for o-CVD we obtain a conducting biopolymer. The vapor oxidation includes also the shallow doping step in the polymerization and results in highly defined, reproducible deposits. We could demonstrate o-CVD on various substrates such as flat surfaces but also mesh-type or sponge-type electrodes, which are effectively covered with PDA through vapor infiltration.

To elucidate the surface topography of a glass-deposited PDA, we apply atomic force microscopy (AFM) (Fig. 4). The images reveal homogeneously formed, pinhole-free surfaces with a root mean square roughness of 3 nm (obtained at $10 \times 10 \mu\text{m}$ images on various spots). Similar morphologies at higher thickness in bulk-like films have been reproduced (not shown). The morphological consistency is also reflected in the optical properties.

In general, PDAs belong to the naturally occurring pigment family of eumelanin, consequently, the optical parameters of PDA are related to the natural chromophore [15]. These are characteristic broad band-monotonic absorbers in the ultraviolet. Exactly such absorption features

Table 1

An overview about the recent status of the PDA deposition parameters.

Method of deposition	Oxidant	Deposition time [h]	Thickness [nm]	Ref.
Solution process	O_2	15	max. 40	[24]
Solution process	$CuSO_4$	80	< 80	[23]
Solution process	O_2	< 80	< 80	[18]
Solution process	O_2	< 30	< 80	[22]
Solution process	O_2	2–60 min	< 10	[25]
o-CVD	H_2SO_4/Na_2SO_4	< 4	< 1500	This work

Fig. 2. Experimental setup of the o-CVD in the tube furnace. PDA is deposited on glass substrates in presence of the monomer and oxidation agent at an elevated reaction temperature of 300 °C under N_2 atmosphere. After the reaction the monomer is transformed into a doped conjugated polymer consisting of quinone and indole derivatives of dopamine.

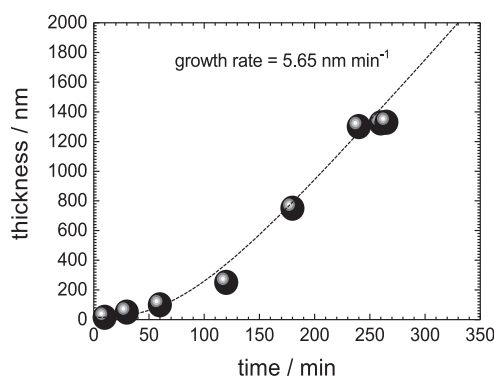


Fig. 3. Film thickness as a function of the deposition time after the o-CVD of PDA.

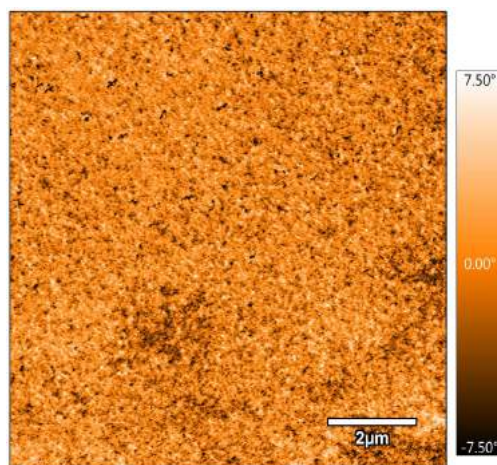


Fig. 4. Phase image of the film demonstrating a homogenous, pin-hole free surface. The film has a thickness of 1 μm .

are found in o-CVD PDA as well – we derive the optical parameters using variable-angle spectroscopic ellipsometry to attain a profound insight (Fig. 5, relevant optical parameters as dielectric function ϵ_1 and ϵ_2). Furthermore, we derive the absorption coefficient α (Fig. 5a). Similar to eumelanin, an exponential increase is observed dominated in the UV region with the absorption peaks at 217 nm (5.71 eV), 238 nm

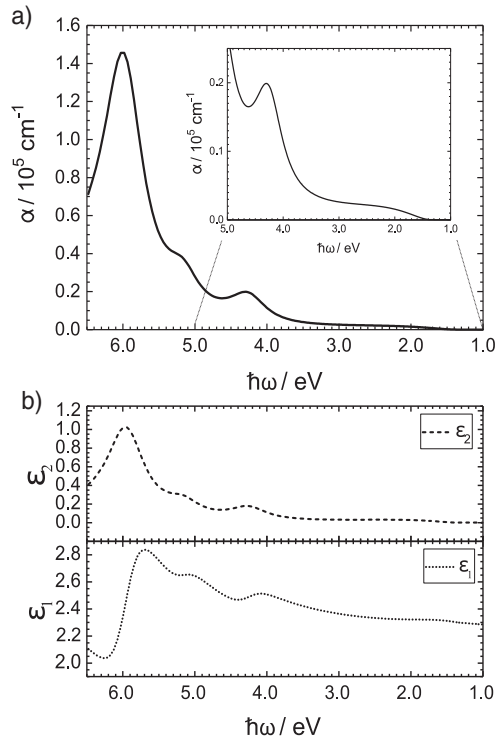


Fig. 5. (a) Absorption coefficient of o-CVD PDA (inset: zoom to the absorption onset). Two onsets are found. (b) Variable angle spectroscopic ellipsometry (VASE, 6 incident angles) on CVD-grown PDA thin films showing the dielectric function in the near-infrared, visible and UV spectral regime. We derive all optical parameters using a point-by-point fit. Note the functions are obtained by Kramers-Kronig relations.

(5.2 eV) and 300 nm (4.13 eV). We relate these strong absorption features to presence of leucodopaminechrome (LDC) and its indole derivatives reminiscent of the archetype UV-photoprotection of melanin skin pigments [15,26,27].

We conclude an absorption onset at approximately 3.72 eV – this is in agreement with previously reported theoretical calculations and experimental data on PDA. The optical dielectric parameters ϵ_1 and ϵ_2 of PDA have been derived using a chemical disorder models (CDM) [15]. Unlike classic conductive polymers alternating combinations of different monomers such as dopamine, LDCs including and its indole derivatives generate convoluted repeating units – CDM can bundle these complex variables and construct effectively broadened molecular orbitals. Consequently the UV-features (but also the corresponding near-IR features) are smeared out *i.e.* monotonic broadband features [15,28–30].

We use Raman and FTIR to expand CDM to the vibronic regime and to further elucidate the structural variety of o-CVD PDA. This allows us to explore a more detailed picture on the influence of discrete structural designs on the electronic properties – including the functional groups and complex IR-electronic features. Thereby we hypothesize that the functional sites are integrative part of the conjugated system thus leading to intimately structures functions-on-conjugation. To examine this entanglement in detail, we relate FTIR and Raman spectra attained from the actual monomer dopamine hydrochloride in comparison with o-CVD PDA and solution PDA (Figs. 6, 7 and 8).

Previous Raman studies have focused the identification of the

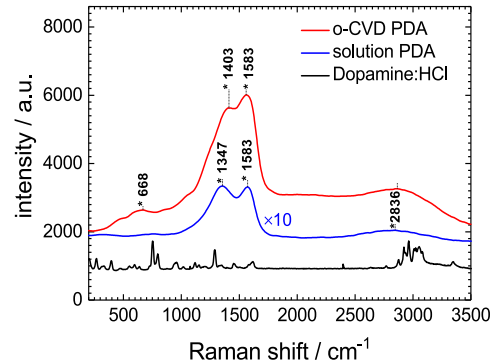


Fig. 6. Raman spectra of dopamine hydrochloride (black), solution PDA (blue, 10-fold expansion) and PDA synthesized by o-CVD (red). The signature peaks at 1403 cm^{-1} and 1583 cm^{-1} of o-CVD appear more intense in o-CVD PDA (as compared to solution PDA). Note 1403 cm^{-1} and 1583 cm^{-1} are aromatic C–N and C–C vibrations. (For interpretation of the references to colour in this figure legend, the reader is referred to the web version of this article.)

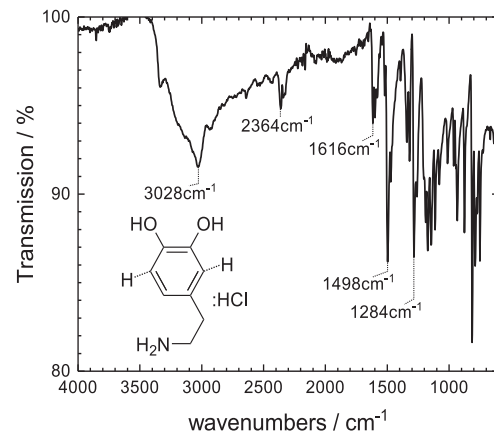


Fig. 7. The FTIR spectrum of dopamine hydrochloride (black).

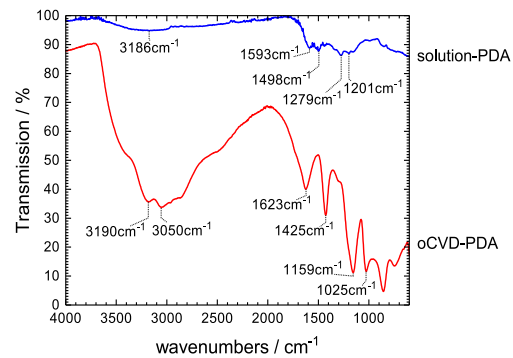


Fig. 8. The FTIR spectrum of solution processed PDA (blue) and PDA synthesized by o-CVD (red). (For interpretation of the references to colour in this figure legend, the reader is referred to the web version of this article.)

functional sites [31–33]. In this work we can use Raman to explore the distinct differences between solution and o-CVD PDA. In the monomer dopamine most pronounced peaks appear at 1616 cm^{-1} , 1455 cm^{-1} , 1349 cm^{-1} and 1287 cm^{-1} (first three assign the aromatic C–C stretching-, the last one aromatic C–H vibrations). In the polymer these peaks are changed - we observe three weak bands at 2836 cm^{-1} , 1583 cm^{-1} and 1347 cm^{-1} in solution-PDA. In o-CVD PDA, these bands are more intense (1583 cm^{-1} and 1403 cm^{-1}) - they refer to C–C vibrations of the aromatic units - hence we conclude that we actually surpass the H-aggregation towards effective C–C coupling in o-CVD PDA. Similarly, this effect is observed in the aromatic C–N bonds (Fig. 6) [31,32]. In o-CVD, weaker peaks at 2854 cm^{-1} and 668 cm^{-1} indicate suppressed aromatic O–H and the stretching and deformation of aromatic rings, respectively, again pointing at the increased C–C polymerization at cost of H-aggregation (Fig. 6).

Similar to Raman, also FTIR vibronic characterization reveals a strong interplay of hydrogen bonds triggering the formation of undesired broken conjugated networks from H-aggregation. We are interested to investigate the changes induced by o-CVD, in particular to explore if C–C coupling is distinct for the building of the desired functionalized poly(paraphenylene (PPP) type of polymer backbone. Therefore, we separately plot the FTIR spectrum of dopamine hydrochloride as control (Fig. 7). Here, we see the broad and strong bands in the $3000\text{--}3400\text{ cm}^{-1}$ region hallmark signatures for intermolecular hydrogen bond oscillations on (aromatic) O–H stretching vibrations [10]. In comparison, the NH_2 functionality in the hydrochloride adduct moves to lower frequency, such as the N–H bands emerge between 2700 cm^{-1} and 2250 cm^{-1} . The intense peaks below 1700 cm^{-1} are attributed to aromatic C=C and C–H bonds.

When polymerized in solution (solution-PDA, blue line), the features between 3400 and 2954 cm^{-1} and $3000\text{--}2100\text{ cm}^{-1}$ remained resembling at blurry and weakened intensity corresponding to the aromatic O–H stretching vibrations region as well as the amine functionality patterns at 1593 cm^{-1} and 1498 cm^{-1} , respectively (Fig. 8) [9,10,34,35].

On the contrary, the spectrum of o-CVD PDA (red line) reveals almost united broad bands in the regions of $3000\text{--}3400\text{ cm}^{-1}$ and $2856\text{--}1623\text{ cm}^{-1}$. We conclude that from the intensity, these features only partly render N–H or O–H vibrations, while the major oscillator corresponds to the broad polaron transition (maximum 3000 cm^{-1}). Moreover, the significant peaks between the $1660\text{--}1425\text{ cm}^{-1}$ relate to the conjugated, cyclic C=N group [10,34,35]. In parallel, strong carbonyl IR absorption bands are observed between 1590 and 1640 cm^{-1} , indicating the prevalent oxidation of the O–H functional groups to the corresponding ketones. Furthermore, the hallmarks of free charge carriers along the conjugated polymer chain are confirmed by the intense infrared-activated vibrations (IRAVs) in between 857 and 1075 cm^{-1} responsible for conductivity of the doped polymer films (as true for the polaron transition at 3000 cm^{-1}).

We denote that these fingerprint FTIR regime in o-CVD PDA is distinctively different to the solution PDA - peaks are by far more intense (we characterized similar amounts and the same setup) and, qualitatively, we clearly see IRAV, polaronic transitions and at the same time functional fingerprints such as cyclic C=N and carbonyl.

In order to confirm the free electron from shallow doping, we characterized the electrical conductivity of o-CVD PDA. Prior art in eumelanin-derived (hence PDA-related) structures has been explained conductivity resulting from protonic motion. Moreover, intrinsic polymer pigments such as UV-absorbing PDA are considered as amorphous and wide-bandgap organic semiconductors - both indications for high activation barriers to establish high mobility thus electrical conductivities. Hints of proton motion in eumelanin, however, gave the strong temperature dependence in presence of high humidity - the latter imperative ingredient to enable electrical transport: Without humidity, eumelanin and polydopamine show typically values across 10^{-13} S/m , while under humid atmosphere, these values increased up

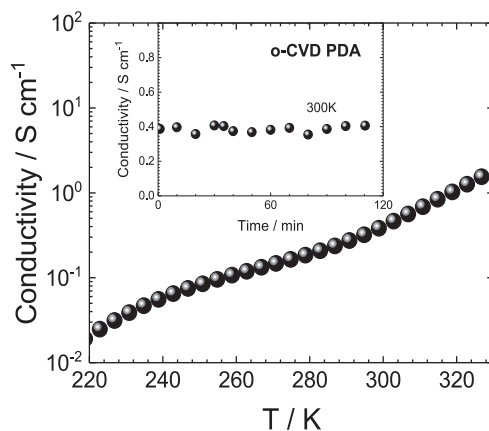


Fig. 9. Four probe conductivity measurement of o-CVD PDA films as a function of time (insert) and temperature.

to 10^{-5} S/m (e.g. at 100% humid atmosphere) [15,36,37]. Especially, Meredith et al. proposed melanin in general to behave as electronic-ionic hybrid conductors with ionic motion responsible for transport [13]. Herein, we report a persistent and substantially higher conductivity of PDA films observed through the o-CVD in H_2SO_4 . We achieve 0.4 S cm^{-1} at 300 K using 4-probe specimen (over a representative time scale and in inert conditions). Note that the temperature dependence reveals a steep rise according to Arrhenius type activation. Above 300 K , however, the transport mechanism is more complex (non-linear), thus we cannot exclude ionic contributions playing a more dominant role (Fig. 9).

We denote that we use controlled Helium atmosphere, while probing the current - leading us to the conclusion that the observed conductivity results predominantly from electrons rather than protonic/ionic movement.

The occurrence of electrical conductivity in PDA proves our strategy to utilize a stronger oxidant to improve the covalent path to form the desired chemical consistency *i.e.* the (functional) poly-paraphenylene. Obviously, the harsh conditions lead to further oxidation and as such include doping as in similar manner found for classic conducting polymers. The presence of free carriers is consequently evidenced by dc conductivity (actually 4 orders of magnitude higher than highest reported earlier for differently synthesized PDAs). We believe that represents a hallmark in biopolymers - a demonstration that tailoring synthesis can assist to implement bio-related themes to electronic devices to serve as catalytic systems or bio-organic conductive linkers.

4. Conclusion

In this study, we developed an o-CVD based synthesis pathway for the polymerization of dopamine to biopolymeric thin films. We adapted the deposition technique in order to generate PDA and demonstrate as such a versatile and simple way to form homogenous and conductive (thin-)films. Based on the spectroscopic analysis we confirm the improved C–C coupling along the polymer chain to render poly-paraphenylene backbone. The structural complexity created from the mutual reactions, intermediates and alternating monomers will continue to elucidate biopolymers in order to attain better control over the actual backbone formed. However, functional biopolymers have shown beneficial properties in particular towards bio-compatibility and stability in aqueous media. As such, we consider the design of an electrically conductive, highly functional and bio-inspired system as milestone in conductive polymers providing access to versatile linking

system between biological and organic matter by electrical signals. Among others, catalysis-related applications have targeted biopolymers - as such our simple route to form functional synthetic polydopamine will be relevant as versatile linker at the interface of ionic and electronic systems.

Acknowledgements

Philipp Stadler is thankful to OEAD (WTZ, IN10/2015) for financial support. Niyazi Serdar Sariciftci acknowledges financial support of the Austrian Science Foundation (FWF) [Z 222-N19] within the Wittgenstein Prize Scheme.

References

- [1] M. Sytnyk, E.D. Glowacki, S. Yakunin, G. Voss, W. Schofberger, D. Kriegner, J. Stangl, R. Trotta, C. Gollner, S. Tollabimazraehno, G. Romanazzi, Z. Bozkurt, M. Havlicek, N.S. Sariciftci, W. Heiss, Hydrogen-bonded organic semiconductor micro- and nanocrystals: from colloidal syntheses to (opto-)electronic devices, *J. Am. Chem. Soc.* 136 (2014) 16522–16532.
- [2] M. Irimia-Vladu, "Green" electronics: biodegradable and biocompatible materials and devices for sustainable future, *Chem. Soc. Rev.* 43 (2014) 588–610.
- [3] M. Irimia-Vladu, E. Glowacki, N.S. Sariciftci, S. Bauer, *Small Organic Molecules on Surfaces*, Springer-Verlag, Berlin Heidelberg, 2013.
- [4] E.D. Glowacki, H. Coskun, M.A. Blood-Forsythe, U. Monkowius, L. Leonat, M. Grzybowski, D. Gryko, M.S. White, A. Aspuru-Guzik, N.S. Sariciftci, Hydrogen-bonded diketopyrrolopyrrole (DPP) pigments as organic semiconductors, *Org. Electron.* 15 (2014) 3521–3528.
- [5] E.D. Glowacki, R.R. Tangorra, H. Coskun, D. Farka, A. Operamolla, Y. Kanbur, F. Milano, L. Giotta, G.M. Farinola, N.S. Sariciftci, Bioconjugation of hydrogen-bonded organic semiconductors with functional proteins, *J. Mater. Chem. C* 3 (2015) 6554–6564.
- [6] E.D. Glowacki, G. Romanazzi, C. Yumusak, H. Coskun, U. Monkowius, G. Voss, M. Burian, R.T. Lechner, N. Demitri, G.J. Redhammer, N. Sunger, G.P. Suranna, S. Sariciftci, Epindolidiones-versatile and stable hydrogen-bonded pigments for organic field-effect transistors and light-emitting diodes, *Adv. Funct. Mater.* 25 (2015) 776–787.
- [7] M. d'Ischia, A. Napolitano, V. Ball, C.-T. Chen, M.J. Buehler, Polydopamine and eumelanin: from structure–property relationships to a unified tailoring strategy, *Acc. Chem. Res.* 47 (2014) 3541–3550.
- [8] D.R. Dreyer, D.J. Miller, B.D. Freeman, D.R. Paul, C.W. Bielawski, Perspectives on poly(dopamine), *Chem. Sci.* 4 (2013) 3796–3802.
- [9] J. Liebscher, R. Mrowczynski, H.A. Scheidt, C. Filip, N.D. Hadade, R. Turcu, A. Bende, S. Beck, Structure of polydopamine: a never-ending story? *Langmuir* 29 (2013) 10539–10548.
- [10] F. Yu, S.G. Chen, Y. Chen, H.M. Li, L. Yang, Y.Y. Chen, Y.S. Yin, Experimental and theoretical analysis of polymerization reaction process on the polydopamine membranes and its corrosion protection properties for 304 stainless steel, *J. Mol. Struct.* 982 (2010) 152–161.
- [11] A. Huijser, A. Pezzella, V. Sundstrom, Functionality of epidermal melanin pigments: current knowledge on UV-dissipative mechanisms and research perspectives, *Phys. Chem. Chem. Phys.* 13 (2011) 9119–9127.
- [12] P. Meredith, T. Sarna, The physical and chemical properties of eumelanin, *Pigment Cell Res.* 19 (2006) 572–594.
- [13] A.B. Mostert, B.J. Powell, F.L. Pratt, G.R. Hanson, T. Sarna, I.R. Gentle, P. Meredith, Role of semiconductivity and ion transport in the electrical conduction of melanin, *Proc. Natl. Acad. Sci.* 109 (2012) 8943–8947.
- [14] A.A.R. Watt, J.P. Bothma, P. Meredith, The supramolecular structure of melanin, *Soft Matter* 5 (2009) 3754–3760.
- [15] Y.L. Liu, K.L. Ai, L.H. Lu, Polydopamine and its derivative materials: synthesis and promising applications in energy, environmental, and biomedical fields, *Chem. Rev.* 114 (2014) 5057–5115.
- [16] Y.L. Li, M.L. Liu, C.H. Xiang, Q.J. Xie, S.Z. Yao, Electrochemical quartz crystal microbalance study on growth and property of the polymer deposit at gold electrodes during oxidation of dopamine in aqueous solutions, *Thin Solid Films* 497 (2006) 270–278.
- [17] R.Z. Ouyang, H.P. Lei, H.X. Ju, Y.D. Xue, A molecularly imprinted copolymer designed for enantioselective recognition of glutamic acid, *Adv. Funct. Mater.* 17 (2007) 3223–3230.
- [18] V. Ball, D. Del Frari, M. Michel, M.J. Buehler, V. Toniazzo, M.K. Singh, J. Gracio, D. Ruch, Deposition mechanism and properties of thin polydopamine films for high added value applications in surface science at the nanoscale, *BioNanoSci.* 2 (2012) 16–34.
- [19] M.E. Lyngø, R. van der Westen, A. Postma, B. Stadler, Polydopamine-a nature-inspired polymer coating for biomedical science, *Nano* 3 (2011) 4916–4928.
- [20] A. Pezzella, A. Iadonisi, S. Valerio, L. Panzella, A. Napolitano, M. Adinolfi, M. d'Ischia, Disentangling Eumelanin "black Chromophore": visible absorption changes as signatures of oxidation state- and aggregation-dependent dynamic interactions in a model water-soluble 5,6-dihydroxyindole polymer, *J. Am. Chem. Soc.* 131 (2009) 15270–15275.
- [21] H. Coskun, A. Aljabour, P. De Luna, D. Farka, T. Greunz, D. Stifter, M. Kus, X.L. Zheng, M. Liu, A.W. Hassel, W. Schofberger, E.H. Sargent, N.S. Sariciftci, P. Stadler, Biofunctionalized conductive polymers enable efficient CO₂ electro-reduction, *Sci. Adv.* 3 (2017) e1700686.
- [22] V. Ball, D. Del Frari, V. Toniazzo, D. Ruch, Kinetics of polydopamine film deposition as a function of pH and dopamine concentration: insights in the polydopamine deposition mechanism, *J. Colloid Interface Sci.* 386 (2012) 366–372.
- [23] F. Bernsmann, V. Ball, F. Addiego, A. Ponche, M. Michel, J.J.D. Gracio, V. Toniazzo, D. Ruch, Dopamine-melanin film deposition depends on the used oxidant and buffer solution, *Langmuir* 27 (2011) 2819–2825.
- [24] H. Lee, S.M. Dellatore, W.M. Miller, P.B. Messersmith, Mussel-inspired surface chemistry for multifunctional coatings, *Science* 318 (2007) 426–430.
- [25] R.A. Zangmeister, T.A. Morris, M.J. Tarlow, Characterization of polydopamine thin films deposited at short times by autoxidation of dopamine, *Langmuir* 29 (2013) 8619–8628.
- [26] W.J. Barreto, S. Ponzoni, P. Sassi, A. Raman, UV-Vis study of catecholamines oxidized with Mn(III), *Spectrochim. Acta A* 55 (1998) 65–72.
- [27] J.D. Simon, Spectroscopic and dynamic studies of the epidermal chromophores trans-urocanic acid and eumelanin, *Acc. Chem. Res.* 33 (2000) 307–313.
- [28] J.M. Gallas, M. Eisner, Fluorescence of melanin dependence upon excitation wavelength and concentration, *Photochem. Photobiol.* 45 (1987) 595–600.
- [29] S.D. Kozikowski, L.J. Wolfram, R.R. Alfano, Fluorescence spectroscopy of Eumelanins, *IEEE J. Quantum Electron.* 20 (1984) 1379–1382.
- [30] P. Meredith, B.J. Powell, J. Riesz, S.P. Nighswander-Rempel, M.R. Pederson, E.G. Moore, Towards structure-property-function relationships for eumelanin, *Soft Matter* 2 (2006) 37–44.
- [31] W.C. Ye, D.A. Wang, H. Zhang, F. Zhou, W.M. Liu, Electrochemical growth of flowerlike gold nanoparticles on polydopamine modified ITO glass for SERS application, *Electrochim. Acta* 55 (2010) 2004–2009.
- [32] A. Samokhvalov, Y. Liu, J.D. Simon, Characterization of the Fe(III)-binding site in sepiolite eumelanin by resonance Raman confocal microspectroscopy, *Photochem. Photobiol.* 80 (2004) 84–88.
- [33] B. Fei, B.T. Qian, Z.Y. Yang, R.H. Wang, W.C. Liu, C.L. Mak, J.H. Xin, Coating carbon nanotubes by spontaneous oxidative polymerization of dopamine, *Carbon* 46 (2008) 1795–1797.
- [34] A. Janotti, S.B. Zhang, S.H. Wei, C.G. Van de Walle, Effects of hydrogen on the electronic properties of dilute GaAsN alloys, *Phys. Rev. Lett.* 89 (2002) 086403.
- [35] M.D. Shultz, J.U. Reveles, S.N. Khanna, E.E. Carpenter, Reactive nature of dopamine as a surface functionalization agent in iron oxide nanoparticles, *J. Am. Chem. Soc.* 129 (2007) 2482–2487.
- [36] J. Mcginness, P. Corry, P. Proctor, Amorphous-semiconductor switching in melanins, *Science* 183 (1974) 853–855.
- [37] J.E. McGinness, Mobility gaps: a mechanism for band gaps in melanins, *Science* 177 (1972) 896–897.

4.8 Manuscript 8

SCIENTIFIC REPORTS

OPEN

Influence of molecular designs on polaronic and vibrational transitions in a conjugated push-pull copolymer

Received: 11 December 2015

Accepted: 23 September 2016

Published: 12 October 2016

Christoph Cobet^{1,*}, Jacek Gasiorowski^{2,*}, Reghu Menon³, Kurt Hingerl¹, Stefanie Schlager⁴, Matthew S. White⁵, Helmut Neugebauer⁴, N. Serdar Sariciftci⁴ & Philipp Stadler⁴

Electron-phonon interactions of free charge-carriers in doped π -conjugated polymers are conceptually described by 1-dimensional (1D) delocalization. Thereby, polaronic transitions fit the 1D-Frohlich model in quasi-confined chains. However, recent developments in conjugated polymers have diversified the backbones to become elaborate heterocyclic macromolecules. Their complexity makes it difficult to investigate the electron-phonon coupling. In this work we resolve the electron-phonon interactions in the ground and doped state in a complex push-pull polymer. We focus on the polaronic transitions using *in-situ* spectroscopy to work out the differences between single-unit and push-pull systems to obtain the desired structural-electronic correlations in the doped state. We apply the classic 1D-Frohlich model to generate optical model fits. Interestingly, we find the 1D-approach in push-pull polarons in agreement to the model, pointing at the strong 1D-character and plain electronic structure of the push-pull structure. In contrast, polarons in the single-unit polymer emerge to a multi-dimensional problem difficult to resolve due to their anisotropy. Thus, we report an enhancement of the 1D-character by the push-pull concept in the doped state - an important view in light of the main purpose of push-pull polymers for photovoltaic devices.

In-situ (operando) spectroscopy on free carrier induced absorption in π -conjugated polymers displays the pronounced electron-phonon coupling due to π -fluctuations. Similar to Raman modes in the ground state, vibronic terms in doped polymers known as infrared-activated vibrations (IRAVs) display symmetry breaking due to presence of charge carriers¹⁻⁴. Originally, these modes have been described in doped and photoexcited simple conjugated systems such as polyacetylene and polythiophenes, where all CSC, CCC and CCH vibrations can be assigned to the spectral response. Meanwhile, polymers developed to more complicated macromolecular structures, so that one-to-one vibrational assignments become difficult. However, there exists crucial interest to resolve the doped state electronics as it provides an insight to optoelectronic devices during operation⁵⁻¹⁰. In this work we took such an *in-situ* operando view to these electronic transitions, which emerge only in the doped state. Electronically these are polaron transitions, which qualitatively relate to the coupling of phonons and free charge carriers. Fitting of these transitions allows an estimation of the strength of inter- and intramolecular forces and hence provides substantial information about carrier dynamics, which can be directly proved in device-structures. We elucidate these dynamics for the first time in a sophisticated push-pull polymer such as PBDTTT-c both in the material and in a device-related style. Interestingly we find agreement with earlier results on 1D delocalization, which appears specifically enhanced by push-pull molecular structures.

¹Center for Surface- and Nanoanalytics, Johannes Kepler University of Linz, A-4040 Linz, Austria. ²Physics Department, Technical University of Chemnitz, 09107 Chemnitz, Germany. ³Department of Physics, Indian Institute of Science, Bangalore 560012, India. ⁴Institute of Physical Chemistry, Johannes Kepler University Linz, Altenbergerstr. 69, 4040 Linz, Austria. ⁵Department of Physics, University of Vermont, Cook Building, 82 University Place, University of Vermont Burlington, VT 05405-0125, USA. *These authors contributed equally to this work. Correspondence and requests for materials should be addressed to P.S. (email: philipp.stadler@jku.at)

Results

Typically polarons emerge from electron-phonon interactions. Their binding energy and the intensity of IR absorption due to polaron excitations scales with a dimensionless coupling constant according to Froehlich

$$\alpha = \frac{e^2}{\hbar} \sqrt{\frac{m_e}{2\hbar\omega_{\text{phonon}}}} \cdot (\varepsilon_{\infty}^{-1} - \varepsilon_0^{-1}) \quad (1)$$

where m_e the effective electron mass and ω_{ph} is the LO-phonon frequency. In conjugated polymers polaron absorption depends strongly on dielectric function between ε_{∞} and ε_0 (high-frequency electronic and static dielectric constant). The term $(\varepsilon_{\infty}^{-1} - \varepsilon_0^{-1})$ defines the effective dielectric constant related to the lattice polarisability. For a given electronic polarisability ε_{∞} maximizes if the measurable static dielectric constant becomes large. Furthermore it is evident that the electron-phonon coupling and thus the intensity of polaronic absorption increase with electron localization i.e. in case of a high effective electron mass m_e .

In this study we compare regioregular poly-3-hexylthiophene (rr-P3HT) and a prominent push-pull system poly[(4,8-bis-(2-ethylhexyloxy)-benzo(1,2-b:4,5-b')dithiophene)-2,6-diyl-alt-(4-(2-ethylhexanoyl)-thieno[3,4-b]thiophene)-2,6-diyl] (PBDTTT-c)^{11,12}. The latter reflects exactly recent developments, where intramolecular dipoles red-shift the band gap to explore infrared (IR) activity. In PBDTTT-c, it is benzodithiophene and thienothiophene, which serve as sequential donor-acceptor pair¹³⁻¹⁸. The IR-activity in push-pull polymers usually pays off by an extraordinary molecular complexity - the number of carbon atoms per monomer increased by a factor of 4 from P3HT to PBDTTT-c. Typically, push-pull polymers afford also an elaborate side-chain engineering to obtain solubility¹⁹⁻²³. Taking PBDTTT-c as an example, little is known about the influence of such complexity to the polaron levels. Therefore we pursue an operando spectroscopic study to achieve this insight, in particular on polaron dynamics²⁴⁻³⁰.

On basis of ground-state and doped-state data we create optical models to visualise polaron differences. Generic oscillators are useful here to assemble these corresponding delta-functions with strong broadening effects (Lorentz-type or Gaussian-type). This allows us to conclude on the molecular interactions dominating the solid-state system^{31,32}. Interestingly we find the complex push-pull polymer to suppress intermolecular forces consequently fitting well 1D-delocalization. This is opposite to highly-crystalline rr-P3HT, where the wave functions spread into inter- and intramolecular identities with diverging intensity. Our results show, that the push-pull concept strengthens the 1D-character - it can drive a conjugated polymer with complex molecular structure towards a simple advantageous optoelectronic structural fingerprint.

The experimental optical model for the pristine polymers (Fig. 1) are shown in the dielectric functions (and the absorption coefficient α) for PBDTTT-c and rr-P3HT, respectively. The latter (Fig. 1a) has maxima at 2.1 and 2.3 eV (imaginary part left scale, ε_2). The feature splitting is a signature of intra- and intermolecular alignment and therewith $\pi - \pi$ stacking³³. This is true for the absorption features between 2 and 4 eV. In detail the shoulder at 2.07 eV is attributed to interchain-delocalized exciton, while the following peaks at 2.27 eV and 2.49 eV are phonon replica of the exciton. The broad absorption shoulder at 2.6 eV refers to the screened $\pi - \pi^*$ transition³⁴. The onset of the absorption is found at 1.9 eV³⁵. The dispersion - consistent with absorption - is reflected in the plot of the real part ε_1 having two strong variations that are connected with two oscillators with maxima at 1.95 and 2.1 eV. All mentioned assignments fit measurements on films and diluted rr-P3HT. Thus we derive a consistent value for the average LO-phonon frequency ω_{ph} at 190 to 200 meV. PBDTTT-c shows different absorption features: Uniting donor (thieno[2,3-b]thiophene) and acceptor (benzodithiophene with alkoxy-side-chains) red-shift the absorption onset to 1.55 eV. The dielectric functions is presented in Fig. 1b with two sharp peaks at 1.75 eV ($\pi - \pi^*$ transition) and 1.9 eV. Unlike rr-P3HT, this splitting is not originated from $\pi - \pi$ - stacking but rather a fingerprint of the push-pull character. In addition to the dielectric function we include the absorption coefficients α for both polymers (Fig. 1c). In rr-P3HT, a different spectral shape of α as compared to ε_2 is apparent - it originates from the important role of the refractive index n_i in thin films. The absorption coefficient has a broad peak with maximum at 2.4 eV, which is a result of dispersion from three oscillators describing the optical transitions. Differently, the absorption coefficient for PBDTTT-c correlates better to the ε_1 -function.

For conducting *in-situ* spectroscopy on the doped-state, we create a long-lived (persistent) species, which allows elucidation by variable angle spectroscopic ellipsometry (VASE) and attenuated total reflection (ATR) FTIR. Persistency is achieved by iodine-doping rr-P3HT and PBDTTT-c while recording spectra. Alternatively, dynamic doping uses the photo-excitation of the polymer in presence of electron acceptor phenyl-C61-butyrac acid methyl ester (PCBM). The latter method mimics the charge-separation processes in an organic photovoltaic cell (bulk-heterojunction). We denote that photo-induced *in-situ* absorption (PIA) measurements are presented for ATR-FTIR in the mid-IR^{36,37}. Combined with persistent doping we obtain a complete survey covering the spectral region between 5.5 and 0.075 eV exactly where vibronic transitions (IRAVs), polaron transitions ($P_{1,2}$) and ground state transitions occur (Fig. 2).

At first we present datasets in the UV-visible and near-IR (5 to 1.0 eV) of doped-state levels introduced by persistent chemical doping (Fig. 3). We show the real (ε_1) and imaginary part (ε_2) of the dielectric function of doped polymers rr-P3HT* and PBDTTT-c*, respectively. For P3HT* ε_2 shows a quenched and broad main absorption peak signal with a maximum at 2.3 eV and a transition between localized polaron state at 1.5 eV, denoted as P_1 . Above 3 eV we cannot observe changes as compared to the ground-state, so we conclude that doping affects mainly π -levels (polarons disrupt loosely-bound HOMO and LUMO states). Contributions from iodine are not apparent (rr-P3HT and PBDTTT-c*). The rr-P3HT* real dielectric function ε_1 repeats the ground state oscillator quenching and displays the concomitant formation of an in-gap P_1 transition at 1.5 eV.

For PBDTTT-c*, we see a similar impact: Quenching in the active absorption region and rise of P_1 . The maxima of PBDTTT-c* are red-shifted as compared to rr-P3HT* due to the lower absorption edge in the ground state.

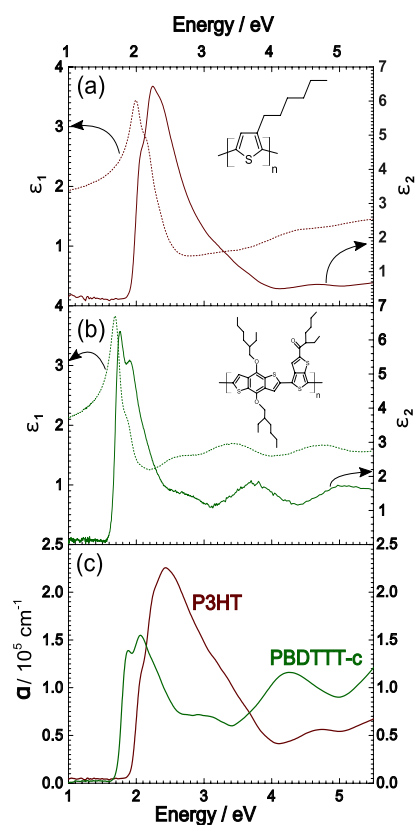


Figure 1. Ellipsometric spectra of ground state rr-P3HT and PBDTTT-c including molecular structure. (a,b) The dielectric functions ϵ_1 , ϵ_2 correspond to the real (left, ϵ_1) and imaginary (right, ϵ_2) part as indicated in the graphs. In (c) we plot the absorption coefficient of both polymers.

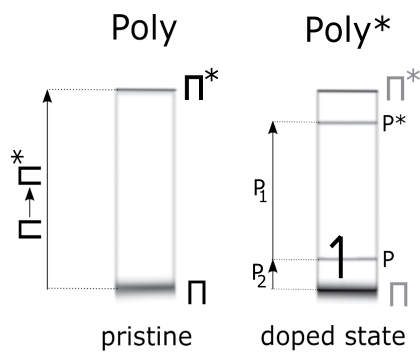


Figure 2. Schematic illustration of the ground state and doped state in a π -conjugated polymer. The characteristic in-gap polaron transitions $P_{1,2}$ are indicated.

Concretely, P_1 arises at 1.2 eV (ϵ_2) (absorption coefficients in Fig. 3c). Between P3HT and P3HT* the decrease of the original absorption feature is significant, which is not the case between PBDTTT-c and PBDTTT-c* - the quantitative changes due to doping are minor, which correlates to the higher oxidation potential of PBDTTT-c.

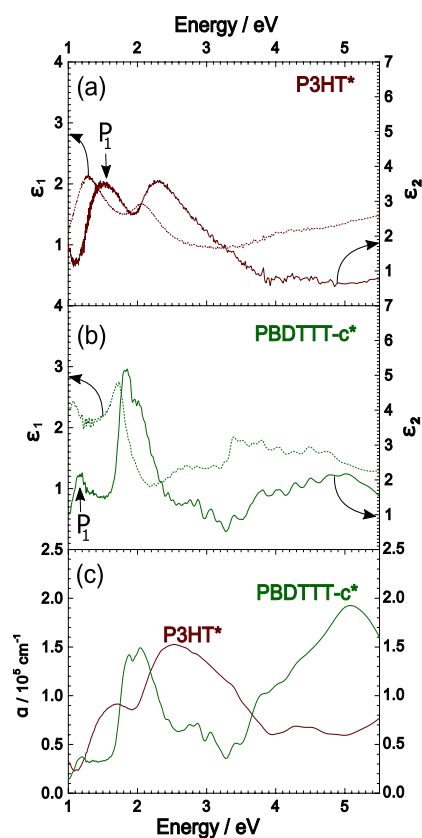


Figure 3. Ellipsometric doped-state spectra on persistently doped rr-P3HT and PBDTTT-c. In (a,b) the rise of the P₁ polarons for both systems (with different intensities) is indicated. The response function of the absorption coefficient in the doped state is also shown in (c).

To probe the low-energy regime with the continuum polaronic excitations (P₂) and the IRAVs, we change to *in-situ* ATR-FTIR to cover the spectral mid-IR region between 0.6 to 0.075 eV. For P3HT* we see a characteristic broad P₂ feature above 0.18 eV to 0.19 with a maximum at 0.35 eV. Below 0.18 eV IRAVs emerge characterized by multiple, intense absorption peaks. In parallel, PBDTTT-c* exhibits a broad P₂ transition with a maximum at 0.39 eV including IRAVs. The latter are broadened as compared to rr-P3HT.

In ATR-FTIR, photo-induced absorption is accessible too. We crosschecked, how doped-state levels are affected by the origin of excitation. In both polymers we cannot report on substantial differences in the spectral response (Fig. 4), unless taking into account quantitative evaluations. Persistent doping with iodide yield quantitative changes, while photo-induced changes are relatively small and, though noise-reduced due to lock-in data acquisition, less precise. Qualitatively, we find the maxima for IRAVs and P₂ transitions at the same positions with minor deviations as indicated in Fig. 4, independently, which method for excitation has been applied. For comparison, we sum up all data on in-gap states in Table 1.

Discussion

The interesting part in evaluation of the presented doped-state spectra affects the differences within the polymer systems. Common rr-P3HT has a simple molecular design but features a complex physical insight: Our approach fitting spectra with a minimum amount of generic oscillators fails, when we stick to a 1D Froehlich-model (details explained in SI). As already discussed in Fig. 1c, rr-P3HT exhibits strong dispersion effects in the ground state likely originating from the strong π -stacking. Therefore the minimum amount of generic oscillators used to reasonably fit the data are 3, which are illustrated in Fig. 4, left. The polaronic absorption lines are then in agreement, if additional intermolecular forces are considered. In the literature, this effect has been also assigned as 2D-polaron^{3,38–40} - accordingly we illustrate the in-gap states in a schematic (Fig. 5). In light of its complex electronic insight, PBDTTT-c appears plain and simple, as far as doped-state dynamics are concerned. This is in contrast to its complicated molecular design consisting of two heterocycles and extensive side-chain branches. In PBDTTT-c, we observe classic 1D-delocalization in agreement

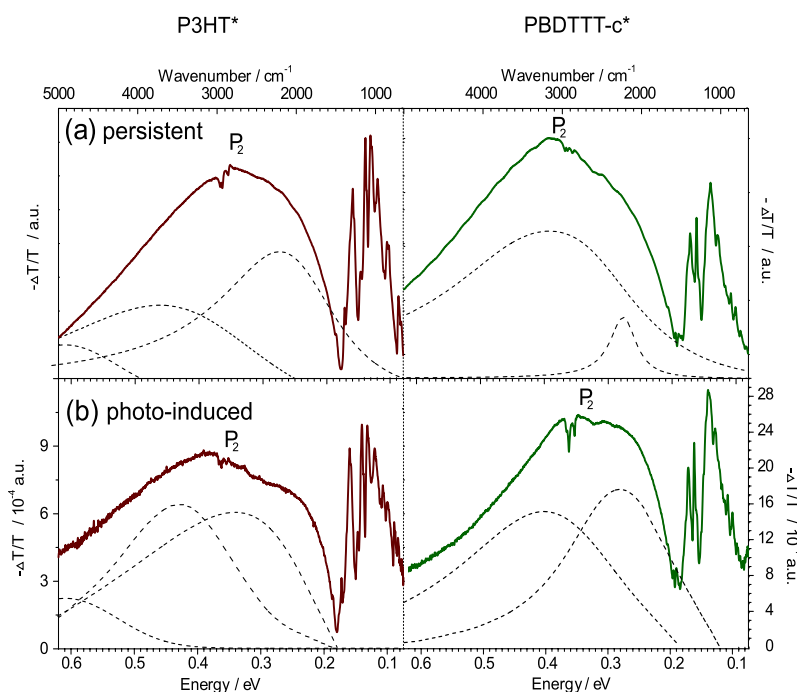


Figure 4. Juxtaposition of persistently- and photodoped *in-situ* spectra by ATR-FTIR exploring P_2 transitions. In the mid-IR regime rr-P3HT (left) and PBDTTT-c (right) show the broad polaronic transitions (P_2) and lower energy IR-Active Vibrational (IRAV) modes. We included generic oscillators (dashed lines) from the underlying model fit - their superposition renders the experimental spectra in precision.

Polymer	absorption edge	π - π^*	π - π -stacking	P_1	P_2
rr-P3HT	1.90	2.30	2.10	1.50	0.35
PBDTTT-c	1.55	1.75	1.90	1.20	0.39

Table 1. Summary of all measured optical transitions referring to the peak maxima (all units in eV). We denote the broadened shape of polaronic transitions.

with the spectral response. The absorption line shape fits a textbook example for 1D Froehlich polaron excitations with relatively high coupling strength and higher effective hole mass. We fit the spectra using two generic oscillators, (Fig. 4, right) and find a proper match with the doped-state spectral features. The latter is not possible in rr-P3HT: P_2 transitions are weaker despite more intense P_1 . We conclude that we have simply more polaronic states, a weaker Froehlich coupling constant, thus less 1D-character. These conclusions are furthermore backed by the ground state spectra: In PBDTTT-c dispersion effects are minor as compared to rr-P3HT seen in the qualitative match of ϵ_2 and the absorption coefficient α . In summary, we show that PBDTTT-c fits the classic description of a 1D Froehlich polaron, while rr-P3HT has more complex spectral responses. This structural insight backs the concept of a 1D-polymers hence 1D-delocalization enhanced by push-pull systems. We conclude it is the inferior molecular symmetry of PBDTTT-c, which features suppressed π -stacking and thus translates to a plain doped-state electronic structure. This work aims to visualize the transition from pristine form to a doped-state for PBDTTT-c as part of a prominent family of push-pull type IR-active polymers for high-performance polymer photovoltaic cells. In direct comparison to rr-P3HT having a simpler core unit and stronger tendency to crystallize, PBDTTT-c offers suppressed π -stacking due to its complex structural asymmetry. In first view we find correlative spectral responses - both systems show intense polaron transitions and IRAV bands. The detailed scans, however, reveal the distinct difference, which highlights the simplicity of the electronic structure of PBDTTT-c. The systems resembles a similar response function in the doped state, as found for original conjugated polymers following the concept of 1D-delocalization. This insight points at the impact of molecular design, which can conserve a major polymer fingerprint - a 1D-character packed in an advanced, sophisticated chemical structure. In light of the high performance response from PBDTTT-c family in organic photovoltaics, our study supports the direction to assemble molecular designs, that foster a 1D-character.

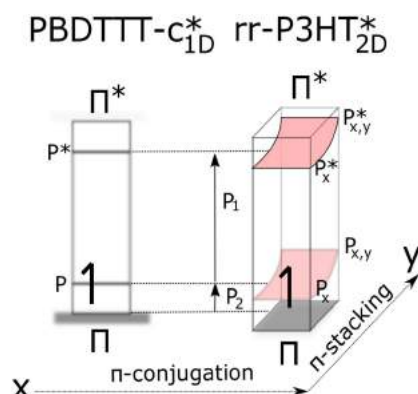


Figure 5. Simplified schematic of 1D and 2D-polarons as found for PBDTTT-c and rr-P3HT. We point at the main finding of *in-situ* spectroscopy that the push-pull system enhances 1D-delocalization, while the single unit system shows a comparatively complex doped-state electronic structure.

Methods

PBDTTT-c was purchased from Solarmer Inc., and used as received. P3HT bought from Rieke Metals (98%) and has been purified prior to use by re-crystallization in n-hexane. As electron acceptor the soluble fullerene derivative, (6,6)-phenyl-C61-butiric acid methyl ester (PCBM) was used. PCBM was purchased from Solenne Inc. (Groningen, The Netherlands). PBDTTT-c or P3HT and PBDTTT-c:PCBM or P3HT:PCBM (1:1 weight ratio) were dissolved in chlorobenzene with concentration of 10 g L^{-1} and 20 g L^{-1} , respectively.

To measure the optical properties of the pristine and doped materials, NIR-Vis-UV variable angle spectroscopic ellipsometry (VASE) is used. The characterization is performed using a Woollam M-2000 (rotating compensator) ellipsometer (spectral range 0.73 to 6.5 eV). VASE results are analysed using WVASE software on basis of three phase layer model. The polymer film dielectric function is fitted using a parametric dispersion model based on generic oscillators. The layer thickness is measure beforehand by DekTak (Bruker). The as-derived preliminary optical model is consequently refined by point-to-point fits and the resulting ε_1 - and ε_2 -functions. The results are crosschecked in terms of the Kramers-Kronig consistency^{41,42}. All VASE measurements are performed on polymer layers deposited by spin coating of the polymer solution on a glass substrate. Doped-state *in-situ* spectra are generated by exposing the sample to iodine vapor - after a saturation time (10 min) numerous VASE-spectra are recorded subsequently³¹.

The mid-IR spectra are recorded using a FTIR spectrometer (Bruker IFS66S) in attenuated total reflection (ATR) mode. A ZnSe crystal is used as the reflection element. The setup used for *in-situ* probing is presented in the supplementary part. Doped-state spectra are recorded in presence of an iodine crystal, which is placed in a closed volume box on top of the polymer-film and ATR-FTIR spectra are recorded *in-situ*. The plots relate the ground state signal (T_{ref} , T is transmission) and subsequent doped-state spectra Ts to a differential spectra ($-\Delta T/T$). We denote that ($-\Delta T/T$) is absorbance A, in first approximation. For quantitative evaluations, we consider the intensity of transmission T as product of all 6 reflections (T equals R^6). We can calculate intensities including Fresnel reflection coefficients assuming an isotropic material and the single attenuated total reflection from ZnSe-parallelepiped at 45° total reflection. In ATR-mode also photo-induced absorption is measured. We apply a lock-in mode, amplified by the FTIR spectrometer and a mechanical shutter. The polymer-fullerene blend is deposited on a ZnSe crystal and photo-excited at 532 nm (P3HT) and 664 nm (PBDTTT-c) diode-lasers through the shutter. A differential spectra ($-\Delta T/T$, T_{dark} and T_{light}) are calculated from sequences of 1000 repetitions of recording 10 single beam spectra in the dark and light, respectively, to reduce the noise level. We denote that photo-induced VASE is not accessible with our equipment to date.

To evaluate the ATR-FTIR spectra for a quantitative analysis we relate the intensities of polarons and IRAVs to the electron-phonon coupling. The Froehlich interaction turns out to be suitable for polymers: The basis of the model is given by following Hamiltonian⁴¹:

$$H_{Fr} = \sum \left(\frac{i \cdot C_F}{q} \right) \left\{ e_q^+ \cdot \exp[i(\vec{q} \cdot \vec{r} - \omega_{ph}t)] - \text{c.c.} \right\} \quad (2)$$

where the prefactor C_F is given by

$$C_F \propto e \cdot \left[\frac{2\pi\hbar\omega_{ph}}{NV} (\varepsilon_\infty^{-1} - \varepsilon_0^{-1}) \right]^{\frac{1}{2}} \quad (3)$$

In those equations q is a phonon wave vector, c_q^+ and c.c. are creation and annihilation operators, ω_{ph} is a phonon frequency, N is the number of charges and V is a volume. The values of ε_∞ and ε_0 are high- and low-frequency dielectric constants. In this picture, electron phonon coupling is either enhanced, if the phonon frequency ω_{ph} increases, or when the “static” dielectric constant ε_0 (below the energy of a selected vibronic transition) is strongly different from the dielectric constant ε_∞ (above the energy of a selected vibronic transition), or equivalently,

$$(\varepsilon_\infty^{-1} - \varepsilon_0^{-1}) = \frac{\varepsilon_0 - \varepsilon_\infty}{\varepsilon_0 \varepsilon_\infty} \quad (4)$$

decreases. Our assumption is now based on the substitution of the phonon frequency by vibrational frequencies - in particular the IRAVs, which appear due to symmetry breaking (polymer deformation). Each one contributes to the difference ($\varepsilon_0 - \varepsilon_\infty$), as well as in the strength of the polaron transition. For the case of chemical doping of rr-P3HT it is clear that the static dipole moment ε_0 increases, which means that ε_0^{-1} vanishes and the coupling coefficient increases in the Fröhlich model - thus allowing a quantitative interpretation.

References

- Girlando, A., Painelli, A. & Soos, Z. G. Electron-phonon coupling in conjugated polymers: Reference force field and transferable coupling constants for polyacetylene. *The Journal of Chemical Physics* **98**, 7459, doi: 10.1063/1.464684 (1993).
- Deng, W.-Q. *et al.* Quantitative prediction of charge mobilities of π -stacked systems by first-principles simulation. *Nature Protocols* **10**, 632–642, doi: 10.1038/nprot.2015.038 (2015).
- Ehrenfreund, E., Vardeny, Z., Brafman, O. & Horovitz, B. Amplitude and phase modes in trans -polyacetylene: Resonant Raman scattering and induced infrared activity. *Physical Review B* **36**, 1535–1553, doi: 10.1103/PhysRevB.36.1535 (1987).
- Lopez-Navarrete, J., Tian, B. & Zerbi, G. Relation between effective conjugation, vibrational force constants and electronic properties in polyconjugated materials. *Solid State Communications* **74**, 199–202, doi: 10.1016/0038-1098(90)91020-H (1990).
- Lee, K. *et al.* Photoinduced absorption and photoinduced reflectance in conducting polymer/methanofullerene films: Nonlinear-optical changes in the complex index of refraction. *Physical Review B* **54**, 10525–10529, doi: 10.1103/PhysRevB.54.10525 (1996).
- Mizrahi, U., Shtrichman, I., Gershoni, D., Ehrenfreund, E. & Vardeny, Z. Picosecond time resolved photoinduced absorption by infrared active vibrations as a probe for charge photogeneration in MEH-PPV/C60 composites. *Synthetic Metals* **102**, 1182–1185, doi: 10.1016/S0379-6779(98)00316-6 (1999).
- Brabec, C. *et al.* Photoinduced FT-IR spectroscopy and CW-photocurrent measurements of conjugated polymers and fullerenes blended into a conventional polymer matrix. *Solar Energy Materials and Solar Cells* **61**, 19–33, doi: 10.1016/S0927-0248(99)00093-8 (2000).
- Wohlgenannt, M., An, C. P. & Vardeny, Z. V. Polarons in Ladder-Type Polymer Films; Recombination Channels and Electron-Phonon Coupling. *The Journal of Physical Chemistry B* **104**, 3846–3850, doi: 10.1021/jp993370m (2000).
- Luzzati, S., Panigoni, M. & Catellani, M. Spectroscopic evidences of photoinduced charge transfer in blends of C60 and thiophene-based copolymers with a tunable energy gap. *Synthetic Metals* **116**, 171–174, doi: 10.1016/S0379-6779(00)00480-X (2001).
- Osterbacka, R., Jiang, X. M., An, C. P., Horovitz, B. & Vardeny, Z. V. Photoinduced Quantum Interference Antiresonances in Conjugated Polymers. *Physical Review Letters* **88**, 226401, doi: 10.1103/PhysRevLett.88.226401 (2002).
- Sirringhaus, H. *et al.* Two-dimensional charge transport in self-organized, high-mobility conjugated polymers. *Nature* **401**, 685–688, doi: 10.1038/44359 (1999).
- Kline, R. J. *et al.* Dependence of Regioregular Poly(3-hexylthiophene) Film Morphology and Field-Effect Mobility on Molecular Weight. *Macromolecules* **38**, 3312–3319, doi: 10.1021/ma047415f (2005).
- Svensson, M. *et al.* High-Performance Polymer Solar Cells of an Alternating Polyfluorene Copolymer and a Fullerene Derivative. *Advanced Materials* **15**, 988–991, doi: 10.1002/adma.200304150 (2003).
- Jespersen, K. G. *et al.* The electronic states of polyfluorene copolymers with alternating donor-acceptor units. *The Journal of Chemical Physics* **121**, 12613, doi: 10.1063/1.1817873 (2004).
- Cheng, Y.-J., Yang, S.-H. & Hsu, C.-S. Synthesis of Conjugated Polymers for Organic Solar Cell Applications. *Chemical Reviews* **109**, 5868–5923, doi: 10.1021/cr900182s (2009).
- Hou, J. *et al.* Synthesis of a Low Band Gap Polymer and Its Application in Highly Efficient Polymer Solar Cells. *Journal of the American Chemical Society* **131**, 15586–15587, doi: 10.1021/ja906497s (2009).
- Brabec, C. J. *et al.* Polymer-Fullerene Bulk-Heterojunction Solar Cells. *Advanced Materials* **22**, 3839–3856, doi: 10.1002/adma.200903697 (2010).
- Pilego, C. *et al.* Synthetic Control of Structural Order in N-Alkylthieno[3,4-c]pyrrole-4,6-dione-Based Polymers for Efficient Solar Cells. *Journal of the American Chemical Society* **132**, 7595–7597, doi: 10.1021/ja103275u (2010).
- Small, C. E. *et al.* High-efficiency inverted dithienogermole-thienopyrrolodione-based polymer solar cells. *Nature Photonics* **6**, 115–120, doi: 10.1038/nphoton.2011.317 (2011).
- He, Z. *et al.* Enhanced power-conversion efficiency in polymer solar cells using an inverted device structure. *Nature Photonics* **6**, 593–597, doi: 10.1038/nphoton.2012.190 (2012).
- Chen, H.-Y. *et al.* Polymer solar cells with enhanced open-circuit voltage and efficiency. *Nature Photonics* **3**, 649–653, doi: 10.1038/nphoton.2009.192 (2009).
- Lǐ, W. *et al.* Efficient Small Bandgap Polymer Solar Cells with High Fill Factors for 300 nm Thick Films. *Advanced Materials* **25**, 3182–3186, doi: 10.1002/adma.201300017 (2013).
- Peet, J. *et al.* Bulk heterojunction solar cells with thick active layers and high fill factors enabled by a bithiophene-co-thiazolothiazole push-pull copolymer. *Applied Physics Letters* **98**, 043301, doi: 10.1063/1.3544940 (2011).
- Srinivasan, S., Neugebauer, H. & Sariciftci, N. S. Electrochemically induced IRAV modes of BeCHA-PPV studied with *in situ* FTIR-ATR Spectroscopy. *Synthetic Metals* **84**, 635–636, doi: 10.1016/S0379-6779(96)04084-2 (1997).
- Lee, K. *et al.* Infrared photoexcitation spectra of conducting polymer/methanofullerene films. *Synthetic Metals* **84**, 857–858, doi: 10.1016/S0379-6779(96)04181-1 (1997).
- Brabec, C. J. *et al.* The spin signature of charged photoexcitations in carbazolyl substituted polydiacetylene. *The Journal of Chemical Physics* **111**, 10354, doi: 10.1063/1.480384 (1999).
- Neugebauer, H. *et al.* Infrared spectroelectrochemical investigations on the doping of soluble poly(isothianaphthene methine) (PIM). *The Journal of Chemical Physics* **110**, 12108, doi: 10.1063/1.479146 (1999).
- Johansson, H. *et al.* Photoinduced ft-ir spectroscopy of conjugated polymer/fullerene composites embedded into conventional host polymer matrices. *Synthetic Metals* **101**, 192–193, doi: 10.1016/S0379-6779(98)01108-4 (1999).
- Kvarnström, C. *et al.* *In situ* ftir spectroelectrochemical characterization of poly(3,4-ethylenedioxythiophene) films. *Synthetic Metals* **101**, 66, doi: 10.1016/S0379-6779(98)01133-3 (1999).
- Miller, E. K., Hingerl, K., Brabec, C. J., Heeger, A. J. & Sariciftci, N. S. Reflectance anisotropy spectroscopy of oriented films of semiconducting polymers. *The Journal of Chemical Physics* **113**, 789, doi: 10.1063/1.481853 (2000).

31. Gasiorowski, J. *et al.* Dielectric Function of Undoped and Doped Poly[2-methoxy-5-(3',7'-dimethyloctyloxy)-1,4-phenylenevinylene] by Ellipsometry in a Wide Spectral Range. *The Journal of Physical Chemistry C* **117**, 22010–22016, doi: 10.1021/jp4061957 (2013).
32. Gasiorowski, J., Menon, R., Hingerl, K., Dachev, M. & Sariciftci, N. S. Surface morphology, optical properties and conductivity changes of poly(3,4-ethylenedioxythiophene):poly(styrenesulfonate) by using additives. *Thin Solid Films* **536**, 211–215, doi: 10.1016/j.tsf.2013.03.1247 (2013).
33. Kim, Y. *et al.* A strong regioregularity effect in self-organizing conjugated polymer films and high-efficiency polythiophene:fullerene solar cells. *Nature Materials* **5**, 197–203, doi: 10.1038/nmat1574 (2006).
34. Lioudakis, L. *et al.* Ultrafast carrier dynamics on conjugated poly(3-hexylthiophene)/[6,6]-phenylC₆₁-butyric acid methyl ester composites. *Applied Physics Letters* **91**, 111117, doi: 10.1063/1.2785120 (2007).
35. Zhang, Y. *et al.* Efficient Polymer Solar Cells Based on the Copolymers of Benzodithiophene and Thienopyrroledione. *Chemistry of Materials* **22**, 2696–2698, doi: 10.1021/cm100417z (2010).
36. Kvarnström, C., Neugebauer, H., Ivaska, A. & Sariciftci, N. Vibrational signatures of electrochemical p- and n-doping of poly(3,4-ethylenedioxythiophene) films: an *in situ* attenuated total reflection Fourier transform infrared (ATR-FTIR) study. *Journal of Molecular Structure* **521**, 271–277, doi: 10.1016/S0022-2860(99)00442-1 (2000).
37. Damlin, P., Kvarnström, C. & Ivaska, A. Electrochemical synthesis and *in situ* spectroelectrochemical characterization of poly(3,4-ethylenedioxythiophene) (PEDOT) in room temperature ionic liquids. *Journal of Electroanalytical Chemistry* **570**, 113–122, doi: 10.1016/j.jelechem.2004.03.023 (2004).
38. Österbacka, R. Two-Dimensional Electronic Excitations in Self-Assembled Conjugated Polymer Nanocrystals. *Science* **287**, 839–842, doi: 10.1126/science.287.5454.839 (2000).
39. Beljonne, D. *et al.* Optical Signature of Delocalized Polarons in Conjugated Polymers. *Advanced Functional Materials* **11**, 229–234, doi: 10.1002/1616-3028%28200106%2911%3A3%3C229%3A%3AAID-ADFM229%3E3.0.CO%3B2-L (2001).
40. Wohlgenannt, M., Jiang, X. M. & Vardeny, Z. V. Confined and delocalized polarons in conjugated oligomers and polymers: A study of the effective conjugation length. *Physical Review B* **69**, 241204, doi: 10.1103/PhysRevB.69.241204 (2004).
41. Yu, P. Y. & Cardona, M. *Introduction* 1–15, doi: 10.1007/978-3-642-00710-1_1 (2010).
42. Gasiorowski, J., Mardare, A. I., Sariciftci, N. S. & Hassel, A. W. Electrochemical characterization of sub-micro-gram amounts of organic semiconductors using scanning droplet cell microscopy. *Journal of Electroanalytical Chemistry* **691**, 77–82, doi: 10.1016/j.jelechem.2012.11.008 (2013).

Acknowledgements

P.S., R.M. and N.S.S. are grateful to OEAD (WTZ, IN10/2015) for financial support. P.S., S.S. and N.S.S. gratefully acknowledge the financial support from the Austrian Fund for Advancement of Science (FWF) within the Wittgenstein Prize scheme (Z222-N19 Solare Energieumwandlung).

Author Contributions

N.S.S., R.M., J.G., M.S.W. and P.S. designed and directed the study. J.G. contributed to all the experimental work. J.G. and P.S. carried out the *in-situ* excited-state spectroscopy. J.G., S.S., M.S.W. and P.S. designed the film-growth process and carried out the experimental work. C.C., K.H. and J.G. performed the optical modelling. C.C., K.H., J.G., H.N., R.M. and P.S. analysed the data. C.C., J.G. and P.S. wrote the manuscript. All authors commented on the paper.

Additional Information

Supplementary information accompanies this paper at <http://www.nature.com/srep>

Competing financial interests: The authors declare no competing financial interests.

How to cite this article: Cobet, C. *et al.* Influence of molecular designs on polaronic and vibrational transitions in a conjugated push-pull copolymer. *Sci. Rep.* **6**, 35096; doi: 10.1038/srep35096 (2016).



This work is licensed under a Creative Commons Attribution 4.0 International License. The images or other third party material in this article are included in the article's Creative Commons license, unless indicated otherwise in the credit line; if the material is not included under the Creative Commons license, users will need to obtain permission from the license holder to reproduce the material. To view a copy of this license, visit <http://creativecommons.org/licenses/by/4.0/>

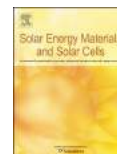
© The Author(s) 2016

4.9 Manuscript 9



Contents lists available at ScienceDirect

Solar Energy Materials & Solar Cells

journal homepage: www.elsevier.com/locate/solmat

Solution processed perovskite solar cells using highly conductive PEDOT:PSS interfacial layer



Getachew Adam^a, Martin Kaltenbrunner^b, Eric Daniel Głowacki^a, Dogukan Hazar Apaydin^a, Matthew Schuette White^a, Herwig Heilbrunner^a, Sekai Tombe^{a,c}, Philipp Stadler^a, Bruno Ernecker^d, Christian Wolfgang Klampfl^d, Niyazi Serdar Sariciftci^a, Markus Clark Scharber^{a,*}

^a Linz Institute for Organic Solar Cells (LIOS), Institute of Physical Chemistry, Johannes Kepler University Linz, Altenbergerstr. 69, 4040 Linz, Austria

^b Department of Soft Matter Physics, Johannes Kepler University Linz, Altenbergerstr. 69, 4040 Linz, Austria

^c Sensor Lab Department of Chemistry, University of Western Cape, Private Bag X17, Bellville, 7535 Cape Town, South Africa

^d Institute for Analytical Chemistry, Johannes Kepler University Linz, Altenbergerstr. 69, 4040 Linz, Austria

ARTICLE INFO

Article history:

Received 7 December 2015

Received in revised form

25 April 2016

Accepted 4 May 2016

Keywords:

Solar cell

Hybrid organic inorganic

Perovskite

Solution processing

ABSTRACT

We have developed a simple and robust process to prepare efficient perovskite solar cells. Pinhole free thin films of $\text{CH}_3\text{NH}_3\text{PbI}_{3-x}\text{Cl}_x$ can be coated on high conductivity poly(3,4-ethylenedioxythiophene) poly(styrene-sulfonate) (PEDOT:PSS), (Clevis PH1000) when the PEDOT:PSS is deposited together with dimethyl sulfoxide (DMSO) and Zonyl as additives. This process enables the fabrication of perovskite solar cells using [6,6]-phenyl-C₆₁-butyric acid methyl ester (PCBM) as electron transport layer with > 12% power conversion efficiency, low hysteresis and excellent operational stability. We have performed a detailed opto-electronic characterization of these solar cells and identified the main loss mechanism limiting the device performance.

© 2016 Elsevier B.V. All rights reserved.

1. Introduction

Efficient, easily processable and low-cost solar cell absorber materials represent the core-target of current photovoltaic research. Organic-inorganic hybrid perovskites based on methyl ammonium lead tri-halide compounds excellently fit the mentioned requirements; their light harvesting properties are tunable by varying the chemical composition, their processing is simple and power-conversion is efficient [1]. Interestingly, these perovskite semiconductors exhibit balanced electron and hole mobilities, long-range diffusion length and long recombination life time of charge carriers [2–4]. The precursors for organic-inorganic hybrid perovskites are readily available at relatively low costs, and can be processed from solution onto rigid or flexible substrates using printing compatible methods [5–11]. The rapid development in device design and fabrication techniques has led to a tremendous increase in the power conversion efficiencies (PCE) of perovskite solar cells in a short period of time from 3% to 4% in 2009 [12] to > 20% in 2015 [5–7]. Theoretical calculations project

the power conversion efficiency to approach the Shockley–Queisser limit of 31.4% [13,14].

Despite the remarkable progress in record cell efficiency, three significant hurdles remain for perovskite photovoltaic technology:

- 1) Improving the long-term stability of the cells,
- 2) Defining standard characterization protocols to eliminate hysteresis artifacts, and
- 3) Forming pinhole-free films of the highly crystalline semiconductor over large areas.

While promising stability data were reported for mesoscopic devices built on TiO_2 and ZrO_2 [11], the high efficiency device stack reported using ITO/PEIE/Y-TiO₂/perovskite/spiro-OMeTAD/Au degrades even in inert atmosphere and in dark within a few hours [5].

Defining the efficiency of perovskite solar cells presents also a challenge compared to more conventional PV technologies. Typically, device efficiencies are extracted from current density–voltage (J–V) curves, which are recorded by sweeping an applied bias across the terminals of the cell and simultaneously measuring the current flowing in the external circuit while the solar cell is exposed to a well-defined or standard light source. Many devices reported in the literature show a strong hysteresis, *i.e.* their J–V

* Corresponding author.

E-mail addresses: getachew_adam.workneh@jku.at (G. Adam), markus_clark.scharber@jku.at (M.C. Scharber).

<http://dx.doi.org/10.1016/j.solmat.2016.05.011>

0927-0248/© 2016 Elsevier B.V. All rights reserved.

curve depends on the sweep direction and also on the bias sweep rate [15–18]. This hysteresis leads to a significant deviation in the measured efficiency depending on the procedure. Precautions for addressing stability and hysteresis during device characterization have been suggested [19].

Reproducible production of pinhole-free films over large areas is an absolute requirement for both commercial fabrication and lab-scale research. Several successful device architectures have been reported with varying electron and hole selective contact materials. Perovskite semiconductors have been coupled with either a planar or mesoporous n-type metal oxide (TiO_2 , Al_2O_3 , ZrO_2 , ZnO) and an organic hole-transport material (HTM) as selective contacts for charge extraction [10,11,20–22]. Planar device structures have also been demonstrated using non-oxide n-type materials like fullerene, as an electron selective contact and a p-type HTM. A typical device stack comprises PEDOT:PSS as p-type material, the organic-inorganic hybrid perovskite as absorber layer and a fullerene derivative as electron selective contact [23–26]. The oxide-free architecture can be solution processed at low temperatures on light weight flexible substrates [27,28]. In all cases, the preparation of pinhole and defect-free perovskite layers is required to optimize device performance. Various processes for making high quality films have been reported. These include vacuum deposition, by co-evaporation of PbI_2 with $\text{CH}_3\text{NH}_3\text{I}$ [9], sequential solution depositions of the two components (spin coating followed by dip coating or two spin coating steps) [8,10,22], spin coating just from one precursor solution [5], and vapor assisted solution processing (e.g. the film growth via reaction of the as deposited film of PbI_2 with $\text{CH}_3\text{NH}_3\text{I}$ vapor) [29]. Approaches using different solvent combinations (solvent engineering) have also shown promising results [26,30]. Solution processing, particularly deposition from a single precursor solution, is in-principle the simplest approach to make perovskite films. However, it has been found that the formation of the perovskite films depends heavily on the processing parameters including the wettability and the chemical compatibility of the underlying surface. Perovskite precursor solutions spin coating recipes, solvent treatment and annealing temperature and times are varied accordingly. Some examples of processing recipes include: a stoichiometric mixture of PbI_2 and $\text{CH}_3\text{NH}_3\text{I}$ dissolved in DMF or DMSO [24], $\text{PbCl}_2 + 3\text{CH}_3\text{NH}_3\text{I}$ dissolved in DMF [20,22], excess $\text{CH}_3\text{NH}_3\text{I}$ by using $\text{PbI}_2 + 3\text{CH}_3\text{NH}_3\text{I}$ [31], and adding a small amount of either $\text{CH}_3\text{NH}_3\text{Cl}$ or $\text{CH}_3\text{NH}_3\text{Br}$ in the host solution of PbI_2 and $\text{CH}_3\text{NH}_3\text{I}$ [32,33].

Processing perovskite solar cells from a single precursor perovskite ink shows a clear possibility of role to role industrial scale production of perovskite solar cells especially when using solution processed polymeric materials instead of high temperature and vacuum processed inorganic oxides as interlayers [34]. Recently high performance solution processed perovskite solar cells without an additional hole transport layer have been reported [35]. Blade-coated perovskite solar cells reported by the Jen-group [36] support the idea that used material and processes are fully printing compatible.

In this work we prepared solar cells based on a planar heterojunction architecture (indium tin oxide (ITO)/ PEDOT:PSS / $\text{CH}_3\text{NH}_3\text{PbI}_{3-x}\text{Cl}_x$ /[6,6]-phenyl- C_{61} -butyric acid methyl ester (PCBM)/ aluminum). We found that the used PEDOT:PSS formulation is critical for the quality of the perovskite layer deposited on top of it and best device performance is obtained when 5% v/v DMSO and 0.7% v/v Zonyl® FS-300 fluoro-surfactant are added to the commercially available Clevios PH1000 dispersion. The recipe is highly reproducible under standard ambient laboratory conditions and does not require special humidity control.

Prepared devices showed minimal hysteresis in their J-V curves, good stability when operated under inert atmosphere or

after encapsulation and power conversion efficiencies in the range of 12–13%. A detailed optoelectronic analysis allowed us to determine the losses limiting the power conversion efficiency of the investigated devices [37].

2. Experimental details

Pre-patterned indium doped tin oxide (ITO) coated glass ($15 \Omega/\text{cm}^2$), PbI_2 (99.9%, Sigma Aldrich), PbCl_2 (99.9%, Sigma Aldrich), methylammonium iodide (Dyesol), dimethylformamide (DMF, dry, Sigma Aldrich), poly(3,4-ethylenedioxythiophene) poly(styrenesulfonate) (PEDOT:PSS, Clevios pH 1000), Zonyl® FS-300 fluorosurfactant (40% in H_2O , Fluka), dimethyl sulfoxide (DMSO, Anal R, VWR chemicals), [6,6]-phenyl- C_{61} -butyric acid methyl ester (PCBM, SolenneBV), chlorobenzene (GPR, VWR chemicals), chloroform (Anal R, VWR chemicals), isopropanol (Anal R, Fisher chemicals) were used as received. Precursor mixed halide solutions were prepared with molar ratio ($0.5\text{PbCl}_2 + 0.5\text{PbI}_2 + 2.2\text{CH}_3\text{NH}_3\text{I}$) (640 mg/ml in DMF) stirred overnight at room temperature in ambient air and filtered with $0.45 \mu\text{m}$ PTFE filter. Perovskite thin films for UV-vis optical absorption and photoluminescence measurements were prepared by spin-coating at 4000 rpm on different substrates from 50% diluted solution of the precursor solution. The fabrication of planar heterojunction perovskite solar cells started with cleaning pre-patterned ITO coated glass substrates sequentially with acetone, Hellmanex®, deionized water and isopropanol in an ultrasonic bath. Different volumes of PEDOT:PSS (Clevios PH1000), DMSO and Zonyl FS300 were carefully mixed. The formulated PEDOT:PSS dispersion was filtered through a $0.45 \mu\text{m}$ RC filter and spin-coated at 1000 rpm for one minute. The PEDOT:PSS layer was then patterned and annealed for 10 min at 110°C , cooled, rinsed with isopropanol by spinning at 4000 rpm to remove the excess surfactant (Zonyl) from the surface, and then annealed for another 10 min at the same temperature. The typical thickness of PEDOT:PSS was found to be ~ 130 nm. The precursor solution was spin-coated (1500 rpm for 20 s and then at 2000 rpm for 5 s) on top. After spin-coating, the substrates were immediately transferred to a hot plate at 110°C where the colorless wet film is turned into glassy dark brown layer in few seconds and then further annealed for 45 min in ambient air. The procedure resulted in a 350–400 nm thick perovskite absorber layer. PCBM (20 mg/ml in 1:1 volume ratio of chlorobenzene and chloroform) was spin coated (1500 rpm for 15 s and then at 2000 rpm for 15 s) on top of the perovskite layer, which yields a thickness of 50–70 nm. The entire processing up to this step is performed in ambient air. The sample was then transferred to a vacuum chamber located inside a nitrogen-filled glove box for the evaporation of the aluminum top electrode at $< 3 \times 10^{-6}$ mbar. The solar cells were encapsulated with a glass cover using a UV-curable epoxy sealant (Ossila E131), with a UV exposure time of 6 min. The fabricated solar cells with an active area of $\sim 0.17 \text{ cm}^2$ were tested on a LOT-QD solar simulator (LS0821). The radiation intensity was adjusted using a calibrated reference silicon diode to $100 \text{ mW}/\text{cm}^2$. External quantum efficiencies (EQEs) were recorded by using a lock-in amplifier (SR830, Stanford Research Systems) and a Jaisle 1002 potentiostat. The potentiostat operated in the two electrode configuration is a high performance current amplifier with a variable gain ranging from 10 to $10^8 \text{ V}/\text{A}$. In addition, the potentiostat allows measuring the EQE-spectra at different applied voltages. The devices were illuminated by monochromatic light from a xenon lamp passing through a monochromator (Oriel Cornerstone) with typical intensities in the range of 10 – $100 \mu\text{W}$. A filter wheel holding long-pass filters and a mechanical chopper was mounted between the xenon lamp and the monochromator. Chopping frequencies in the

range of 73–273 Hz were used. A calibrated silicon diode (Hamamatsu S2281) was used as a reference. A halogen lamp (Philips 50 W, 12 V) provided a variable white light bias to the solar cells while the EQE was measured. To determine the power conversion efficiency of the prepared solar cells, the illuminated area of the solar cell was defined using a shadow mask (0.13 cm²). In a first step the current-voltage curve was recorded with a Keithley 2400 source-measurement unit under illumination (solar simulator). The voltage was increased slowly (20 mV/s) and the current-voltage curve was determined close to steady state-conditions. To check for hysteresis a reverse voltage scan was performed decreasing the voltage by 20 mV/s. In a second step the short circuit current was recorded (steady state value) with a Keithley 2400. A maximum-power-point tracking algorithm was used to measure the steady-state power output of the solar cell. The external quantum efficiency was determined operating the solar cell under short circuit conditions and 1 sun illumination. The short circuit current calculated using the EQE-data allowed the determination of the spectral mismatch factor (MM) of our solar simulator. We found values > 0.95 for the investigated devices. This mismatch factor was used to correct the maximum power point measurement. UV–vis absorption spectra of perovskite films were recorded using a double beam UV–vis spectrometer (Perkin Elmer 1050) equipped with an integrating sphere. A Bruker Dektak XT profilometer was used to measure layer thicknesses. Photoluminescence and electroluminescence spectra of various devices were measured using a Shamrock SR-303i monochromator and an Andor iDus Si-CCD. Samples were excited at 473 nm (5 mW) using a solid-state laser or a supercontinuum light source (NKT EXB6) connected to a VIS-NIR SuperK Select Box. A set of long-pass filters was used to avoid any distortion of the recorded spectra by the laser light. Electroluminescence spectra were recorded while applying different potentials with a Keithley 2401. The integrated electroluminescence was detected measuring the emitted photon current with a calibrated large-area Si-photodetector (Hamamatsu S2281) positioned close to the sample. Preliminary stability studies were performed on an ORIEL solar simulator. Surface and cross section scanning electron microscopy (SEM) images were made using a ZEISS 1540XB CrossBeam Scanning microscope equipped with a focused ion-beam (FIB) unit. Gas chromatography coupled with mass spectrometry (GC–MS) measurements were performed on a 6890 GC with a 5935C mass selective detector (both Agilent Technologies, Waldbronn, Germany) equipped with a MPS2-XL headspace autosampler from Gerstel (Mülheim/Ruhr, Germany). The carrier gas used was helium and a ZB-624 GC-column, 60 m × 0.25 mm I.D. film thickness 1.40 μm (Phenomenex, Aschaffenburg, Germany) was employed. 500 μl of the gas-phase above PEDOT:PSS-films coated on glass substrates was analyzed after the films were heated to 140 °C for 10 min; the MS was operated in the full-scan mode.

3. Results and discussion

3.1. Thin perovskite film

High-quality perovskite films with no voids inside the active layer are a key requirement in making planar perovskite solar cells. We optimized our system by testing different deposition procedures and characterized the resulting films using a scanning electron microscope. Fig. 1 shows different perovskite films deposited on a) glass coated with ITO, b) glass coated with ITO and PEDOT:PSS (Clevios PH1000), c) glass coated with ITO and PEDOT:PSS (Clevios PH1000) processed with 5% v/v DMSO, d) glass coated with ITO and PEDOT:PSS (Clevios PH1000) processed with 0.7% v/v Zonyl[®] FS-300, glass coated with ITO and PEDOT:PSS (Clevios

PH1000) processed with 0.7% v/v Zonyl[®] FS-300 and 2.5% v/v DMSO e), 5% v/v DMSO f), 10% v/v DMSO g), 15% v/v DMSO h), 20% v/v DMSO i).

The perovskite film on ITO coated glass comprises domains separated by large holes (Fig. 1(a)). Perovskite layers processed on neat PEDOT:PSS show many small holes (Fig. 1(b)). The addition of DMSO or Zonyl to PEDOT:PSS reduces the number and size of defects in the perovskite films (Fig. 1(c) and (d)). By using both additives and adding ≥ 5% DMSO continuous layers are formed. The role of the additives DMSO and Zonyl is still not fully understood. DMSO is known to increase the conductivity of PEDOT:PSS films [38]. Zonyl is often used to improve the wettability of the PEDOT:PSS dispersion on hydrophobic substrates [39]. Also the mechanical properties and the surface nano-morphology of PEDOT:PSS layers can be altered by DMSO and Zonyl additives [40]. Alternatively, additives remaining in the deposited film may improve the crystallization of the perovskite on the PEDOT:PSS surface. DMSO is a good solvent for PbI₂, the remaining DMSO may hinder crystallization of PbI₂ at the surface, providing an amorphous seed layer from which a more compact perovskite film can grow [41]. However, preliminary GC–MS investigations on PEDOT:PSS layers deposited with different additive concentrations revealed that the treatments performed after spin-coating remove a significant fraction of the DMSO trapped in the film (Fig. S1). While untreated PEDOT:PSS layers show strong DMSO signals (even for the Clevios PH1000 used as received), all treated samples show a weak DMSO signal with similar amplitudes. This suggests that the surface energy and the nano-morphology of the PEDOT:PSS layer play a crucial role in the formation of the perovskite layer in our process. In our work we found that the formulation PEDOT:PSS (Clevios PH1000) with 0.7% v/v Zonyl[®] FS-300 and 5% v/v DMSO allows the preparation of efficient solar cells with a high yield and we focused on further investigations on samples processed with this formulation. The basic optical and structural (X-ray) characterizations are summarized in the Supporting Information (Figs. S2 and S3). They show that our process yields typical perovskite material and the films do not contain larger volumes of unreacted lead-halides.

3.2. Solar cell characterization

After optimizing the compact pinhole free perovskite film, solar cells were fabricated with a device architecture of ITO/PEDOT:PSS/Perovskite/PCBM/Al. A schematic of the device layer structure is shown in Fig. 2(a) and a cross-sectional SEM of a solar cell is shown in Fig. 2(b). This cross-section is consistent with the SEM image surface morphology in Fig. 1, where the boundaries between continuous perovskite crystallites are well-resolved, and it is clearly visible that the film is closed. The layer of PCBM can be seen to conformally coat the top of the perovskite film, filling in the space between the tops of adjacent crystallites.

The photovoltaic performances of the solar cells were investigated using three independent methods to ensure consistency and accuracy. Power conversion efficiencies were determined by current-voltage characterization by sweeping the voltage from negative to positive and positive to negative values. The J_{SC} of the devices was calibrated against the integrated external quantum efficiency. Finally, the cells were tested under maximum power point tracking to rule out any hysteresis effects and to observe performance stability. Fig. 3(a) shows the current-voltage curve of one of the investigated perovskite solar cells. Only a small hysteresis is visible which is typical for the devices prepared following the procedure described above. Fig. 3(b) shows the corresponding maximum power point scan. The inset is the photo of the encapsulated and contacted solar cell where no changes in color or performance of the solar cells were observed after encapsulation.

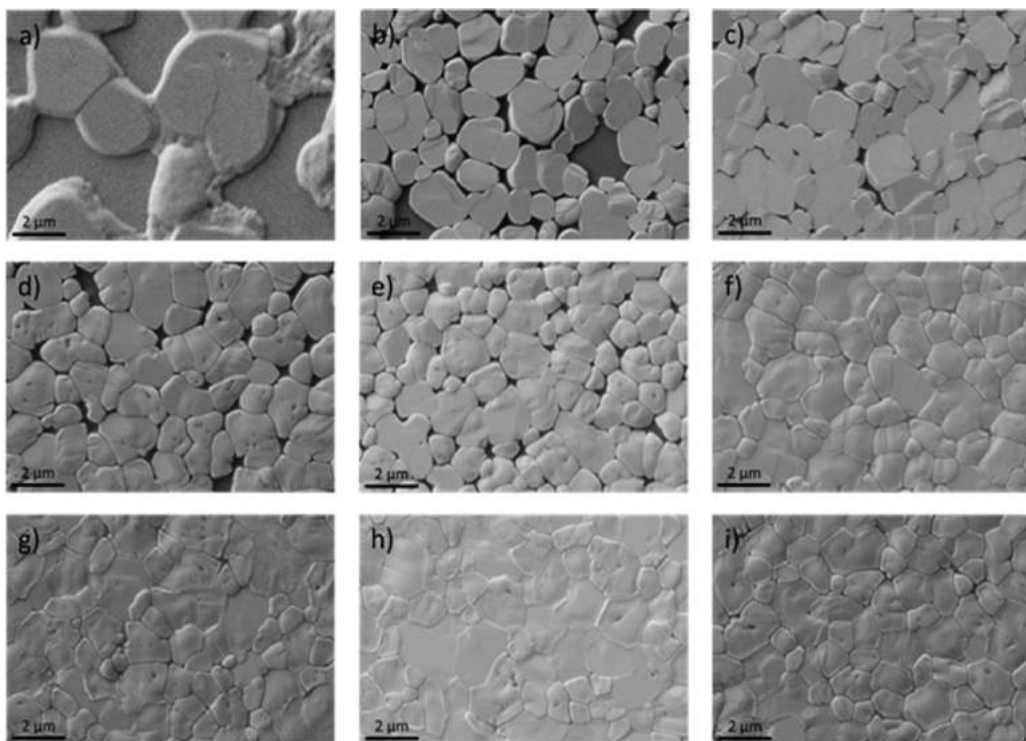


Fig. 1. SEM images of perovskite films coated on top of (a) Glass/ITO, (b) PEDOT:PSS (Clevios PH1000), (c) PEDOT:PSS (Clevios PH1000) processed with 5% v/v DMSO, (d) PEDOT:PSS (Clevios PH1000) processed with 0.7% v/v Zonyl[®] FS-300, (e) PEDOT:PSS (Clevios PH1000) processed with 0.7% v/v Zonyl[®] FS-300 and 2.5% v/v DMSO, (f) and 5% v/v DMSO, (g) and 10% v/v DMSO, (h) and 15% v/v DMSO, and (i) and 20% v/v DMSO.

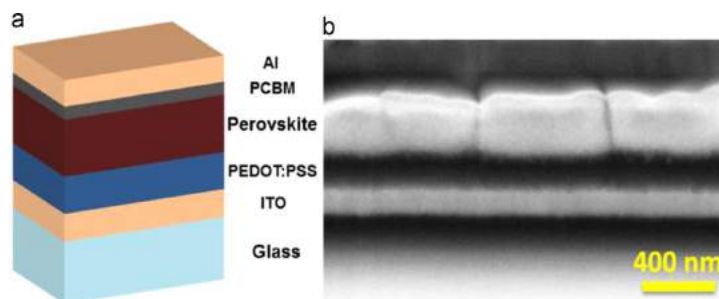


Fig. 2. (a) Schematic diagram of the solar cell stacked layers, and (b) Cross-sectional SEM showing the structure ITO/PEDOT:PSS/Perovskite/PCBM/Al.

Devices do show low leakage currents at reverse bias (Fig. S4a) and good stability when operated under continuous solar illumination (Fig. 3(b)). Under 1 sun illumination, typical devices deliver open circuit voltages in the range of 0.93–0.97 V, fill factors between 0.7 and 0.75, and short circuit currents around 17 mA/cm² resulting in power conversion efficiencies in the range of 12–12.5% (Fig. S4b). Current-voltage curves shown in Fig. 3(a) are corrected for the spectral mismatch of the solar simulator by external quantum efficiency measurements. The corresponding EQE-spectrum is shown in Fig. 4(a).

The EQE peaks around 550 nm, reaching a maximum external quantum efficiency of ~80%. In the blue (300–450 nm) and the

near-IR (650–800 nm) the spectral response is substantially smaller leading to a significant reduction of the photocurrent. This loss can be attributed to parasitic absorption in the ITO (300–450 nm) and the PEDOT:PSS layer (both spectral regions) as well as the poor reflectance of the metal back electrode (aluminum). Due to the roughness of the perovskite/PCBM bilayer, the 110 nm thick aluminum layer deposited as top electrode is a poor reflector. Studying the light bias and the reverse bias dependence of the EQE spectrum shows that neither a dc-illumination up to 1 sun nor negative voltages up to -1 V changes the EQE spectrum (Fig. S5). This illustrates that under short circuit conditions charge carrier extraction is essentially complete. In addition the absence of a

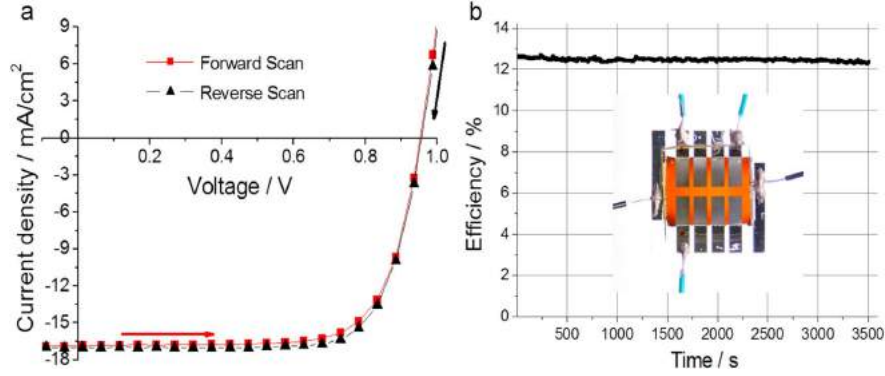


Fig. 3. (a) Current-voltage curve of the perovskite solar cell, forward and reverse scan 20 mV/s. (b) Maximum power point scan corrected for the spectral mismatch. The inset is the photo of the encapsulated and contacted solar cell.

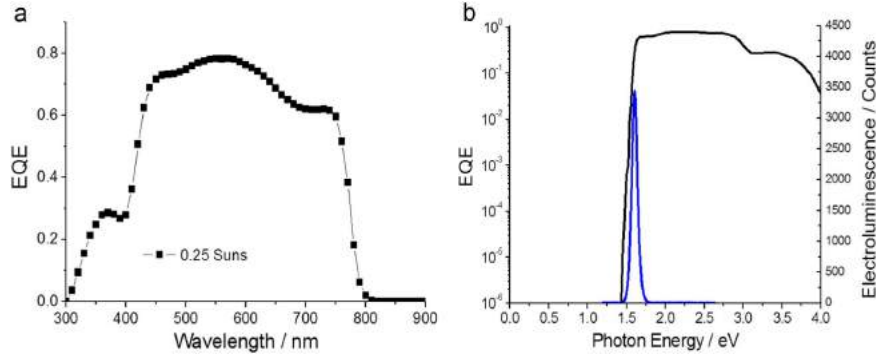


Fig. 4. (a) External quantum efficiency spectrum measured under 0.25 suns white-light bias, and (b) EQE spectrum and electroluminescence spectrum of the same perovskite solar cell.

light bias dependence confirms that the short circuit current scales linearly with the light intensity [42]. Fig. 4(b) shows the EQE spectrum of a typical device on a logarithmic scale. The EQE decreases rapidly below 1.5 eV suggesting that the number of photoactive states in the absorber band gap is very small. The electroluminescence of the same device is also shown in Fig. 4(b) with a narrow emission peaking at ~ 1.6 eV or 775 nm. Applying the relations first derived by Rau [43] and later on used by various different authors [33,44], the radiative limit of the open circuit voltage ($V_{oc,rad}$) and the power conversion efficiency of a solar cell can be determined. The current-voltage curve of an ideal photovoltaic device, with only radiative recombination of charge carriers allowed, is given by

$$J = J_{0,rad} \times \left[\exp\left(\frac{qV}{k_B T}\right) - 1 \right] - J_{PH} \quad (1)$$

where J is the current density, $J_{0,rad}$ is the diode saturation current, q is the unit charge, V is the applied bias, k_B is the Boltzmann constant, T the temperature and J_{PH} is the photocurrent density. According to Rau, $J_{0,rad}$ can be calculated by

$$J_{0,rad} = q \times \int EQE_{PV}(E) \times \Phi_{BB}(E) dE \quad (2)$$

where EQE_{PV} is the external quantum efficiency of the solar cell and Φ_{BB} is the spectral photon flux at 300 K. J_{PH} can be calculated in the same way by replacing the 300 K black body radiation by

the Air Mass 1.5 Global (AM1.5 G) spectrum. The rearrangement of Eq. (1) leads to

$$V_{oc,rad} = \frac{k_B T}{q} \times \ln \left(\frac{J_{PH}}{J_{0,rad}} + 1 \right) \quad (3)$$

This analysis does not include Ohmic or any non-radiative recombination losses. Therefore it gives an upper performance limit for the device with known external quantum efficiency. Calculated parameters for four typical devices prepared within this study are summarized in Table 1. The large difference between the measured and the calculated radiative open circuit voltage suggests that non-radiative recombination plays an important role in the studied devices. By measuring the photon flux of electroluminescence emitted by the solar cell ($J_{em}(V)$) when operated under forward bias at different injection currents $J_{inj}(V)$, the external quantum efficiency of the LED ($EQE_{LED}(V)$) can be determined. $EQE_{LED}(V)$ is given by $J_{em}(V)/J_{inj}(V)$ and the value is closely related to the external-radiative efficiency (ERE) defined by Green [45]. If the $EQE_{LED} < 1$, $J_{0,rad}$ in Eqs. 1 and 3 need to be replaced by $J_{0,rad}/EQE_{LED}$, where the EQE_{LED} is determined at current densities comparable to the photocurrent density generated by AM1.5 G solar radiation.

For all investigated solar cells we find $EQE_{LED} < 10^{-6}$ (Fig. 5 and Fig. S6). Recalculating the open circuit voltages using Eq. (3) and including EQE_{LED} , values close to the actual measured voltages are found. All data are summarized in Table 2.

Table 1
Calculated parameters for devices prepared within this study using Eqs. (1)–(3) and the corresponding EQE spectra.

	$J_{0,rad}$ [mA/cm ²]	J_{PH} [mA/cm ²]	$V_{oc,rad}$ [V]	$V_{oc,measured}$ [V]	ΔV_{oc} [V]
Device 1	1.14×10^{-21}	16.70	1.32	0.97	0.35
Device 2	1.14×10^{-21}	16.66	1.32	0.96	0.36
Device 3	1.24×10^{-21}	16.83	1.32	0.94	0.38
Device 4	1.55×10^{-21}	17.10	1.31	0.97	0.34

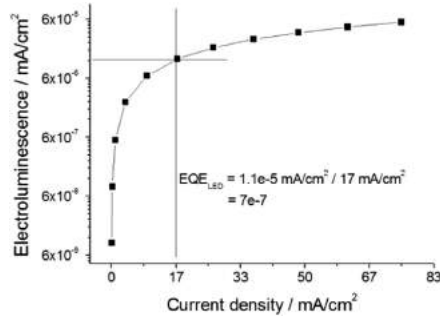


Fig. 5. Electroluminescence versus driving current measured on one of the prepared solar cells.

Table 2
Calculated EQE_{LED} , $V_{oc,cor}$ corrected and V_{oc} measured for four typical devices using Eq. (3).

	EQE_{LED}	$V_{oc,cor}$ [mV]	$V_{oc,measured}$ [mV]
Device 1	7×10^{-7}	0.954	0.97
Device 2	7×10^{-7}	0.954	0.96
Device 3	4×10^{-7}	0.937	0.94
Device 4	8×10^{-7}	0.95	0.97

Eq. (1) can also be used to determine the maximum power conversion efficiency of the studied devices assuming only radiative recombination and no electrical losses due to serial or parallel parasitic resistors. With the measured EQE_{PV} and, considering only radiative recombination leads to a maximum efficiency of 20% ($V_{oc}=1.32$ V, $FF=91\%$, $I_{sc}=16.7$ mA/cm²), Eq. (1) predicts a power conversion efficiency of 14% ($V_{oc}=0.95$ V, $FF=88\%$, $I_{sc}=16.7$ mA/cm²) when the measured EQE_{LED} is included. Photoluminescence spectra of a solar cell recorded at -1 V, under short circuit and open circuit conditions, are shown in Fig. 6(a). The sample is excited using a diode-laser (473 nm) and the solar cell delivers a current of 0.6 mA (equivalent to ~ 0.2 suns). The spectrum comprises an emission which does not depend on the applied bias and a feature around 1.6 eV which increases with increasing bias. Fig. 6(b) shows photoluminescence (PL) spectra recorded at various different biases corrected with the spectrum recorded at -1 V. As discussed by Tvingstedt et al. this bias-dependent photoluminescence is a signature of an ideal solar cell [46]. While at short circuit the photoluminescence should be quenched, at open circuit photo-induced charges recombine radiatively. In the studied devices a residual PL-signal is found at I_{sc} which increases exponentially upon increasing the bias voltage (Fig. 6(c)). The principle of detailed balance dictates the emitted photon flux (Φ_{em}) is proportional to $EQE_{PV}(E)$ times the black body radiation at 300 K (Φ_{BB}). Therefore, the spectrum calculated via $EQE_{PV}(E) \times \Phi_{BB}(E)$ should reproduce the photoluminescence and electroluminescence of the corresponding solar cell. In Fig. 6 (d) a comparison of the three spectra is shown indicating close overlap. At lower energy, i.e. in the spectral region where the EQE

is very small, the calculated spectrum shows some deviations from the PL and EL spectrum (Fig. S7). The detailed analysis above reveals that the devices studied here show the typical characteristics of planar perovskite solar cells. However, compared to mesoscopic and planar devices using TiO₂ or Al₂O₃ as interfacial layers on the transparent conductive oxide or some devices deposited via vapor deposition, the investigated devices show a smaller open circuit voltage. The presented results suggest that the low quantum yield of radiative recombination causes the observed open circuit voltage loss.

Tvingstedt et al. reported an EQE_{LED} of 1.2×10^{-4} and an open circuit voltage of 1.08 V for an inverted, vapor-processed CH₃NH₃PbI₃-PCBM solar cell [42]. A one-hundred times smaller EQE_{LED} leads to a V_{oc} loss of ~ 50 mV, resulting in an open circuit voltages observed for our devices. Therefore one obvious strategy to improve the performance of the studied solar cells is reducing the non-radiative recombination of photo-induced charges. Defects in the absorber layer, and at interfaces/surfaces may act as recombination centers. Further optimization of the growth conditions may reduce the number of defects in the perovskite film. The choice of alternative interlayers may also help improving the radiative recombination quantum yield in our solar cells. As shown in Fig. S2, using PEDOT:PSS and PCBM leads to a strong quenching of the perovskite photoluminescence, suggesting that these widely-used interlayers are not ideal candidates. Alternative interlayers leading to less PL-quenching while still supporting selective charge extraction should also lead to higher open circuit voltages.

Preliminary device simulation work suggests that bulk-recombination plays an important role in the investigated devices. Current-voltage curves recorded in the dark and under illumination can be simulated reasonably well by using a simple replacement circuit based on the diodes with an ideality-factor n of 1 and 2 connected in parallel. A 1-diode model requires an ideality factor around 1.75 and a diode saturation current ($\sim 1 \times 10^{-7}$ mA/cm²). In classical inorganic solar cells an ideality factor 1 is related to band-to-band recombination while $n=2$ is often interpreted as recombination that occurs via deep-level states or at interfaces and grain boundaries [47,48]. Eq. (1) also predicts that devices should show a $FF > 85\%$ at solar illumination intensities while prepared devices show fill factors $\leq 75\%$. We attribute the lower fill factor to Ohmic losses. Investigated devices showed a serial resistance around 25 Ω and a parallel resistance around 6 k Ω . As shown in Fig. S8, the fill factor of our devices increases upon decreasing the illumination intensity. This suggests that the serial resistance is too high and additional bus bars and electrodes with a lower sheet resistance could increase the overall efficiency of the prepared devices. Also the losses in the EQE_{PV} could be reduced by improving the optical design of the solar cell. An anti-reflection coating on the front side of the device, transparent electrode and interfacial layers with smaller absorbance and a high quality reflector as back electrode could lead to higher external quantum efficiencies (EQE_{PV} and EQE_{PL}) and to larger short circuit current and open circuit voltage.

In summary, we have developed a simple and reliable manufacturing process for planar perovskite solar cells comprising

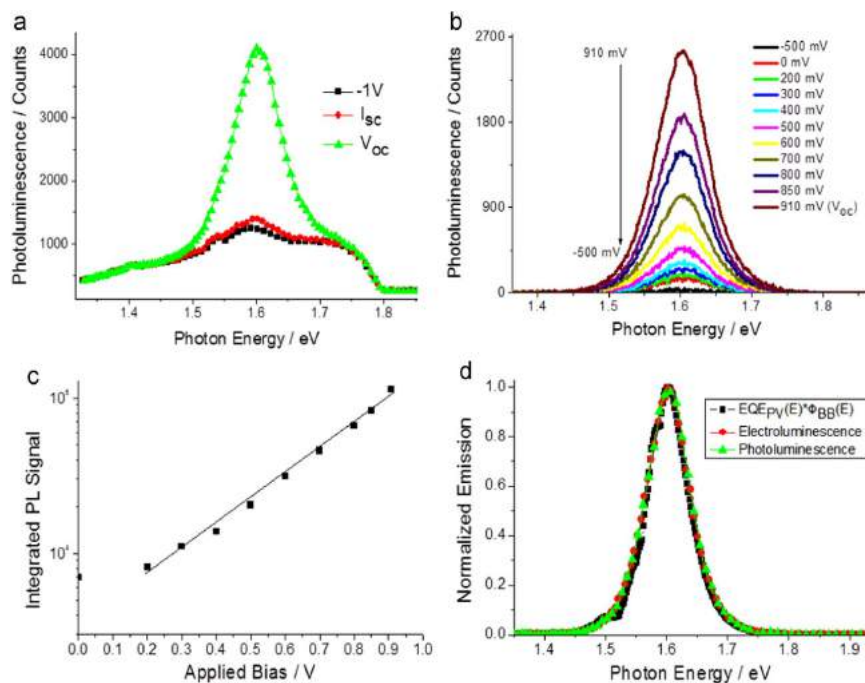


Fig. 6. Photoluminescence (a) measured at -1 V, short circuit and open circuit condition, (b) measured at various voltage biases, (c) Signal intensity as a function of applied voltage bias. (d) Electroluminescence, $ECE_{PV}(E) \times \Phi_{BG}(E)$ spectra.

PEDOT:PSS and PCBM as interfacial layers. We found that the use of DMSO and Zonyl as processing additives for the used PEDOT:PSS affects the quality of the perovskite absorber layer processed on top of this layer. Prepared devices show a good operational stability and a moderate hysteresis when the current-voltage curve is recorded at 20 mV/s in forward and reverse direction. The radiative recombination quantum yield is found to be small, leading to observed losses in the open circuit voltage. Our analysis shows that this type of perovskite solar cells can reach efficiencies of 20% upon reducing optical, electrical, and non-radiative recombination losses. Replacing the PEDOT:PSS hole transport layer with a material that does not quench the photo- and electroluminescence is the key step to realizing the full potential.

Acknowledgment

We would like to acknowledge the Austrian Research Promotion Agency (FFG) (flex! PV KOOP-IF 838621) and the Austrian Science Fund FWF (Wittgenstein Prize of N.S. Sariciftci Z222-N19) for financial support. Sekai Tombe gratefully acknowledges the financial support from L'Oréal-UNESCO For Women In Science Sub-Saharan Africa and the National Research Foundation of South Africa (NRF).

Appendix A. Supporting information

Supplementary data associated with this article can be found in the online version at <http://dx.doi.org/10.1016/j.solmat.2016.05.011>.

References

- [1] J.H. Noh, S.H. Im, J.H. Heo, T.N. Mandal, S.I. Seok, Chemical management for colorful, efficient, and stable inorganic-organic hybrid nanostructured solar cells, *Nano Lett.* 13 (2013) 1764–1769.
- [2] S.D. Stranks, G.E. Eperon, G. Grancini, C. Menelaou, M.J.P. Alcocer, T. Leijtens, L. M. Herz, A. Petrozza, H.J. Snaith, Electron-hole diffusion lengths exceeding $1 \mu\text{m}$ in an organometal trihalide perovskite absorber, *Science* 342 (2013) 341–344.
- [3] G. Xing, N. Mathews, S. Sun, S.S. Lim, Y.M. Lam, M. Grätzel, S. Mhaisalkar, T. C. Sum, Long-range balanced electron- and hole-transport lengths in organic-inorganic $\text{CH}_3\text{NH}_3\text{PbI}_3$, *Science* 342 (2013) 344–347.
- [4] C.S. Ponce, J.T.J. Savenije, M. Abdellah, K. Zheng, A. Yartsev, T. Pascher, T. Harlang, P. Chabera, T. Pullerits, A. Stepanov, J.P. Wolf, V. Sundström, Organometal halide perovskite solar cell materials rationalized: ultrafast charge generation, high and microsecond-long balanced mobilities, and slow recombination, *J. Am. Chem. Soc.* 136 (2014) 5189–5192.
- [5] H. Zhou, Q. Chen, G. Li, S. Luo, T.B. Song, H.S. Duan, Z. Hong, J. You, Y. Liu, Y. Yang, Interface engineering of highly efficient perovskite solar cells, *Science* 345 (2014) 542–546.
- [6] N.J. Jeon, J.H. Noh, W.S. Yang, Y.C. Kim, S. Ryu, J. Seo, S.I. Seok, Compositional engineering of perovskite materials for high-performance solar cells, *Nature* 517 (2015) 476–480.
- [7] W.S. Yang, J.H. Noh, N.J. Jeon, Y.C. Kim, S. Ryu, J. Seo, S. I. Seok, High-performance photovoltaic perovskite layers fabricated through intramolecular exchange, *Science* 348 (2015) 1234–1237.
- [8] J.H. Im, I.H. Jang, N. Pellet, M. Grätzel, N.G. Park, Growth of $\text{CH}_3\text{NH}_3\text{PbI}_3$ cuboids with controlled size for high-efficiency perovskite solar cells, *Nat. Nanotechnol.* 9 (2014) 927–932.
- [9] M. Liu, M.B. Johnston, H.J. Snaith, Efficient planar heterojunction perovskite solar cells by vapour deposition, *Nature* 501 (2014) 395–398.
- [10] J. Burschka, N. Pellet, S.J. Moon, R.H. Baker, P. Gao, M.K. Nazeeruddin, M. Grätzel, Sequential deposition as a route to high-performance perovskite-sensitized solar cells, *Nature* 499 (2013) 316–319.
- [11] A. Mei, X. Li, L. Liu, Z. Ku, T. Liu, Y. Rong, M. Xu, M. Hu, J. Chen, Y. Yang, M. Grätzel, H. Han, A hole-conductor-free, fully printable mesoscopic perovskite solar cell with high stability, *Science* 345 (2014) 295–298.
- [12] A. Kojima, K. Teshima, Y. Shirai, T. Miyasaka, Organometal halide perovskites as visible-light sensitizers for photovoltaic cells, *J. Am. Chem. Soc.* 131 (2009) 6050–6051.

- [13] W.-J. Yin, J.-H. Yang, J. Kang, Y. Yan, S.-H. Wei, Halide perovskite materials for solar cells: a theoretical review, *J. Mater. Chem. A* 3 (2015) 8926–8942.
- [14] W.-J. Yin, T. Shi, Y. Yan, Unique properties of halide perovskites as possible origins of the superior solar cell performance, *Adv. Mater.* 26 (2014) 4653–4658.
- [15] H.J. Snaith, A. Abate, J.M. Ball, G.E. Eperon, T. Leijtens, N.K. Noel, S.D. Stranks, J.T.W. Wang, K. Wojciechowski, W. Zhang, Anomalous hysteresis in perovskite solar cells, *J. Phys. Chem. Lett.* 5 (2014) 1511–1515.
- [16] E.L. Ungert, E.T. Hoke, C.D. Bailie, W.H. Nguyen, A.R. Bowring, T. Heumüller, M. G. Christoforo, M.D. McGehee, Hysteresis and transient behavior in current-voltage measurements of hybrid-perovskite absorber solar cells, *Energy Environ. Sci.* 7 (2014) 3690–3698.
- [17] J.M. Frost, K.T. Butler, A. Walsh, Molecular ferroelectric contributions to anomalous hysteresis in hybrid perovskite solar cells, *APL Mater.* 2 (2014) 081506.
- [18] R.S. Sanchez, V.G. Pedro, J.W. Lee, N.G. Park, Y.S. Kang, I.M. Sero, J. Bisquert, Slow dynamic processes in lead halide perovskite solar cells, Characteristic times and hysteresis, *J. Phys. Chem. Lett.* 5 (2014) 2357–2363.
- [19] M. Grätzel, The light and shade of perovskite solar cells, *Nat. Mater.* 13 (2014) 838–842.
- [20] M.M. Lee, J. Teuscher, T. Miyasaka, T.N. Murakami, H.J. Snaith, Efficient hybrid solar cells based on meso-superstructured organometal halide perovskites, *Science* 338 (2012) 643–647.
- [21] K. Wojciechowski, M. Saliba, T. Leijtens, A. Abate, H.J. Snaith, Sub-150 °C processed meso-superstructured perovskite solar cells with enhanced efficiency, *Energy Environ. Sci.* 7 (2014) 1142–1147.
- [22] D. Liu, T.L. Kelly, Perovskite solar cells with a planar heterojunction structure prepared using room-temperature solution processing techniques, *Nat. Photonics* 8 (2014) 133–138.
- [23] J. You, Z. Hong, Y.M. Yang, Q. Chen, M. Cai, T.B. Song, C.C. Chen, S. Lu, Y. Liu, H. Zhou, Y. Yang, Low-temperature solution-processed perovskite solar cells with high efficiency and flexibility, *ACS Nano* 8 (2014) 1674–1680.
- [24] J.S.S. Park, Y.C. Kim, N.J. Jeon, J.H. Noh, S.C. Yoon, S.I. Seok, Benefits of very thin PCBM and LiF layers for solution-processed p–i–n perovskite solar cells, *Energy Environ. Sci.* 7 (2014) 2642–2646.
- [25] P. Docampo, J.M. Ball, M. Darwich, G.E. Eperon, H.J. Snaith, Efficient organometal trihalide perovskite planar-heterojunction solar cells on flexible polymer substrates, *Nat. Commun.* 4 (2013) 2761.
- [26] W. Nie, H. Tsai, R. Asadpour, J.-C. Blancon, A.J. Neukirch, G. Gupta, J.J. Crochet, M. Chhowalla, S. Tretiak, M.A. Alam, H.-L. Wang, A.D. Mohite, High-efficiency solution-processed perovskite solar cells with millimeter-scale grains, *Science* 347 (2015) 522–525.
- [27] M. Kaltenbrunner, M.S. White, E.D. Glowacki, T. Sekitani, T. Someya, N. S. Sariciftci, S. Bauer, Ultrathin and lightweight organic solar cells with high flexibility, *Nat. Commun.* 3 (2012) 770.
- [28] M. Kaltenbrunner, G. Adam, E.D. Glowacki, M. Drack, R. Schwödiauer, L. Leonat, D.H. Apaydin, H. Groiss, M.C. Scharber, M.S. White, N.S. Sariciftci, S. Bauer, Flexible high power-per-weight perovskite solar cells with chromium oxide–metal contacts for improved stability in air, *Nat. Mater.* 14 (2015) 1032–1039.
- [29] Q. Chen, H. Zhou, Z. Hong, S. Luo, H.S. Duan, H.H. Wang, Y. Liu, G. Li, Y. Yang, Planar heterojunction perovskite solar cells via vapor-assisted solution process, *J. Am. Chem. Soc.* 136 (2014) 622–625.
- [30] N.J. Jeon, J.H. Noh, Y.C. Kim, W.S. Yang, S. Ryu, S.I. Seok, Solvent engineering for high-performance inorganic-organic hybrid perovskite solar cells, *Nat. Mater.* 13 (2014) 897–903.
- [31] S. Sun, T. Salim, N. Mathews, M. Duchamp, C. Boothroyd, G. Xing, T.C. Sumbce, Y.M. Lam, The origin of high efficiency in low-temperature solution-processable bilayer organometal halide hybrid solar cells, *Energy Environ. Sci.* 7 (2014) 399–407.
- [32] Y. Zhao, K. Zhu, CH₃NH₃Cl-assisted one-step solution growth of CH₃NH₃PbI₃: structure, charge-carrier dynamics, and photovoltaic properties of perovskite solar cells, *J. Phys. Chem. C* 118 (2014) 9412–9418.
- [33] B. Suarez, V.G. Pedro, T.S. Ripolles, R.S. Sanchez, L. Otero, I.M. Sero, Re-combination study of combined halides (Cl, Br, I) perovskite solar cells, *J. Phys. Chem. Lett.* 5 (2014) 1628–1635.
- [34] X. Huang, K. Wang, C. Yi, T. Meng, X. Gong, Efficient perovskite hybrid solar cells by highly electrical conductive PEDOT:PSS hole transport layer, *Adv. Energy Mater.* 6 (2016) 1501773.
- [35] Z. Yong, H. Xiaotian, C. Lie, H. Zengqi, F. Qingxia, L. Yawen, Z. Lin, C. Yiwang, Flexible, hole transporting layer-free and stable CH₃NH₃PbI₃/PC 61BM planar heterojunction perovskite solar cells, *Org. Electron* 30 (2016) 281–288.
- [36] Z. Yang, C.-C. Chueh, F. Zuo, J.H. Kim, P.-W. Liang, K.-Y.A. Jen, High-performance fully printable perovskite solar cells via blade-coating technique under the ambient condition, *Adv. Energy Mater.* 5 (2015) 1500328.
- [37] W. Tress, N. Marinova, O. Inganäs, M.K. Nazeeruddin, S.M. Zakeeruddin, M. Grätzel, Predicting the open-circuit voltage of CH₃NH₃PbI₃ perovskite solar cells using electroluminescence and photovoltaic quantum efficiency spectra: the role of radiative and non-radiative recombination, *Adv. Energy Mater.* 5 (2015) 1400812.
- [38] R. Po, C. Carbonera, A. Bernardi, F. Tinti, N. Camaioni, Polymer- and carbon-based electrodes for polymer solar cells: Toward low-cost, continuous fabrication over large area, *Sol. Energy Mater. Sol. Cells* 100 (2012) 97–114.
- [39] M.M. Voigt, R.C.I. Mackenzie, C.P. Yau, P. Atienzar, J. Dane, P.E. Keivanidis, D.D. C. Bradley, J. Nelson, Gravure printing for three subsequent solar cell layers of inverted structures on flexible substrates, *Sol. Energy Mater. Sol. Cells* 95 (2011) 731–734.
- [40] S. Savagatrup, E. Chan, S.M. Renteria-Garcia, A.D. Printz, A.V. Zaretski, T. F. O'Connor, D. Rodriguez, E. Valle, D.J. Lipomi, Plasticization of PEDOT:PSS by common additives for mechanically robust organic solar cells and wearable sensors, *Adv. Funct. Mater.* 25 (2015) 427–436.
- [41] Y. Wu, A. Islam, X. Yang, C. Qin, J. Liu, K. Zhang, W.W. Peng, L. Han, Retarding the crystallization of PbI₂ for highly reproducible planar-structured perovskite solar cells via sequential deposition, *Energy Environ. Sci.* 7 (2014) 2934–2938.
- [42] D.J. Wehenkel, K.H. Hendriks, M.M. Wienk, R.A.J. Janssen, The effect of bias light on the spectral responsivity of organic solar cells, *Org. Electron.* 13 (2012) 3284–3290.
- [43] U. Rau, Reciprocity relation between photovoltaic quantum efficiency and electroluminescent emission of solar cells, *Phys. Rev. B* 76 (2007) 085303.
- [44] U. Rau, U.W. Paetzold, T. Kirchartz, Thermodynamics of light management in photovoltaic devices, *Phys. Rev. B* 90 (2014) 035211.
- [45] M.A. Green, Radiative efficiency of state-of-the-art photovoltaic cells, *Prog. Photovolt: Res. Appl.* 20 (2012) 472–476.
- [46] K. Tvingstedt, O. Malinkiewicz, A. Baumann, C. Deibel, H.J. Snaith, V. Dyakonov, H.J. Bolink, Radiative efficiency of lead iodide based perovskite solar cells, *Sci. Rep.* 4 (2014) 6071.
- [47] J.F. Geisz, M.A. Steiner, I. Garcia, S.R. Kurtz, D.J. Friedman, Enhanced external radiative efficiency for 20.8% efficient single-junction GaInP solar cells, *Appl. Phys. Lett.* 103 (2013) 041118.
- [48] J. You, Y.M. Yang, Z. Hong, T.-B. Song, L. Meng, Y. Liu, C. Jiang, H. Zhou, W.-H. Chang, G. Li, Y. Yang, Moisture assisted perovskite film growth for high performance solar cells, *Appl. Phys. Lett.* 105 (2014) 183902.

4.10 Manuscript 10

Chapter 16

Polarons in Conjugated Polymers



Christoph Cobet, Jacek Gasiorowski, Dominik Farka
and Philipp Stadler

Abstract Conjugated polymers and polymer blends are key components in the development of organic electronics and (photo-) electrocatalysis. In particular, the possibility to produce organic but highly conducting films make these compounds very attractive. Therefore, enormous effort was put in the understanding and improvement of the electrical conductivity of polymer films. Conjugated polymers in their pristine form are mostly insulating or rarely semiconducting. The alternating single and double bonds in each π -conjugated polymer chain give rise to the formation of a band gap; the HOMO-LUMO gap. Semiconducting or conducting properties are obtained for example by optical, chemical, or electrochemical doping. The doping can be permanent as in the case of the polymer blends like PEDOT:PSS or short term. In both cases, the injected charge carriers commonly self-localize due to the strong electron-phonon interaction which yields in the formation of new quasi-particles called polarons. As a result, characteristic sub-band gap excitations emerge in optical measurements which extend from UV to the medium infrared spectral range. Optical methods in general, and spectroscopic ellipsometry in particular, are thus apparent characterization methods in scientific investigations as well as candidates to solve in-line monitoring and control issues. In the following section, we will briefly review the basic concepts of polymer “doping”, the formation of polarons and the origin of sub-band gap excitations. In a survey of methods we will shortly discuss ATR-FTIR and transmission/reflection spectroscopy results. A specific attention will be drawn

C. Cobet (✉) · J. Gasiorowski (✉)
Center of Surface and Nanoanalytics (ZONA), Johannes Kepler
University Linz, Altenbergerstrasse 69, 4040 Linz, Austria
e-mail: christoph.cobet@jku.at

J. Gasiorowski
e-mail: j.gasiorowski@evgroup.com

J. Gasiorowski · D. Farka · P. Stadler
Linz Institute of Organic Solar Cells (LIOS), Johannes Kepler
University Linz, Altenbergerstrasse 69, 4040 Linz, Austria

J. Gasiorowski
EV Group E.Thallner GmbH, DI Erich Thallner Str. 1,
4782 St. Florian am Inn, Austria

© Springer International Publishing AG, part of Springer Nature 2018
K. Hinrichs and K.-J. Eichhorn (eds.), *Ellipsometry of Functional
Organic Surfaces and Films*, Springer Series in Surface Sciences 52,
https://doi.org/10.1007/978-3-319-75895-4_16

355

on the in-situ spectroelectrochemical characterization, since electrochemical doping provides control on the doping level and allows e.g. a quantification of exchanged charges. In-situ ellipsometry could be used to monitor respective changes in the polymer optoelectronic properties. We will not aim for an overview about known types of conducting polymers in general or state of the art developments in organic electronics. The focus is a discussion of the physics of UV-VIS-MIR polaronic and electronic excitations as well as state-of-the-art ellipsometric characterization.

16.1 Introduction

In search of cheap and easy to produce materials in semiconductor technology, organic polymers gain a lot of attention due to the enormous flexibility to tailor their physical and chemical properties. On one hand this flexibility is certainly linked to the huge variability in the chemical structure of polymers which can be easily modified and even further extended by producing blends. On the other hand, it is linked to their exceptional electronic properties which combine attributes of localized molecular electron orbitals with electronic band structure properties known from inorganic crystalline semiconductors. Thus it is relatively easy to tune their behavior from insulator to semiconductor and further to a conducting state.

16.1.1 π -Conjugation

Organic polymers are basically build up by sp^2 hybridized carbon which give rise to the formation of carbon-carbon σ -bonds (the back bone of the polymer) and double bonds containing π -electron orbitals. In isolated small molecules or in the monomer units of the polymer, these orbitals are very well described in terms of a localized electron configuration. The asymmetric π hybridization of p-orbitals defines for example the highest occupied molecular orbital (HOMO) while the symmetric π^* counterpart represents the lowest unoccupied molecular orbital (LUMO). The energetic gap between these two electron levels determines in optical experiments the electronic absorption edge E_g . With the formation of polymer chains, which may contain a (periodic) sequence of double bonds, the π -electronic orbitals could overlap. As a result the localized π -electrons delocalize in one dimension and form electronic bands along the polymer chains. Polymers with these π -electron bands are known as π -conjugated polymers. The strength of the π -conjugation depend on the specific chemical structure but is also influenced by the conformation of the monomers in the polymer chain. A typical example is the twist of aromatic rings in a polymer chain which reduce the orbital overlap [1, Chap. 20] [2]. A “re-”localization of the π -electrons in twisted configurations e.g. leads to a measurable higher HOMO-LUMO gap (E_g) as a consequence of degenerating electron orbitals and quantum size effect.

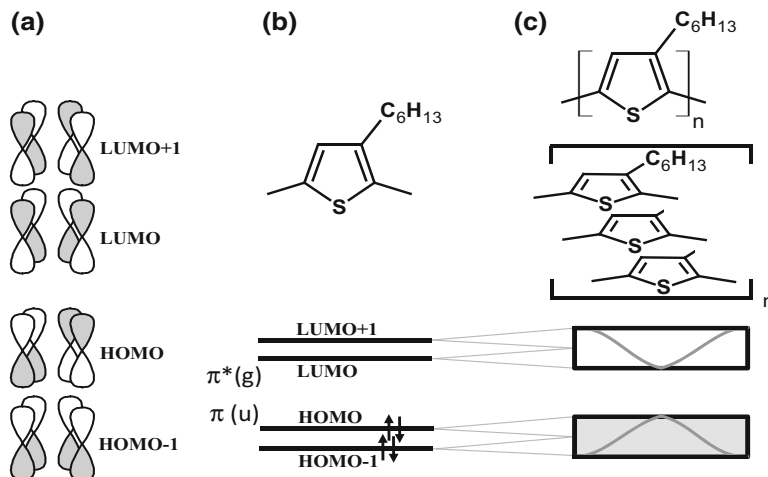


Fig. 16.1 Schematic representation of filled and empty π -orbitals in an isolated monomer (a), (b) and the formation of electronic bands due to π -conjugation in polymer chains or by intermolecular overlapping orbitals due to a π - π -stacking (c). The thiophene rings of P3HT are chosen as a representative example. The π -orbitals are labeled with respect to their energy and occupation highest occupied molecular orbital (HOMO) and lowest unoccupied molecular orbital (LUMO) as well as concerning their symmetry gerade/even (g) and ungerade/odd (u)

The polymer film properties depend on the intra-molecular configuration, but also to a reasonable extent on the aggregation structure. If polymers aggregate in films, Van der Waals forces between the polymer chains could yield locally in a crystal like stacking of the polymer chains. Commonly these structures are discussed in terms of a π - π stacking of the polymers. Independent from the question whether the underlying dipole-dipole interaction is dominated by the π -electrons, it is evident that the inter-chain overlap of π -orbitals could also induce an electron delocalization which is now perpendicular to the polymer chains. Different π -conjugation in combination with the π - π stacking may result locally in a 0D, 1D, 2D, or 3D electronic band structure. The concept of the formation of π -electron bands is illustrated in Fig. 16.1 by means of poly(3-hexylthiophene) (P3HT) as an example polymer. The symmetry of the system refers to the anisotropy in the electronic and optical properties. The excitation across the HOMO-LUMO transition is only allowed for an electric field parallel to the P3HT polymer chains. However, the final electronic and optical properties of the film depend very much on the ordering of the polymer chains. It should be noted at this point that a typical polymer film contains a domain like structuring and film properties like the conductivity or the effective dielectric function may depend very much on the internal ordering and the domain boundaries.

16.1.2 Polarons and Metal-Insulator Transitions

The typical band gap of conjugated polymers is larger than 1.5 eV [3]. The pristine polymers are thus intrinsically insulating and conductivity is usually obtained by charge injection, *it est* by a reduction or oxidation of the polymer chains. The electron orbital/band structure reformation upon charging, however, turned out to be rather complex and the mechanisms assigned to the finally obtained conductivity are in parts still under discussion. A charging of the polymer by adding or removing electrons does not result immediately in an incompletely filled band which could account for a conductivity increase. Adding an excess charge in a polymer chain rather induce locally a new equilibrium geometry which differ from that in the ground state. In inorganic semiconductors a local crystal deformation due to an excess charge is well known and described in terms of polarons - a concept which was first introduced by Landau in 1933 [4]. The formation of these quasi particles, which consist of a charge and a structure deformation, is theoretically described by the electron-phonon interactions. The coupling is generated by the polarization field of the longitudinal optical (LO) phonons. In the “weak-coupling limit” Fröhlich proposed from perturbation theory a Hamiltonian where the interaction strength is linear to the polarization field and expressed by the dimensionless Fröhlich coupling constant α [5]. The formation of polarons and related excitations are thus enhanced in ionic crystals and polar materials. Modifications of the Fröhlich model are, however, required for systems where short-range interaction get essential (small polarons) or in case of reduced dimensionality (1D-polarons). Such systems are better represented in the Holstein, Holstein-Hubbard, or Su-Schrieffer-Heeger model. Concerning a detailed description we would refer at this point to respective review papers [6, 7] and books like those of Alexandrov et al. [8, 9].

The polaron formation in polymers is closely related to the Franck–Condon principle. The latter concept considers conformational changes in molecules due to an electronic excitation by a photon. The time scale of this optical excitation is much smaller than the motion of nuclei and the optical transition thus takes place between the ground state and an electronic plus vibrational excited state which could relax afterwards towards the new equilibrium structure. Polarons in polymers are typically discussed for a persistent charge transfer from an donor/acceptor to the polymer chains or, in the case of the photo induced doping, for screened electron-hole pairs with a long life time. The local relaxation of the polymer chains thus induces new relatively sharp electronic levels. For the discussion of polaronic optical resonances, we would use an empirical description of the new states which refers to an often cited publication of Brédas and Steet [10]. Primarily, it is assumed that adding or removing a charge in π -conjugated polymers is mainly governed by a hole or an excess charge in the π -electron bands while the σ back bone of the polymer remains intact. As depicted in Fig. 16.2 this would yield in first approximation a delocalized hole in the HOMO band or a delocalized electron in the former LUMO band, respectively. However, it was mentioned already that this situation is in most of the polymers energetically not stable. The total energy minimum of the polymer is obtained by a

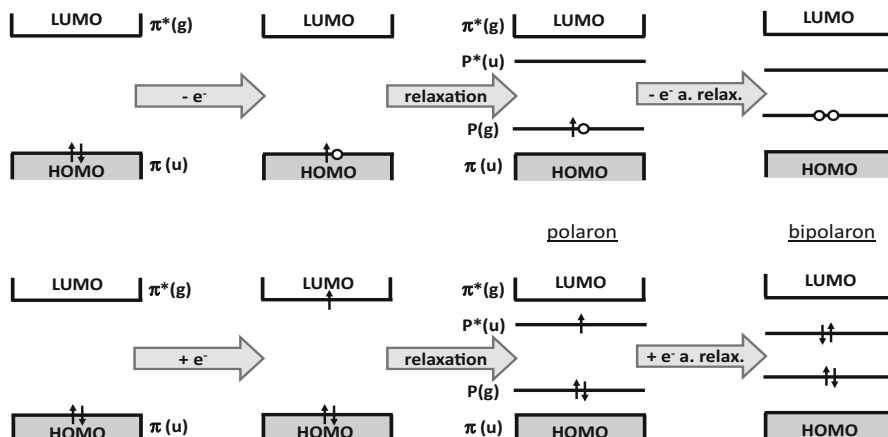


Fig. 16.2 Illustration of one-electron energy levels in polymer chains and the formation of in-gap polaronic states (P and P*) upon p-type (upper part) and n-type (lower part) doping. The transformation from the pristine, the ionization, the relaxation in a polaronic structure, and further ionization/relaxation in a hypothetical bipolaronic structure is depicted from left to right. The (bi)polaronic in-gap states are localized electronic states due to the self localization processes in isolated polymer chains

“self localization” of the charge due to a local relaxation of the polymer chain structure (Fig. 16.3). As a consequence of this relaxation the π -electrons will reorganize locally in a new orbital structure and it is assumed in particular that the unpaired electrons/holes form a new bonding/antibonding orbital pair which is energetically seated in the HOMO-LUMO band gap of the pristine material (Fig. 16.2). Like in the case of inorganic crystals, this new local structure is denoted as a polaron. The spin $\pm 1/2$ character is e.g. detectable in electron spin resonance (ESR) also known as paramagnetic resonance (EPR) measurements [11, Chap. 7] [12]. Furthermore it should be noted that the HOMO band is still completely occupied while the LUMO is still empty. The polaron itself has usually a relatively high effective mass [13] and thus none or only a minor increase of the conductivity is expectable.

In optical spectra the new polaron orbitals, however, should be measurable by some new dipole resonances. Primarily, one could expect a new electronic transition (P1) between the new orbitals formed by the unpaired charge which should occur energetically below the HOMO-LUMO transition (Fig. 16.4). Additional resonances (PE_g) may arise if filled double bonds remain in the polaronic section. Such resonances may overlap energetically with the HOMO-LUMO optical transition in the remaining pristine polymer. By symmetry arguments [14] some of the transitions between paired and unpaired π -electrons at the polaron side are not allowed or suppressed. Transitions between the HOMO and LUMO bands of the remaining pristine polymer and the polaron orbitals are also unlikely because of the small or vanishing spatial overlap. However, as depicted in Fig. 16.4 one could expect a transition (P2)

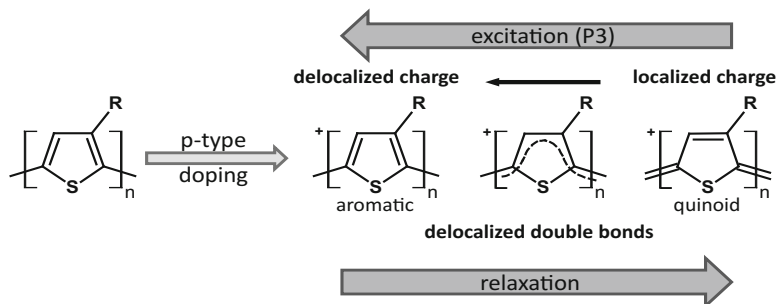


Fig. 16.3 Schematic representation of the p-type doping induced relaxation of the P3HT polymer structure. Upon the positive charging the polymer chain change locally from aromatic to a quinoid structure. Not shown is the parallel reduction of the inter thiophene bond length and the more planar orientation of the thiophene rings in the quinoid arrangement. Relaxation and excitation processes in the doped state can be understood as (self)localization and delocalization of the charge where a strong delocalization refers to almost homogeneous aromatic structure

between the filled and half filled polaron π -orbitals [14]. The respective transition energy is typically in the order of 0.3–0.5 eV. In many publications, the authors do not distinguish between the latter transition and an excitation of the polaron charge in its local potential well which we denote in Fig. 16.4 as P3. The P3 transition is explained in the Fröhlich polaron model as a polaron scattering process where the incoming photon is absorbed by the polaron in its ground (initial) state [15]. Upon scattering at least one LO phonon is generated which leaves the polaron in an excited (final) state. The onset of this absorption is thus defined by a “long-wavelength” LO-phonon frequency. But it peaks at somewhat higher energies. The line shape and position of the maximum depend on the Fröhlich coupling constant and the polaron dimensionality [13]. Above the latter absorption peak, additionally LO-phonon side bands may arise. It should be mentioned that probably neither the one-electron model nor the Fröhlich model correctly represents the complexity of the IR excitations. Both contain approximations which are not applicable in the case of strong electron-phonon coupling in polymers.

It was pointed out already by Brédas et al. [10, 16] that the charge induced relaxation of the polymer in a new structure is a “manifestation of a strong electron-phonon coupling”. As an example we use in Fig. 16.3 the relaxation of a polythiophene polymer like P3HT after positive charging. In the pristine form the thiophene rings are of an aromatic structure which relaxes in quinoid-like structure upon positive charging. This transformation is accompanied by shortening of the bonds between the thiophene rings [1, Chap. 1] [14, 17]. The before periodically tilted thiophene rings rearrange, furthermore, in a more coplanar structure. A polaron excitation as described before in the Fröhlich model is equivalent to a delocalization of the charge within the polymer chain [18] and the local quinoid-like structure fades out until the polymer chain resembles entirely in an aromatic structure.

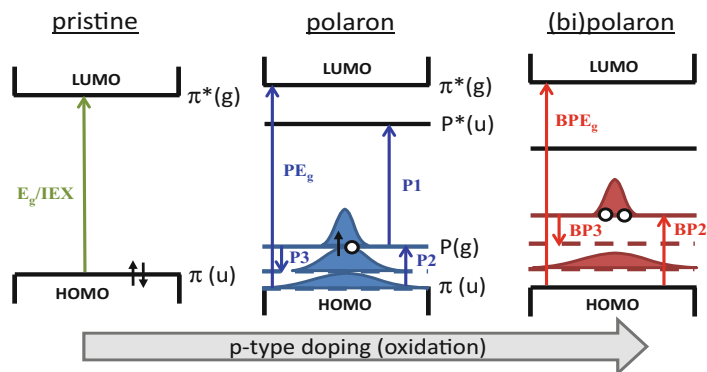


Fig. 16.4 Schematic illustration of possible optical π -electron excitations in the undoped (pristine) material and at polaronic or bipolaronic sides in the doped state. We would note that the presented one-electron picture should be used with care. Due to the strong electron-phonon coupling the single particle band theory is not able to describe the full complexity of the processes. The definition of a P2 transition is here motivated from the one-electron view as an excitation from empty to half filled valence states. The definition of P3 excitation is motivated by the Fröhlich polaron model as an excitation of the polaron in its self generated potential well and is probably best described by Fig. 16.3. The dashed lines symbolize the polaron states with increasing charge delocalization. The total energy of the system increases with the increasing charge delocalization which is the polaron binding energy.

It should be noted that the discussed new polaron states and the respective electronic transitions are sharp and defined only in the small polaron limit. In the “large polaron” limit intra- and/or inter-chain delocalization due to the π - π -stacking yields in a formation of electronic bands as it was described for π -electron system in the pristine uncharged state [14, 19, 20]. Furthermore intra- and/or inter-chain disorder contribute additionally to a broadening of absorption peaks [21].

A bit more controversially discussed is the electronic structure in case of a “further increased” charging which is frequently described by a situation where a second electron is removed from a polymer chain. If it is energetically favored that the two polarons couple, a localized distortion is obtained which contains two charges of the same type. This quasi particle is called bipolaron and has zero (integer) spin. The polaronic orbitals or bands are now completely empty (p-type doping) or completely filled (n-type doping). The P1 optical absorption between the polaronic orbitals/bands should therefore disappear while the P2/P3 absorption remains or increases at bipolaronic sides (BP2/BP3). Furthermore one could expect that the BP2 bipolaron absorption emerges at somewhat higher photon energies in comparison to the P2 polaron transition due to a further shift of the (bi)polaron in-gap levels. However, neither a vanishing of the NIR-VIS polaron absorption (P1) nor the disappearance of the unpaired spin is an unambiguous indication of a bipolaron formation. A reasonable increase of the polymer conductivity is usually obtained at relatively high charge concentrations. The existence of bipolarons alone, however,

cannot explain the increase in the conductivity. The above bipolaron model contains again no half filled electronic bands but locally filled or empty orbitals. The effective mass of a bipolaron should be even larger than this of a single polaron. However, the overlap of (bi)polarens at “higher” charging levels should yield again in a formation of (bi)polaron bands [22, 23]. If the correlation strength exceeds a certain level, these bands split in filled and empty bands which are separated by a small gap (Mott transition). Pure one-dimensional systems are supposed to be always insulating. Likewise metal-insulator transitions are discussed in presents of disorder in the system. Local variation again cause a localization of polaron electron wave functions and in particular one-dimensional systems tend to be insulating (Anderson transition) [24]. Whether the formation of bipolarons or metal like bands could be observed depend very much on the particular polymer and the respective film structure. Some examples will be discussed in the following based on optical/ellipsometric results.

All the distinct electronic orbitals and bands which come along with the formation of polarons, bipolarons, or metallic states produce, as discussed, a number of new dipole allowed optical transitions. These changes of the optical properties in the visible spectral range are that strong that many conjugated polymers were also intensively studied because of their electrochromic properties [25]. The application of conjugated polymers e.g. in electrochromic displays promised higher contrast ratios and faster response times. Most of the conjugated polymers switch between a transmissive and a colored state upon doping. But also switching between different colors is possible [1, Chap. 21].

The strong optical effect of doping is used from the beginning as a probe to study fundamental aspects of the polaron formation. By far most of the optical investigations apply reflection or transmission methods. In the IR spectral range enhanced thin film sensitivity is commonly obtained within attenuated total reflection experiments (ATR). A methodical review of these methods is provide e.g. in Chap. 21 (*Characterization of Thin Organic Films with Surface-Sensitive FTIR Spectroscopy*). But, in particular Fourier-transform infrared (FTIR) results are usually interpreted in a pure chemical manner by means of differential absorption properties of the investigated film without making use of the polarization dependency. Ellipsometric experiments are in comparison still underrepresented although the method could provide quantitative results concerning the complex dielectric function (complex refractive index) and physical parameters like the film thickness. One reason is certainly the relative complexity of the necessary data evaluation (Chap. 1: *Ellipsometry: A Survey of Concepts*). In the following examples, we will discuss the optical response of polarons primarily based on ellipsometric results. But additionally we add a critical review of some basic relationships among the different methods, with the goal to provide a conceptional comparability and to draw the attention on fundamental deficiencies among the optical spectra published in literature.

16.1.3 Charge Injection

Before turning to the optical characterization of polarons, we would spend a few words how the charge injection is achieved in the polymers. In analogy to inorganic semiconductor technology, the charge injection in polymers is commonly referred to the synonym “doping”. In common, it requires an electron/hole source which could be a chemical element. But in contrast to inorganic semiconductor crystals, this donor/acceptor is typically not inserted in the polymer chain. The finding that a persistent doping is nevertheless feasible was a key step in the discovery of conduction polymers [26, 27] and acknowledged by the Nobel Prize in Chemistry in 2000. In literature one can find a huge number of different “doping” recipes. But in general they can be divided into four principal groups [11]:

(1) Chemical p- or n-type doping (oxidation or reduction): The chemical doping was utilized in the first discovery of polymer conductivity in polyacetylene films. The charge transfer is achieved by exposing and mixing the polymer with oxidizing or reducing reagents which can be considered as acceptor or donor impurities in inorganic semiconductors. In order to obtain p-type doping the polymer could be e.g. exposed to halides like I_2 or Br_2 which form finally charge transfer complex between the polymer and the I^- or Br^- anions. An closely related method of p-type doping is called “protonation” where polymers containing a nitrogen atom are exposed to acid vapor (e.g. HCl). The strong dipole moment of the acid results in the shift of the lone electron pair at the nitrogen atom generating positive charge. Such doping is applied for example in polyaniline or polyazomethines [28]. A n-type doping can be obtained by exposing polymer thin films to Li [29] or Na atoms which requires a (ultra)high-vacuum chamber.

(2) Electrochemical p- or n-type doping: A drawback of the chemical doping is in general the difficulty to control the doping level as well as the problem of inhomogeneity. Electrochemical doping in contrast promise a very good control of the charging level and lateral homogeneous results. The polymer is deposited on a conducting electrode (the working) electrode and attached in an electrochemical cell containing an electrolyte. Common electrolytes used in polymer electrochemistry consist of organic solvents like propylene carbonate, acetone, or acetonitrile and a conducting salts like tetrabutylammonium hexafluorophosphate (TBA-PF6, $C_{16}H_{36}F_6NP$), nitrobenzol, or lithium tetrafluoroborate $LiBF_4$ due to their broad electrochemical window. During the electrochemical doping the working electrode supplies or collects the redox electrons while anions or cations diffuse from the electrolyte in the polymer film in order to ensure the charge neutrality. The doping level is controlled by the potential between the polymer and the electrolyte i.e. the counter electrode. Each potential is assigned to a specific doping level defined by the electrochemical equilibrium.

(3) Field induced “doping” - Charge injection at metal-polymer interfaces: The concept of a field induced charging refers to the operation principle of polymer based field effect transistors. At interfaces charges can be added or removed from

the π -orbitals/bands of the polymer due to a contact potential difference which is either externally applied or is a result of a different work function like in a Schottky contact. The main difference in comparison to chemical or electrochemical doping is the absence of counter ions introduced in the polymer. Thus the field induced doping is not persistent if the externally applied field is switched off.

(4) Photo-induced “doping”: Photo-induced doping can be obtained only in polymer blends. In such, the film is illuminated with light of a photon energy above the HOMO-LUMO gap. The induced electron-hole pair can be of intra- as well as of inter-chain character. Persistent free charges and the formation of polarons is obtained only if the electron-hole pair separates like in a p-n junction. The life time depend on several factors as the exciton binding energy and the band offset within the polymer blend structure. In specific cases, air can play the role of a n-type semiconductor leading to photooxidation process.

16.2 P3HT

Among the (semi-)conducting polymers, poly(3-hexylthiophene)(P3HT) is probably one of the most frequently investigated model systems with applications in organic optoelectronics like solar cells, light-emitting diodes, or transistors [30]. P3HT is a p-type (hole) conducting polymer. In organic photovoltaic devices it is used for example in the active layer as an electron donor material. P3HT is relatively ease to synthesize and shows pronounced optoelectronic properties which make it also an ideal model system in order to study the fundamental properties of doping in polymers. Details concerning the application of P3HT in organic photovoltaic (OPV) and organic light emitting diodes (OLEDs) as well as a discussion of the pristine material optical properties are also presented in Chaps. 12 (*Polymer Blends and Composites*) and 15 (*Conjugated polymers: Relationship between morphology and optical properties*).

16.2.1 Dielectric Function

Figure 16.5 shows the dielectric function (DF) of regioregular (rr-)P3HT as it is known for the pristine undoped state. The presented spectrum was measured by transmission ellipsometry on a 56 nm film in electrolyte at potentials where the P3HT is completely undoped. Unintentional doping by illumination or oxidation from air is thus avoided. The film was spin-casted on glass covered with indium-tin oxide (ITO) [31]. Details about the measurement will be described in the section about the electrochemical doping.

The example P3HT film shows a very strong out-of-plane anisotropy. The oscillator strength of the contributing absorption resonances is strongly reduced in the

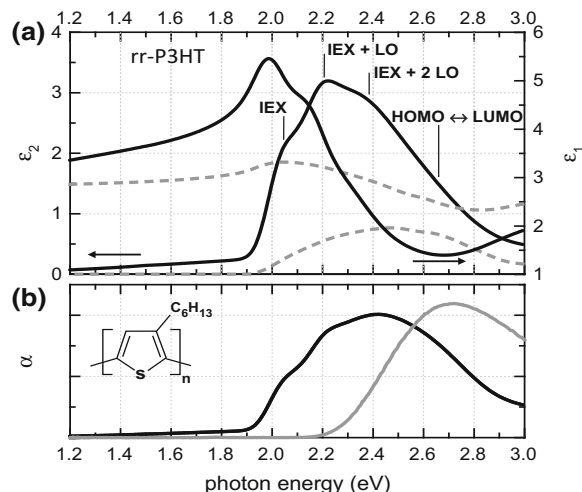


Fig. 16.5 **a** Anisotropic dielectric function of un-doped P3HT measured by transmission ellipsometry. The black line corresponds to the in-plane while the dashed gray line corresponds to the out-of-plane component. The film under investigation was spin casted on a glass substrate covered with ITO and is measured in a 0.1 M Bu_4NPF_6 electrolyte solution in anhydrous acetonitrile at a potential of -200 mV against a Ag/AgCl quasi reference electrode. **b** Absorption spectrum of the un-doped P3HT film calculated from the ellipsometric results (black line) in comparison to an absorption spectrum measured in transmission through a P3HT solution in chlorobenzene (gray line) [31]

DF perpendicular to the surface in the presented spectral range. Such a behavior is typical for P3HT [32] and many other conjugated polymer films [33, 34] where the interaction with the substrate provokes a predominate alignment of the polymer chains parallel to the interface. A detailed ellipsometric study of the anisotropy of P3HT was published in [32]. In this work the authors discuss also the influence of the substrate by comparing spin-coated and drop-cast P3HT films on glass and Si. The orientation selectivity of excitations is explainable by the common nature of the contributing absorption structures in the considered spectral range. All the near band gap optical transitions in P3HT are dipole π - π^* transitions. Their excitation requires an electric field component parallel to the P3HT conjugated polymer chain [35]. An out-of-plane excitation of the π - π^* transitions in the visible and ultra violet spectral range (VIS-UV) is thus dipole forbidden if the polymer chains are all parallel aligned to the surface.

In this connection it should be noted that the measured anisotropies are obtained by assuming a homogeneous film. Such a commonly used assumption actually needs to be confirmed. However, since a strong out-of-plane anisotropy is observed also by “averaging” over the whole film, one can assume that the average volume fraction of the polymer strands with a perpendicular orientation to the surface is generally small. In other words the substrate induced polymer orientation of the polymers retains in

the entire film. This behavior can be explained by a relatively strong inter-molecular interaction and is discussed in polymers by means of the π - π stacking [31–34].

The absorption onset of P3HT in the pristine “undoped” form is induced by a distinct resonance at 2.04 eV which is assigned to a delocalized inter-chain singlet exciton (IEX) [36]. Two more resonances follow energetically above the IEX at 2.20 and 2.37 eV almost equidistant in energy. The latter transitions are vibronic sidebands of the IEX with an additional excitation of one or two LO-phonons (Fig. 16.5a). The relatively broad absorption structure between 2.6 and 2.7 eV is finally attributed to the screened intra-chain HOMO-LUMO transition (E_g) and thus coincide to π - π^* transition in isolated P3HT polymer chains. The latter association gets evident if one compares the absorption spectrum of the film (calculated from the in-plane DF) with the absorption spectrum measured e.g. in transmission for diluted P3HT. Such a comparison is shown in Fig. 16.5b. The diluted and therefore separated P3HT polymer chains disclose only one relatively broad absorption peak around 2.7 eV which is the just defined intra-chain HOMO-LUMO transition. The distinct film resonances at lower energies are absent. A small red shift of the film HOMO-LUMO transition is explainable by the polarizability of the surrounding P3HT molecules i.e. coupling and screening effects.

The inter-chain character of the IEX was demonstrated based on its dependency on the degree of the π - π stacking and the crystallinity of the film (Fig. 16.1). Generally, it could be shown that the IEX amplitude vanish for totally disordered films or P3HT-blend structures where the individual P3HT chains have no direct contact [37, 38]. Figure 12.4 in Chap. 12 shows for example the effect of thermal annealing on the IEX structures for spin coated P3HT films. Worth mentioning in this connection is the relative large oscillator strength of the HOMO-LUMO transition in the out-of-plane film DF (dashed line in Fig. 16.5a). If we consider that the π - π^* transitions require an electric field component parallel to the polymer chains, we can conclude that a non vanishing absorption in the out-of-plane DF yields from polymers which are upright orientated to the substrate plane. Such a molecular orientation is in particular expected in disordered areas where the IEX contributions are small. A detailed analysis of the optical anisotropy of π - π^* transitions could thus provide already further insights in the inner film structure.

16.2.2 Iodine Doping

As mentioned before, chemical doping by exposing conjugated polymers to oxidizing or reducing agents was used already in the first attempts to modify the electronic properties of polymers. Iodine is one of the strongest oxidizing elements and is thus often used in order to obtain p-type doping i.e. a positive charging of the polymer. In general all p-type doping methods should produce very similar changes in the optical absorption spectra. According to the polaron picture described in the introduction, some new transitions in energy below the absorption edge are expected [39, 40].

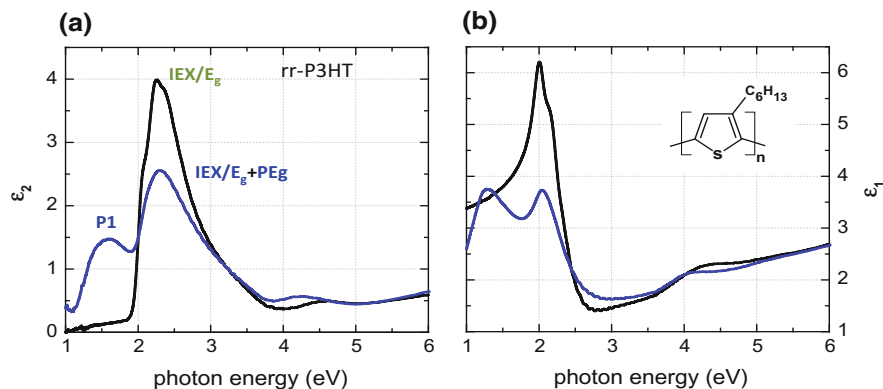


Fig. 16.6 In-plane dielectric function of P3HT (structure in the inset) in the nominally undoped (black line) and iodine saturated doped state (blue line). The imaginary part of dielectric function is plotted in the left panel (a) and the real part in the right panel (b) [41]

The iodine doping of P3HT is therefore used as a prototype example in order to demonstrate the doping induced changes in the optical response of polymers.

We use again a rr-P3HT film of 35 nm which was spin casted on an ITO/glass substrate as an example. The particular film was annealed at 150 °C for 3 min in a nitrogen atmosphere. The doping was performed by exposing the sample to iodine vapor for 10 min. A relatively long doping time is used in order to obtain a saturation which allows a subsequent ellipsometric measurement under relatively stable conditions [41]. The DF of the iodine doped P3HT is shown in Fig. 16.6 (blue line) in comparison to the as before measured DF of the pristine film (black line). Within the used measurement geometry the calculated DF represents the in-plane DF component.

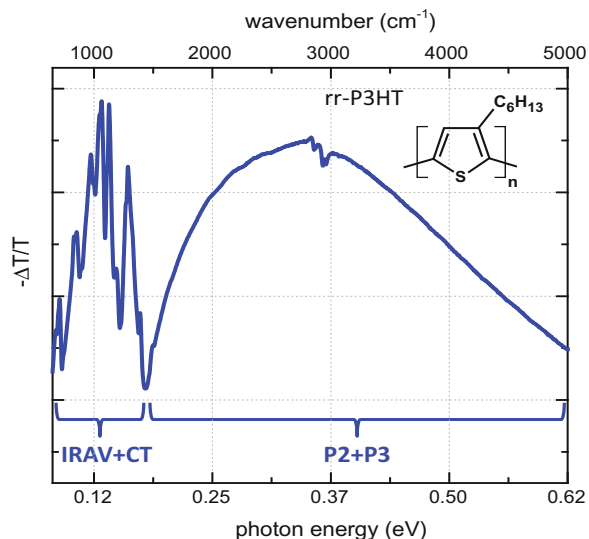
After doping the film optical properties disclose two eye-catching modifications. The π - π^* transitions measured before between 2 and 3.5 eV appear now very much reduced in amplitude. At the same time a new peak shows up at 1.6 eV. Both changes resemble the before discussed formation of polaronic states in the band gap of the pristine material (Fig. 16.2). The new absorption feature at 1.6 eV thus refers to the P1 transition as shown in Fig. 16.4. The unpaired spin in the polaron state is proven e.g. in EPR measurements [42].

A closer inspection of the DF changes upon iodine doping discloses further that the remaining, as well as the new appearing absorption features broaden in comparison to the pristine material. This broadening turned out to be not specific for the iodine doping but is rather a result of a more principle property. Among the new polaron transition feature we could expect again a splitting due to the formation of inter chain excitons and respective LO-phonon replica as discussed in the pristine material. The self localization of the positive charge within a polymer chain was already discussed in terms of a local relaxation of the polymer structure. In the case of P3HT, the

π electron system change from an aromatic configuration in a quinoid-like structure upon doping (Fig. 16.3) [10, 40]. The relaxation is expected to extend at least over three monomers (Figs. 16.3 and 16.12) and includes a planarization of the monomer units [16, 19, 43]. The polaron electronic states thus broaden due to the spreading of the polarons with in the chain (large polaron approximation) and the interaction of neighboring π - π stacked polymer chains. The latter yields in an additional splitting of polaron states and the formation of bands (2-3D polarons) [14, 22]. Both effects; the delocalization of polaronic states along as well as perpendicular to the polymer chains; were already discussed for the undoped π electron orbitals and visualized in Fig. 16.1. Different is now that undoped and doped areas as well as various degrees of localization of the polarons could coexist in the film which leads to an increased complexity and general broadening of the contributing absorption structures.

The quantitative determination of the film DF by means of ellipsometric measurements allows additionally a discussion of the different transition oscillator strength. In the case of the iodine doped P3HT it is already visible by eye that the decrease of the transition strength between 2 and 3.5 eV is not compensated by the new structure around 1.6 eV. At the same time the DF above 3.5 eV does not change on the doping at all. By sum rule arguments, the first moment of the imaginary part of DF is proportional to the density of the contributing (π) electrons [45, 46]. However, the p-type charging alone could not explain the overall reduction of the transition strength in the spectral range between 1 and 3.5 eV. The missing oscillator strength is thus most likely shifted to transitions in the IR. According to the drawn polaron theory at least one additional electronic transition is expected in the IR - the P2 transition depicted in Fig. 16.4.

Fig. 16.7 Iodine doping induced changes in the P3HT optical response measured by ATR-FTIR after 12 s exposure [44]



Typically ATR-FTIR spectroscopy is used to analyze the polaronic absorption of thin films in the IR spectral range. Figure 16.7 shows a differential ATR spectrum of the iodine doped P3HT film [44]. Accordingly, the absorption increases in the whole IR spectral range. But the new absorption emerges clearly in two distinct spectral regions. A broad doping induced absorption band appears above 1800 cm^{-1} which contain various contributions and the line shape differs from the simple Lorentz oscillator model [8, 9]. However, in principle the band is attributed to the π -electron in-gap transition P2 and the polaronic excitation/relaxation P3 (Fig. 16.4). In the Fröhlich polaron model, the P3 transition is described as a LO-phonon excitation. The onset of the broad P3 absorption band at 1800 cm^{-1} is in this model defined by the long wavelength LO-phonon frequency. In terms of the discussed doping induced structure relaxation in the P3HT polymer chain, the P3 excitation could be interpreted as a delocalization of the polaron as presented in Fig. 16.3.

Below 1800 cm^{-1} new doping induced infrared active vibrations (IRAV) modes appear [47, 48]. Before just Raman active modes are activated by the polaron due to changes in the symmetry relative to the pristine material. The high intensity of IRAV mode absorption is again a result of the electron-phonon coupling. The IRAV-modes may be additionally superimposed by a broad absorption feature which is attributed to a charge transfer transition (CT) between the polymer chains [21].

16.3 Electrochemical Doping of P3HT

An obvious problem of the iodine doping and the chemical doping in general is the lack of control concerning the amount of transferred charges or in other words the oxidation/reduction stage of the of the polymers. Closely related to the control problem is also the question of a quantification of the charging. Like in the described iodine doping one can probably find saturation at a certain density but the instability on one hand and the re-crystallization of iodine in the film on the other make it difficult to obtain reproducible results. The electrochemical doping of conjugated polymers in contrast provides full control on the induced charge density by means of the applied electrochemical potential. By cyclic voltammetry (CV) or in chronoamperometry it is furthermore possible to quantify the charge transfer. Electrochemical impedance spectroscopy could provide additionally a determination of the conductivity upon doping variations [49].

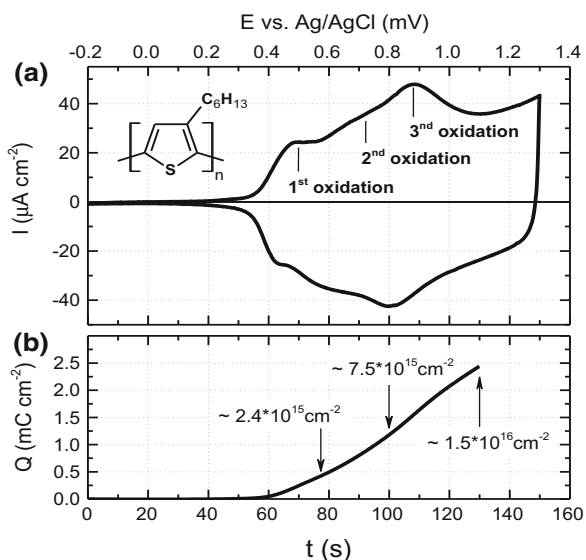
Spectroelectrochemical investigations of polymers are therefore already widely used to study doping induced fundamental aspects like a structural relaxation, an insulator to metal transition, changes of the electronic structure and the formation quasi particles like polarons [50–53]. The applied in-situ spectroscopic methods are almost exclusively of absorption and reflection type. An analytical disadvantage of the electrochemical approach could be seen in the fact that the film under investigation is covered with an electrolyte which is usually not transparent over wide areas in the IR spectral range. (FTIR)-ATR spectroscopy has in this connection the advantage that the light transmission through the electrolyte is avoided.

16.3.1 (Spectro-)Electrochemistry

For spectroelectrochemical investigations on rr-P3HT, an electrochemical cell like the quartz cuvette as shown in Fig. 16.10b could be used. In such a cell the polymer film is deposited on a conducting substrate (ITO/glass) and is used as the working electrode (WE). The electrochemical potential E of the WE is controlled by a potentiostat with respect to a reference electrode. In the given example a Ag/AgCl wire is used as a quasi reference electrode (QRE) [54]. The potential dependent electrochemical charge transfer due to an oxidation or reduction of the polymer film is measured as a current between the WE and a counter electrode (CE) which is typically made of platinum. A common electrolyte solution is composed of 0.1 M/L Bu_4NPF_6 ($\text{Bu}_4\text{NPF}_6 \rightleftharpoons \text{Bu}_4\text{NP}^+ + \text{PF}_6^-$) in anhydrous acetonitrile.

The electrochemical redox properties of spin casted P3HT films are presented in Fig. 16.8a based on a CV recorded with 10 mV/s [31, 42]. In anodic scan direction, one can identify three major oxidation peaks which contain a couple of sub-structures. In the cathodic scan the P3HT film turns back in the undoped state with respective negative reduction current. The processes are reversible and the cycle can be repeated a couple of times without degradation of the film. Each peak in the CV can be associated with a certain oxidation/doping stage of the film. A precise assignment is difficult. But already the fact that the P3HT film possess more than one or two oxidation levels clearly supports the assumption of inter-chain interactions due to the π - π stacking. The increase of complexity due to the formation of inter-chain structures could increase the number of distinguishable oxidation/doping levels. Beside

Fig. 16.8 Cyclic voltammogram of P3HT in a Bu_4NPF_6 -acetonitrile solution recorded with a scan rate of 10 mV/s (a) In panel b shows the charge density in the film accumulating in the anodic sweep from -0.2 to 1.1 V [31]



of an identification of oxidation stages, it could be instructive already, to investigate the charge density in the film at different doping levels. The time integral (the first moment) of the anodic current, which is measured in CV, provides this information. The measured current tells us how many electrons are transferred from polymer film to the ITO and leave a positively charge hole in the P3HT polymer chains. The charge neutrality is maintained with the intercalation of an equal number of PF_6^- anions (A^- in Fig. 16.12) in the film. The successive increase of positive charges in the P3HT film upon the electrochemical oxidation is plotted in Fig. 16.8b. With the known film thickness this calculation disclose that the “donor” concentration increase by $3.4 \times 10^{20} \text{ cm}^{-3}$ upon the first oxidation step. The second and third oxidation steps yield in an overall anodic charge transfer of 1.2 and 2.4 mC/cm^2 , respectively, which corresponds to a total “donor” concentration in the film of 1×10^{21} and finally of about $2 \times 10^{21} \text{ cm}^{-3}$. An upper limit approximated from the monomer density in the film [31, 55] yields a number of $4\text{--}5 \times 10^{20}$ thiophene rings per cubic cm. The second oxidation step thus corresponds to a positive charging of about 20% of the thiophene monomers and with the third oxidation this value increase to almost 50%.

In-situ UV-VIS transmission and ATR-FTIR experiments show that the increasing electrochemical charging of the P3HT film leads to a monotonously decrease of all $\pi\text{-}\pi^*$ transition which have been identified in the pristine polymer (Fig. 16.5) while the NIR and IR absorption structures (P1, P2/P3, IRAV, and CT) monotonously increase at the same time [42]. That the p-type doping induced modifications in the electronic structure are not explainable just by a continuous transformation from the pristine to a oxidized state becomes obvious in the spectral range between 1.2 and 2 eV. The P1 polaron transition structure, which was seen already in the iodine doped films, increase up to 800 mV, but decrease again at higher potentials (Fig. 16.9b). Furthermore, one can observe a splitting of the broad P2/P3 IR absorption in the ATR-FTIR spectra (red arrows Fig. 16.9a). A precise interpretation based on the ATR-results is in fact difficult and the determination of the intrinsic material dielectric properties could facilitate a better identification of transition resonances or their spectral positioning.

16.3.2 *In-situ Spectroelectrochemical Ellipsometry*

The unquestioned advantage of common transmission experiments is on one hand the simplicity of the method. On the other hand it is also of big advantage if the film properties can be investigated in standard glass cuvettes which are typically used in electrochemical experiments. In this connection it seems reasonable to combine the advantages of ellipsometric measurements and the ability to investigate the films in a standard glass cuvette by means of transmission ellipsometric measurements [31]. In such an experiment the light beam is straight transmitted through a glass cuvette, the electrolyte, and the sample which consists of a transparent substrate (e.g. glass), a transparent conducting film (e.g. ITO), and the polymer film under investigation. The sample surface must be tilted against the light beam in order to

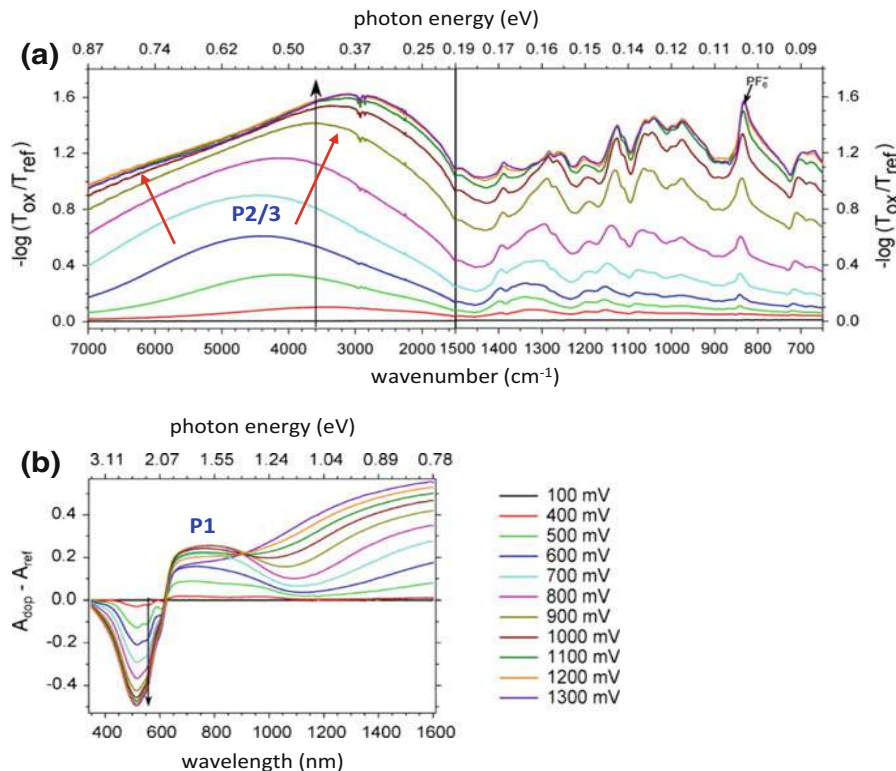


Fig. 16.9 Electrochemical doping induced changes in the P3HT optical response measured **a** by in-situ ATR-FTIR and **b** by UV-VIS transmission spectroscopy at different potentials between 100 and 1300 mV. The spectra measured at 0 mV are used in this examples as a reference. Reprinted from [42] with permission from WILEY-VCH

allow an ellipsometric analysis by means of the difference in light transmission for parallel and perpendicular polarization components respective the plane of incidence. Polarization effects and intensity losses at the outer cuvette surfaces can be suppressed by two index matching prisms which are attached to the cuvette and thus ensure perpendicular light incidence (lower part Fig. 16.10).

Some attention has to be drawn on the extraction of the film optical properties because several interfaces inside the cuvette contribute to the measure polarization change which is represented by the ellipsometric angles Ψ and Δ . The upper part of Fig. 16.10 shows a schematic example for the light propagation through the internal interfaces. A physical/mathematical description of the light transmission through such an ensemble can be obtained with the known theories of light propagation in media and the reflection/transmission of plan waves at planar interfaces [56–58]. Of major importance in such a structure is the coherence length of the light. Commonly

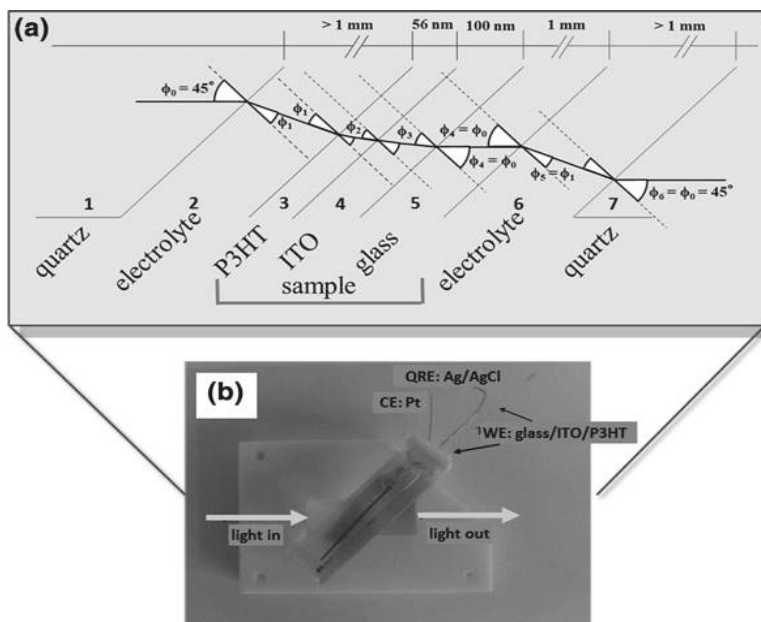


Fig. 16.10 Schematic diagram of the light propagation through the glass cuvette including a polymer film on an ITO/glass substrate (a). Layers represented in red are thinner than the coherence length of conventional light sources and interference has to be taken into account in an ellipsometric layer modeling procedure. In the lower part b we show a real experiment image of a filled glass cuvette with connectors for the quasi reference electrode (QRE), the counter electrode (CE) and the ITO/glass working electrode (WE). Reproduced from: [31]

used light sources have a coherence length of a few micrometers. Accordingly, the distance of interfaces like those given by the two sides of the glass substrate is bigger than the coherence length. In our example only the polymer and the ITO films are thinner. Therefore just in these two layers forward and backwards traveling waves have a defined phase relation and interference effects have to be taken into account.

In the case of isotropic media the Abeles matrix method can be applied to solve the problem and to calculate finally the film optical properties [57, 59]. In this formalism the total electric field at a planar boundary between a layer i and j is composed of left and right traveling waves. The respective complex fields are arranged in columnar vectors of the form $E'_i = (E'_{i,l}, E'_{i,r})^T$ and $E_j = (E_{j,l}, E_{j,r})^T$. With the Fresnel transmission and reflection coefficients $t_{ij}(\epsilon_i, \epsilon_j, \phi)$ and $r_{ij}(\epsilon_i, \epsilon_j, \phi)$ an interface transmission matrix of the form:

$$\hat{H}_{ij} = \frac{1}{t_{ij}} \begin{pmatrix} 1 & r_{ij} \\ r_{ij} & 1 \end{pmatrix}, \quad (16.1)$$

can be defined which connects the fields on both sides of the boundary ($E'_i = H_{ij} E_j$). For a phase correct matching of the fields from the right side of a layer to the left side of the same layer, furthermore, a propagation matrix is defined according to:

$$\hat{L}_i = \begin{pmatrix} e^{-i\beta_i} & 0 \\ 0 & e^{-i\beta_i} \end{pmatrix}, \quad (16.2)$$

where

$$\beta = \frac{2\pi}{\lambda_0} n_i d_i \cos(\phi_i). \quad (16.3)$$

In case of layers, which are much thicker than the coherence length of the light, it is sufficient to use the identity matrix in order to match the electric fields directly to the next boundary. Interference effects are thus excluded. The electric fields on both sides of our glass cuvette with an internal structure as depicted in Fig. 16.10, can be thus calculated with the stack matrix \hat{S} defined by:

$$\begin{pmatrix} S_{11} & S_{12} \\ S_{21} & S_{22} \end{pmatrix} = \hat{H}_{67} \hat{H}_{56} \hat{H}_{45} \hat{L}_4 \hat{H}_{34} \hat{L}_3 \hat{H}_{23} \hat{H}_{12}. \quad (16.4)$$

In transmission experiments with light propagating from the left to the right through the cuvette, we just need the S_{22} component of the stack matrix which defines the overall transmission coefficient

$$t = 1/S_{22}. \quad (16.5)$$

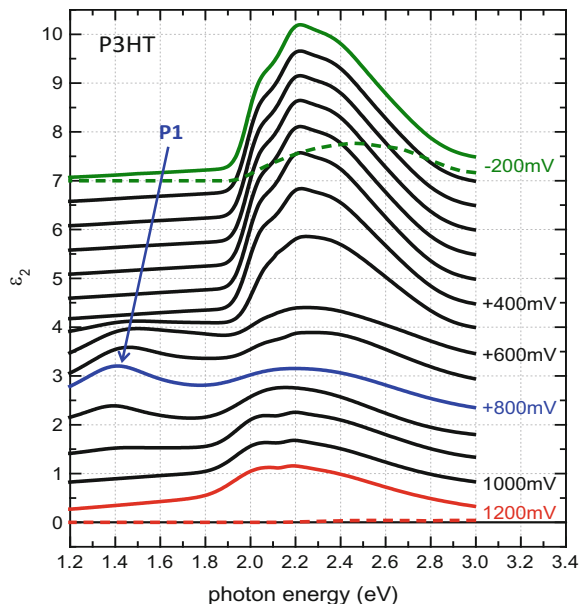
For isotropic media, s- and p-polarized waves are eigenmodes and can be calculated separately with the respective Fresnel equations ((1.13), Chap. 1). The ellipsometric angles Ψ and Δ can be finally calculated by the known relation:

$$\frac{t_p}{t_s} = \frac{S_{22}^s}{S_{22}^p} = \tan \psi e^{i\Delta}. \quad (16.6)$$

The film optical properties like the dielectric function ε or the thickness d of the polymer film are determined in a comparison with the experimental results by means of a respective fit algorithm.

The Abeles method is also applicable for anisotropic media, as long as the optical axes are all parallel or perpendicular to the plane of incidence and the surface normal of the interfaces. In such a case the s- and p-polarized waves are still eigenmodes and can be calculated separately. However, as an alternative one can use the Berreman transfer matrix formalism which is implemented nowadays in many ellipsometric software packages. In this formalism forward and backward traveling waves are calculated with differential 4×4 transfer matrices and an explicit definition of reflection and transmission coefficients at boundaries is avoided. With this approach it is possible to calculate the wave propagation in arbitrary anisotropic media [57, 58, 60, 61]. Interferences in layers thicker than the coherence length of the light can be

Fig. 16.11 Imaginary part of the in-plane dielectric function of P3HT at different electrochemical potentials which were measured against a Ag AgCl QRE. The electrochemical doping is connected in this example by an intercalation of PF_6^- anions. An offset of 0.5 is used between the spectra for clarification of the trend and the two dashed line represent the out-of-plane dielectric function at -200 and 1200 mV. [31]



suppressed with a simple workaround. By averaging over a number of arbitrarily chosen layer thicknesses (e.g. $\pm 10\%$ of the real layer thickness), the interference structures in thicker layers smear out and one can calculate the polarization dependent transmission in terms of Ψ and Δ also for structures as depicted in Fig. 16.10.

Figure 16.11 shows a series of dielectric function spectra for electrochemical potentials between -200 and $+1200$ mV. The plotted imaginary part of the in-plane DF are obtained by a parametric fit of the measured Ψ and Δ values. In this fit it was assumed that the dielectric function consists of a number of Gauss-Lorentzian oscillators which differ in the in-plane and out-of-plane DF only concerning their oscillator strength. The parallel received out-of-plane DF's are exemplarily shown for the extreme potentials. The undoped film optical properties at -200 mV were already used in Sect. 16.2.1 and Fig. 16.5 to discuss the undoped P3HT properties.

In agreement with CV results the DF do not change up to a potential of about 300 mV. With the first and second oxidation step between 350 and 800 mV the oscillator strength of the π - π^* transitions of the pristine material (the IEX, the IEX+LO, and the screened HOMO-LUMO band-to-band transition) continuously decrease by a factor of two. At the same time the polaron related P1 transition appears. The latter P1 resonance reaches a maximal amplitude at 800 mV. At this potential the peak maximum emerges at 1.4 eV. But noticeable is also a significant red shift from the first appearance with increasing potential. Such a behavior is expected in case of an increasing inter- and intra-chain overlap of the polaronic chain sections (Figs. 16.1 and 16.12). The polaronic character of the new absorption structure is additionally

confirmed by (EPR) measurements which show an increasing signal and thus prove the unpaired electron spin in localized polaronic states [42]. From CV it is known that about 20% of the thiophene monomers are charged at 800 mV. The high polaron density explains on one hand the strength of the polaron absorption. But it is also apparent that a higher doping could not further increase the number of polarons. If one considers that a polaron in P3HT extends over three or more thiophene units, a further generation of localized polarons is simply not possible.

In connection with the iodine doping of P3HT, we have discussed already a general broadening of the electronic resonances after the iodine exposure. This behavior is clearly traceable in the in-situ ellipsometric spectra. The IEX and the IEX+LO transitions as well as screened HOMO-LUMO band-to-band absorption first decrease in amplitude but broaden in particular upon the second oxidation step. A possible reason for the broadening could be seen in the coexistence of polaronic and pristine sections in the P3HT polymer chains in combination with the already discussed inter and intra-chain overlapping of (bi)polarons orbitals. Regarding transition energies and peak amplitudes/width the electrochemically induced polaronic transition spectrum is truly very similar to those obtained for iodine-doped P3HT films (Fig. 16.6) [19, 41, 62]. Best comparable with the saturated iodine doping is probably the electrochemical oxidation at 600 or 700 mV. Both doping types include an incorporation of counter anions, i.e. the I^- and PF_6^- , respectively, which may induce additional broadening effects.

Above 800 mV the polaron-related P1 transition disappears again although the p-type doping is still increasing. It finally vanishes almost completely at potentials above the third oxidation peak. One might think that the vanishing of the P1 polaron transition, which is accompanied by a disappearing EPR signal, is attributed to the formation of bipolarons as depicted in Fig. 16.4. Such an interpretation would be consistent with the ATR-FTIR results shown in Fig. 16.9a. Aside from the general increase of the IR absorption one can observe a blue and a red shifting feature. The blue shift is in fact expectable for P2 (BP2) transition if one assumes a "further relaxation" due to the pairing of positive charges. On the other hand we have mentioned already the very high doping level above 800 mV. About every second thiophene ring is finally positively charged at 1200 mV and (bi)polarons may strongly overlap. Highly interesting in this connection is the recovery of the IEX features between 2.0 and 2.4 eV in the ellipsometric spectra. The recovery of inter-chain excitonic "fine" structures and the very high doping concentration rather suggest that the P3HT chains entirely relax in a new structure like pictured in the bottom of Fig. 16.12. A formation of bipolarons as a new quasi-particle is triggered in a strict definition by an energy gain due to the polymer relaxation which exceeds the Coulomb repulsion between two positive charges. The total Gibbs free energy minimization includes in electrochemical experiments the freely tunable electric potential which could compensate also Coulomb repulsion forces. The chemical doping with the strongly oxidizing iodine saturates clearly in a polaron structure and a bipolaron formation seems to be energetically excluded.

Hence, ellipsometric spectra at high electrochemical potentials are explainable in the view of strongly overlapping polarons. They form polaronic bands which

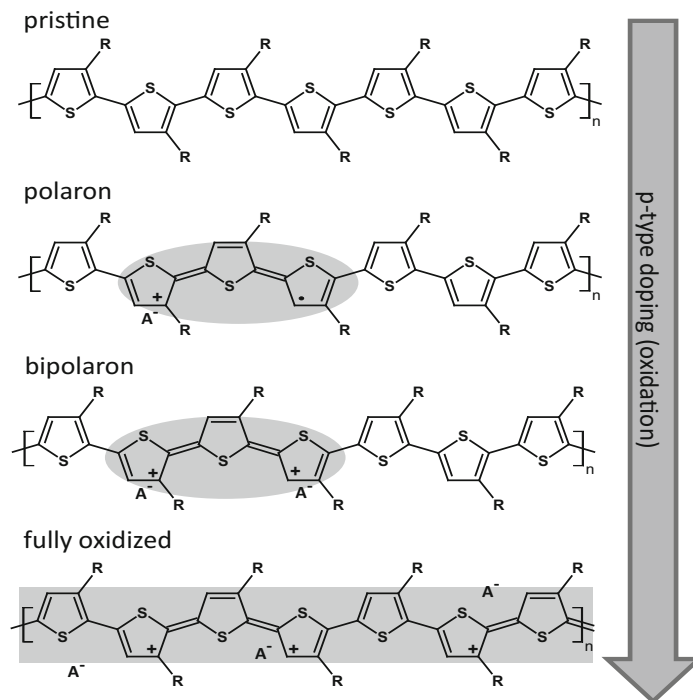


Fig. 16.12 Illustration of the (bi)polaron bond configuration in P3HT polymer chains at different p-type doping levels

energetically overlap with the HOMO and LUMO bands of the pristine material. This would yield in a band structure where the Fermi level is finally shifted in the HOMO levels of the pristine material (compare Fig. 16.4). Notice, such a model is also totally consistent with EPR measurements.

In electrochemical impedance measurements, it was demonstrated, furthermore, that a first significant conductivity increases is obtained in connection with the third oxidation step [49]. In this potential range the conductivity increases by almost three orders of magnitude up to $\approx 8 \text{ Scm}^{-1}$. Such an increase in the hole-mobility is not consistent with the formation of self localized bipolarons but could be easily explainable if intra- as well as inter-chain polaronic bands merge with the HOMO bands and thus generate a metallic regime due to an incompletely filled valence band [63]. Especially the inter-chain transport is a key feature in the attempt to obtain high film conductivity [64]. It should be noticed that the periodic arrangement of quinoid and aromatic thiophene rings in the polymer chain (Fig. 16.12) could be interpreted as the result of a Peierls's instability [65–68]. At room temperature, the π -electronic orbitals are equally distributed over the thiophene rings (comp. Fig. 16.3) which correspond to a half filled metallic band. But at low temperature a Peierls's transition is likely in

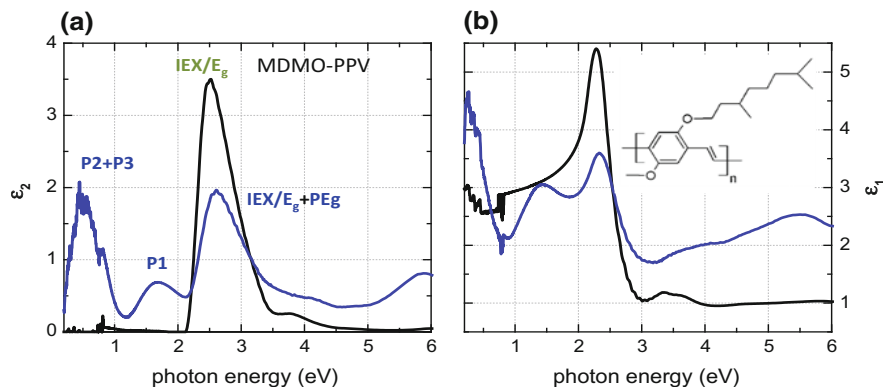


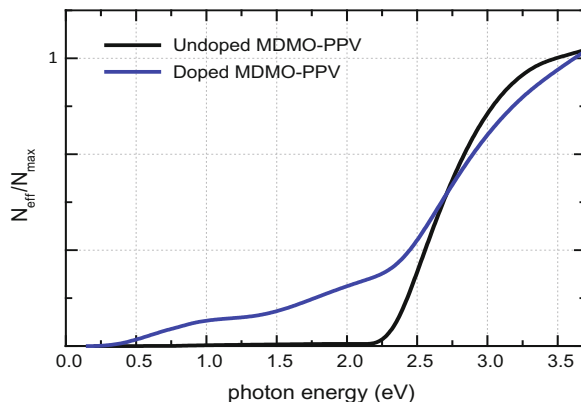
Fig. 16.13 In-plane dielectric function of MDMO-PPV (structure in the inset) in the nominally undoped (black line) and iodine saturated doped state (blue line). The imaginary part of dielectric function is plotted in the left panel (a) and the real part in the right panel (b) [72]

particular in 1D and 2D systems [69]. The doubling of the unit cell shown in Fig. 16.12 may yield in such a low temperature state again in an insulating/semiconducting band structure. Worth mentioning in this connection is, additionally, the continuous increase of the out-of-plane anisotropy upon doping (Fig. 16.11). It supposes an increasing ordering within the film. A possible explanation is found in the shorting of bonds between the thiophene rings in the quinoid structure.

16.4 MDMO-PPV - Iodine Doping

As a second material example, we show ellipsometric results obtained on poly[2-methoxy-5-(3',7'-dimethyloctyloxy)-1,4-phenylene-vinylene] (MDMO-PPV). Like P3HT it is a semiconducting polymer with application in organic solar cells and OLEDs [70]. Hoppe et al. have determined the DF in the UV-VIS spectral with a combination of reflection and transmission measurement [71]. Here we would like to discuss a comprehensive ellipsometric study where FTIR- and UV-VIS-IR ellipsometry is used [72] to obtain an overview about the polaron optical response. Figure 16.13 shows the DF of MDMO-PPV for the pristine and iodine doped state as well as a graphic formula of the MDMO-PPV polymer. In this experiment the polymer was directly spin casted onto a glass slide from a pyridine solution. Both the UV-VIS as well as the IR measurements were treated in this experiment in a joined point-by-point layer fit in order to obtain a full range film DF. Some artifacts remain at the connection point of the two spectral regions although the same film preparation was used in both experiments. However, the results are, nevertheless, conclusive enough to discuss some general polaron properties in more detail.

Fig. 16.14 Effective number of electrons (π -electron density) in MDMO-PPV and its integral evolution in the spectral range of π - π^* transitions. The black line represents the pristine and the blue line iodine doped MDMO-PPV film (comp. Fig. 16.13)



The pristine MDMO-PPV dielectric function (black line in Fig. 16.13) is very much similar to those of P3HT. A single relatively broad absorption peak with maximum at 2.5 eV dominates the UV-VIS spectral range. It is attributed again to π - π^* transitions in the polymer chain. A fine structure due to excitonic or LO-phonon contribution is not visible in the case of MDMO-PPV. One could speculate whether these structures are just not resolved in this experiment or suppressed due to a higher degree of conformational disorder and/or less π - π stacking. The latter assumption is at least consistent with the fact that the film could be unambiguously fitted with an isotropic film DF.

After doping (blue line in Fig. 16.13) two new transition features appear in the DF at ≈ 1.7 eV and ≈ 0.5 . Both peaks are described already in terms of the polaron P1 and P2/P3 transitions (Fig. 16.4). In addition a high-energy peak emerge at ≈ 5.9 eV which is probably not relating to the π electron system. The broad π - π^* absorption peak around at 2.5 eV decreases, as expected, by about one half. The small but clearly observable blue shift of the peak maximum could be explained by a screening of IEXs and the respective transfer of oscillator strength to higher photon energies like it is seen for P3HT. In the IR below 0.2 eV, new dipole allowed infrared active vibrations (IRAVs) appear [47].

In connection with the iodine doping of P3HT we have discussed already the question whether the oscillator strength of π - π^* transitions of pristine material is entirely shifted to the new π -electron structures P1-P3 in the NIR and IR. The ellipsoidally determined wide range DF of the MDMO-PPV example allows now a quantitative analysis. According to sum rule arguments the total oscillator or, a bit more precisely formulated, the first moment of the imaginary part of DF is proportional to the effective number of (valence) electrons [45, 46]:

$$N_{eff} \sim \int \omega \epsilon_2(\omega) d\omega. \quad (16.7)$$

In the present example, we assume that all optical transitions between 0.2 and 3.5 eV are ascribed to the π electron system. With the iodine p-type doping, some of the π -electrons are removed from the polymer chains. However, the comparison of the iodine and electrochemical doping of P3HT has shown that the charging obtained by chemical doping is relatively small in comparison to the total number of π -electrons in the film. If we thus approximate that the number of π -electrons is almost constant, the oscillator strength of the attenuate 2.5 eV absorption structure should shift in another spectral range. In order to test this assumption, the accumulative effective number of electrons is plotted for the spectral range between 0.2 and 3.5 eV. The black line in Fig. 16.14 shows the pristine polymer while the blue line is representing the iodine doped state with polarons. In the comparison it becomes evident that the oscillator strength of the π - π^* transitions is solely redistributed among the P1-P3 transitions. A possible doping induced conductivity is ascribe to the formation of metallic π -bands. These metallic π -electrons should generate a Drude tail in the DF which may emerge below 0.2 eV. From the sum rule arguments, however, this would add additional contribution to effective number of electrons which would violate the sum rule argumentation. The IR-DF between 0.05 and 0.2 eV, in fact, shows no signature of a Drude like behavior.

16.5 Polaron Formation in Push-Pull Polymers

In a last example we discuss a more sophisticated so called push-pull polymer. In such polymers intramolecular dipoles red-shift the band gap to generate a NIR optical activity [73]. A prominent representative of these π -conjugated polymers is the Poly[(4,8-bis-(2-ethylhexyloxy)-benzo(1,2-b:4,5-b')dithiophene)-2,6-diyl-alt-(4-(2-ethylhexanoyl)-thieno[3,4-b] thiophene)-2-6-diyl] in short PBDTTT-c [74–76]. In this polymer benzodithiophene and thienothiophene units serve as sequential donors and acceptors [77]. The extraordinary molecular complexity, however, considerably complicates the electronic structure. Simply the number of carbon atoms per monomer increases already by a factor of 4 from P3HT to PBDTTT-c. Additional side-chain are required to obtain solubility. The complexity of the push-pull polymer finally suppresses intermolecular interaction in contrast to the highly-crystalline rr-P3HT.

Figure 16.15 (black line) shows the ellipsometrically determined DF of a pristine PBDTTT-c film [62]. The presented film properties are obtained by a parametric layer fit with an independently determined film thickness and are refined within a point-to-point calculation. Various details in the thereby determined DF differ from the previously discussed polymers although the general line shape remains comparable. The spectral range between 1 and 3 eV is again characterized by the dominating π - π^* absorption structure. But the absorption onset is considerably red shifted due to the orbital interaction of the unified donor (thieno[2,3-b]thiophene) and acceptor (benzodithiophene with alkoxy-side-chains) units. Unlike rr-P3HT, the two sharp peaks at 1.75 and 1.9 eV could not originated from π - π stacking and may show

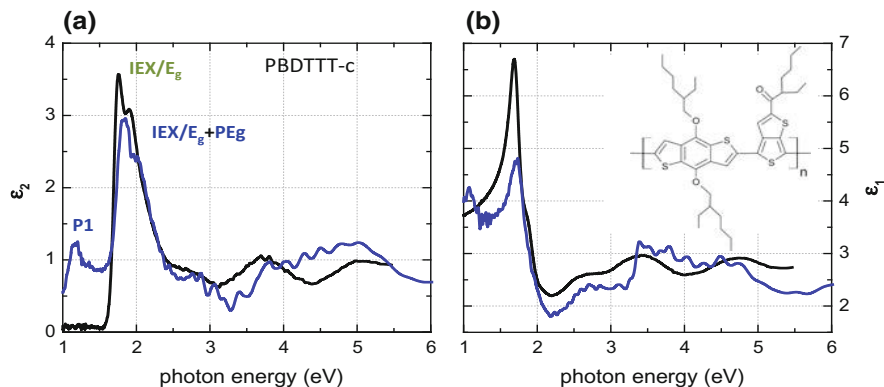


Fig. 16.15 Dielectric function of PBDTTT-c (structure in the inset) in the nominally undoped (black line) and iodine saturated doped state (blue line). The imaginary part of dielectric function is plotted in the left panel (a) and the real part in the right panel (b) [62]

rather a fingerprint of the push-pull character. Above 2.5 eV one can observe at least three additional absorption structures. But an identification of the latter UV transition is problematic if one considers the complexity of the structure.

A relatively persistent p-type doping is again achieved by an exposure of the PBDTTT-c film to iodine vapor. Respective ellipsometric spectra are shown in Fig. 16.15 (blue line). The results could not achieve the usual signal to noise level of ellipsometry, due to the limitation in integration time. But the doping effect is clearly visible. For PBDTTT-c one can observe a similar doping impact as it is known for e.g. P3HT. This is a quenching of the main π - π^* absorption structure and in parallel a P1 peak is rising in NIR part of the DF spectrum. The P1 resonance arises at a somewhat smaller photon energy (1.2 eV) consistently to the lower absorption edge of the ground state. But the P1 amplitude as well as the decrease of the original absorption feature is significantly smaller than those of P3HT or MDMO-PPV. The smaller effect upon doping correlates to the higher oxidation potential of PBDTTT-c. Remarkable is the small peak width of the polaronic P1 structure and the absence of the before discussed broadening of all other transition features. As already mentioned, the π - π stacking forces are much smaller in the PBDTTT-c film. Polarons are thus inherently localized in a single polymer chain and thus more close to the 1D polaron picture with self localization in each chain.

Related changes in the IR P2+P3 transition structures are best seen in a direct comparison of the P3HT and PBDTTT-c (ATR) spectra as shown in Fig. 16.16. The broad absorption band of P3HT*, which spreads above the long-wavelength LO-phonon (from ≈ 190 meV) to higher energies, has in PBDTTT-c* a clear peak like maximum at about 380 meV. The latter structure is described as a relaxed excited state in the Fröhlich polaron model [8, Sect. 16.1.2]. The existence of this peak is typical for strong electron-phonon coupling constants ($\alpha > 5$) and the Fröhlich coupling in

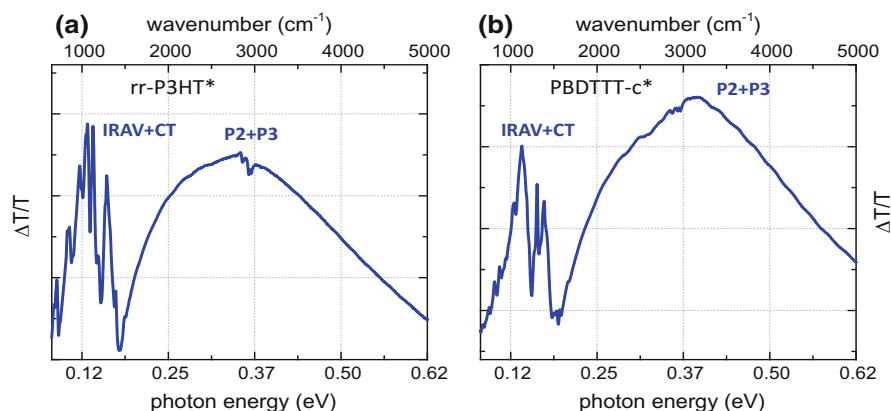


Fig. 16.16 Comparison of the iodine induced ATR-FTIR modifications in rr-P3HT (left panel **a**) and PBDTTT-c (right panel **b**) after 12 s exposure [62]

fact increases with a lowering of the dimensionality. In conclusion, PBDTTT-c fits much more to the classic 1D Fröhlich polaron model than P3HT or MDMO-PPV although the complexity of the system is much bigger and less polarons are generated by iodine doping.

16.6 Comments on Transmission (UV-VIS) and ATR Spectroscopy

Most of the pioneering work [39, 78, 79] and of the following investigations concerning the optical response of polarons in polymers make use of transmission (absorption), ATR, and related spectroscopic techniques. The comparison of the ellipsometrically determined DF of P3HT with the respective film absorption spectrum (black lines in Fig. 16.5) exemplary disclose already some difficulties which has to be considered in the interpretation of the different results. The peak positions and the general line shape differ considerably between the imaginary part of the DF and the absorption spectrum.

The optical properties of a material are typically represented by the complex refractive index (\tilde{n}) or the dielectric function (ε):

$$\tilde{n} = n + i\kappa = \sqrt{\varepsilon} = \sqrt{\varepsilon_1 + i\varepsilon_2}. \quad (16.8)$$

In theoretical publications one can find, furthermore, spectra of the real part of the optical conductivity $\sigma_1 = \omega\varepsilon_0\varepsilon_2$, where $\hbar\omega$ is the photon energy and ε_0 is the vacuum permittivity. All three quantities are discussed under assumption that the

film is optically isotropic. This is a reasonable approximation if we consider that transmission experiments are usually assembled in a normal incident geometry and that the polymer films are in-plane isotropic.

The primarily determined quantity in transmission experiments is a relative intensity i.e. the transmittance T . Disregarding reflections at the film boundaries, the transmittance is a function of the film thickness d and the wavelength of the light:

$$T = \frac{I}{I_{ref}} = e^{-\frac{2\omega}{c}\kappa d} = e^{-\alpha d}. \quad (16.9)$$

The herein used parameter α is the absorption coefficient (Fig. 16.5b). The absorbance of a material is calculated from the transmittance with the negative decadic logarithm (Lambert–Beer law):

$$A = -\log(T/T_{ref}) = \Delta\alpha d \log(e) \quad (16.10)$$

The **absorbance A** is thus **proportional to the absorption coefficient α** and the film thickness d and is therefore commonly used in order to discuss the material optical properties based on transmission experiments. The herein used approximations are valid as long as the absorption of light insight in the entire film is much bigger than the reflected intensity (e.g. in thick films with small α). The decadic logarithm is used by historical reasons.

In Fig. 16.17 we use the results of a simulated transmission experiment in order to illustrate peculiarities which may occur in transmission experiments based on a single Lorentz oscillator. The comparison discloses two major problems. First, the energy position of the absorbance maximum does not coincide with the resonance energy of the electronic transition. Second, the line shape and amplitude of the absorbance structure is altered significantly by the multiple light reflection at boundaries and a conceivable determination of the dielectric function by a Kramers-Kronig-analysis would be falsified.

ATR experiments are analyzed under the assumption that a light beam, which is n -times reflected at the boundary between the film and the ATR-crystal under total reflection conditions, loses intensity due to the absorption in the evanescent field in the film. The intensity reduction upon each reflection can be calculated for the two principle polarizations by means of the absolute values of the respective reflection coefficients [80, 81]:

$$R_s = |r_s|^2 = 1 - \frac{n_p \cos(\theta)}{(n_p^2 - n^2) \sqrt{n_p^2 \sin^2(\theta) - n^2}} n\kappa \quad \text{and} \quad (16.11)$$

$$R_p = |r_p|^2 = 1 - \frac{n_p n \kappa (2n_p^2 \sin^2 \theta - n^2) \cos(\theta)}{(n_p^2 - n^2) ((n_p^2 - n^2) \sin^2 \theta - n^2) \sqrt{n_p^2 \sin^2(\theta) - n^2}} n\kappa, \quad (16.12)$$

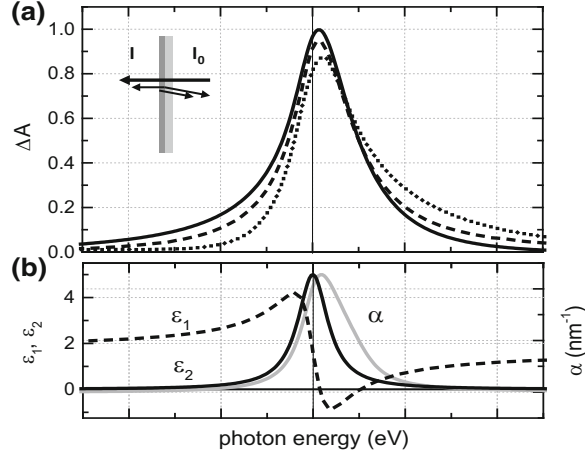


Fig. 16.17 Simulated differential absorbance spectra **a** for a thin film with a single Lorentz oscillator absorption. The respective dielectric function is plotted in the lower panel **(b)**. The differential absorbance is calculated for a normal incidence experiment where the amplitude of the oscillator is set to zero in the reference spectra. Three different sample scenarios are simulated: a free standing 50 nm film (solid line), a film on a glass substrate (dotted line), a film on a glass substrate with a 50 nm ITO coating (dashed line). The absorption coefficient α (gray line) is shown in **b** for comparison

where n_p is the refractive index of the ATR-prism and θ is the angle of incidence (typically values are between 40° and 60°). These relations are derived with the assumption of weak absorption in the film [81] and assume that the total reflection condition is maintained for each wavelength. Under the latter condition, any reflectivity different from one is due to absorption (energy dissipation) in the film. The second term in (16.11) and (16.12) can be thus associated to the right hand side of (16.9). The total transmittance T through the ATR prism is:

$$T = R^n \quad (16.13)$$

ATR results are often presented in two different forms; either in terms of $\Delta T/T_{ref}$ or by means of $-\log(T/T_{ref})$. In case of weak absorption the second term in (16.11) and (16.12) is small and one can use the approximation $-\ln(1-x) = x$. Under consideration of the principle relation $\log(y^n) = n * \ln(y)/\log(e)$ it is thus evident that both representations of the ATR results are equivalent. In particular it is worth mentioning that the **ATR results are proportional to $n\kappa$ and thus to ϵ_2** .

A comparison of ATR-results and the respective film DF is again graphically demonstrated with simulated spectra containing a single Lorentz-oscillator (Fig. 16.18). For weakly absorbing films (oscillator amplitude 10 times smaller than in the lower panel) the ATR-peak amplitude and line shape matches very good with the DF. But just for slightly higher oscillator amplitudes the total reflection condition

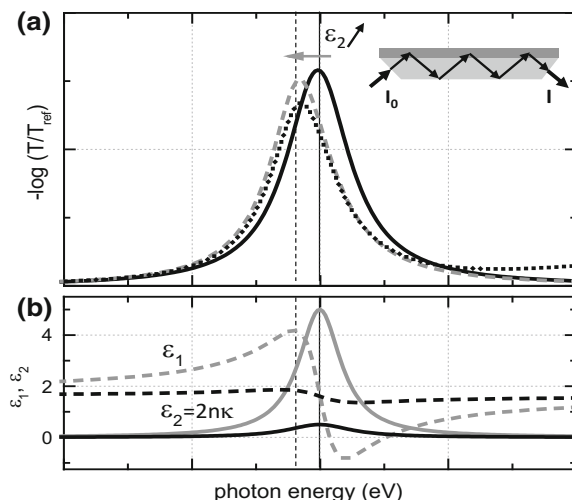


Fig. 16.18 Simulation of relative ATR transmission spectra **a** for a thin film with a single Lorentz oscillator absorption. The respective dielectric function is plotted in the lower panel **(b)**. The relative ATR transmission is calculated for an angle of incidence of 50° and a film of 5 nm where the amplitude of the oscillator is set to zero in the reference spectra. Three different sample scenarios are simulated: a weakly absorbing film (oscillator amplitude 10 times smaller than in **(b)**) on a high refractive index ATR-prism ($n = 3$) (solid line), with a 5 nm ITO coating (dotted line), and without ITO but with the higher oscillator amplitude (dashed line)

is already falsified and the obtained peak position shifts to lower photon energies towards the maximum in the real part of the film dielectric function (dashed line in Fig. 16.18). In real experiments and in particular in the spectral range of strong and narrow IR phonon absorption lines it could be problematic to ensure whether the weak absorption limit (the ATR-conditions) is valid. The situation gets even more complicated if further layers like a conducting ITO film are introduced (dotted line). The dispersion of the real and imaginary part of the dielectric function of those films superimpose with the film response. It should be noted that these effects are not eliminated with the reference measurement and further increase if interferences effects come into play. It is generally also difficult to deduce correct absolute values for the absorption coefficient. The latter depends on the number of reflections, the propagation length in the film and is finally influenced by multiple reflections at the entrance and exit surface of the ATR-prism. However, with the optical models used in common ellipsometric software packages a complete description is possible. An ellipsometric determination of film dielectric properties (ϵ_1 and ϵ_2) with a single total internal reflection is for example presented in [82].

Acknowledgements The authors would like to thank Kurt Hingerl, Niyazi S. Sariciftci, Helmut Neugebauer, and Reghu Menon for their valuable comments and enlightening discussions. Furthermore, we acknowledge manifold contributions of Achim W. Hassel, Günther Knör, Jan Philipp

Kollender, Andrei I. Mardare, Kerstin Oppelt, Thomas Plach, Stefanie Schlager, Matthew S. White, Karin Wiesauer, and Cigdem Yumusak for the results presented here.

References

1. *Handbook of Conducting Polymers, Conjugated Polymers: Theory, Synthesis, Properties, and Characterization*, vol. I–II, 3rd edn. ed. by T.A. Skotheim, J.R. Reynolds (CRC Press, Boca Raton, London, New York, 2006)
2. J.L. Brédas, G.B. Street, B. Thémans, J.M. André, *J. Chem. Phys.* **83**, 1323 (1985)
3. E. Bundgaard, F.C. Krebs, *Sol. Energy Mater. Sol. Cells* **91**, 954 (2007)
4. D.T. Haar, *Collected Papers of L.D. Landau* (Gordon and Breach, Science Publishers, New York, London, Paris, 1965)
5. H. Fröhlich, *Adv. Phys.* **3**, 325 (1954)
6. J.T. Devreese, *J. Phys. Condens. Matter* **19**, 26 (2006)
7. J.T. Devreese, A.S. Alexandrov, *Rep. Prog. Phys.* **72**, 066501 (2009)
8. *Polarons in Advanced Materials*, ed. by A.S. Alexandrov (Springer, Dordrecht, 2007)
9. D. Emin, *Polarons* (Cambridge University Press, Cambridge, New York, Melbourne, 2013)
10. J.L. Brédas, G.B. Street, *Acc. Chem. Res.* **18**, 309 (1985)
11. A.J. Heeger, N.S. Sariciftci, E.B. Namdas, *Semiconducting and Metallic Polymers* (Oxford University Press, Oxford and New York, 2010)
12. S.-I. Kuroda, *Int. J. Mod. Phys. B* **9**, 221 (1995)
13. F.M. Peeters, J.T. Devreese, *Phys. Rev. B* **36**, 4442 (1987)
14. D. Beljonne et al., *Adv. Funct. Mater.* **11**, 229 (2001)
15. S.N. Klimin, J. Tempere, J.T. Devreese, *Phys. Rev. B* **94**, 1 (2016)
16. J.L. Brédas, R.R. Chance, R. Silbey, *Phys. Rev. B* **26**, 5843 (1982)
17. D. Bertho, C. Jouanin, *Phys. Rev. B* **35**, 626 (1987)
18. A.A. Bakulin et al., *Science* (80-.) **335**, 1340 (2012)
19. R. Österbacka, C. An, X.M. Jiang, Z. Vardeny, *Science* (80-.) **287**, 839 (2000)
20. O. Bubnova, X. Crispin, *Energy Environ. Sci.* **5**, 9345 (2012)
21. C.M. Pochas, F.C. Spano, *J. Chem. Phys.* **140**, 244902 (2014)
22. S. Stafström et al., *Phys. Rev. Lett.* **59**, 1464 (1987)
23. D.J. Thouless, *Phys. Rev. Lett.* **39**, 1167 (1977)
24. B.I. Shklovskii, A.L. Efros, in *Electronic Properties of Doped Semiconductors*, vol. 45, Springer Series in Solid-State Sciences, ed. by M. Cardona (Springer, Berlin, Heidelberg, 1984)
25. P.R. Somani, S. Radhakrishnan, *Mater. Chem. Phys.* **77**, 117 (2002)
26. H. Shirakawa et al., *J. Chem. Soc. Chem. Commun.* **578** (1977)
27. A.J. Heeger, *Angew. Chemie* **40**, 2591 (2001)
28. J. Gasiorowski et al., *J. Phys. Chem. C* **117**, 2584 (2013)
29. Y. Taguchi et al., *J. Am. Chem. Soc.* **128**, 3313 (2006)
30. R. Ludwig, *Angew. Chemie* **115**, 3580 (2003)
31. C. Cobet et al., *Submitt. to Adv. Mater. Interfaces* (2017)
32. U. Zhokhavets, G. Gobsch, H. Hoppe, N.S. Sariciftci, *Thin Solid Films* **451–452**, 69 (2004)
33. U. Zhokhavets et al., *Chem. Phys. Lett.* **418**, 347 (2006)
34. M. Campoy-Quiles, P.G. Etchegoin, D.D.C. Bradley, *Phys. Rev. B* **72**, 045209 (2005)
35. T. Tsumuraya, J.-H. Song, A. Freeman, *Phys. Rev. B* **86**, 075114 (2012)
36. E. Lioudakis, A. Othonos, I. Alexandrou, Y. Hayashi, *Appl. Phys. Lett.* **91**, 111117 (2007)
37. Y. Kim et al., *Nat. Mater.* **5**, 197 (2006)
38. P.G. Karagiannidis et al., *Mater. Chem. Phys.* **129**, 1207 (2011)
39. Z. Vardeny et al., *Phys. Rev. Lett.* **56**, 671 (1986)
40. A.J. Heeger, S. Kivelson, J.R. Schrieffer, W.P. Su, *Rev. Mod. Phys.* **60**, 781 (1988)
41. J. Gasiorowski et al., *J. Phys. Chem. C* **118**, 16919 (2014)

42. C. Enengl et al., *ChemPhysChem* **17**, 3836 (2016)
43. Y. Furukawa, *J. Phys. Chem.* **100**, 15644 (1996)
44. J. Gasiorowski, Dissertation, Johannes Kepler University Linz (2013)
45. *Handbook of Optical Constants of Solids*, vol. 111, ed. by E.D. Palik (Academic Press, San Diego, Chestnut Hill, 1998)
46. P.Y. Yu, M. Cardona, *Fundamentals of Semiconductors*, 3rd edn. (Springer, Berlin, Heidelberg, New York, 1996)
47. E. Ehrenfreund, Z. Vardeny, O. Brafman, B. Horovitz, *Phys. Rev. B* **36**, 1535 (1987)
48. A. Girlando, A. Painelli, Z.G. Soos, *J. Chem. Phys.* **98**, 7459 (1993)
49. J. Gasiorowski, A.I. Mardare, N.S. Sariciftci, A.W. Hassel, *J. Electroanal. Chem.* **691**, 77 (2013)
50. N.S. Sariciftci et al., *J. Chem. Phys.* **96**, 7164 (1992)
51. A.K. Agrawal, S.A. Jenekhe, *Chem. Mater.* **8**, 579 (1996)
52. H. Neugebauer et al., *J. Chem. Phys.* **110**, 12108 (1999)
53. C. Kvarnström et al., *Synth. Met.* **101**, 66 (1999)
54. A.W. Hassel, K. Fushimi, M. Seo, *Electrochem. Commun.* **1**, 180 (1999)
55. T. Erb et al., *Adv. Funct. Mater.* **15**, 1193 (2005)
56. H.G. Tompkins, *A User's Guide to Ellipsometry* (Academic Press Inc, San Diego, 1993)
57. R.M.A. Azzam, N.M. Bashara, *Ellipsometry and Polarized Light* (North-Holland Publishing Company, Amsterdam, New York, Oxford, 1987)
58. P. Yeh, *Optical Waves in Layered Media* (Wiley, New York, Chichester, Weinheim, Brisbane, Singapore, Toronto, 1988)
59. M.V. Klein, T.E. Furtak, *Optik* (Springer, Berlin, Heidelberg, 1988)
60. M. Schubert, *Phys. Rev. B* **53**, 4265 (1996)
61. H. Tompkins, E.A. Irene, *Handbook of Ellipsometry* (Springer, Heidelberg, 2005)
62. C. Cobet et al., *Sci. Rep.* **6**, 35096 (2016)
63. S. Panero, S. Passerini, B. Scrosati, *Mol. Cryst. Liq. Cryst.* **229**, 97 (1993)
64. P. Kar, *Doping Conjugated Polymers* (Wiley, Hoboken, 2013)
65. B. Horovitz, *Solid State Commun.* **88**, 983 (1993)
66. J. Wosnitzer, *Fermi Surfaces of Low-Dimensional Organic Metals and Superconductors* (Springer, Berlin, Heidelberg, 1996)
67. D. Jérôme, H.J. Schulz, *Adv. Phys.* **31**, 299 (2006)
68. C. Cobet, E. Speiser, in *Defin. Anal. Opt. Prop. Mater. Nanoscale A Collect. Thoughts, Opin. Ideas Data that Have Matur. Over Years Exploit. Ellipsom. a Range Characterisation Needs*, ed. by M. Losurdo (Ges. für Mikro- und Nanoelektronik, Wien, 2010)
69. D.K. Campbell, A.R. Bishop, K. Fesser, *Phys. Rev. B* **26**, 6862 (1982)
70. S.E. Shaheen et al., *Appl. Phys. Lett.* **78**, 841 (2001)
71. H. Hoppe, N.S. Sariciftci, D. Meissner, *Mol. Cryst. Liq. Cryst.* **385**, 113 (2002)
72. J. Gasiorowski et al., *J. Phys. Chem. C* **117**, 22010 (2013)
73. C. Duan, F. Huang, Y. Cao, *J. Mater. Chem.* **22**, 10416 (2012)
74. H.-Y. Chen et al., *Nat. Photonics* **3**, 649 (2009)
75. J. Hou et al., *J. Am. Chem. Soc.* **131**, 15586 (2009)
76. J. Gasiorowski, A.I. Mardare, N.S. Sariciftci, A.W. Hassel, *Electrochim. Acta* **113**, 834 (2013)
77. K.G. Jespersen et al., *J. Chem. Phys.* **121**, 12613 (2004)
78. J.L. Brédas, J.C. Scott, K. Yakushi, G.B. Street, *Phys. Rev. B* **30**, 1023 (1984)
79. M.J. Nowak, S.D.D.V. Rughooputh, S. Hotta, A.J. Heeger, *Macromolecules* **20**, 965 (1987)
80. N.J. Harrick, *Internal Reflection Spectroscopy* (Wiley, New York, 1967)
81. M. Milosevic, in *Internal Reflection and ATR Spectroscopy*, vol. 176, Chemical Analysis, ed. by M.E. Vitha (Wiley, Hoboken, New Jersey, 2012)
82. M. Poksinski, H. Arwin, *Proteins Solid-Liquid Interfaces*, Principles and Practice (Springer, Berlin, Heidelberg, 2006), pp. 105–118

4.11 Manuscript 11



Isotropic metallic transport in conducting polymers

Philipp Stadler^{a, b, *}

^a Linz Institute of Organic Solar Cells and Institute of Physical Chemistry, Johannes Kepler University Linz, Altenberger Straße 69, 4040 Linz, Austria

^b Linz Institute of Technology, Johannes Kepler University Linz, Altenberger Straße 69, 4040 Linz, Austria

ARTICLE INFO

Keywords:

Conducting polymers
Metal-insulator transition
Isotropic metallic transport
Hall-effect
Positive magnetoconductivity
Scattering length

ABSTRACT

Conducting polymers represent an emerging class of conductors combining notable optoelectronic and thermoelectric properties; however, the electrical performance remains a limiting factor. This review provides an overview of the relevant parameters driving the rarely observed metal-insulator transition. Recent magnetotransport measurements provide clearer insight to study the proximity to the metallic state, *i.e.* the exact quantification of scattering and mobility. From that, one conclusion is the desired isotropic metallic phases depend on coherence and intermolecular radii.

1. Introduction

Conducting polymers (CPs) have emerged to a valuable class of alternative molecular conductors [1–3]. They combine excellent processability and significant conductivity appreciated in various fields of organic electronics, *e.g.* for thermoelectric active layers [4–9] and for transparent electrodes [10–15]. Since their discovery by Heeger, MacDiarmid and Shirakawa [16,17], the conductivity has shown an enormous improvement from early nematic to today (thin-film) *isotropic* systems with conductivities beyond 4000Scm^{-1} [18–23].

In this article, we mainly treat on recent developments of the metallicity in doped poly(3,4-ethylenedioxythiophenes) (PEDOTs). One continuous goal has been the improvement of the electrical conductivity towards isotropic, metal-like and facile-processed systems. However, transport in conducting polymers is complex and depends on multiple factors such as the arrangement of the conjugated doped polycations and their corresponding anions [24,25]. The multiple interactions (covalent, ionic and weaker intermolecular bonds) can easily result in disorder such as amorphism and inhomogeneity; impurities and structural and molecular defects [26].

Fortunately, several works demonstrated that the latter extrinsic disorder can be overcome with the consequence of a metal-insulator transition (MIT, Fig. 1) [18,19,34–39,23,27–33]. For such a *metallic* conducting polymer, the transport still splits up in three regimes: Insu-

lating or exponential regime, an intermediate transition or critical regime and, ultimately, a metallic regime. In the insulating and transition regime, the temperature coefficient of resistivity (TCR) remains negative, as for semiconductors and disordered matter, and follows the theory of weak localization. The resistivity ρ (inverse conductivity σ) increases with temperature following a power law with an exponent β close to 0.25 (Fig. 1b and Eq. 1) [40].

$$\rho(T) \approx T^{-\beta} \quad (1)$$

At lower temperatures, in the transition regime, the power law is no longer valid. Here, the conductivity gradually decreases until reaching a minimum (σ_{min}) at the metal-insulator transition (MIT). At temperatures below the conductivity minimum, the TCR finally turns positive and σ increases like for a crystalline metal (metallic regime).

This review discusses the parameters inducing the metal transition and the signatures of metallic transport in conducting polymers, including a discussion of the reasons for the frequent observation of extended transition regimes without explicit metal-insulator transition. The study conveys further the differences of conducting polymers compared to classic metals and elucidates the relevant factors, why present system show the metallic phase only at low temperatures and, further, what efforts are required to increase the transition temperature and, thus, the metallic nature of the polymers.

Abbreviations: CP, conducting polymer or conductive polymer; MIT, metal-insulator transition; TCR, temperature coefficient of resistivity; IRAV, infrared activated vibrations; PA, polyacetylene; PPy, polypyrrole; PANi, polyaniline; PEDOT, poly(3,4-ethylenedioxythiophene); 1D, one-dimensional; VPP, vapor-processed polymer; MFP, mean-free-path; MT, magnetotransport; ML, magnetolocalization; MC, magnetoconductivity.

* Corresponding author at: Linz Institute of Organic Solar Cells and Institute of Physical Chemistry, Johannes Kepler University Linz, Altenberger Straße 69, 4040 Linz, Austria.
Email address: Philipp.Stadler@jku.at (P. Stadler)

<https://doi.org/10.1016/j.synthmet.2019.06.004>

Received 19 February 2019; Received in revised form 30 May 2019; Accepted 4 June 2019

Available online xxx

0379-6779/© 2019.

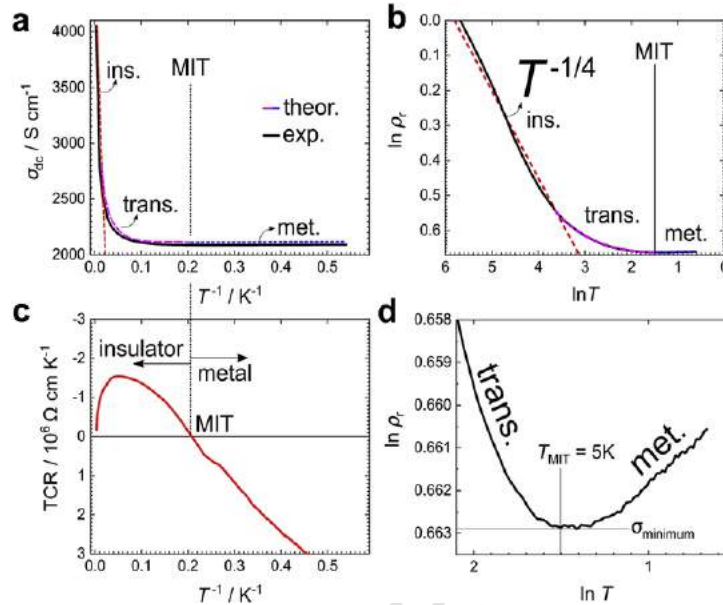


Fig. 1. Temperature profile of conductivity (σ) of an almost ideal (*i.e.* no extrinsic disorder) conducting polymer: (a) Inverse temperature plot shows the different regimes (ins. = insulator; trans. = transition; met. = metal regime). Particularly the low- T part is at first glance T -independent. (b) The logarithmic plot of the relative resistivity ($\rho_r = \rho_{300K}/\rho_r$) indicates the exponent (idealized case is $-1/4$, indicated as red dashed line) between room temperature and low temperature, the transition regime deviating from the power law and the metallic regime with the rise of conductivity (σ). (c) The temperature coefficient of resistivity (TCR) changes at the metal-insulator transition observed in the inverse temperature plot and (d) in the logarithmic plot with the local conductivity minimum at the MIT (5K) and subsequent rise of σ as T is further decreased. Reproduced with permission from Ref. [19] (For interpretation of the references to colour in this figure legend, the reader is referred to the web version of this article).

2. Carrier localization: intrinsic and extrinsic disorder

Carrier localization in CPs is partly an intrinsic phenomenon. It originates from the phononic disorder, *i.e.* the thermal distortion caused by one-dimensionality, and the weak intermolecular bonds such as van der Waals [41]. On top, there exist extrinsic sources of disorder in general relating to defects caused by amorphism, substrate/surface effects and inhomogeneity summarized as topological, spatial and energetic disorder [19,23,27,28,42–45].

Conducting polymer research has notoriously focused the systematic exclusion of all sources of extrinsic disorder in order to break localization and achieve metallic conductivity [44,46–48]. Judiciously-processed examples have demonstrated a metallic transition at low temperatures: polypyrrole (PPy), polyacetylene (PA), and recently, poly(3,4-ethylenedioxythiophene) (PEDOT) show a low-temperature (low- T) metal-insulator transition [18,19,23,27,28]. There exists a single exceptional case of a high temperature metallic state in polyaniline (PAni), which we assign to the particular different nature of doping [49].

The discrepancy between crystalline metals and metallic CPs is the negative temperature coefficient of resistivity (TCR) observed at room temperatures. The metallic state occurs only at low- T (all around 4–7K) in a regime, where phononic distortions become negligible.

In today's commonly used CPs, the classic metal-insulator transitions is rarely observed. The residual extrinsic disorder in such films eliminates the metal-insulator transition or, shifts the transition to lower temperatures. (Fig. 1).

These commonly observed effects are well-known and, in various cases, regarded as substrate- or surface-related. Backscattering, surface

inhomogeneity and defects are practically hard to avoid and require thorough processing techniques combined with subsequent post-treatment to diminish disorder. Interestingly, also the magnitude of conductivity σ at room temperatures does not exclude extrinsic disorder, as the σ is a volumetric parameter. In this context, recent works have proposed a correction term for the conductivity in molecular systems [42].

Magnetotransport (MT) represents the appropriate technique, to explore residual disorder in those polymers close to the metallic transition. MT can quantify extrinsic disorder and, on top, provide qualitative information about the origins. MT includes the measurement of the Hall-coefficient, subsequently an estimate of the band mobility, as well as the mean-free-path of scattering λ_{mf} . These parameters represent valuable information about extrinsic disorder, the coherence among the molecules and an estimate of the intrinsic conductivity.

2.1. Intrinsic phononic disorder

Phononic disorder in conjugated polymer matter is stronger as compared to metals [50]. It represents the product of strong electron-phonon coupling emerging from molecular anisotropy (1D-character of polymers) and its impact on the weak intermolecular bonds [42]. Phononic disorder is intrinsic in doped polymers. One consistent indication is the intense infrared activated vibrations (IRAVs) [46,51]. They originate from numerous doping-activated vibronic oscillators and occur in the mid-infrared below 1500 cm^{-1} (186 meV) [52,53]. Thus, IRAVs are a first estimate of the magnitude of the coupling, since they contribute to the total phononic distortions affecting the intermolecular bonding strength.

Intermolecular transfer integrals are relevant for the metal-insulator transition; theoretically, the transition energy $k_b T_{MIT}$ is proportional to the actual bonding strength, apart from the size of the monomer, the doping and, importantly, phononic distortions [26,54,55]. Here, phonons entail characteristic merits of CPs such as the broad window of transparency [18,52,53], and active thermoelectricity [45,56] (Fig. 2).

Phononic localization is strong at room temperature; therefore, CPs possess non-metallic electrical transport at room temperature, which gradually approaches the metallic phase as temperature is decreased [33,44]. One goal in transport studies focusses the separation of intrinsic and extrinsic disorder, or, the separation of delocalized and localized carriers. Such splitting is simplified at low temperatures. Here, the conductivity profile reveals the real quality of the conducting polymer system, in particular its proximity to the isotropic metallic state.

2.2. Extrinsic disorder

Extrinsic sources of disorder, often connoted as topological, spatial and energetic disorder, are caused by imperfection in the structure. They convey all disorder effects, which are suppressible by optimization e.g. by advancing the order among the chains or by implementing techniques to reduce impurities. Topological or spatial disorder relate to amorphism and inhomogeneity e.g. abrupt interfaces from film-processing, surface and substrate effects, solvent intercalations and presence of impurities. Energetic disorder relates more to defects in the conjugated π -system. These emerge by too harsh conditions during synthesis [57,58].

The quality of commonplace conducting polymers has increased over the years, so that today commercial products with overall low defect density are state-of-the-art [43,60,61]. Solvent processing is presently the desired way to deposit thin-films, but does not provide a satisfying level of conductivity. Metallic phases are exceptional [23], because solvent processing can introduce residual extrinsic disorder (not least emerging from the low film thickness, impurity, solvent intercalation, abrupt interfaces). Vapor-processed polymers (VPPs) have shown higher degree of homogeneity and thus less extrinsic disorder finally leading to metallic CPs. VPPs are synthesized by chemical vapor deposition with the merit of united polymerization, doping and deposition [11,19,57,62–66]; however, here energetic disorder can arise through over-oxidation and the usage of aggressive oxidants in combination with heat. Ultimately, electropolymerization is an alternative successful, but elaborate method to obtain a metallic polymer [27,67,68].

2.3. Metal-insulator transition

At first glance, the quality of any conducting polymer becomes apparent by showing the conductivity (σ) inverse (or logarithmic) temperature profile (Fig. 3). In the insulating regime, the value of σ decreases by $T^{-\beta}$. The magnitude of the exponent β represents a measure of the proximity to the metallic state. In ideal case 0.25, it will be higher as extrinsic disorder is present (Eq. 1). The subsequent transition regime deviates from this power law with a gradually decreasing exponent. It should be narrow and approach the local conductivity minimum at the MIT. Thus, signatures of metallic conducting polymers are a low value of the relative resistivity (ρ_r), a narrow transition regime and β close to 0.25.

At sufficient low temperature, the minimum conductivity marks the actual metal-insulator transition. Until now, MITs have been reported in few polymer systems, among them PPy, PANi, PA and, recently, two types of PEDOT (acid-treated and VPP) and PBTTT (Fig. 4) [18,19,23,27,28,38].

The local conductivity minima (σ_{min}) occur consistently between 4–7 K at ambient pressure. Below these minima, the sign of TCR changes sign to positive (i.e. σ increases with decreasing temperature). These metallic polymers exemplify systems with practically no extrinsic disorder. Such situation is a direct result of careful processing and synthesis. The similar transition temperatures (4–7 K, Fig. 4) indicate that there exists a relation in conjugated systems: One hypothesis is that the intermolecular bonding strength is proportional to the transition energies $k_b T_{MIT}$. Assuming that intermolecular binding is characteristically van der Waals type, the final metal-insulator transition temperature will then depend on the radius among the polymer chains.

Thus, a reduction of the effective radius must rise the transition temperature T_{MIT} . Compressed metallic conducting polymers, polyacetylene (anisotropic), PPy and, recently, PEDOT (isotropic), show such temperature increase [19,26,69]. Based on these results, the relation of $k_b T_{MIT}$ and the interchain transfer integral have to be discussed in a greater picture [70,71].

2.4. Magnetoconductivity in the transition regime

Magnetoconductivity (MC) is useful study the metallic transition in conducting polymers. MC provides detailed insights to the scattering mechanism i.e. the magnitude of the average scattering length and, thus, the coherence among the molecules and the free charge carriers. This represents a valuable information, particularly to quantify the intensity of intermolecular overlap and the overall order.

In general, the magnetic field (B) induces carrier localization, i.e. it decreases the conductivity (magnetolocalization, ML). ML is observed in all CPs and relates to electron-electron interactions according to

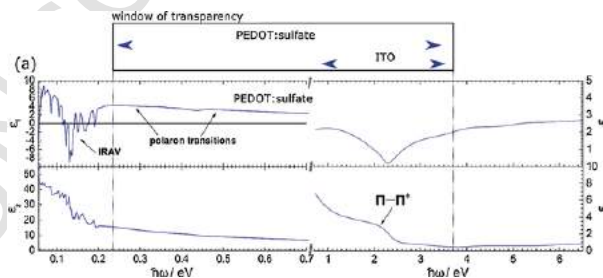


Fig. 2. Phononic distortions in CPs: Below 200 meV strong infrared-activated vibrations emerge in the mid-infrared spectrum (dielectric function) of highly-doped CPs. Reproduced with permission from Ref. [18].

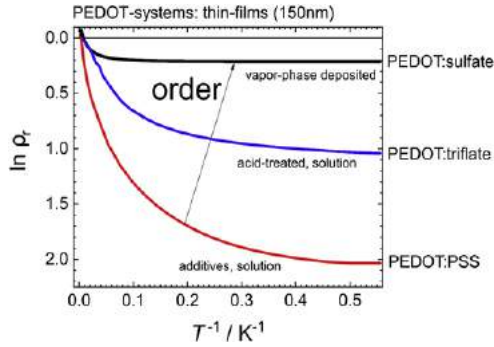


Fig. 3. Relative resistivity – inverse temperature profiles: Thin-films of PEDOT (with different processing techniques and different anions) show the effect of extrinsic disorder, in particular seen at low-T: (i) a higher ratio of the relative resistivity and (ii) stronger insulating and transition regime in case of higher disorder. Reproduced with permission from Ref. [18,59].

weak localization [19,28,76,42,43,46,55,72–75]. ML becomes stronger by decreasing temperature by the factor $T^{-3/2}$. The exact relation to B is a power law with quadratic exponent. In addition, every system has individual constants relating to the electron-electron interactions (dis-

cussed elsewhere) [72,73,77].

$$\Delta\sigma_{ML} = \sigma_{T,B} - \sigma_{T,B=0} = -const. \left(\frac{g \cdot \mu_B}{k_B}\right)^2 \cdot T^{-3/2} \cdot B^2 \quad (g \cdot \mu_B \cdot B < k_B T) \quad (2)$$

The final magnitude of ML depends on the ratio of $k_B T$ and B (derived by multiplication with μ_B (Bohr's magneton) and the g -factor, the gyromagnetic constant, ~ 2 for molecular matter). ML does not provide much information about extrinsic disorder.

In (semi)metallic CPs, however, there exists a second positive magnetic contribution to the conductivity (σ), which only depends on B and coherence: the positive magnetoconductivity (positive MC, $\Delta\sigma_{pos,MC}$). This effect is independent from the base conductivity ($\sigma_{B=0}$) of the system, and, therefore, can be considerably small as compared to the absolute value of σ and, particularly at low-T, as compared to the magnitude of ML. According to the Hikami-Larkin-Nagaoka equation, $\Delta\sigma_{pos,MC}$ relates to the quantum resonance of the field with a quadratic exponent in the orthogonal case (negligible spin-orbit coupling) [78]; its magnitude depends ultimately on the conductance G_0 , the magnetic field and the coherence volume (volume element given by the mean-free-path of charge carriers, λ_{MFP}^3) (Eq. 3).

$$\Delta\sigma_{pos,MC} = + \left(\frac{1}{12\pi^2}\right) \left(\frac{e}{h}\right)^2 G_0 \cdot \lambda_{MFP}^3 \cdot B^2 \quad (3)$$

In case of weak localization, ML and positive MC are additive effects: At low-T and low B , positive MC is dominant and gradually displaced by ML by increasing B . Subsequently one must zoom into the

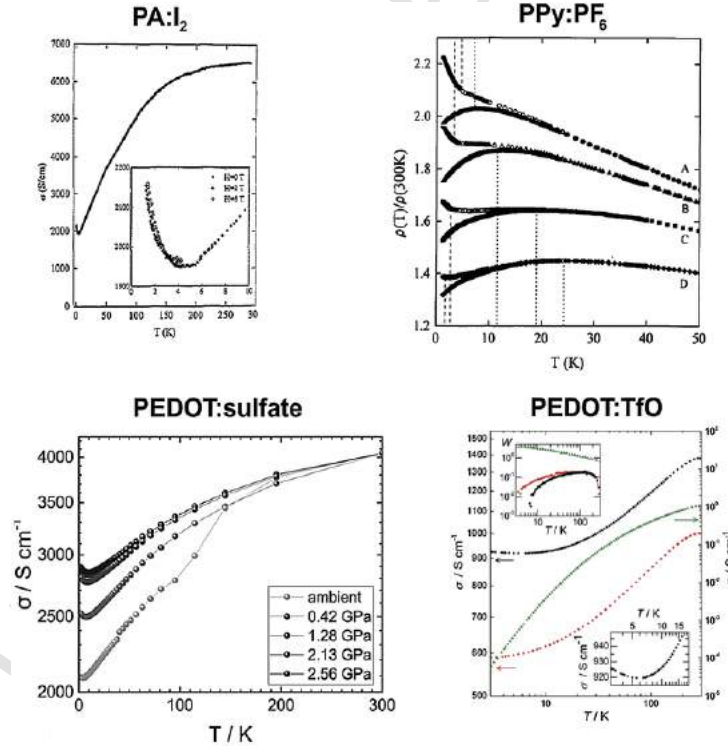


Fig. 4. Examples of metallic conducting polymers: Polyacetylene doped with iodine (PA:I₂, metal-insulator transition or conductivity minimum at 4K), polypyrrole:PF₆ (PPy:PF₆, MIT at 7K, other samples B, C, D are under pressure), poly-(3,4-ethylenedioxythiophene):sulfate (PEDOT:sulfate) and PEDOT:triflate, respectively, (MIT at 5K and 6K). Reproduced with permission from Ref. [19,23,27,28].

low-B regime in order to see the positive MC-effect at low temperatures (Fig. 5b and d). At higher temperatures, metallic CPs show only positive MC.

Positive MC is a characteristic phenomenon of weak localization and reported for conductors with intrinsic disorder such as doped silicon, metal alloys or amorphous metals. Thus, its occurrence in CPs shows a proximity to the metallic state, as it can only appear when charge carriers are sufficiently delocalized. Accordingly, positive MC can be used to derive the mean free path λ_{MFP} of the scattered charge carriers (Eq. 4), either by evaluating the magnitude of the slope (using σ vs. B^2 plot), or by taking the value of B at maximum magnetoconductivity indicating the optimum resonance condition between free charge carriers and magnetic field. For convenience, the latter can be plotted as the magnetic penetration depth or the Landau orbit size (L_D) to read out λ_{MFP} (Fig. 5e and Eq. 4).

$$\lambda_{\text{MFP}} \cong L_{D,\text{max.MC}} \text{ with } L_D = \sqrt{\frac{\hbar}{e \cdot B}} \quad (4)$$

The magnitude of λ_{MFP} provides an estimation of the average electron coherence *i.e.* the order and strength of the intermolecular overlap. The advantage of the positive MC is that it occurs above the MIT, even in CPs without explicit MIT. It shows that there is substantial degree of delocalization and, overall, almost negligible amount of extrinsic disorder in the system.

λ_{MFP} scales with temperature by the exponential relation of $T^{-3/4}$ (weak localization) [47,59,76,79]. Such temperature-profile suggests inelastic scattering, however, only in the transition or insulating regime. At the conductivity minimum at the MIT, positive MC splits up into two peaks – one relating to inelastic, one to elastic scattering (Fig. 6).

Since inelastic scattering must be larger (damping term), such splitting could be an indication of a molecular phase transition. In the metallic regime, the positive MC merges to a single peak (Fig. 6). Here, the scattering is elastic. Such transition is in agreement with the sign-flip of the TCR and the rise of the conductivity. One conclusion is

that the elastic-metallic regime relates to a molecular-structural phase transition, where the intermolecular overlap is substantially increased [69].

2.5. Mobility characterization

The Hall-effect in CPs has been frequently discussed [44,67,80–86]. Similar to the positive magnetoconductivity, the observation of the Hall-voltage indicates a band-structure and, thus, coherence among molecules. In the metallic regime, the Hall-effect should be therefore similar as for metals, but up to now, there are no experimental data available. Fortunately, prior art has reported Hall measurements in the transition and insulating regime in various CPs [18,67,82,83].

One problem is there, that the transport is ambivalent and a fraction of the carriers is localized. Therefore, the Hall-voltage is substantially reduced by a disorder term connoted as Hall screening. Since its exact impact is difficult to quantify (because of temperature dependence), the evaluation of the Hall-voltage remains vague. Recently, a molecular phase model has been suggested that estimates the disorder parameters and the subsequent magnitude of Hall screening [44]. The model provides a solution in order to estimate the band mobility from the Hall-voltage in the insulating regime at or close to room temperatures. Empirically, however, such evaluation has to resolve the probing of tiny Hall-voltages and provide adequate fitting parameters to extract trustable band mobilities. Recently, lock-in measurements and careful model fits have reported reliable mobilities [82].

At low- T , in the transition regime close to the MIT, the Hall-voltage evaluation is less problematic. Since the phononic disorder is less intense, the magnitude is larger. Anyhow, disorder models are still required in order to derive band mobilities [87,88]. The values for the band mobility are in the range of $30 \text{ cm}^2\text{V}^{-1}\text{s}^{-1}$ [18]. The magnitude of the band mobility suggests that, ultimately, electrical transport in molecular systems remains mobility-limited. The results correlate to the coherence measured from magnetoconductivity.

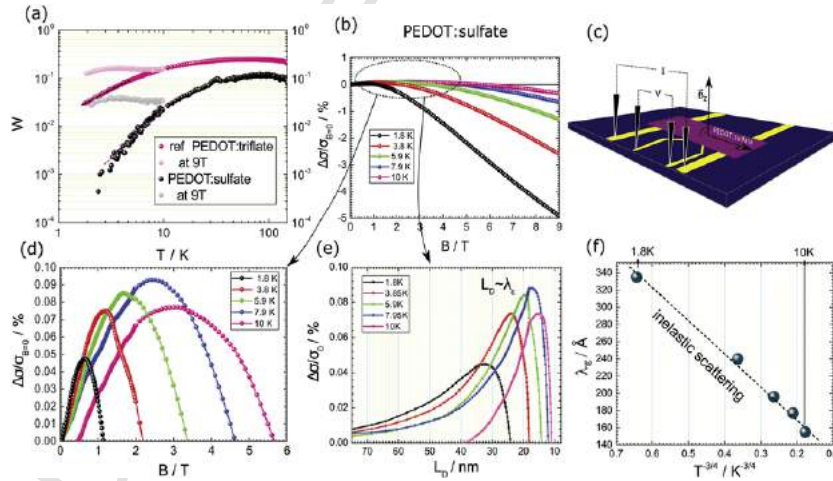


Fig. 5. Magnetoconductivity in metallic CP. (a) W (logarithmic derivative) of the conductivity *versus* $\log T$ shows the proximity to the metallic state, in particular for the black PEDOT:sulfate. The grey dots show the change of the conductivity at a magnetic field (B) of 9T (negative *i.e.* decreasing magnetoconductivity or magnetolocalization). (b) The same effect shown as absolute magnetoconductivity change (%): magnetolocalization particular stronger at low- T s and high B . (c) Schematic of the sample specimen: 4-wire probe. (d) Zoom in the positive part revealing a positive (*i.e.* increasing) magnetoconductivity *versus* B peaking at the maximum conductivity. The maximum shifts towards higher B as the temperature increases. (e) Plot of the positive magnetoconductivity using the magnetic penetration depth (the Landau orbit size, L_D) instead of B . The peak maximum corresponds to the mean free scattering path λ_{MFP} . (f) Fit of λ_{MFP} vs. $T^{-3/4}$ indicating the inelastic scattering (derived from weak localization) in the transition regime of the polymer. Reproduced with permission from Ref. [18].

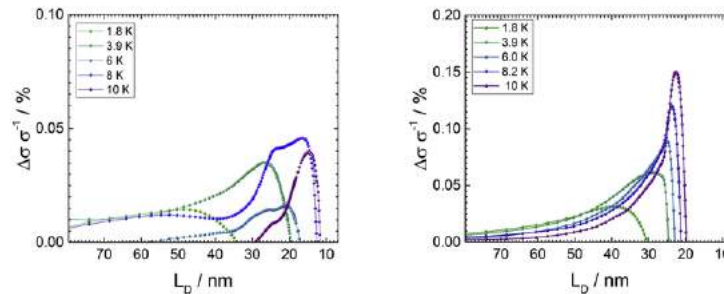


Fig. 6. Positive magnetoconductivity (relative magnetoconductivity versus the Landau orbit size L_D) at the metal-insulator transition. At ambient pressure (left) the positive magnetoconductivity shows a double-peak between 6 to 10 K, while under pressure (right) the entire system has a single-peak response and lower peak maxima. The latter case is interpreted as elastic scattering (transition temperature under pressure is 10 K), while the ambient sample is split in an elastic (low-T, 1.8 K and 3.9 K line) and both, ambivalent (double peak elastic and inelastic at 6 K, 8 K and 10 K). Reproduced with permission from Ref. [19].

Alternatively, or complementary to Hall, terahertz domain spectroscopy (THz) can be used to evaluate the band mobility and the DC conductivity [89–93]. The transmission spectra at low THz frequencies (e.g. around 0.13–3 THz) represent a non-destructive spectroscopic technique to study the DC conductivity and mobility. In (semi)metallic conducting polymers the classic Drude model can be used (assuming a single energy-independent scattering time) to model the spectra and obtain the (complex) conductivity and, by estimating the doping concentration n and effective mass m^* , the mobility (Eq. 5).

$$\hat{\sigma}(\omega) = \frac{ne^2\tau}{m^* \cdot (1 - i\omega\tau)} \quad (5)$$

For highly conducting polymers, THz parameters have been shown to be similar to electric measurements. However, for the case of rather low-conductivity systems, the classic Drude model is not appropriate. Such polymers require a more elaborate spectral fitting and aiding information (e.g. as proposed in the localized Drude model) [94]. Low-conductivity samples have been investigated using combined THz domain and infrared reflection spectroscopy to estimate the conductivity and mobility.

3. Conclusions and outlook

The emergence of a metal-insulator transition in conducting polymers, even when occurring at low temperatures, is an important step towards superior electrical transport. Isotropic metallic polymers can play a lead role as sustainable contenders for transparent conducting oxides, rare earth based magnets, noble metal catalysts and heavy metal thermoelectric active layers. The here discussed metallic phases in numerous polymers provides the evidence that extrinsic sources of disorder can be effectively suppressed with the consequence that low-temperature isotropic metallic phases are no longer exceptional. In particular combined processing and synthesis strategies represent successful routes to achieve superior homogeneity and isotropy – a clear advancement compared to earlier metallic polymers, which are dominated by nematic phases e.g. polyacetylene or polypyrrole with explicit anisotropy factors.

Nonetheless, further efforts are required, particularly to improve the intrinsic properties. These are mainly the intense phonon scattering and the weakness of the intermolecular transfer integrals. Theoretical calculations as well as the here deeper discussed magnetotransport measurements show that both effects prevent metallic states at higher temperatures [95–97]. In order to increase the metallic character of polymers, one has to improve those intrinsic properties thus to shift the metal-insulator transition temperature towards room temperatures. This requires to strengthen the intermolecular binding [66,98]. Experi-

mentally, this concept has been proven by using small ion doping, incorporation of stronger hydrogen binding among the molecules and by applying hydrostatic pressure. Consistently, these led to increase the metallic regime towards room temperature [27,49]. Such fully metallic polymers represent serious alternatives for the aforementioned applications in optoelectronics, magnetics and thermoelectrics, but also open new fields for instance (photo)electrocatalysis.

Declaration of Competing Interest

The author declares no competing interests.

Acknowledgements

P.S. is grateful to the Austrian Exchange Service (OEAD, IN10/2015) for financial support. P.S. acknowledges the financial support from the Austrian Science Foundation (FWF I3822-N37, "Sustainable Catalysis"). The author thanks N. Serdar Sariciftci and Reghu Menon for fruitful discussions. This project was supported by the European Regional Development Fund (ERDF, IWB 2014-2020, 2018-98299, "Artificial Food") and the your career grant from the Linz Institute of Technology (LIT, LIT-2017-4-YOU-005, "Conductive Biopolymer Carbonate Reduction") at the Johannes Kepler University Linz.

References

- O. Bubnova, Z.U. Khan, A. Malti, S. Braun, M. Fahlman, M. Berggren, X. Crispin, Optimization of the thermoelectric figure of merit in the conducting polymer poly(3,4-ethylenedioxythiophene), *Nat. Mater.* 10 (2011) 429–433, <https://doi.org/10.1038/nmat3012>.
- Y.H. Kim, C. Sachse, M.L. Machala, C. May, L. Müller-Meskamp, K. Leo, Highly conductive PEDOT:PSS electrode with optimized solvent and thermal post-treatment for ITO-free organic solar cells, *Adv. Funct. Mater.* 21 (2011) 1076–1081, <https://doi.org/10.1002/adfm.201002290>.
- N. Kim, B.H. Lee, D. Choi, G. Kim, H. Kim, J.-R. Kim, J. Lee, Y.H. Kahng, K. Lee, Role of Interchain Coupling in the metallic state of conducting polymers, *Phys. Rev. Lett.* 109 (2012) 106405, <https://doi.org/10.1103/PhysRevLett.109.106405>.
- E. Jin Bae, Y. Hun Kang, K.-S. Jang, S. Yun Cho, Enhancement of thermoelectric properties of PEDOT:PSS and tellurium-PEDOT:PSS hybrid composites by simple chemical treatment, *Sci. Rep.* 6 (2016) 18805, <https://doi.org/10.1038/srep18805>.
- J. Luo, D. Billep, T. Waechter, T. Otto, M. Toader, O. Gordan, E. Sherebet, J. Martin, M. Hietschold, D.R.T. Zahn, T. Gessner, Enhancement of the thermoelectric properties of PEDOT:PSS thin films by post-treatment, *J. Mater. Chem. A Mater. Energy Sustain.* 1 (2013) 7576, <https://doi.org/10.1039/c3ta11209h>.
- H. Park, S.H. Lee, F.S. Kim, H.H. Choi, I.W. Cheong, J.H. Kim, Enhanced thermoelectric properties of PEDOT:PSS nanofilms by a chemical dedoping process, *J. Mater. Chem. A Mater. Energy Sustain.* 2 (2014) 6532, <https://doi.org/10.1039/c3ta14960a>.
- T. Park, C. Park, B. Kim, H. Shin, E. Kim, Flexible PEDOT electrodes with large thermoelectric power factors to generate electricity by the touch of fingertips, *Energy Environ. Sci.* 6 (2013) 788, <https://doi.org/10.1039/c3ee23729j>.

- [8] O. Bubnova, Z.U. Khan, A. Malti, S. Braun, M. Fahlman, M. Berggren, X. Crispin, Optimization of the thermoelectric figure of merit in the conducting polymer poly(3,4-ethylenedioxythiophene), *Nat. Mater.* 10 (2011) 429–433, <https://doi.org/10.1038/nmat3012>.
- [9] M. Scholdt, H. Do, J. Lang, A. Gall, A. Colmsmann, U. Lemmer, J.D. Koenig, M. Winkler, H. Boettner, Organic semiconductors for thermoelectric applications, *J. Korean Inst. Electr. Electron. Mater. Eng.* 39 (2010) 1589–1592, <https://doi.org/10.1007/s11664-010-1271-8>.
- [10] Y. Xia, K. Sun, J. Ouyang, Solution-processed metallic conducting polymer films as transparent electrode of optoelectronic devices, *Adv. Mater.* 24 (2012) 2436–2440, <https://doi.org/10.1002/adma.201104795>.
- [11] A. Ugur, F. Katmis, M. Li, L. Wu, Y. Zhu, K.K. Varanasi, K.K. Gleason, Low-dimensional conduction mechanisms in highly conductive and transparent conjugated polymers, *Adv. Mater.* 27 (2015) 4604–4610, <https://doi.org/10.1002/adma.201502340>.
- [12] B.J. Worfolk, S.C. Andrews, S. Park, J. Reinspach, N. Liu, M.F. Toney, S.C.B. Mannsfeld, Z. Bao, Ultrahigh electrical conductivity in solution-sheared polymeric transparent films, *Proc. Natl. Acad. Sci.* 112 (2015) 14138–14143, <https://doi.org/10.1073/pnas.1509958112>.
- [13] X. Crispin, F.L.E. Jakobsson, A. Crispin, P.C.M. Grim, P. Andersson, A. Volodin, C. van Haesendonck, M. Van der Auweraer, W.R. Salaneck, M. Berggren, 2006.200, The origin of the high conductivity of (PEDOT–PSS) plastic Electrodes, *Chem. Mater.* 18 (2006) 4354–4360, <https://doi.org/10.1021/cm061032+>.
- [14] O. Bubnova, Z.U. Khan, H. Wang, S. Braun, D.R. Evans, M. Fabretto, P. Hojati-Talemi, D. Dagnelund, J.-B. Arlin, Y.H. Geerts, S. Desbief, D.W. Breiby, J.W. Andreasen, R. Lazzaroni, W.M. Chen, I. Zozoulenko, M. Fahlman, P.J. Murphy, M. Berggren, X. Crispin, Semi-metallic polymers, *Nat. Mater.* 13 (2014) 190–194, <https://doi.org/10.1038/nmat3824>.
- [15] Aa. Farah, Sa. Rutledge, A. Schaarschmidt, R. Lai, J.P. Freedman, A.S. Helmy, Conductivity enhancement of poly(3,4-ethylenedioxythiophene)-poly(styrenesulfonate) films post-spincoating, *J. Appl. Phys.* 112 (2012)113709, <https://doi.org/10.1063/1.4768265>.
- [16] A.J. Heeger, Semiconducting and metallic polymers: the fourth generation of polymeric materials, *J. Phys. Chem. B* 105 (2001) 8475–8491, <https://doi.org/10.1021/jp011611w>.
- [17] A.G. MacDiarmid, A.J. Heeger, Organic metals and semiconductors: the chemistry of polyacetylene, (CHX), and its derivatives, *Synth. Met.* 1 (1980) 101–118, [https://doi.org/10.1016/0379-6779\(80\)90002-8](https://doi.org/10.1016/0379-6779(80)90002-8).
- [18] D. Farka, H. Coskun, J. Gasiorowski, C. Cobet, K. Hingerl, L.M. Uiberlacker, S. Hild, T. Greunz, D. Stifter, N.S. Sariciftci, R. Menon, W. Schoefberger, C.C. Mare, A.W. Hassel, C. Schwarzinger, M.C. Scharber, P. Stadler, Anderson-localization and the Mott-Loeffel-regel limit in glassy-metallic PEDOT, *Adv. Electron. Mater.* (2017)1700050, <https://doi.org/10.1002/aeml.201700050>.
- [19] D. Farka, A.O.F. Jones, R. Menon, N.S. Sariciftci, P. Stadler, Metallic conductivity beyond the Mott minimum in PEDOT: sulphate at low temperatures, *Synth. Met.* 240 (2018) 59–66, <https://doi.org/10.1016/j.synthmet.2018.03.015>.
- [20] O. Bubnova, Z.U. Khan, H. Wang, S. Braun, D.R. Evans, M. Fabretto, P. Hojati-Talemi, D. Dagnelund, J.-B. Arlin, Y.H. Geerts, S. Desbief, D.W. Breiby, J.W. Andreasen, R. Lazzaroni, W.M. Chen, I. Zozoulenko, M. Fahlman, P.J. Murphy, M. Berggren, X. Crispin, Semi-metallic polymers, *Nat. Mater.* 13 (2014) 190–194, <https://doi.org/10.1038/nmat3824>.
- [21] M.N. Gueye, A. Carella, N. Massonnet, E. Yvenou, S. Brenet, J. Faure-Vincent, S. Pouget, F. Rietdorf, H. Okuno, A. Benayad, R. Demadrille, J.-P. Simonato, Structure and expert engineering in PEDOT thin films: practical tools for a dramatic conductivity enhancement, *Chem. Mater.* 28 (2016) 3462–3468, <https://doi.org/10.1021/acs.chemmater.6b01035>.
- [22] T.-R. Chou, S.-H. Chen, Y.-T. Chiang, Y.-T. Lin, C.-Y. Chao, Highly conductive PEDOT:PSS films by post-treatment with dimethyl sulfoxide for ITO-free liquid crystal display, *J. Mater. Chem. C* 3 (2015) 3760–3766, <https://doi.org/10.1039/C5TC00276A>.
- [23] N. Massonnet, A. Carella, A. de Geyer, J. Faure-Vincent, J.-P. Simonato, Metallic behaviour of acid doped highly conductive polymers, *Chem. Sci.* 6 (2015) 412–417, <https://doi.org/10.1039/C4SC02463J>.
- [24] S. Kivelson, W.-P. Su, J.R. Schrieffer, A.J. Heeger, Missing bond-charge repulsion in the extended Hubbard model: effects in polyacetylene, *Phys. Rev. Lett.* 58 (1987) 1899–1902, <https://doi.org/10.1103/PhysRevLett.58.1899>.
- [25] M.J. Winokur, J. Maron, Y. Cao, A.J. Heeger, Disorder and staging in iodine-doped polyacetylene, *Phys. Rev. B* 45 (1992) 9656–9662, <https://doi.org/10.1103/PhysRevB.45.9656>.
- [26] Y. Cao, P. Smith, A.J. Heeger, Mechanical and electrical properties of highly oriented polyacetylene films, *Synth. Met.* 41 (1991) 181–184, [https://doi.org/10.1016/0379-6779\(91\)91033-7](https://doi.org/10.1016/0379-6779(91)91033-7).
- [27] R. Menon, C.O. Yoon, D. Moses, A.J. Heeger, Pressure and magnetic field dependence of the low temperature resistivity of PF6-doped polypyrrole, *Synth. Met.* 64 (1994) 53–57, [https://doi.org/10.1016/0379-6779\(94\)90274-7](https://doi.org/10.1016/0379-6779(94)90274-7).
- [28] R. Menon, Conductivity and magnetoconductance in iodine-doped polyacetylene, *Synth. Met.* 80 (1996) 223–229, [https://doi.org/10.1016/S0379-6779\(96\)03706-X](https://doi.org/10.1016/S0379-6779(96)03706-X).
- [29] C.O. Yoon, M. Reghu, A.J. Heeger, E.B. Park, Y.W. Park, K. Akagi, H. Shirakawa, Effect of anisotropy on conductivity and magnetoconductance in heavily doped polyacetylene, *Synth. Met.* 69 (1995) 79–80, [https://doi.org/10.1016/0379-6779\(94\)02372-6](https://doi.org/10.1016/0379-6779(94)02372-6).
- [30] K. Väkiparta, R. M., M.R. Andersson, Y. Cao, D. Moses, A.J. Heeger, Temperature dependence of the electrical conductivity of potassium-doped polyacetylene as a function of pressure and magnetic field, *Phys. Rev. B* 47 (1993) 9977–9980, <https://doi.org/10.1103/PhysRevB.47.9977>.
- [31] Y.-W. Park, A.J. Heeger, M.A. Druy, A.G. MacDiarmid, Electrical transport in doped polyacetylene, *J. Chem. Phys.* 73 (1980) 946–957, <https://doi.org/10.1063/1.440214>.
- [32] L.W. Shacklette, R.R. Chance, D.M. Ivory, G.G. Miller, R.H. Baughman, Electrical and optical properties of highly conducting charge-transfer complexes of poly(p-phenylene), *Synth. Met.* 1 (1980) 307–320, [https://doi.org/10.1016/0379-6779\(80\)90020-X](https://doi.org/10.1016/0379-6779(80)90020-X).
- [33] M. Nyman, O.J. Sandberg, S. Dahlström, D. Spoltore, C. Körner, Y. Zhang, S. Barlow, S.R. Marder, K. Leo, K. Vandewal, R. Österbacka, Doping-induced carrier profiles in organic semiconductors determined from capacitive extraction-current transients, *Sci. Rep.* 7 (2017) 5397, <https://doi.org/10.1038/s41598-017-05499-3>.
- [34] D. Brault, M. Lepinoy, P. Limelette, B. Schimaltz, F. Tran Van, Electrical transport crossovers and thermopower in doped polyaniline conducting polymer, *J. Appl. Phys.* 122 (2017)225104, <https://doi.org/10.1063/1.5003576>.
- [35] R. Menon, C.O. Yoon, D. Moses, A.J. Heeger, Y. Cao, Transport in polyaniline near the critical regime of the metal-insulator transition, *Phys. Rev. B* 48 (1993) 17685–17694, <https://doi.org/10.1103/PhysRevB.48.17685>.
- [36] A.N. Aleshin, V.I. Kozub, D.-S. Suh, Y.W. Park, Low-temperature saturation of dephasing in heavily doped polyacetylene, *Phys. Rev. B* 64 (2001)224208, <https://doi.org/10.1103/PhysRevB.64.224208>.
- [37] Y.W. Park, E.S. Choi, D.S. Suh, Metallic temperature dependence of resistivity in perchlorate doped polyacetylene, *Synth. Met.* 96 (1998) 81–86, [https://doi.org/10.1016/S0379-6779\(98\)00078-2](https://doi.org/10.1016/S0379-6779(98)00078-2).
- [38] T. Harada, H. Ito, Y. Ando, S. Watanabe, H. Tanaka, S. Kuroda, Signature of the insulator-metal transition of a semicrystalline conjugated polymer in ionic-liquid-gated transistors, *Appl. Phys. Express.* 8 (2015)021601, <https://doi.org/10.7567/APEX.8.021601>.
- [39] S. Zanetini, J.F. Dayen, C. Etrillard, N. Leclerc, M.V. Kamalakar, B. Doudin, Magnetoconductance anisotropy of a polymer thin film at the onset of metallicity, *Appl. Phys. Lett.* 106 (2015)063303, <https://doi.org/10.1063/1.4908526>.
- [40] A.I. Larkin, D.E. Khmel'nitskii, Activation conductivity in disordered systems with large localization length, *Sov. Phys. JETP* 56 (1982) 647–652.
- [41] H.T. Yi, Y.N. Gartstein, V. Podzorov, Charge carrier coherence and Hall effect in organic semiconductors, *Sci. Rep.* 6 (2016) 23650, <https://doi.org/10.1038/srep23650>.
- [42] K. Kang, S. Watanabe, K. Broch, A. Sepe, A. Brown, I. Nasrallah, M. Nikolka, Z. Fei, M. Heeney, D. Matsumoto, K. Marumoto, H. Tanaka, S. Kuroda, H. Sirringhaus, 2D coherent charge transport in highly ordered conducting polymers doped by solid state diffusion, *Nat. Mater.* 15 (2016) 896–902, <https://doi.org/10.1038/nmat4634>.
- [43] P. Stadler, D. Farka, H. Coskun, E.D. Glowacki, C. Yumusak, L.M. Uiberlacker, S. Hild, L.N. Leonat, M.C. Scharber, P. Klapetek, R. Menon, N.S. Sariciftci, Local order drives the metallic state in PEDOT:PSS, *J. Mater. Chem. C* 4 (2016) 6982–6987, <https://doi.org/10.1039/C6TC02129H>.
- [44] H.T. Yi, Y.N. Gartstein, V. Podzorov, Charge carrier coherence and Hall effect in organic semiconductors, *Sci. Rep.* 6 (2016) 23650, <https://doi.org/10.1038/srep23650>.
- [45] S.D. Kang, G.J. Snyder, Charge-transport model for conducting polymers, *Nat. Mater.* 16 (2017) 252–257, <https://doi.org/10.1038/nmat4784>.
- [46] R.S. Kohlman, A. Zibold, D.B. Tanner, G.G. Ihas, T. Ishiguro, Y.G. Min, A.G. MacDiarmid, A.J. Epstein, Limits for metallic conductivity in conducting polymers, *Phys. Rev. Lett.* 78 (1997) 3915–3918, <https://doi.org/10.1103/PhysRevLett.78.3915>.
- [47] A.B. Kaiser, Electronic transport properties of conducting polymers and carbon nanotubes, *Rep. Prog. Phys.* 64 (2001) 1.
- [48] A. Aleshin, R. Kiebooms, R. Menon, A.J. Heeger, Electronic transport in doped poly(3,4-ethylenedioxythiophene) near the metal-insulator transition, *Synth. Met.* 90 (1997) 61–68, [https://doi.org/10.1016/S0379-6779\(97\)81227-1](https://doi.org/10.1016/S0379-6779(97)81227-1).
- [49] K. Lee, S. Cho, S. Heum Park, A.J. Heeger, C.-W. Lee, S.-H. Lee, Metallic transport in polyaniline, *Nature* 441 (2006) 65–68, <https://doi.org/10.1038/nature04705>.
- [50] A. Girlando, A. Painelli, Z.G. Soos, Electron/phonon coupling in conjugated polymers: Reference force field and transferable coupling constants for polyacetylene, *J. Chem. Phys.* 98 (1993) 7459–7465, <https://doi.org/10.1063/1.464684>.
- [51] K. Lee, A.J. Heeger, Optical investigation of intra and interchain charge dynamics in conducting polymers, *Synth. Met.* 128 (2002) 279–282, [https://doi.org/10.1016/S0379-6779\(02\)00006-1](https://doi.org/10.1016/S0379-6779(02)00006-1).
- [52] C. Cobet, J. Gasiorowski, D. Farka, P. Stadler, Polarons in conjugated polymers, in: K.-J. Hinrichs, Eichhorn Karsten (Eds.), *Ellipsom. Funct. Org. Surfaces Film.*, 2018, pp. 355–387, https://doi.org/10.1007/978-3-319-75895-4_16.
- [53] C. Cobet, J. Gasiorowski, R. Menon, K. Hingerl, S. Schlager, M.S. White, H. Neugebauer, N.S. Sariciftci, P. Stadler, Influence of molecular designs on polaronic and vibrational transitions in a conjugated push-pull copolymer, *Sci. Rep.* 6 (2016) 35096, <https://doi.org/10.1038/srep35096>.
- [54] Y. Yamashita, J. Tsurumi, F. Hinkel, Y. Okada, J. Soeda, W. Zajackowski, M. Baumgarten, W. Pisula, H. Matsui, K. Müllen, J. Takeya, Transition between band and hopping transport in polymer field-effect transistors, *Adv. Mater.* 26 (2014) 8169–8173, <https://doi.org/10.1002/adma.201403767>.
- [55] R. Menon, C.O. Yoon, D. Moses, A.J. Heeger, Y. Cao, Transport in polyaniline near the critical regime of the metal-insulator transition, *Phys. Rev. B* 48 (1993) 17685–17694, <https://doi.org/10.1103/PhysRevB.48.17685>.

- [56] H. Wang, U. Ail, R. Gabrielsson, M. Berggren, X. Crispin, Ionic seebeck effect in conducting polymers, *Adv. Energy Mater.* 5 (2015) 1500044 <https://doi.org/10.1002/aenm.201500044>.
- [57] J.P. Lock, S.G. Im, K.K. Gleason, Oxidative chemical vapor deposition of electrically conducting poly(3,4-ethylenedioxythiophene) films, *Macromolecules* 39 (2006) 5326–5329, <https://doi.org/10.1021/ma060113o>.
- [58] K. Zuber, M. Fabretto, C. Hall, P. Murphy, Improved PEDOT conductivity via suppression of crystallite formation in Fe(III) tosylate during vapor phase polymerization, *Macromol. Rapid Commun.* 29 (2008) 1503–1508, <https://doi.org/10.1002/marc.200800325>.
- [59] D. Farka, H. Coskun, P. Bauer, D. Roth, B. Bruckner, P. Klapetek, N.S. Sariciftci, P. Stadler, Increase in electron scattering length in PEDOT:PSS by a triflic acid post-processing, *Monatsh. Chem. Mon.* 148 (2017) 871–877, <https://doi.org/10.1007/s00706-017-1973-1>.
- [60] Y. Honma, K. Itoh, H. Masunaga, A. Fujiwara, T. Nishizaki, S. Iguchi, T. Sasaki, Mesoscopic 2D charge transport in commonplace PEDOT:PSS films, *Adv. Electron. Mater.* 4 (2018) 1700490 <https://doi.org/10.1002/aem.201700490>.
- [61] Y. Du, X. Cui, L. Li, H. Tian, W.-X. Yu, Z.-X. Zhou, Dielectric properties of DMSO-Doped-PEDOT:PSS at THz frequencies, *Phys. Status Solidi* 255 (2018) 1700547 <https://doi.org/10.1002/psbb.201700547>.
- [62] P. Kovacic, G. del Hierro, W. Livernois, K.K. Gleason, Scale-up of oCVD: large-area conductive polymer thin films for next-generation electronics, *Mater. Horiz.* 2 (2015) 221–227, <https://doi.org/10.1039/C4MH00222A>.
- [63] X. Wang, A. Ugur, H. Goktas, N. Chen, M. Wang, N. Lachman, E. Kalfon-Cohen, W. Fang, B.L. Wardle, K.K. Gleason, Room temperature resistive volatile organic compound sensing materials based on a hybrid structure of vertically aligned carbon nanotubes and conformal oCVD/ICVD polymer coatings, *ACS Sens.* 1 (2016) 374–383, <https://doi.org/10.1021/acssens.5b00208>.
- [64] A.M. Coclite, R.M. Howden, D.C. Borrelli, C.D. Petruczuk, R. Yang, J.L. Yagüe, A. Ugur, N. Chen, S. Lee, W.J. Jo, A. Liu, X. Wang, K.K. Gleason, 25th anniversary article: CVD polymers: a new paradigm for surface modification and device fabrication, *Adv. Mater.* 25 (2013) 5392–5423, <https://doi.org/10.1002/adma.201301878>.
- [65] S. Lee, K.K. Gleason, Enhanced optical property with tunable band gap of cross-linked PEDOT copolymers via oxidative chemical vapor deposition, *Adv. Funct. Mater.* 25 (2015) 85–93, <https://doi.org/10.1002/adfm.201402924>.
- [66] H. Coskun, A. Aljabour, P. De Luma, D. Farka, T. Greunz, D. Stifter, M. Kus, X. Zheng, M. Liu, A.W. Hassel, W. Schöfberger, E.H. Sargent, N.S. Sariciftci, P. Stadler, Biofunctionalized conductive polymers enable efficient CO₂ electroreduction, *Sci. Adv.* 3 (2017) e1700686 <https://doi.org/10.1126/sciadv.1700686>.
- [67] T. Hasan Gilani, T. Masui, G.Yu. Logvenov, T. Ishiguro, Low-temperature Hall effect and thermoelectric power in metallic PF₆-doped polypyrrole, *Synth. Met.* 78 (1996) 327–331, [https://doi.org/10.1016/0379-6779\(96\)80156-1](https://doi.org/10.1016/0379-6779(96)80156-1).
- [68] R. Menon, C.O. Yoon, D. Moses, Y. Cao, A.J. Heeger, Tuning through the critical regime of the metal-insulator transition in conducting polymers by pressure and magnetic field, *Synth. Met.* 69 (1995) 329–332, [https://doi.org/10.1016/0379-6779\(94\)02471-A](https://doi.org/10.1016/0379-6779(94)02471-A).
- [69] J. Ma, J.E. Fischer, Y. Cao, A.J. Heeger, X-ray structural study of trans-polyacetylene at high pressure, *Solid State Commun.* 83 (1992) 395–399, [https://doi.org/10.1016/0038-1098\(92\)90075-K](https://doi.org/10.1016/0038-1098(92)90075-K).
- [70] W.P. Su, J.R. Schrieffer, A.J. Heeger, Soliton excitations in polyacetylene, *Phys. Rev. B* 22 (1980) 2099–2111, <https://doi.org/10.1103/PhysRevB.22.2099>.
- [71] N.F. Mott, *Metal-Insulator Transitions*, Taylor & Francis LTD, 1974.
- [72] G. Bergmann, Physical interpretation of weak localization: a time-of-flight experiment with conduction electrons, *Phys. Rev. B* 28 (1983) 2914–2920, <https://doi.org/10.1103/PhysRevB.28.2914>.
- [73] G. Bergmann, Weak localization in thin films, *Phys. Rep.* 107 (1984) 1–58, [https://doi.org/10.1016/0370-1573\(84\)90103-0](https://doi.org/10.1016/0370-1573(84)90103-0).
- [74] R. Menon, K. Vákiparta, Y. Cao, D. Moses, Pressure dependence of the conductivity and magnetoconductance in oriented iodine-doped polyacetylene, *Phys. Rev. B* 49 (1994) 16162–16170, <https://doi.org/10.1103/PhysRevB.49.16162>.
- [75] Y. Nogami, H. Kaneko, H. Ito, T. Ishiguro, T. Sasaki, N. Toyota, A. Takahashi, J. Tsukamoto, Low-temperature electrical conductivity of highly conducting polyacetylene in a magnetic field, *Phys. Rev. B* 43 (1991) 11829–11839, <https://doi.org/10.1103/PhysRevB.43.11829>.
- [76] P.W. Anderson, Absence of diffusion in certain random lattices, *Phys. Rev.* 109 (1958) 1492–1505, <https://doi.org/10.1103/PhysRev.109.1492>.
- [77] T.F. Rosenbaum, R.F. Milligan, G.A. Thomas, P.A. Lee, T.V. Ramakrishnan, R.N. Bhatt, K. DeConde, H. Hess, T. Perry, Low-temperature magnetoresistance of a disordered metal, *Phys. Rev. Lett.* 47 (1981) 1758–1761, <https://doi.org/10.1103/PhysRevLett.47.1758>.
- [78] S. Hikami, A.I. Larkin, Y. Nagaoka, Spin-orbit interaction and magnetoresistance in the two dimensional random system, *Prog. Theor. Phys. Suppl.* 63 (1980) 707–710, <https://doi.org/10.1143/PTP.63.707>.
- [79] I. Shlimak, M. Kaveh, State of Mott minimal metallic conductivity in a scaling approach to the metal-insulator transition in doped semiconductors, *Phys. Rev. B* 58 (1998) 15333–15335, <https://doi.org/10.1103/PhysRevB.58.15333>.
- [80] S. Wang, M. Ha, M. Manno, C. Daniel Frisbie, C. Leighton, Hopping transport and the Hall effect near the insulator-metal transition in electrochemically gated poly(3-hexylthiophene) transistors, *Nat. Commun.* 3 (2012) 1210, <https://doi.org/10.1038/ncomms2213>.
- [81] B. Lee, Y. Chen, D. Fu, H.T. Yi, K. Czelen, H. Najafov, V. Podzorov, Trap healing and ultralow-noise Hall effect at the surface of organic semiconductors, *Nat. Mater.* 12 (2013) 1125–1129, <https://doi.org/10.1038/nmat3781>.
- [82] P. Stadler, L.N. Leonat, R. Menon, H. Coskun, S. van Frank, C. Rankl, M.C. Scharber, Stable Hall voltages in presence of dynamic quasi-continuum bands in poly(3,4-ethylene-dioxythiophene), *Org. Electron.* 65 (2019) 412–418, <https://doi.org/10.1016/j.orgel.2018.12.001>.
- [83] K. Seeger, W.D. Gill, T.C. Clarke, G.B. Street, Conductivity and Hall effect measurements in doped polyacetylene, *Solid State Commun.* 28 (1978) 873–878, [https://doi.org/10.1016/0038-1098\(78\)90177-1](https://doi.org/10.1016/0038-1098(78)90177-1).
- [84] R.S. Klein, Investigation of the Hall effect in impurity-hopping conduction, *Phys. Rev. B* 31 (1985) 2014–2021, <https://doi.org/10.1103/PhysRevB.31.2014>.
- [85] T. Uemura, M. Yamagishi, J. Soeda, Y. Takatsuki, Y. Okada, Y. Nakazawa, J. Takeya, Temperature dependence of the Hall effect in pentacene field-effect transistors: possibility of charge decoherence induced by molecular fluctuations, *Phys. Rev. B* 85 (2012) 035313 <https://doi.org/10.1103/PhysRevB.85.035313>.
- [86] J.-F. Chang, T. Sakanoue, Y. Olivier, T. Uemura, M.-B. Dufour-Madee, S.G. Yeates, J. Cornil, J. Takeya, A. Troisi, H. Sirringhaus, Hall-effect measurements probing the degree of charge-carrier delocalization in solution-processed crystalline molecular semiconductors, *Phys. Rev. Lett.* 107 (2011) 066601 <https://doi.org/10.1103/PhysRevLett.107.066601>.
- [87] L. Friedman, Hall conductivity of amorphous semiconductors in the random phase model, *J. Non. Solids* 6 (1971) 329–341, [https://doi.org/10.1016/0022-3093\(71\)90024-X](https://doi.org/10.1016/0022-3093(71)90024-X).
- [88] L. Friedman, N.F. Mott, The Hall effect near the metal-insulator transition, *J. Non. Solids* 7 (1972) 103–108, [https://doi.org/10.1016/0022-3093\(72\)90021-X](https://doi.org/10.1016/0022-3093(72)90021-X).
- [89] F. Yan, E.P.J. Parrott, B.S.-Y. Ung, E. Pickwell-MacPherson, Solvent doping of PEDOT:PSS: effect on terahertz optoelectronic properties and utilization in terahertz devices, *J. Phys. Chem. C* 119 (2015) 6813–6818, <https://doi.org/10.1021/acs.jpcc.5b00465>.
- [90] M. Yamashita, C. Otani, H. Okuzaki, M. Shimizu, Nondestructive measurement of carrier mobility in conductive polymer PEDOT:PSS using Terahertz and infrared spectroscopy, *IEEE, 2011 XXXth URSI Gen. Assem. Sci. Symp* (2011) 1–4, <https://doi.org/10.1109/URSIGASS.2011.6050616>.
- [91] E. Nguema, V. Vigneras, J.L. Miane, P. Mounaix, Dielectric properties of conducting polyaniline films by THz time-domain spectroscopy, *Eur. Polym. J.* 44 (2008) 124–129, <https://doi.org/10.1016/j.eurpolymj.2007.10.020>.
- [92] T.-I. Jeon, D. Grischkowsky, A.K. Mukherjee, R. Menon, Electrical characterization of conducting polypyrrole by THz time-domain spectroscopy, *Appl. Phys. Lett.* 77 (2000) 2452–2454, <https://doi.org/10.1063/1.1319188>.
- [93] T.-I. Jeon, D. Grischkowsky, A.K. Mukherjee, R. Menon, Electrical and optical characterization of conducting poly-3-methylthiophene film by THz time-domain spectroscopy, *Appl. Phys. Lett.* 79 (2001) 4142–4144, <https://doi.org/10.1063/1.1427754>.
- [94] M. Yamashita, C. Otani, M. Shimizu, H. Okuzaki, Effect of solvent on carrier transport in poly(3,4-ethylenedioxythiophene)/poly(4-styrenesulfonate) studied by terahertz and infrared-ultraviolet spectroscopy, *Appl. Phys. Lett.* 99 (2011) 143307 <https://doi.org/10.1063/1.3647574>.
- [95] G. Brocks, Polarons and bipolarons in oligothiophenes: a first principles study, *Synth. Met.* 102 (1999) 914–915, [https://doi.org/10.1016/S0379-6779\(98\)00958-8](https://doi.org/10.1016/S0379-6779(98)00958-8).
- [96] P. Vogl, D.K. Campbell, First-principles calculations of the three-dimensional structure and intrinsic defects in trans-polyacetylene, *Phys. Rev. B* 41 (1990) 12797–12817, <https://doi.org/10.1103/PhysRevB.41.12797>.
- [97] U. Salzner, Electronic structure of conducting organic polymers: insights from time-dependent density functional theory, *Wiley Interdiscip. Rev. Comput. Mol. Sci.* 4 (2014) 601–622, <https://doi.org/10.1002/wcms.1194>.
- [98] H. Coskun, A. Aljabour, L. Uiberacker, M. Strobel, S. Hild, C. Cobet, D. Farka, P. Stadler, N.S. Sariciftci, Chemical vapor deposition - based synthesis of conductive polydopamine thin-films, *Thin Solid Films* 645 (2018) 320–325, <https://doi.org/10.1016/j.tsf.2017.10.063>.

List of manuscripts

Manuscript 1

P. Stadler, D. Farka, H. Coskun, E. D. Głowacki, C. Yumusak, L. M. Uiberlacker, S. Hild, L. N. Leonat, M. C. Scharber, P. Klapetek, R. Menon, N. S. Sariciftci, Local order drives the metallic state in PEDOT:PSS, *J. Mater. Chem. C* 4 (29) (2016) 6982–6987. doi:10.1039/C6TC02129H.

Manuscript 2

D. Farka, H. Coskun, P. Bauer, D. Roth, B. Bruckner, P. Klapetek, N. S. Sariciftci, P. Stadler, Increase in electron scattering length in PEDOT:PSS by a triflic acid post-processing, *Monatshefte für Chemie - Chemical Monthly* 148 (5) (2017) 871–877. doi:10.1007/s00706-017-1973-1.

Manuscript 3

D. Farka, H. Coskun, J. Gasiorowski, C. Cobet, K. Hingerl, L. M. Uiberlacker, S. Hild, T. Greunz, D. Stifter, N. S. Sariciftci, R. Menon, W. Schoefberger, C. C. Mardare, A. W. Hassel, C. Schwarzinger, M. C. Scharber, P. Stadler, Anderson-Localization and the Mott-Ioffe-Regel Limit in Glassy-Metallic PEDOT, *Advanced Electronic Materials* (2017) 1700050doi:10.1002/aelm.201700050.

Manuscript 4

D. Farka, A. O. Jones, R. Menon, N. S. Sariciftci, P. Stadler, Metallic conductivity beyond the Mott minimum in PEDOT: Sulphate at low temperatures, *Synthetic Metals* 240 (2018) 59–66. doi:10.1016/j.synthmet.2018.03.015.

Manuscript 5

P. Stadler, L. N. Leonat, R. Menon, H. Coskun, S. van Frank, C. Rankl, M. C. Scharber, Stable Hall voltages in presence of dynamic quasi-continuum bands in poly(3,4-ethylene-dioxythiophene), *Organic Electronics* 65 (2019) 412–418. doi:10.1016/j.orgel.2018.12.001.

Manuscript 6

H. Coskun, A. Aljabour, P. De Luna, D. Farka, T. Greunz, D. Stifter, M. Kus,

X. Zheng, M. Liu, A. W. Hassel, W. Schöfberger, E. H. Sargent, N. S. Sariciftci, P. Stadler, Biofunctionalized conductive polymers enable efficient CO₂ electroreduction, *Science Advances* 3 (8) (2017) e1700686. doi:10.1126/sciadv.1700686.

Manuscript 7

H. Coskun, A. Aljabour, L. Uiberlacker, M. Strobel, S. Hild, C. Cobet, D. Farka, P. Stadler, N. S. Sariciftci, Chemical vapor deposition - based synthesis of conductive polydopamine thin-films, *Thin Solid Films* 645 (August 2017) (2018) 320–325. doi:10.1016/j.tsf.2017.10.063.

Manuscript 8

C. Cobet, J. Gasiorowski, R. Menon, K. Hingerl, S. Schlager, M. S. White, H. Neugebauer, N. S. Sariciftci, P. Stadler, Influence of molecular designs on polaronic and vibrational transitions in a conjugated push-pull copolymer, *Scientific Reports* 6 (2016) 35096. doi:10.1038/srep35096.

Manuscript 9

G. Adam, M. Kaltenbrunner, E. D. Głowacki, D. H. Apaydin, M. S. White, H. Heilbrunner, S. Tombe, P. Stadler, B. Ernecker, C. W. Klampfl, N. S. Sariciftci, M. C. Scharber, Solution processed perovskite solar cells using highly conductive PEDOT:PSS interfacial layer, *Solar Energy Materials and Solar Cells* 157 (2016) 318–325. doi:10.1016/j.solmat.2016.05.011

Manuscript 10

C. Cobet, J. Gasiorowski, D. Farka, P. Stadler, Polarons in Conjugated Polymers, in: K.-J. Hinrichs, Karsten, Eichhorn (Ed.), *Ellipsometry of Functional Organic Surfaces and Films*, 2018, pp. 355–387. doi:10.1007/978-3-319-75895-4_16.

Manuscript 11

P. Stadler, Isotropic metallic transport in conducting polymers, *Synthetic Metals* (2019) *early view*. doi:10.1016/j.synthmet.2019.06.004.

5 Teaching activities

5.1 Lectures and courses

1. Lecture “Current topics in physical chemistry” – organic semiconductors (1.5 ECTS)
Lecture on current topics and fundamentals in physical chemistry, with focus on conducting polymers, transport phenomena and related concurrent topics in electronics and optoelectronics.
Lecture ID: 346.050 (2014, ongoing)
2. Lecture “Organic electronics” (3.0 ECTS)
Lecture on current topics and fundamentals in organic electronics.
Lecture ID: 346.778 (2015, ongoing)
3. Laboratory in physical chemistry I – practical laboratory course (4.8 ECTS)
Laboratory course in physical chemistry, subsection electrochemistry.
Lecture ID: 349.060 and 349.201 and 349.001 (2015 to 2019)
4. Lecture “Physical Chemistry – Electrochemistry” (1.5 ECTS)
Lecture in bachelor program
Lecture ID: 349.010 (2018)
5. Lecture “Spectroelectrochemistry” (3.0 ECTS)
Special lecture on spectroelectrochemistry (combined spectroscopic methods and electrochemistry, particular focus infrared, Raman, UV-vis and related)
Lecture ID: 346.220 (2018, ongoing)
6. Laboratory “Technische Elektrochemie” (1.5 ECTS)
Laboratory course in master programm chemistry and chemical engineering.
Lecture ID: 317.002 (2018, ongoing)

5.2 Supervision of PhD, Master and Bachelor Students

1. **2015, Supervision of Shaimaa A. Mohammed, PhD**
S.A.M. received a travel grant from the ICTP (International Centre for Theoretical Physics, ANEX fellowship program) in the framework of African Network

for Solar Energy (ANSOLE) and joined my team to work on organic solar cells. She finished her degree in July 2015. Currently she holds a faculty position at Center for Photonic and Smart Materials, Zewail City of Science and Technology, Egypt as leading scientist. CV.

2. **2015 to 2018, Supervision of Halime Coskun-Aljabour, PhD**

Halime Coskun-Aljabour started her PhD program in December 2015 and worked on the development of functional conducting polymers. She defended her PhD in December 2018 (passed with distinction). She received a best-presentation prize at the EMRS Fall meeting in Warsaw 2017. CV.

3. **2015 to 2018, Supervision of Domink Farka, PhD**

Dominik Farka started his PhD program in March 2015 and worked on the development of metallic conductivity in PEDOT systems. He defended his PhD in May 2018. He joined the Institute of Semiconductor and Solid State Physics as post-doctoral fellow from May to December 2019. In 2017, he was appointed as excellent student fellow to join the Lindau Nobel meeting.

Undergraduate supervision (bachelor & master)

1. **2019, Supervision of David Doppelbauer (Master program technical physics, ongoing)**

Topic: "ZnCo₂O₄ as (Photo)Electrocatalyst for the Oxygen Evolution Reaction"
D.D. joined my team to work on photoelectrochemical water splitting in the framework of the FWF project "Sustainable Catalysis".

2. **2019, Co-supervision of Markus Gusenbauer (Master program technical physics, ongoing)**

Topic: "Transparent all-oxide solar cells"

3. **2019, Supervision of Frantisek Jirik (Bachelor program biochemistry, ongoing)**

Topic: "Photoelectrochemical CO₂ Reduction using polydopamine"

F.J. joined my team in the framework of the EFRE (European Funds for Regional Development) project "Artificial Food".

4. **2019, Supervision of Stefan Poellner (Bachelor program chemistry, ongoing)**

Topic: "Investigation of Polydopamine as a Catalyst for Oxygen Evolution Reaction"

S.P. joined my team for generating full-cycle energy conversion in the framework of the FWF project "Sustainable Catalysis".

6 List of Publications

6.1 Scientific papers (peer reviewed / SCI indexed)

1. M. Takeda, K. Hojo, K. Umemoto, M. C. Scharber, P. Stadler, C. Yumusak, N. S. Sariciftci, M. S. White, M. Furis, S. Okada, T. Yoshida, J. Matsui, A. Masuhara, Photoconductive Properties of Dibenzotetrathiafulvalene-Tetracyanoquinodimethane (DBTTF-TCNQ) Nanorods Prepared by the Reprecipitation Method, *Journal of Nanoscience and Nanotechnology* 19 (8) (2019) 4599–4602. doi:10.1166/jnn.2019.16346.
2. H. Langhals, U. Ritter-Faizade, P. Stadler, M. Havlicek, A. Hofer, N. S. Sariciftci, Persistent radical anions in the series of peri-arylenes: broadband light absorption until far in the NIR and purely organic magnetism, *Monatshefte für Chemie - Chemical Monthly* doi:10.1007/s00706-019-02404-8.
3. K. Uda, Y. Tsuda, S. Okada, R. Yamakado, L. Sun, Y. Suzuri, M. S. White, M. Furis, P. Stadler, O. Dimitriev, T. Yoshida, Concerted Photoluminescence of Electrochemically Self-Assembled CuSCN/Stilbazolium Dye Hybrid Thin Films, *ACS Omega* 4 (2) (2019) 4056–4062. doi:10.1021/acsomega.8b03632.
4. P. Stadler, L. N. Leonat, R. Menon, H. Coskun, S. van Frank, C. Rankl, M. C. Scharber, Stable Hall voltages in presence of dynamic quasi-continuum bands in poly(3,4-ethylene-dioxythiophene), *Organic Electronics* 65 (2019) 412–418. doi:10.1016/j.orgel.2018.12.001.
5. H. Sun, H. Takahashi, N. Nishiumi, Y. Kamada, K. Sato, K. Nedu, Y. Matsushima, A. Khosla, M. Kawakami, H. Furukawa, P. Stadler, T. Yoshida, Vanadium Redox Flow Batteries Fabricated by 3D Printing and Employing Recycled

- Vanadium Collected from Ammonia Slag, *Journal of The Electrochemical Society* 166 (9) (2019) B3125–B3130. doi:10.1149/2.0251909jes.
6. D. Farka, A. O. Jones, R. Menon, N. S. Sariciftci, P. Stadler, Metallic conductivity beyond the Mott minimum in PEDOT: Sulphate at low temperatures, *Synthetic Metals* 240 (2018) 59–66. doi:10.1016/j.synthmet.2018.03.015.
 7. A. Aljabour, H. Coskun, D. H. Apaydin, F. Ozel, A. W. Hassel, P. Stadler, N. S. Sariciftci, M. Kus, Nanofibrous cobalt oxide for electrocatalysis of CO₂ reduction to carbon monoxide and formate in an acetonitrile-water electrolyte solution, *Applied Catalysis B: Environmental* 229 (2018) 163–170. doi:10.1016/j.apcatb.2018.02.017.
 8. H. Coskun, A. Aljabour, L. Uiberlacker, M. Strobel, S. Hild, C. Cobet, D. Farka, P. Stadler, N. S. Sariciftci, Chemical vapor deposition - based synthesis of conductive polydopamine thin-films, *Thin Solid Films* 645 (August 2017) (2018) 320–325. doi:10.1016/j.tsf.2017.10.063.
 9. X. Zheng, P. De Luna, F. P. García de Arquer, B. Zhang, N. Becknell, M. B. Ross, Y. Li, M. N. Banis, Y. Li, M. Liu, O. Voznyy, C. T. Dinh, T. Zhuang, P. Stadler, Y. Cui, X. Du, P. Yang, E. H. Sargent, Sulfur-Modulated Tin Sites Enable Highly Selective Electrochemical Reduction of CO₂ to Formate, *Joule* doi:10.1016/j.joule.2017.09.014.
 10. H. Coskun, A. Aljabour, P. De Luna, D. Farka, T. Greunz, D. Stifter, M. Kus, X. Zheng, M. Liu, A. W. Hassel, W. Schöfberger, E. H. Sargent, N. S. Sariciftci, P. Stadler, Biofunctionalized conductive polymers enable efficient CO₂ electroreduction, *Science Advances* 3 (8) (2017) e1700686. doi:10.1126/sciadv.1700686.
 11. B. Sun, O. Voznyy, H. Tan, P. Stadler, M. Liu, G. Walters, A. H. Proppe, M. Liu, J. Fan, T. Zhuang, J. Li, M. Wei, J. Xu, Y. Kim, S. Hoogland, E. H. Sargent, Pseudohalide-Exchanged Quantum Dot Solids Achieve Record Quantum Efficiency in Infrared Photovoltaics, *Advanced Materials* (2017) 1700749doi:10.1002/adma.201700749.
 12. D. Farka, H. Coskun, J. Gasiorowski, C. Cobet, K. Hingerl, L. M. Uiberlacker, S. Hild, T. Greunz, D. Stifter, N. S. Sariciftci, R. Menon, W. Schoefberger, C. C.

- Mardare, A. W. Hassel, C. Schwarzinger, M. C. Scharber, P. Stadler, Anderson-Localization and the Mott-Ioffe-Regel Limit in Glassy-Metallic PEDOT, *Advanced Electronic Materials* (2017) 1700050 doi : 10.1002/aelm.201700050.
13. D. Farka, H. Coskun, P. Bauer, D. Roth, B. Bruckner, P. Klapetek, N. S. Sariciftci, P. Stadler, Increase in electron scattering length in PEDOT:PSS by a triflic acid post-processing, *Monatshefte für Chemie - Chemical Monthly* 148 (5) (2017) 871–877. doi:10.1007/s00706-017-1973-1.
 14. Y. Tsuda, H. Sun, L. Sun, S. Okada, A. Masuhara, P. Stadler, N. S. Sariciftci, M. S. White, T. Yoshida, Electrochemical self-assembly of CuSCN-DAST hybrid thin films, *Monatshefte für Chemie - Chemical Monthly* 148 (5) (2017) 845–854. doi:10.1007/s00706-017-1929-5.
 15. A. Toba, J. Matsui, K.-i. Nakayama, T. Yoshida, C. Yumusak, P. Stadler, M. C. Scharber, M. S. White, N. S. Sariciftci, A. Masuhara, Organic Microboxes Prepared by Self-assembly of a Charge-transfer Dye, *Chemistry Letters* 46 (4) (2017) 557–559. doi:10.1246/cl.161191.
 16. A. Aljabour, D. H. Apaydin, H. Coskun, F. Ozel, M. Ersoz, P. Stadler, N. S. Sariciftci, M. Kus, Improvement of Catalytic Activity by Nanofibrous CuInS₂ for Electrochemical CO₂ Reduction, *ACS Applied Materials & Interfaces* 8 (46) (2016) 31695–31701. doi:10.1021/acsami.6b11151.
 17. G. Adam, M. Kaltenbrunner, E. D. Głowacki, D. H. Apaydin, M. S. White, H. Heilbrunner, S. Tombe, P. Stadler, B. Ernecker, C. W. Klampfl, N. S. Sariciftci, M. C. Scharber, Solution processed perovskite solar cells using highly conductive PEDOT:PSS interfacial layer, *Solar Energy Materials and Solar Cells* 157 (2016) 318–325. doi:10.1016/j.solmat.2016.05.011.
 18. D. Marinotto, S. G. Danelli, A. Giaretta, E. Lucenti, P. Stadler, E. Tordin, G. Mattei, G. Scavia, R. Ugo, E. Cariati, Thermal layer-by-layer preparation of oriented films of a Cu(i) ionic inorganic–organic hybrid material showing semi-conducting and SHG properties, *J. Mater. Chem. C* 4 (29) (2016) 7077–7082. doi:10.1039/C6TC02388F.
 19. P. Stadler, D. Farka, H. Coskun, E. D. Głowacki, C. Yumusak, L. M. Uiberlacker, S. Hild, L. N. Leonat, M. C. Scharber, P. Klapetek, R. Menon, N. S. Sariciftci,

- Local order drives the metallic state in PEDOT:PSS, *J. Mater. Chem. C* 4 (29) (2016) 6982–6987. doi:10.1039/C6TC02129H.
20. C. Cobet, J. Gasiorowski, R. Menon, K. Hingerl, S. Schlager, M. S. White, H. Neugebauer, N. S. Sariciftci, P. Stadler, Influence of molecular designs on polaronic and vibrational transitions in a conjugated push-pull copolymer, *Scientific Reports* 6 (2016) 35096. doi:10.1038/srep35096.
 21. S. A. Mohamed, J. Gasiorowski, K. Hingerl, D. R. Zahn, M. C. Scharber, S. S. Obayya, M. K. El-Mansy, N. S. Sariciftci, D. A. Egbe, P. Stadler, CuI as versatile hole-selective contact for organic solar cell based on anthracene-containing PPE-PPV, *Solar Energy Materials and Solar Cells* 143 (2015) 369–374. doi:10.1016/j.solmat.2015.07.003.
 22. G. Adam, F. Aslan, E. Portenkirchner, P. Stadler, M. C. Scharber, N. S. Sariciftci, Electrocatalytic Reduction of Carbon Dioxide using Sol-gel Processed Copper Indium Sulfide (CIS) Immobilized on ITO-Coated Glass Electrode, *Electrocatalysis* 6 (4) (2015) 405–413. doi:10.1007/s12678-015-0257-y.
 23. C. Enengl, S. Enengl, M. Havlicek, P. Stadler, E. D. Glowacki, M. C. Scharber, M. White, K. Hingerl, E. Ehrenfreund, H. Neugebauer, N. S. Sariciftci, The Role of Heteroatoms Leading to Hydrogen Bonds in View of Extended Chemical Stability of Organic Semiconductors, *Advanced Functional Materials* 25 (42) (2015) 6679–6688. doi:10.1002/adfm.201503241.
 24. S. Enengl, C. Enengl, P. Stadler, H. Neugebauer, N. S. Sariciftci, Spectroelectrochemical Studies on Quinacridone by Using Poly(vinyl alcohol) Coating as Protection Layer, *ChemPhysChem* 16 (10) (2015) 2206–2210. doi:10.1002/cphc.201500165.
 25. P. Stadler, S. A. Mohamed, J. Gasiorowski, M. Sytnyk, S. Yakunin, M. C. Scharber, C. Enengl, S. Enengl, D. A. M. Egbe, M. K. El-Mansy, S. S. A. Obayya, N. S. Sariciftci, K. Hingerl, W. Heiss, Iodide-Capped PbS Quantum Dots: Full Optical Characterization of a Versatile Absorber, *Advanced Materials* 27 (9) (2015) 1533–1539. doi:10.1002/adma.201404921.
 26. F. Aslan, G. Adam, P. Stadler, A. Goktas, I. H. Mutlu, N. S. Sariciftci, Sol-gel derived In₂S₃ buffer layers for inverted organic photovoltaic cells, *Solar Energy*

- 108 (2014) 230–237. doi:10.1016/j.solener.2014.07.011.
27. P. Stadler, B. R. Sutherland, Y. Ren, Z. Ning, A. Simchi, S. M. Thon, S. Hoogland, E. H. Sargent, Joint Mapping of Mobility and Trap Density in Colloidal Quantum Dot Solids, *ACS Nano* 7 (7) (2013) 5757–5762. doi:10.1021/nn401396y.
 28. O. Voznyy, D. Zhitomirsky, P. Stadler, Z. Ning, S. Hoogland, E. H. Sargent, A Charge-Orbital Balance Picture of Doping in Colloidal Quantum Dot Solids, *ACS Nano* 6 (9) (2012) 8448–8455. doi:10.1021/nn303364d.
 29. Z. Ning, Y. Ren, S. Hoogland, O. Voznyy, L. Levina, P. Stadler, X. Lan, D. Zhitomirsky, E. H. Sargent, All-Inorganic Colloidal Quantum Dot Photovoltaics Employing Solution-Phase Halide Passivation, *Advanced Materials* 24 (47) (2012) 6295–6299. doi:10.1002/adma.201202942.
 30. D. Zhitomirsky, M. Furukawa, J. Tang, P. Stadler, S. Hoogland, O. Voznyy, H. Liu, E. H. Sargent, N-Type Colloidal-Quantum-Dot Solids for Photovoltaics, *Advanced Materials* 24 (46) (2012) 6181–6185. doi:10.1002/adma.201202825.
 31. S. Schaur, P. Stadler, B. Meana-Esteban, H. Neugebauer, N. Serdar Sariciftci, Electrochemical doping for lowering contact barriers in organic field effect transistors, *Organic Electronics* 13 (8) (2012) 1296–1301. doi:10.1016/j.orgel.2012.03.020.
 32. M. Ullah, A. Pivrikas, I. Fishchuk, A. Kadashchuk, P. Stadler, C. Simbrunner, N. Sariciftci, H. Sitter, Electric field and grain size dependence of Meyer–Neldel energy in C60 films, *Synthetic Metals* 161 (17-18) (2011) 1987–1990. doi:10.1016/j.synthmet.2011.07.008.
 33. M. Ullah, A. Pivrikas, I. I. Fishchuk, A. Kadashchuk, P. Stadler, C. Simbrunner, N. S. Sariciftci, H. Sitter, Effect of source-drain electric field on the Meyer–Neldel energy in organic field effect transistors, *Applied Physics Letters* 98 (22) (2011) 223301. doi:10.1063/1.3584131.
 34. G. Schwabegger, M. Ullah, M. Irimia-Vladu, M. Baumgartner, Y. Kanbur, R. Ahmed, P. Stadler, S. Bauer, N. Sariciftci, H. Sitter, High mobility, low voltage operating C60 based n-type organic field effect transistors, *Synthetic Metals* 161 (19-20) (2011) 2058–2062. doi:10.1016/j.synthmet.2011.06.042.

35. M. Kaltenbrunner, P. Stadler, R. Schwödiauer, A. W. Hassel, N. S. Sariciftci, S. Bauer, Anodized Aluminum Oxide Thin Films for Room-Temperature-Processed, Flexible, Low-Voltage Organic Non-Volatile Memory Elements with Excellent Charge Retention, *Advanced Materials* 23 (42) (2011) 4892–4896. doi:10.1002/adma.201103189.
36. M. Ullah, A. K. Kadashchuk, P. Stadler, A. Kharchenko, A. Pivrikas, C. Simbrunner, N. S. Sariciftci, H. Sitter, Effect of film morphology on charge transport in C60 based Organic Field Effect Transistors, in: *Materials Research Society Symposium Proceedings*, 2010.
37. M. Ullah, I. I. Fishchuk, A. Kadashchuk, P. Stadler, A. Pivrikas, C. Simbrunner, V. N. Poroshin, N. S. Sariciftci, H. Sitter, Dependence of Meyer–Neldel energy on energetic disorder in organic field effect transistors, *Applied Physics Letters* 96 (21) (2010) 213306. doi:10.1063/1.3435477.
38. P. Stadler, A. M. Track, M. Ullah, H. Sitter, G. J. Matt, G. Koller, T. B. Singh, H. Neugebauer, N. Serdar Sariciftci, M. G. Ramsey, The role of the dielectric interface in organic transistors: A combined device and photoemission study, *Organic Electronics* 11 (2) (2010) 207–211. doi:10.1016/j.orgel.2009.10.017.
39. C. S. S. Sangeeth, P. Stadler, S. Schaur, N. S. Sariciftci, R. Menon, Interfaces and traps in pentacene field-effect transistor, *Journal of Applied Physics* 108 (11) (2010) 113703. doi:10.1063/1.3517085.
40. S. Abd Al-Baqi, G. Henandez-Sosa, H. Sitter, B. Singh, P. Stadler, N. Sariciftci, Rubrene thin film characteristics on mica, in: *Springer Proceedings in Physics*, Vol. 129, 2009. doi:10.1007/978-3-540-95930-4_7.
41. P. Stadler, A. Fuchsbauer, G. Hesser, T. Fromherz, G. Matt, H. Neugebauer, S. Sariciftci, Negative differential resistance in C60 diodes, in: *Springer Proceedings in Physics*, Vol. 129, 2009. doi:10.1007/978-3-540-95930-4_31.
42. A. Pivrikas, P. Stadler, H. Neugebauer, N. S. Sariciftci, Substituting the postproduction treatment for bulk-heterojunction solar cells using chemical additives, *Organic Electronics* 9 (5) (2008) 775–782. doi:10.1016/j.orgel.2008.05.021.

43. P. Stadler, G. Hesser, T. Fromherz, G. J. Matt, H. Neugebauer, S. N. Sariciftci, Current filamentation and negative differential resistance in C60 diodes, *physica status solidi (b)* 245 (10) (2008) 2300–2302. doi:10.1002/pssb.200879610.
44. P. Stadler, K. Oppelt, T. B. Singh, J. G. Grote, R. Schwödiauer, S. Bauer, H. Pigmayer-Brezina, D. Bäuerle, N. S. Sariciftci, Organic field-effect transistors and memory elements using deoxyribonucleic acid (DNA) gate dielectric, *Organic Electronics* 8 (6) (2007) 648–654. doi:10.1016/j.orgel.2007.05.003.
45. T. B. Singh, P. Senkarabacack, P. Stadler, H. Neugebauer, N. S. Sariciftci, J. Grote, Interfacial Effects in Organic Thin-Film Transistors, in: *Frontiers in Optics*, OSA, Washington, D.C., 2006, p. OPWC2. doi:10.1364/OPE.2006.OPWC2.
46. T. B. Singh, N. Marjanović, P. Stadler, M. Auinger, G. J. Matt, S. Günes, N. S. Sariciftci, R. Schwödiauer, S. Bauer, Fabrication and characterization of solution-processed methanofullerene-based organic field-effect transistors, *Journal of Applied Physics* 97 (8) (2005) 083714. doi:10.1063/1.1895466.

6.2 Patent

1. P. Stadler, H. Coskun, Elektrode zur elektrokatalytischen Wasserstoffentwicklungsreaktion AT520548 B1 2019-05-15 (2019).

6.3 Book chapters and reviews

1. P. Stadler, Isotropic metallic transport in conducting polymers, *Synthetic Metals* 240 (2019) 59–66. doi:10.1016/j.synthmet.2019.06.004.
2. C. Cobet, J. Gasiorowski, D. Farka, P. Stadler, Polarons in Conjugated Polymers, in: K.-J. Hinrichs, Karsten, Eichhorn (Ed.), *Ellipsometry of Functional Organic Surfaces and Films*, 2018, pp. 355–387. doi:10.1007/978-3-319-75895-4_16.
3. P. Stadler, A. M. Track, G. Koller, N. S. Sariciftci, M. G. Ramsey, Dipole-Controlled Energy Level Alignment at Dielectric Interfaces in Organic Field-Effect Transistors, 2013, pp. 273–293. doi:10.1007/978-3-642-33848-9_11.

6.4 Scientific conference proceedings & papers

1. T. Yoshida, M. S. White, G. Trimmel, P. Stadler, Solution-based emerging hybrid solar cells, *Monatshefte für Chemie - Chemical Monthly* 148 (5) (2017) 793–794. doi:10.1007/s00706-017-1974-0.
2. M. Ullah, A. K. Kadashchuk, P. Stadler, A. Kharchenko, A. Pivrikas, C. Simbrunner, N. S. Sariciftci, H. Sitter, Effect of film morphology on charge transport in C60 based Organic Field Effect Transistors, in: *Materials Research Society Symposium Proceedings*, 2010.
3. S. Abd Al-Baqi, G. Henandez-Sosa, H. Sitter, B. Singh, P. Stadler, N. Sariciftci, Rubrene thin film characteristics on mica, in: *Springer Proceedings in Physics*, Vol. 129, 2009. doi:10.1007/978-3-540-95930-4_7.
4. P. Stadler, A. Fuchsbauer, G. Hesser, T. Fromherz, G. Matt, H. Neugebauer, S. Sariciftci, Negative differential resistance in C60 diodes, in: *Springer Proceedings in Physics*, Vol. 129, 2009. doi:10.1007/978-3-540-95930-4_31.
5. P. Senkarabacak, P. Stadler, T. Singh, H. Neugebauer, N. Sariciftci, J. Grote, Interfacial effects in organic thin-film transistors, in: *Optics InfoBase Conference Papers*, 2006.

6.5 Thesis

1. P. Stadler, *Interfacial Effects in Organic Thin-Film Transistors*, Diploma Thesis, Johannes Kepler University Linz, Faculty of Natural Sciences and Engineering, 2007.
2. P. Stadler, *Interfacial Effects in Organic Semiconductor Heterojunctions*, PhD Thesis, Johannes Kepler University Linz, Faculty of Natural Sciences and Engineering, 2011.

7 Curriculum Vitae

Curriculum Vitae Philipp Stadler

• PERSONAL INFORMATION

Stadler, Philipp; Date of birth: **4.6.1981** Nationality: **Austria**

URL for web site: www.jku.at/ipc

Bibliometrics: 50 peer-reviewed papers & patents

ResearchID: [F-6773-2014](https://orcid.org/0000-0001-6459-5574);

ORCID: <https://orcid.org/0000-0001-6459-5574>



• EDUCATION

2011 PhD (passed with distinction) "Interfacial effects in organic semiconductor heterojunctions"

Department of Chemistry, University of Linz, Austria

2007 Master "Hysteresis in Bio-Organic Field-Effect Transistors"

Department of Chemistry, University of Linz, Austria

1999-2000 Military Service

1999 School leaving examination Matura at Gymnasium Freistadt, Upper Austria

• CURRENT POSITION(S)

2015 – University Assistant

Institute of Physical Chemistry, University of Linz, Austria

• PREVIOUS POSITIONS

2012 – 2015 Post Doctoral Position

Linz Institute of Organic Solar Cells, University of Linz, Austria

2011 – 2012 Post Doctoral Position

Department of Electrical and Computer Engineering, University of Toronto, ON, Canada (Prof. Edward H. [Sargent's group](#))

• SABBATICAL

06/2016 – 09/2016 Scholarship/sabbatical "Internationalization of University of Linz", Department of Electrical and Computer Engineering, University of Toronto, ON, Canada

• (CO-)SUPERVISION OF GRADUATE STUDENTS AND POSTDOCTORAL FELLOWS

2015 [Shaimaa A. Mohammed](#) (framework of African Network for Solar Energy, PhD degree in 2015), currently faculty position at Center for Photonic and Smart Materials, Zewail City of Science and Technology. [CV](#)

2015 – 2018 [Halime Coskun-Aljabour](#) (PhD candidate, start Dec. 2015, Defense 20.Dec.2018). HCA received a best-presentation prize at EMRS Fall meeting Warsaw 2017. [CV](#)

2015 – 2018 Dominik Farka (PhD candidate start March 2015, Defense 9.May 2018), D.F. holds a position as post doctoral fellow at the Institute of Semiconductor and Solid State Physics, JKU, Austria. [CV](#)

• **TEACHING ACTIVITIES**

2015 – now Institute of Physical Chemistry / University of Linz (lecturer)
Lecture “Organic electronics” (3.0 ECTS)
Lecture “Current topics in physical chemistry” – org. semiconductors (1.5 ECTS)
Laboratory in physical chemistry I – 3 practical laboratory course (4.8 ECTS)
Lecture “Physical Chemistry – Electrochemistry” (1.5 ECTS)
Lecture “Spectroelectrochemistry” (3.0 ECTS)
Lecture “Technische Elektrochemie” (1.5 ECTS)

• **HIGHLIGHTS – VISIBILITY IN SCIENTIFIC MEETINGS**

2016 **Main organizer**, Symposium in EMRS Meeting (Fall) 2016 in Warsaw (PL), “Solution-based emerging hybrid solar cells”, 56 scientific contributions
<https://link.springer.com/article/10.1007/s00706-017-1974-0>

2017 **Main organizer**, Symposium in MRS Spring Meeting 2017 in Phoenix (USA), “Nanostructured Quantum-Confined Materials for Advanced Optoelectronics”, 125 scientific contributions
<http://www.mrs.org/spring2017/spring-2017-symposia/?code=ED6>

2020 **Main organizer**, (intended) Symposium in MRS Fall Meeting 2020 in Boston (USA), “Sustainable Catalysis”, *submitted*

• **INVITED CONTRIBUTIONS**

1. Material Research Society, Spring 2011: “In-situ photoemission on an organic field-effect transistor”
2. Prague Macromolecular Meeting, 2017: “3rd generation conductive polymers – metallic, transparent conductors and functional electrodes”
3. Austrian Chemistry Day 2017: Conductive polymers – transparent conductors and functional electrodes
4. Austrian Chemistry Society Meeting 2018: Chapter Physical Chemistry – Electrochemistry: “Bio-inspired functional motifs for selective metal-devoid electrocatalysis”
5. 4DMS Electrochemical Society Meeting 2018, Yonezawa, Japan: “Conductive biopolymers for selective metal-devoid electrocatalysis”
6. EMRS Fall Meeting 2019 Warsaw: “In-situ ATR-FTIR spectroelectrochemistry”

• **SCIENTIFIC GRANTS AS PRINCIPAL INVESTIGATOR**

2018 – 2020 “Sustainable Catalysis”, Austrian Science Foundation (FWF), Joint Project Japan-Austria
Volume: EUR 200 000.-

- 2019 – 2021 “Artificial Food”, European Fund for Development (EFRE)
Volume: EUR 230 000.-
- 2019 – 2020 “Carbonate Reduction”, Linz Institute of Technology (LIT)
Volume: EUR 110 000.-
- 2015 – 2018 “Nanomorphology in conducting polymers”, Austrian Exchange Service (OEAD), Indian-Austrian project
Volume: EUR 20 000.-

- **OTHER SCIENTIFIC ACTIVITIES**

Invited as Opponent in PhD Defence of [Daniel Balasz](#) (Phd), Prof. M. A. Loi, Groningen University, 2018

- **ACTIVITY AS REFEREE**

Reviewer for ACS Nano, Advanced Materials and sub-journals, Science Advances, Organic Electronics, Thin Solid Films, Solar Energy Materials and Solar Cells, Journal of Mat. Chem. C

Guest Editor for Chemical Monthly, Springer (2016), special edition.

Review activities for the The Netherlands Organisation for Scientific Research (NWO)

- **MEMBERSHIPS OF SCIENTIFIC SOCIETIES**

2017 – Material Research Society

2009 – Member of Austrian Chemical Society (Chapter Physical Chemistry)

- **MAJOR COLLABORATIONS**

Vice-President University of Toronto Professor Edward H. [Sargent](#)

Department of Electrical and Computer Engineering, University of Toronto, ON, Canada

Professor Reghu [Menon](#)

Department of Physics, Indian Institute of Science, Bangalore, India

Professor Tsukasa [Yoshida](#)

Research Center for Organic Electronics, Yamagata University, Yonezawa, Japan

- **CAREER BREAKS**

4.01.2013 – 3.04.2013 Paternity leave

SCIENTIFIC CAREER

My PhD has been focused in the endeavoring scientific field of organic electronics. In 2011, during my first post-doctoral fellowship, I moved into the field of colloidal quantum dots in Professor E. H. Sargent’s laboratory at the University of Toronto (Canada) – one of the world-leading groups in emerging photovoltaics. My early achievements both during PhD and as post-doctoral fellow have been published in several high-impact publications.

In 2013 I moved to Linz (Austria) and after an interruption (paternity leave for 3 months) I took over several positions as post-doctoral fellow (University of Linz, Linz Institute of Organic Solarcells) in solar cell-related projects. In 2015, I finally was promoted as university assistant

(assistant Professor) at the Institute of Physical Chemistry, University of Linz (Austria). Here, I conceived and set up a new laboratory for conducting (functional) polymers. I initiated my independent research direction toward the development of novel electrocatalysts based on organic conducting matter.

SOCIAL, TECHNICAL AND SCIENTIFIC SKILLS

I have excellent language skills in English. I have contributed to more than 10 peer-reviewed international journals as corresponding author, I contributed as active writer in book chapters, patents, funding agency reports and funding agency proposals. In addition, I have excellent skills in my native language German and I hold a level of B2 in Spanish.

I am experienced working in international atmosphere and in an international joint projects. I am used to be a member in an intercultural team. I have continuously active collaborations with scientific groups in Canada, India and Japan.

My technical, theoretical and lecture skills involve the broad field of (organic) electronics, quantized systems as well as electrochemistry and optics. These skills include administrative experience in building up laboratories, international calls for tender, negotiations and correspondence with international companies and agencies as well as laboratory safety and organization. I have demonstrated leadership by organizing scientific symposia for the material research society (MRS) and I have been invited at various international conferences and universities as speaker, committee member or visitor to present my research and initiate collaboration.

Since 2015 I received 5 scientific grants as principal investigator (PI) with a total volume of 554kEuro. Two grants are international joint projects (one with India, one with Japan). One grant is an early-career grant to establish my own research. Two grants started at the beginning of 2019. A list of all grants is shown in the appendix.

Appendix: All ongoing grants and funding as principal investigator (PI)

<i>Project Title</i>	<i>Funding source</i>	<i>Amount (kEuros)</i>	<i>Period</i>	<i>Role of the PI</i>	<i>Topic</i>
IN-2015-10	OeAD GmbH (WTZ)	20	2015-2018*	PI, coordinator Co-PI: Prof. Reghu Menon , Indian Institute of Science, Bangalore	Development of conducting polymers
W911NF-17-1-0169	Army Research Office (ARO support for symposium organizer)	4 (USD)	2017	PI, coordinator or main organizer	Symposium support at the material research society MRS (2017, Phoenix, AZ, USA)
Sustainable Catalysis	Austrian Science Foundation (FWF)	190k	2018-2020	PI (Joint Project with Japan) Co-PI: Prof. Tsukasa Yoshida , Yamagata University	conducting polymer electrocatalysts, energy conversion
CarboRed LIT-2017-4-YOU-005	Linz Institute of Technology (LIT)	109k	2019-2020	PI, Young Career Project	conducting polymers, carbonate reduction; electrocatalysis
Artificial Food (ArtFood)	EFRE Upper Austria, Funds for regional development	240k	2019-2020	PI	CO ₂ -recycling to carbon fragments; electrocatalysis

*closed in 2018, Jan.